Numéro National de Thèse : 2017LYSEN053

THESE de DOCTORAT DE L'UNIVERSITE DE LYON

opérée par

l'Ecole Normale Supérieure de Lyon

Ecole Doctorale N°206
Ecole Doctorale de Chimie

Spécialité de doctorat : Chimie

Soutenue publiquement le 21/12/2017, par :

Fabien CARON

Bridging the gap between spectroscopic and catalytic properties of supported CoMoS catalysts

(Rationalisation des propriétés catalytiques des catalyseurs CoMoS supportés par approches spectroscopiques)

Devant le jury composé de :

Sylvette Brunet, Directrice de Recherche CNRS, Université de Poitiers	Rapporteur
Arnaud Travert, Professeur, Université de Caen	Rapporteur
Daniel Bianchi, Professeur Emérite, Université Claude Bernard Lyon 1	Examinateur
Xavier Carrier, Professeur, Université Pierre et Marie Curie, Paris VI	Examinateur
Silvia Bordiga, Professeur, Université de Turin, Italie	Examinatrice
Pascal Raybaud, Ingénieur de recherches HDR., IFPEN	Directeur de thèse
Mickaël Rivallan, Ingénieur de recherches, IFPEN	Examinateur
Antoine Daudin, Ingénieur de recherches, IFPEN	Examinateur

- Remerciements -

Cette thèse a été réalisée à IFP Energies Nouvelles au sein de la division Catalyse et Séparation, département Catalyse par les Sulfures. Je tiens donc en premier lieu à remercier Mr Denis Guillaume et M. Luc Nougier ainsi que Mme. Magalie ROY-AUBERGER pour m'avoir accueilli au sein de l'entreprise.

Je remercie également M. Pascal Raybaud et Mme. Silvia Bordiga qui m'ont suivi et accompagné en tant que directeur et co-directrice de thèse. Je souhaite également remercier chaleureusement M. Mickaël Rivallan et M. Antoine Daudin, mes co-promoteurs de thèse, qui m'ont encadré, conseillé et apporté leur expérience tout au long de la thèse.
Je tenais aussi à remercier, Mme. Sylvette Brunet et M. Arnaud Travert d'avoir bien voulu juger ce mémoire et en être les rapporteurs ainsi que M. Xavier Carrier et M. Daniel Bianchi de s'être rendus disponible pour participer au jury de thèse.

Je tiens également à remercier M. Jean-Marc Schweitzer et M. Alberto Silvia pour leur aide dans le domaine de la catalyse et cinétique ainsi que Mme. Cristhèle Legens et M. Philippe Lecour pour leur aide pour les analyses XPS, Mme. Séverine Humbert pour sa précieuse aide en modélisation moléculaire, Mme. Anne-Sophie Gay et Mme. Anne-Lise Taleb pour leur temps passé à la réalisation de clichés TEM et STEM, ainsi que l'ensemble de l'équipe du bureau d'étude pour la conception de l'unité GC-DRIFT.

Je tiens aussi à remercier tous les membres du département Catalyse par les Sulfures de m'avoir accueilli et accompagné tant sur le plan professionnel que sur le plan humain : Anne, Julie, Véronique, Gracinda, George, Jean-Louis, Amaury, Julien, Matthieu, Denis, Malaurie, Elodie, Marie-Paule…
Je tiens également à remercier l'équipe du laboratoire d'infrarouge et de RMN, Manu, Frédéric et Laurent avec qui j'ai apprécié travailler et simplement passer du temps.

Je tiens également à remercier les techniciens et ingénieurs que j'ai côtoyé pendant ces trois années, Luis, Antoine, Antoine, Nicolas, Nicolas, Manu, Fréderic, Cédric, Isabelle, David, Sylvain, Arnaud, Christophe, Nadège, Anthony, Philippe.
Je remercie aussi M. Eric Volland et tous les membres de l'ALSIP tennis, ainsi que Mme. Isabelle Clemencon et M. David Goncalves, mes coéquipiers de double.
Enfin un grand merci aux doctorants, post-doctorants et amis, Emile, Kevin, Wei, Zlatko, Leonor et Ruben, Marisa, Larissa, Sonia, Clément, Matthieu, Jérôme, ainsi qu'à mes co-bureaux qui ont eu la 'joie' de partager un bureau commun avec moi, Rick, Luis, Dina et Svetan.

Un grand merci à des amis Caro, Céline, Cora, Rick, Etienne, Pedro, Leonel, Magalie, Bilel, Tinhinane, Edith, Amélie, Sandrine, Fanélie, Daniele, Luc, Paola, Teresa et Susana, pour leurs grains de folie ;)
La team de Toulon/Arêches/Mazan qui a su me faire passer des week-ends détente pendant ces 3 ans, Camille, Violette, Pauline, Lulu, Rose, Matthieu, Julien et Mickäel.

Enfin mes dernières pensées iront vers ma famille et belle famille, mes parents, Père et Mère, mes deux sœurs, Céline et Pauline, ma compagne Hélène, qui m'ont soutenu (et supporté) pendant ces trois ans.

Table of contents

- General Introduction -.....1

- Chapter I - State of the art, challenges and strategies.....7

1 Hydrodesulfurization of FCC gasoline 9

1.1 Industrial and environmental issues.....9

1.2 Nature of the FCC gasoline 10

1.3 Selective HDS processes of the FCC gasoline.....12

2 HDS catalysts 13

2.1 General aspects 13

2.2 Active phase 15

2.2.1 Supported non-promoted catalysts 15

2.2.1.1 Precursor's oxide catalyst 15

2.2.1.2 Active phase models 16

2.2.1.3 Nano-scale structure.....19

2.2.2 Supported and promoted catalysts 22

2.2.2.1 Oxide state catalyst 23

2.2.2.2 Promoter effects on the morphology of the active phases.....24

2.2.2.3 Nano-scale structure of the CoMoS slab 26

3 Supports 28

3.1 Alumina support 28

3.1.1 Generalities.....28

3.1.2 Structure and physical characteristics of the supports 29

3.1.3 Surface properties of alumina 33

3.1.4 Alumina models.....34

3.1.4.1 Peri's Model 34

3.1.4.2 Tsyganenko and Filimonov's Model 35

3.1.4.3 Knözinger's Model 35

3.1.4.4 Busca's Model 37
3.1.4.5 Digne's Model 38

3.2 Silica 41
3.2.1 Generalities 41
3.2.2 Structure and physical characteristics 41

4 Influence of catalytic properties on selective HDS 46

4.1 Hydrodesulfurization and Hydrogenation reaction 46
4.1.1 Thiophene and derivative compounds: reactivity and HDS mechanism 46
4.1.2 Olefins: reactivity and hydrogenation mechanism 50
4.1.3 Nature of the sites involved 54

4.2 Reactivity and HDS/HYDO selectivity 60
4.2.1 Active phase and promoter effects 60
4.2.2 Supports effects 62
4.2.2.1 Indirect effect of the support 65
4.2.2.2 Direct effect of the support 68

5 Strategy and methodology 70

5.1 Strategy 70
5.2 Methodology 71

6 References 73

- Chapter II - Experimental methods 83

1. Catalysts and preparation 84

1.1 Target promoted catalysts 84
1.2 Experimentalprotocol 84

2. Oxide phase characterization 86

2.1 X-Ray Fluorescence 86
2.1.1 Principle 86
2.1.2 Results 87

2.2 Electron Micro Probe Analyzer (EPMA or Castaing micro probe) 88
2.2.1 Principle 88
2.2.2 Results 88
2.3 X-ray diffraction analysis 89
2.3.1 Principle 89
2.3.2 Results 90
3. Appendices 91

- Chapter III - Catalytic performances of the alumina and silica supported catalysts 99

1 Introduction 101
2 Experimental 102
2.1 Catalysts preparation 102
2.2 High pressure catalytic tests 103
2.2.1 Catalytic test conditions 103
2.2.2 GC analysis system 104
2.2.3 Transformation of 3MT and 23DMB2N 108
2.2.4 Conversion, yield and selectivity calculations 111
2.2.5 Activity calculation 112
3 Results and discussion 114
3.1 Co/Mo ratio effect 114
3.1.1 Evolution of 3MT and (23DMB2N+23DMB1N) conversions 114
3.1.1 Product distributions 116
3.1.1.1 Products from 3MT transformation 116
3.1.1.2 Products from 23DMB2N transformation 120
3.1.2 HDS/HYDO selectivity 123
3.2 Support effect 123
3.2.1 Evolution of 3MT and (23DMB2N+23DMB1N) conversions 124
3.2.2 Product distributions 127

3.2.2.1 Products from 3MT transformation 127
3.2.2.2 Products from 23DMB2N transformation 131
3.2.3 HDS/HYDO selectivity 134
3.3 Mo coverage effects 136
3.3.1 3MT and (23DMB2N+23DMB1N) conversion 137
3.3.2 Products distribution 138
3.3.2.1 Products from 3MT transformation 138
3.3.2.2 Products from (23DMB2N+23DMB1N) transformation 140
3.3.3 HDS/HYDO selectivity 142
4 Conclusions 144
5 Appendixes 146
6 References 171

- Chapter IV - Support's effects on the physico-chemical properties of the Co promoted MoS_2 phase 173

1 Introduction 175
2 Experiments 178
2.1 Catalysts preparation 178
2.2 Catalysts characterization 182
2.2.1 X-ray photoelectron spectroscopy (XPS) 182
2.2.2 High resolution transmission electron microscopy (HRTEM) 183
2.2.3 2D morphology model of CoMoS slabs 184
3 Results and discussion 187
3.1 Morphology and size analysis the CoMoS nano-crystallites 187
3.1.1 Analysis of mean sizes and stacking number by HRTEM 187
3.1.2 HR HAADF STEM analysis 190
3.1.2.1 2D and 3D morphology analysis 190
3.1.2.2 Effect of $\delta\theta$-Al_2O_3 facets on the CoMoS crystallites' sizes 193
3.1.2.3 Role of hydroxyls groups as function of the exposed facets 195

3.1.3 Impact on the catalytic activity and genesis of the active phase 197
3.1.4 Possible role of the corners and edges of γ-Al_2O_3 crystallites..... 199
3.2 Molybdenum and cobalt surface speciation 200
3.2.1 Analysis of Mo 3d levels BE by XPS and DFT 202
3.2.1.1 Case of dMo=2.2 at.nm^{-2} 202
3.2.1.2 Electronic effect of the support 203
3.2.1.3 Size effect correlated with low coordination edge sites 204
3.2.1.4 Promoter effect on Mo binding energy 207
3.2.1.5 Effect of Mo surface coverages 208
3.2.1.6 Mo species quantification..... 210
3.2.2 Analysis of Co 2p levels BE by XPS 211
3.2.2.1 Co species quantification 213
3.2.2.2 $(Co/Mo)_{slab}$ atomic ratio..... 215
3.3 2D morphology model of the CoMoS slab 216
3.3.1 Distribution of Co and Mo atoms at M-edge and S-edge 216
3.3.2 2D morphology model of the CoMoS slab vs catalytic activity of the HDS catalysts 220
4 Conclusion 222
5 Appendices..... 226
6 References..... 250

- Chapter V -Surface sites speciation of supported CoMoS phase probed by NO molecule: a combined IR and DFT study.....255

1 Introduction 256
2 Experimental and theoretical methods..... 258
2.1 Catalysts preparation..... 258
2.2 FTIR experiment..... 259

2.3 Chemometric method 260
2.4 DFT calculations 260
2.4.1 Total energy 260
2.4.2 Frequency calculations 262
3 Results and discussion 263
3.1 δθ-Al_2O_3 supported CoMoS catalysts 263
3.2 DFT calculation of NO adsorption on CoMoS edges 267
3.3 Comparison of Al_2O_3 and SiO_2 supported catalysts 276
3.4 Chemometric analysis 279
4 NO FTIR – structure – catalytic activity relationships 283
4.1 Total area of NO sorbed on HDS catalyst vs 2D morphology model of the CoMoS slab 283
4.2 Total area of NO sorbed on HDS catalyst vs catalytic activity of the HDS catalysts 284
5 Conclusions 286
6 References 288

- Chapter VI - In situ and operando DRIFT and ATR-IR characterization of 3-methylthiophene interactions on CoMoS/alumina and CoMoS/silica catalysts 291

1 Introduction 292
2 Experimental 296
2.1 Catalysts preparation 296
2.2 Characterization 297
2.2.1 Injection system set-up 297
2.2.2 DRIFT spectroscopy 298
2.2.3 ATR-IR spectroscopy 299

3 Results and discussion 299

3.1 In situ DRIFT 299

3.1.1 Alumina supported catalyst 299

3.1.2 Silica supported catalyst 303

3.2 Operando DRIFT Reaction of 3MT on CoMoS/γ-Al_2O_3 306

3.3 Insights into surface species by ATR-IR 308

4 Conclusion and perspectives 311

5 Appendices 313

6 References 317

- General Conclusions and Perspectives - 321

- General introduction -

- General introduction -

In the twenty-first century, many European environmental regulations aimed at decreasing toxic compound contents, especially sulphur-based ones, in the gasolines formulation. Sulphur specifications have become increasingly drastic and should not exceed 10 ppm in most part of Europe and many other countries around the world.[1–3]

Indeed, when combustion occurs in the automotive motors, sulphur compounds give mainly sulphur oxides SO_x, such as SO_2, which contributes to atmospheric pollution and are harmful to human health.[2,4] Thus, petrochemical companies have to remove sulfur contained in hydrocarbons and simultaneously produce gasolines with high-octane hydrocarbon molecules (such as olefins).

Gasoline cuts produced in refineries by the Fluid Catalytic Cracking (FCC) unit still contain a high concentration of sulfur. Hence, HyDroTreatment processes (HDT) are extensively used to remove undesirable sulfur containing molecules to produce more valuable, clean, and environmentally friendly fuels. Catalysts industrially used in the gasoline hydrodesulphurization (HDS) process are based on transition metal sulfide (TMS), usually a CoMoS phase, supported on alumina. Within this project, we will investigate the CoMoS phase supported on three relevant supports: two aluminas (γ-Al_2O_3, $\delta\theta$-Al_2O_3) and one silica (SiO_2) support.

Thus, regarding the main challenges highlighted above, research has to take up a threefold challenge: increasing the gasoline production ensuring a deep HDS of sulphur compounds while restricting the olefins hydrogenation (HYDO) in order to avoid the loss of octane number of gasoline.

The HDS/HYDO catalyst selectivity is thus a crucial parameter of this current issue. Several studies have been carried out to elucidate which driving forces control HDS catalyst selectivity. Influence of the TMS active phase, nature and morphology, on the activity and selectivity to the HDS catalysts has been extensively described in the literature over the past years, with a special focus also on the role of the promoter Co on the MoS_2 phase. More recently, the literature is concerned with describing the role of the support, as a non-

innocent component of the catalyst, which must be accounted for. Indeed, studies have underlined that the support may play significant roles on the catalytic performances of the HDS catalysts:

- an indirect role by modifying the MoS_2 active phase structural properties as its size, its two-dimensional or three-dimensional morphology , or its cobalt distribution.
- a direct role by taking part to the HDS and/or HYDO reactions: stabilization or destabilization of intermediates, reactants or products .

However, most of the published works attempt to investigate exclusively one key parameter in details and its effect on the activity and selectivity to the HDS catalysts which could be restrictive or limited only to the dedicated study.

Thus, the main objective of this project is to explore the possible cooperative and/or synergistic effect between various properties of the CoMoS active phase and its support by considering and analyzing the contribution of the most relevant parameters together which could, directly or indirectly, affect the catalytic performances of the HDS catalysts.

In order to i) bridge the gap between the catalytic performances observed and specific features of the CoMoS active phase and its support and ii) provide a rational interpretation of selectivity trend observed on the FCC gasoline, a multi-technique approach have been adopted. For that purpose, we will combine various spectroscopic techniques and density functional theory calculations on well-defined catalytic systems or models.

In that way, the manuscript is divided in six different chapters:

The **chapter I** is composed of three major sections providing general aspects on the HDT processes of FCC gasoline, the CoMoS active phase, with its associated support, and an overview of some relevant parameters impacting the HDS catalyst reactivity and selectivity reported so far. Finally, in line with the state of the art established, strategies and methodology adopted for the thesis is presented. Then, some aspects of the common experimental part (preparation of catalysts mainly) is exposed in the **chapter II**. Other more specific experimental and theoretical aspects will be also presented in each dedicated chapter.

Following on from these chapters, the results obtained in the present work will be reported and discussed in four subsequent chapters.

High pressure catalytic tests will be performed to collect a large set of experimental data in order to evaluate the promotor effect (Co/Mo ratio), the support effect and the impact of the molybdenum concentration at the support's surface on the activities and the selectivity for the CoMoS supported catalysts chosen. With the aims of making the link with the features of the HDS catalysts (CoMoS phase and support), qualitative and quantitative interpretation of the catalytic performances, as function of the three parameters mentioned above, will be discussed in **chapter III**.

The following chapters will address the characterization of HDS catalysts, the CoMoS active phase and its support, by different spectroscopic approaches.

A direct approach will be undertaken by using common spectroscopic analyses in the **chapter IV**. In this manner, a detailed physico-chemical description of the CoMoS phase as function of the promotor, support and dMo effects will be obtained. In that respect, High Resolution Transmission Electron Microscopy (HRTEM), Fourier-Transform Infrared Spectroscopy (FTIR) and X-ray Photoelectron Spectroscopy (XPS) will be performed. Additionally, to explore in more details the nature and the consequence of the interaction between the CoMoS phase and its support, High-resolution scanning transmission electron microscopy analysis (HRSTEM) will be undertaken. Thanks to these analyses, a 2D morphology model of the CoMoS phase, taking into different parameters (including the nature of the support) will be built and discussed. Catalytic performances will be then faced to this 2D nanoscale description of the CoMoS phase with respect to the nature of the support.

Following this, an indirect spectroscopic approach will be employed in order to attempts to discriminate the nature of the active site of the CoMoS sulfide phase in relation with the support used (**Chapter V**). To achieve this, the NO molecule, a specific probe molecule of the active sites of the CoMoS phase, will be used and followed by Fourier-transform infrared spectroscopy (FTIR). Second derivative and chemometric treatments combined with DFT calculations will be applied to describe the nature of the CoMoS sites. This multi-technique approach will be helpful to revisit the knowledge of the active site.

Then, an in situ spectroscopic approach will be undertaken in the **chapter VI** which aims at describing the surface catalyst reactivity by using a model molecule representative of sulphur compounds of FCC gasoline in conditions close to the HDS working conditions. Subsequently, interactions of 3-methylthiophene (3MT) will be followed by in situ/operando IR spectroscopy. Adsorption and desorption measurements will be performed in dynamic conditions by using Diffuse and Attenuated Total Reflectance approaches (DRIFT and ATR-IR). Thus, interactions between, support, active phase and reactant will be described and discussed.

Finally, a general conclusion will summarize the more relevant results and the relevant parameters which attempt to bridge the gap between the catalytic performances observed and specific features of the CoMoS active phase and its associated support. Some perspectives will be finally exposed.

- Chapter I -

State of the art, challenges and strategies

Table of contents

1 Industrial challenges of selective hydrodesulfurization of FCC gasoline 9

1.1 Industrial and environmental issues 9

1.2 Nature of the FCC gasoline 10

1.3 Selective HDS processes of the FCC gasoline 12

2 HDS catalysts 13

2.1 General aspects 13

2.2 Active phase 15

2.2.1 Supported non-promoted catalysts 15

2.2.1.1 Precursor's oxide catalyst 15

2.2.1.2 Active phase models 16

2.2.1.3 Nano-scale structure 19

2.2.2 Supported and promoted catalysts 22

2.2.2.1 Oxide state catalyst 23

2.2.2.2 Promoter effects on the morphology of the active phases 24

2.2.2.3 Nano-scale structure of the CoMoS slab 26

3 Supports 28

3.1 Alumina support 28

3.1.1 Generalities 28

3.1.2 Structure and physical characteristics of the supports 29

3.1.3 Surface properties of alumina 33

3.1.4 Alumina models 34

3.1.4.1 Peri's Model[117] 34

3.1.4.2 Tsyganenko and Filimonov's Model [115] 35

3.1.4.3 Knözinger's Model [116] 35
3.1.4.4 Busca's Model 37
3.1.4.5 Digne's Model 38

3.2 Silica 41
3.2.1 Generalities 41
3.2.2 Structure and physical characteristics 41

4 Influence of catalytic properties on selective HDS 46
4.1 Hydrodesulfurization and hydrogenation reactions 46
4.1.1 Thiophene and derivative compounds: reactivity and HDS mechanism 46
4.1.2 Olefins: reactivity and hydrogenation mechanism 50
4.1.3 Nature of the sites involved 54
4.2 Reactivity and HDS/HYDO selectivity 60
4.2.1 Active phase and promoter effects 60
4.2.2 Supports effects 62
4.2.2.1 Indirect effect of the support 65
4.2.2.2 Direct effect of the support 68

5 Strategy and methodology of the thesis 70
5.1 Strategy 70
5.2 General methodology 71

6 References 73

- Chapter 1 -
State of the art, challenges and strategy

1 Industrial challenges of selective hydrodesulfurization of FCC gasoline

Many European environmental regulations aimed at decreasing toxic compound contents, especially sulfur-based ones, in the gasoline formulation. Sulfur specifications have become increasingly drastic and should not exceed 10 ppm.[1] Moreover, similar specifications around the same value are adopted in the USA[2] and spread overs many other countries around the world as China[3].

1.1 Industrial and environmental issues

In 2012, oil is the most important part of the total primary energy supply, and represents more than 30%. Thus, petroleum refining is an industrial key process where crude oil, extracted over the world, is transformed into end-use products with a high additional value. A large and various range of products is obtained from petrochemicals raw materials, food grade, medical grade paraffin oils to aviation fuels, heavy fuel oil or even merely transportation fuels.

The latter and especially gasoline, represents an important pool in a petroleum refining.[4] Indeed, gasoline is worldwide used for the vehicles transportation. That is why, the main objective of petroleum refining during the 70's and early was to increase the gasoline production from the crude oil feedstock. However, this worldwide used is not without making an impact on the environment on global or local way.

Research on the cleaning of gasoline, including hydrotreatment process to remove the undesirable N, O and more particularly S containing molecules, has become an important subject of environmental catalysis studies worldwide.

From an industrial point of view, elimination of sulfur impurities from FCC gasoline is required two major points.[5]:

- Protection of the catalysts used in latter stages of the refining process.
- Protection of automotive catalytic converter based on noble metals (NOx trap) from sulfur oxide which is a poison for it.

However, environmental problems are nowadays one of the driving forces of research and development of HDS catalysts, in particular for the gasoline treatment. When combustion occurs in the automotive motors, sulfur compounds give mainly sulfur oxides SO_x, such as SO_2, which contributes to atmospheric pollution and are harmful to human health. [5]
Therefore, many European environmental regulations aimed at decreasing toxic compound contents, especially sulfur-based ones, in the gasoline formulation. As shown in Table 1 sulfur specifications have become increasingly drastic and should not exceed 10 ppm since 2009.[1] Moreover, similar specification around 10 ppm is adopted in the USA[2] and spread overs many other countries around the world as China.[3]

Table 1. Changes in standards specification on impurity in Gasoline. [6,7]

	2000	2005	2009
S (ppm wt)	150	50	10
Benzene (%vol)	1	1	1
Aromatics (%vol)	42	35	35
Olefins (%vol)	18	18	18

For the following of this study, interest focuses on gasoline production and the removal process of the sulfur containing molecules.

1.2 Nature of the FCC gasoline

To obtain used-gasoline, crude oil has to undergo various treatments.[4] Transforming processes are performed in order to produce a gasoline with performance consistent with the associated specification, i.e. an octane number between 95 and 98.[1,8] Process named Catalytic Reforming and Isomerization are then carried out in upgrading of the gasoline from crude oil distillation cut.

In addition, vacuum distillate represents also a notable feedstock to raise the yield of gasoline from crude oil. To obtain gasoline from it, Fluid Catalytic Cracking is mainly performed. Once treated, FCC gasoline represents approximately 30 to 40% of the gasoline pool which meets to a real industrial issue [7,8]. Nevertheless, FCC gasoline contributes for 90 % of the total sulfur content present in the global gasoline pool. [6,10–14] Focusing on the FCC gasoline, HDT are extensively used to produce more valuable, clean, and environmentally friendly fuels. The typical composition of an FFC gasoline is presented in a Figure 1.

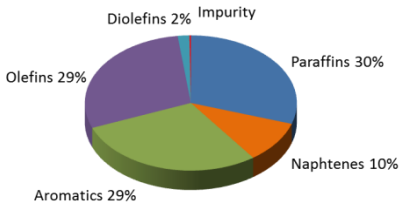

Figure 1. Typical composition of an FCC gasoline.[6]

Thus, a deep HDS of gasoline is crucial to produce a clean fuel (by removing sulfur) compliant with environmental specifications with increased yield of gasoline from crude oil.[6,15,16] The unsaturated hydrocarbons, naphthenes, aromatics and olefins, represent almost three quarters of them. C_5 to C_{12} hydrocarbons are presents with a major part of 5 to 7 carbon atom chain. Regarding to olefins branched or cyclic olefins proportion is more important than linear.

Sulfur content is around 1000 ppm, more or less, depends on the crude oil feedstock. Regarding the composition, thiophene and alkylthiophenes represent 60% and over of the sulfur compounds. The remaining fraction is composed of heavy sulfur compounds such as benzothiophene derivates and unknown compounds (Table 2). [6,17–19]

Table 2. Gas chromatographic analysis of thiophene derivatives in FCC naphtha.[6,13]

Compounds	Percents ratio of total thiophenes (sulfur %)	Sulfur content in naphta µg/g
Thiophene	6.3	69.2
2-Methylthiophene	10.0	109.8
3-Methylthiophene	13.8	152.6
Dimethylthiophenes	35.4	389.8
Unknown thiophene	4.0	43.9
Iso-propylthiophene	2.4	26.4
Methyl ethylthiophene	4.2	46.1
Trimethylthiophene	5.6	61.5
Unknown thiophene	1.6	17.6
Trimethylthiophene	4.1	45.0
4-Carbons-alkylthiophene	10.5	116.4
Unknown thiophene	2.1	23.0

1.3 Selective HDS processes of the FCC gasoline

As just presented above, the FCC gasoline contains mainly thiophene and its alkyl-thiophenic derivatives. In order to remove them, specific HDS refining processes are performed[13].
HDS reaction consists of reacting sulfur compounds with H_2 to form saturated hydrocarbons and hydrogen sulfide as the schematic reaction below:

$$\textit{Sulfide molecules} + H_2 \xrightarrow{\textit{Catalyst}} \textit{Saturated hydrocarbons} + H_2S \qquad \textit{Eq 1}$$

The most common industrial HDS process was developed by Axens company under the trade name Prime G+. [20] This technology results in minimal olefin saturation in the case of FCC gasoline desulfurization.[12] The first step is the diolefins selective hydrogenation under H_2 following by a separation step of a light fraction without any sulfur compounds and a heavier fraction. Then, HDS is performed on this heavier fraction to form gasoline in agreement with the environmental specification. [13,20]

Nevertheless, working conditions used by this fixed bed reactor process, H_2 flow, high temperature and H_2 pressure (Table 3) should imply also olefin hydrogenation reaction which decreases the gasoline octane number. [13,21]

$$\textit{Olefins} + H_2 \xrightarrow{\textit{Catalyst}} \textit{Saturated hydrocarbons} + H_2S \qquad \textit{Eq 2}$$

Table 3. Operating condition of the HDS gasoline process: Prime G+.[6,20]

Temperature (°C)	Pressure (Mpa)	Liquid hourly space velocity (h^{-1})	H_2/HC ratio (v/v)
220-290	1.5-3.0	3.0-8.0	300-600

That is why, to prevent this olefins hydrogenation side-reaction, selective catalysts are used and the process is qualified of selective. Thus, one of the main challenge of gasoline HDS is to develop selective HDS catalysts which allows sulfur removal from FCC gasoline while maintaining the performance quality owed to olefins. Consequently, a key criteria for environmental concerns is the study of HDS/HYDO selectivity, especially parameters which could influence it.

2 HDS catalysts

2.1 General aspects

Regarding the industrial process, HDS is usually conducted over specific catalyst based on molybdenum or tungsten sulfided supported on transition alumina. Structures are based on metal disulfide with XS_2 stoichiometry where X is a transition metal of the group VI elements as Mo or W. Additionally, the metal sulfide phase reactivity can be tuned/enhanced after its decoration by a promoter to form an YXS phase, where Y is a transition metal of the group VIII elements, usually Ni or Co atoms. This transition metal sulfide phase (so-called "TMS phase"), is dispersed on a solid support. Support with a high surface area is generally chosen for a well-dispersed active phase. γ-alumina or silica supports with a high surface area and mechanical resistance and with both economical and practical standpoints are supports of choice. [8,20,22,23]

Thus, these two categories of supports will be described in details in section 3 especially regarding their syntheses, structure and surface state with own physical characteristics and chemical properties.

Usually, industrial catalysts are marketed in oxide state and then an *in situ* activation by a sulfidation step under partial pressure of H_2S/H_2 at high temperature is performed before

the HDS reaction. HDS activity and HDS/HYDO selectivity of these catalysts depend on various parameters, especially metal/promoter and active phase/support relationship and sulfidation operating conditions. Nevertheless, a general trend has been established according to the reaction as reported in Table 4. [5,24] It appears that mixed phase based on Co and Mo is the active phase of interests for the selective HDS.

Table 4. Classification of the sulfided catalysts by metal-promoter according to the reaction.[5]

Hydrodesulfurization	Co-Mo	>	Ni-Mo	>	Ni-W	> Co-W
Aromatic and olefin hydrogenation	Ni-W	>	Ni-Mo	>	Co-Mo	> Co-W

To improve the performance of the HDS catalyst, several studies have been carried out. Indeed, each step in the catalyst preparation is relevant from the choice of a precursor, active phase and support to the synthesis and post-treatment performed. CoMoS catalysts are generally prepared by the incipient wetness impregnation method with an aqueous, acidic solution of Co and Mo salt precursors solution using γ-Al_2O_3 or SiO_2 as support. Generally, ammonium heptamolybdate $(NH_4)_6Mo_7O_{24}$ or molybdenum trioxide MoO_3 is used as Mo precursor and cobalt being introduced in the solution as cobalt nitrate $Co(NO_3)_2$ or cobalt hydroxide $Co(OH)_2$, for instance[6,25,26]. Successive co-impregnation can be performed. Then, impregnation step is generally followed by thermal ageing step and then calcined in air around 400°C to obtained precursor's oxide catalysts. Finally, activation of the catalyst is done by sulfiding the mixed or mono- oxide species to form the transition metal sulfided phase denoted CoMoS. Sulfidation is performed under H_2/H_2S (10%H_2S) mixture flow between 300 and 600°C. Dimethyl disulfide is also used to obtain a sulfided catalyst. [6] The active phase formed is a layer lattice of molybdenum disulfide phase decorated with cobalt atoms supported on aluminum oxide.

Moreover, the nature of this active phase can be modified or enhanced by changing nature of precursor, by introduction of heteroatom additives as especially phosphorus [27,28], fluorine [29–31] or organic as citric acid [32]. Replacing the sulfides of transition metals by nitrides or carbides have been assumed have an impact on it [33,34]. Studies were also conducted on various supports to evaluated the catalytic performances in HDS as transition alumina, silica, carbon, titania and zirconia [26,31,35–39]. Post-treatment as sulfidation conditions [40,41] have been also studied to obtain the most efficient catalyst i.e obtain the

mixed sulfided CoMoS phase with the better rate by avoiding refractory sulfur species as Co_9S_8.

For the following of this bibliographic study, we will especially focus on the non-promoted MoS_2 and promoted CoMoS supported catalyst at the macroscopic and nanoscopic scales. The surface reactivity of these catalysts in hydrodesulfurization (HDS) and hydrogenation (HYDO) reactions will be described and the main parameters/catalyst properties which influence the activity and selectivity of HDS versus HYDO reaction will be introduced.

2.2 Active phase

During the last five decades, methodologies have been developed to characterize HDS catalyst's surface from the macroscopic up to the atomic scale. In this way, structure models have been proposed. Description of their structures (in the active state) is a key parameter in order to understand and enhance the reactivity of these catalysts. In the first part below, only the structure of the MoS_2 phase will be discussed.

2.2.1 Supported non-promoted catalysts

First, oxide precursors are dispersed on the surface of the alumina oxide support. Then, the MoS_2 active phase is formed by sulfidation of these oxide species.

2.2.1.1 Precursor's oxide catalyst

The active phase of non-promoted HDS catalyst is generally composed of both Mo transition metal and sulfur atoms interacting to form a layer lattice of molybdenum disulfide phase, MoS_2, supported on alumina oxide.

Before the sulfidation, oxide precursors are dispersed at the surface of the alumina oxide support. However, the detailed nature, structure and metal – support interactions (MSI) of the molybdenum species in the oxide precursor state of the catalyst are still under debate.[42] Table 5 summarizes some of the proposed theories existing in literature (not exhaustive).

Table 5. Structure of the calcined Mo/Al_2O_3 according the literature.

Supposed Mo species present on alumina support and characteristics	Experimental techniques	Refs.
Mo-OH strong interaction on Al_2O_3 creates MoO_3 monolayer	ESR and thermodynamics	[43–45]
Molybdenum is present in small entities or chains, amorphous and disordered.	^{1}H-NMR	[46,47]
	EXAFS	[42,48,49]
For high-loading Mo/Al_2O_3 catalysts (15 wt% MoO_3): Mo is present in a highly dispersed phase.	IR emission spectroscopy	[50]
Aggregated Mo species for low Mo-loading MoO_3 is detected for high Mo-loading. Symmetry and coordination changes with Mo loading.	RAMAN	[51–53]
Mo monolayer for a Mo surface density > 4.2 at.nm^{-2} of support	IR/TPD	[54]

Finally, the sulfidation of the oxide form is done to form the MoS_2 active phase. This final step is carried out under H_2/H_2S gas mixture flow to reduce Mo^{+VI} to Mo^{+IV}. [55,56]

The balanced chemical equation for the reaction between MoO_3 and H_2S to form MoS_2 phase can be write as follows:

$$MoO_3 + 2\,H_2S + H_2 = MoS_2 + 3\,H_2O \qquad Eq\ 3$$

Once the catalyst sulfided, the catalytic reaction can take place. Nevertheless, in order to understand reaction mechanisms and properties implied, it is necessary to obtain a complete description of surface sites structure. Thus, several models have been developed in the literature.

2.2.1.2 Active phase models

MoS_2 unit cell has a layer lattice structure based on the stacking of slabs, with a hexagonal geometry composed of sulfur and molybdenum atoms with the following atom sequence S-Mo-S. The nature of the bonding between S and Mo atoms is mixed: ionic and covalent bonds while the cohesion of the structure between two slabs occurs by van der Waals force

between the sulfur atoms. [57–59] Thickness or stacking in the present case, length, composition in terms of site location characterizes precisely the MoS_2 slab unit.

According to Prins et al. [60], MoS_2 unit cell might be oriented in two different ways on the support surface: either parallel or perpendicular i.e. respectively the MoS_2 unit in interaction with the support respectively by basal or edge bonding. Thus, Mo-O-Al bonds are formed between MoS_2 and the support.

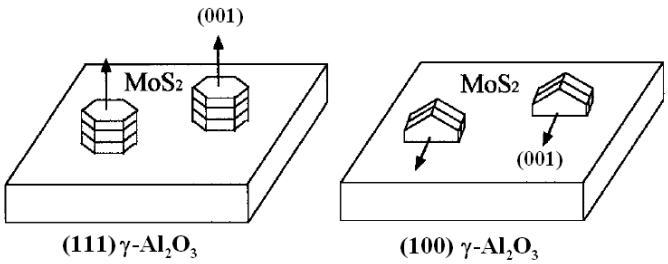

Figure 2. Structure of the Mo/γ-Al_2O_3 sulfided catalysts, geometric orientation of the slabs on the alumina surface.[60,61]

Indeed, in the case of γ-Al_2O_3 support, Prins *et al.*[60] and Sakashita *et al.*[61] have shown that the MoS_2 basal plane is oriented parallel to the (111) surface of γ-Al_2O_3 and perpendicular to the (100) γ-Al_2O_3 surface (Figure 2). Hayden and coworkers[62] suggested that the MoS_2 orientation is parallel or perpendicular to the surface depending on the state of the Mo-O-Al bond. Indeed, for a sulfidation temperature between 400°C and 625°C, breaking of Mo-O-Al bond could appear and promote the perpendicular orientation.

The two first detailed models of the structure of MoS_2/Al_2O_3 catalyst was the monolayer model developed by Schuit and coworkers [42,63] and the intercalation model developed by Voorhoeve and Stuiver in the 70's. [64] But these two models were not sufficient to describe the morphology active phase.

Additionally, several studies have been carried out to describe the 2D morphology of the MoS_2 slabs. Unanimously recognized by the scientist community, Kasztelan[65] proposed a relevant 2D morphologies of MoS_2 based on geometry modeling by correlating catalytic activity data with the Mo content of the active phase. Chain, triangular, rhombohedric and hexagonal geometries were identified along with different nature of Mo and S sites: edge, corner, basal sites. The most stable geometry of the slabs highlighted in this study is

hexagonal more or less distorted. Indeed, it was established that an optimum size of the MoS_2 slab can be obtained for Mo_{edge}/Mo ratio where Mo_{edge} is the number of Mo at the edge and Mo the total number of Mo ions (Figure 3).

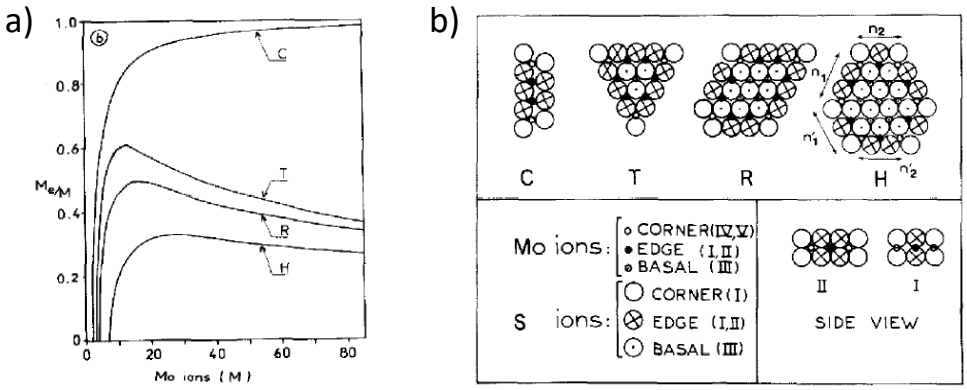

Figure 3. (a) Top view of the different symmetrical MoS_2 single slabs (C: chain, T: triangle, R: rhomb and H: hexagon) with the different types of ions and their local environment (I, II, III, IV, V).[65] (b) Variation of the specific number of edge Mo ions (Me/M) versus the slab size M for the different symmetrical MoS_2 slab shapes.[65]

Fifteen years later, thanks to the progress of thermodynamic DFT approaches, a further nano-scale description of MoS_2 slabs have been investigated dealing with the electronic, structural and energetic properties of the MoS_2, especially the edges exposed on the MoS_2 slabs. Two energetically competing edges surface stable were highlighted: the (1 0 -1 0) and the (-1 0 1 0) planes corresponding respectively to molybdenum edge called M-edge and the sulfur edge called S-edge.[6,66,67] Figure 4 present a 2D view of the MoS_2 crystallite and perspective view of MoS_2 edge surfaces.

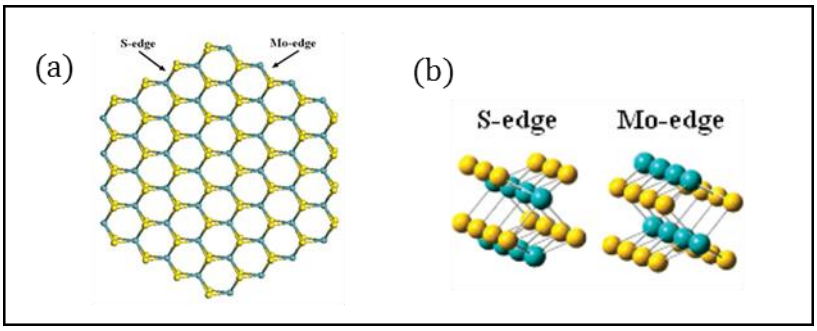

Figure 4. (a) Hexagonal MoS_2 crystallite exposing M- and S-edges.[68] (b) Perspective view of optimized MoS_2 edge surfaces: with bare M-edge and fully saturated S-edge. (Yellow balls: S atoms, blue balls: Mo atoms).

These two surfaces are polar. One contains excess positive charge, M-edge, the other excess negative charge, S-edge. Different type of Mo site can be identified. Mo atoms on the MoS_2

slab are located either on the corner, edge or basal plane. Moreover, the sulfo-reductive (catalyst activation) or reactive conditions used drive the sulfur coverage of MoS_2 edges. Thus, structures of the edge and corner of the MoS_2 slabs are not exclusive and Mo coordination with sulfur atoms is directly impacted. Features of the Mo atoms on a corner, edge, and basal plane are resumed in the Table 6[69].Mo atoms on the MoS_2 slab are located either on the corner, edge or basal plane. Moreover, the sulfo-reductive (catalyst activation) or reactive conditions used drive the sulfur coverage of MoS_2 edges. Thus, structures of the edge and corner of the MoS_2 slabs are not exclusive and Mo coordination with sulfur atoms is directly impacted. Characteristics of the Mo atoms on a corner, edge, and basal plane are resumed in the Table 6.[69]

Table 6. Characteristics of the Mo atoms of the MoS_2 slab.

Localization of the Mo site on the MoS_2 slab	S-coordination	Comments
Mo-basal plane	6	Mo-basal sites are considered stable regarding the S-coordination.
Mo/M-edge	4 to 8	Coordination depends of S-coverage.
Mo/S-edge	3 to 6	Coordination depends of S-coverage.
Mo/Corner	3 to 6	Coordination depends of S-coverage and electronic environment of the Mo is different of Mo of the M- or S-edge.

2.2.1.3 Nano-scale structure

As discussed previously, the sulfur coverage draws the edge structure. Thus, to describe MoS_2 at the nano-scale structure and thus understand the reactivity, theoretical studies have been conducted to estimate the stability of the M- and S-edge structures as function of the sulfo-reductive or reactive conditions of the catalyst. Raybaud and coworkers [6,67,70,71] have used a thermodynamic model combined with DFT calculation to determine the equilibrium stable edge structures of the MoS_2 system in the sulfo-reductive conditions in order The assumed sulfo-reductive equilibrium of the MoS_2 system is described by equation 4.

$$H_2S_{(g)} + MoS_{2(s)} = H_{2(g)} + (MoS_2 + S)_{(s)} \qquad Eq\ 3$$

Going from left to right corresponds to the dissociation of H_2S, the adsorption of a sulfur atom on the MoS_2 surface (leading to an over-stoechiometric TMS phase) and the formation of molecular hydrogen in the gas phase.[66]

In order to describe this equilibrium between the surface and the gaseous molecules and to link the energy of the M- or S-edges with the sulfo-reductive conditions, a thermodynamic variable is used: chemical potential of sulfur, $\Delta\mu_S$. The variation of $\Delta\mu_S$ as a function of reactive conditions is reported in the Figure 5 (a). For a typical sulfo-reductive HDS conditions (around 623 K and p_{H2S}/p_{H2} = 0.18) the chemical potential difference is around – 0.8 eV. The edge energy as a function of both $\Delta\mu_S$ and sulfur coverage at the edge is represented on the Figure 5 (b). It reveals that the energy of the M-edge is lower than the energy of the S-edge in the HDS process conditions (see chemical potential range [0 ; – 1.0 eV]).

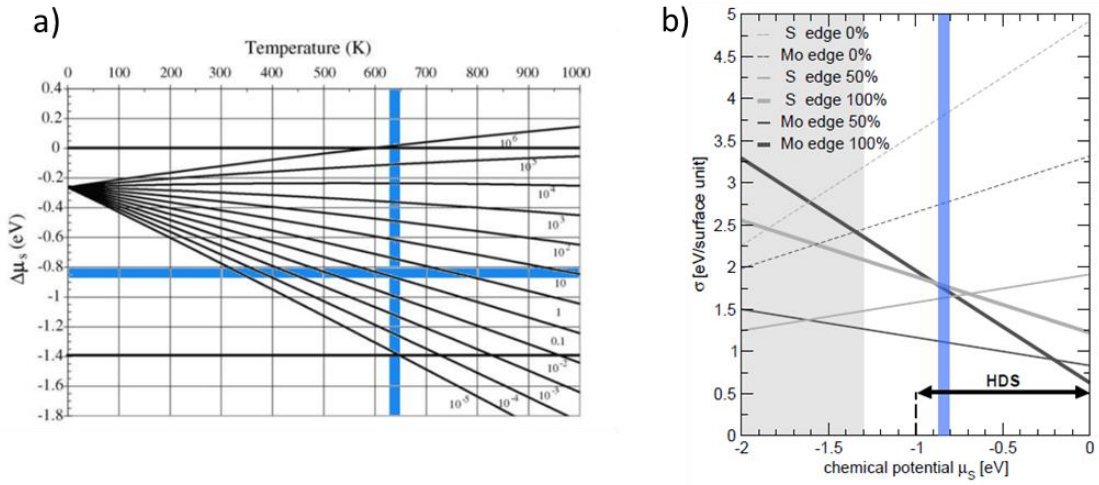

Figure 5. (a) $\Delta\mu S$ values as function of temperature and p_{H2S}/p_{H2} ratio: the shaded region represents the domain of usual sulfo-reductive HDS condition.[71] (b) Variation of the surface energy as a function of chemical potential of sulfur. Realistic HDS working (black double arrow) and sulfo-reductive conditions (blue box). MoS_2 is unstable in the grey-shaded region.[71]

Moreover, Schweiger *et al.*[71] relates the impact of the chemical potential of sulfur on the 2D morphology of the MoS_2 slab as depicted in Figure 6(a). To achieve that, they follow the evolution of two limit morphologies of MoS_2 namely the triangular and hexagonal morphologies according to the variation of $\Delta\mu_S$. Combining the calculation of the most stable surface edge energy (S or M) as a function of $\Delta\mu_S$ with the Gibbs–Curie–Wulff [72]

relationship, allows to plot a diagram of the MoS_2 morphology where the M-edge percentage is expressed as a function of $\Delta\mu_S$.

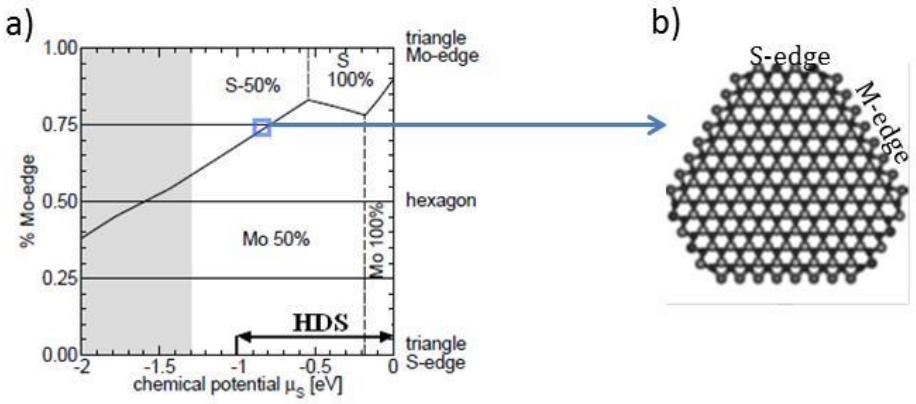

Figure 6. (a) Morphology of the MoS_2 nano-size particles as a function of chemical potential of sulfur. The ordinate axis represents the percentage of M-edge.[71] (b) Morphology of MoS_2 expected in sulfo-reductive conditions.

This morphology diagram of MoS_2 shows that in sulfo-reductive conditions (blue box: around 623 K and pH_2S/pH_2 = 0.18) the predicted shape is a deformed hexagon where 70 % of the edge are the M-edge and both M- and S-edge are covered by 50% of sulfur (Figure 6 (b)). However, it is important to note that the HDS reaction occurs in stronger working reductive conditions and at lower temperature which could significantly change the MoS_2 morphology. Thus, the M-edge proportion should be lower than 50% but the sulfur coverage of both edges should be kept constant around 50%. Table 7 summarizes the shape of the MoS_2 slab and nature of the edge exposed as function of $\Delta\mu_S$.

Studies using scanning tunneling microscopy (STM) have fully confirmed the last studies by visualizing 2D morphology of MoS_2 at the nano-scale. Tøpsøe, Lauritsen and co-workers[73,74] have identified the morphology of MoS_2 model slabs supported on gold surface (111) by STM experiment. In particular, under purely sulfiding (H_2S) environment imposed on the Mo cluster and at low temperature corresponding to a sulfur chemical potential close to 0, a triangular shape was observed consistent with the 2D triangular morphology deducted from DFT calculation. Besides, the modification of the MoS_2 shape, from triangular to hexagonal, was also confirmed by STM experiments after increasing the H_2 pressure into the chamber of the microscope (Figure 7).

Table 7. Shape of the MoS_2 slab and nature of the edge exposed as function of $\Delta\mu_S$. [69]

$\Delta\mu_S$	Shape of the MoS_2 slab	Nature of the edge exposed
High value	Triangular or truncated triangular	- M-edges on the long sides and a small area of S-edges at the corners, where the triangle is capped.
Intermediate value	Deformed hexagonal	- M-edges on the long sides S-edges on the small sides
	Hexagonal	- Equal quantity of M- and S-edge
	Deformed hexagonal	- S-edges on the long sides M-edges on the small sides
Low value	Triangular or truncated triangular	- S-edges on the long sides and a small area of M-edges at the corners, where the triangle is capped.

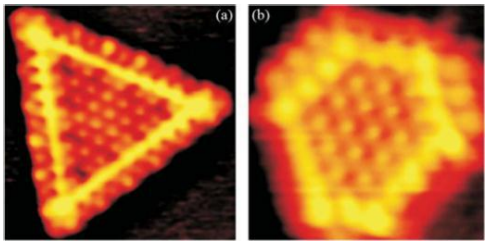

Figure 7. Atomically resolved STM image (Vt = 5.2 mV, It = 1.28 nA) of a triangular single-layer MoS_2 nanoclusters on Au(111). Image dimensions are 41×42 Å² (b) Atom-resolved STM image (Vt = 39.1 mV, It = 0.31 nA) showing a typical hexagon-shaped single-layer MoS_2 nanocluster synthesized under reducing conditions (7% H_2S). Image dimensions are 27×28 Å². [74]

2.2.2 Supported and promoted catalysts

In order to enhance the HDS catalyst in term of activity and selectivity, a second transition metal of the VIII group elements is added to the Mo-based HDS selective catalyst, typically cobalt. This metal called promoter is added during the impregnation step of the support with the Mo precursor. Then, oxide precursors are formed according the same way of the unprompted catalyst as further described in the part 2.2.1.

2.2.2.1 Oxide state catalyst

According to the results of several techniques, especially laser Raman and EXAFS spectroscopies, the presence of promoter atoms does not seem to affect greatly the oxide Mo species on the alumina surface presents the nature of the Mo species adsorbed on the surface of unpromoted MoS_2. These studies have indicated that the structure of the non-promoted catalyst remains almost the same in the promoted catalyst. Additional infrared study of NO adsorption and Mössbauer emission spectroscopy (MES) results indicate that octahedral Co is the dominating cobalt species in calcined state at low temperature (< 575°C). These studies also indicate that the Co is located at the surface of the alumina interacting likely with the Mo species according to the magnetic susceptibility and ESR measurement.[50,75]

Moreover, MES investigations conducted by Wivel et al.[76] have shown that cobalt may be present in both octahedral and tetrahedral environment and that the nature of the oxide species may depend on the metal content. Table 8 summarizes the different cobalt species observed in various literatures.

As already mentioned previously, oxide precursors are subsequently sulfided to form TMS phase which will be active in HDS reaction. This new promoted active phase is composed of both Mo and Co atoms to form the so-called CoMoS phase. However, during the sulfidation step, the cobalt oxide species can be partly sulfided to form Co_9S_8 phase. This latter, is not efficient in HDS reaction.

Table 8. Different cobalt species.

Experiments	loading	Cobalt species observed	Refs
Mössbauer emission spectroscopy	Low Co loading	Tetrahedrally and octahedrally coordinated Co species	[77]
	High Co loading *Co/Mo=0.5 and >*	Tetrahedrally and octahedrally coordinated Co species + Co_3O_4	
EXAFS	Low Co loading *0.5 Co/nm² of support Mo > 2,5Mo/nm²*	$CoMoO_4$ Form by co-precipitation Co and Mo salts during the impregnation step	[78,79]
	Higher Co loading *3.5 Co/nm² of support*	$CoAl_2O_4$	
Mössbauer emission spectroscopy	High Co loading *3.5 Co/nm² Co/Mo=0,5*	CoO and Co_3O_4 are also identified	[80]

Several studies have been carried out to elucidate the CoMoS structure and to confirm the decoration of the MoS_2 active phase by the Co-promoter on the edges of non-promoted MoS_2 slab.

2.2.2.2 Promoter effects on the morphology of the active phases

Several studies have been developed to locate the Co atoms within the HDS catalyst. In the monolayer model, Schuit et al. [42,63] assigned to Co atoms the role of stabilizer of the MoS_2 monolayer. Co atoms are supposed to substitute some Al atoms in the surface layer adjacent to the monolayer. In the intercalation model[81] Co is supposed to occupy octahedral intercalation position in the van der Waal's gap between the slabs.[64] A synergy model has also been developed by Delmon and coworkers.[82]

In this model, the promoting effect was attributed to a contact between the Co_9S_8 and MoS_2 phases. This contact was suggested to result in spill-over of hydrogen from Co_9S_8 to MoS_2, thereby enhancing the intrinsic activity of the MoS_2.[82,83] An illustration of the contact synergy model is presented in Figure 8.

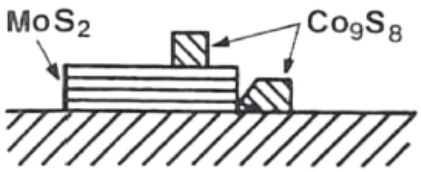

Figure 8. Contact synergy model of the CoMo catalyst. Interaction between MoS_2 and Co_9S_8 phases. [82]

The most relevant accepted model which best describes the TMS phase to date is the Co-Mo-S model developed by Tøpsøe and coworkers[84]. This model is based on direct *in situ* Mössbauer physico-chemical measurements to elucidate the active state of the promoted catalyst. Representation of this model is shown in Figure 9.

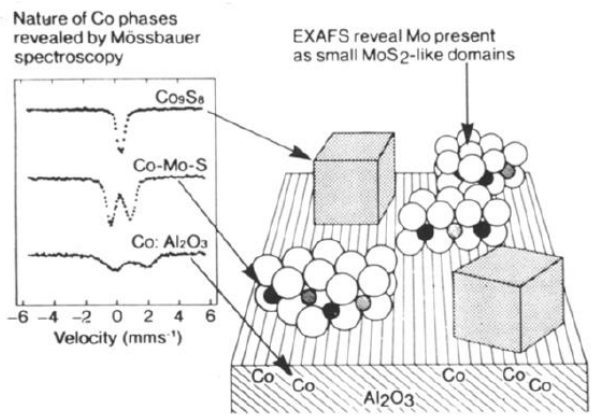

Figure 9. Schematic view of the Al_2O_3-supported CoMoS catalyst with the presence of different phases.[85]

The Co-Mo-S phase was highlighted mainly by *in situ* MES[85], extended X-ray absorption spectroscopy (EXAFS)[86] and infrared spectroscopy[87] studies. A detailed structure of the Co-Mo-S was described which consists in MoS_2-like structures with the promoter atoms, Co, located at the edge in five-fold coordinated sites at the (10-10) edge planes of MoS_2 in a tetragonal pyramidal-like geometry. MES and EXAFS studies assumed that these sites can interconvert to a four-fold coordination by removal of one or more sulfur atoms in the first coordination sphere of Co. In this model, two types of CoMoS structure are assumed. For alumina supported catalyst, the single slabs structure called Type I CoMoS interacts strongly with the support via Mo-O-Al bonding located at the edge of the slab. Type II CoMoS is defined as multiple slab formed where support interactions with the slabs are weaker and the edge free. [88]

However, the CoMoS mixed phased described above is not the only one present on the support. Based on thermogravimetric analysis (TGA) and XRD, Chung and Massoth[89] demonstrate by MES experiments (Figure 9) that Co is present in three locations after sulfidation: in the alumina, in Co_9S_8 and in the mixed phase CoMoS. Alstrup *et al.*[90] also confirm this result by distinguishing CoMoS phase from Co_9S_8 phase in XPS experiments with different binding energies.

In parallel to the Co-Mo-S model, Kasztelan geometrical model[65] was developed to propose the most relevant 2D morphologies of MoS_2 active phase. Thus, by considering the work on the non-promoted catalyst, the Co-Mo-S morphology is described as a hexagonal MoS_2 slab decorated by cobalt atoms at its edges.

2.2.2.3 Nano-scale structure of the CoMoS slab

In a similar way as for non-promoted catalyst, the equilibrium morphologies of CoMoS phase[91] could be plotted as seen in Figure 10 in order to describe specifically the nature, shape and edge composition of the MoS_2 slab considered.

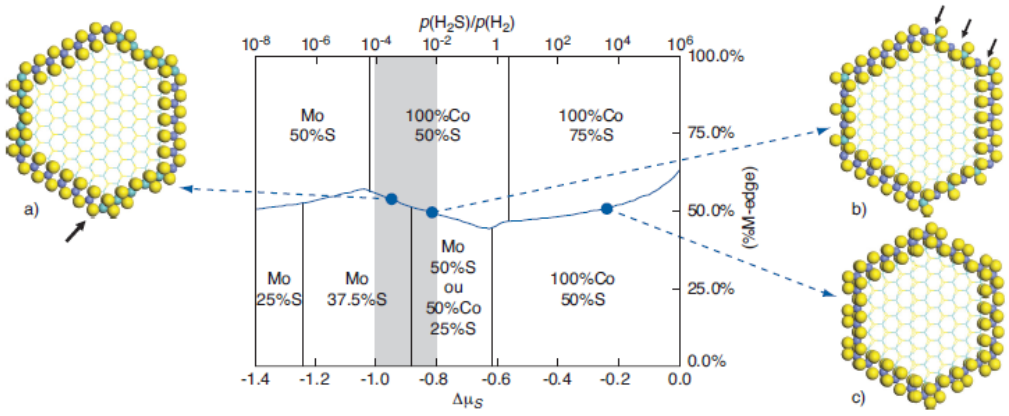

Figure 10. Morphology diagrams for the CoMoS nano-crystallites as a function of ΔμS and $p(H_2S)/p(H_2)$ (for T = 525 K). The percentage of M-edge is indicated by the blue broken line. The S-edge compositions are reported above the blue line, and the M-edge compositions are below this line. The shaded region visualizes the range of usual HDS conditions. The insets give the ball and stick representations of three possible CoMoS morphologies, with mixed sites indicated by arrows (yellow balls: Sulfur, green balls: molybdenum, blue balls: cobalt).[91]

From this equilibrium phase diagram, the morphology of the CoMoS can be determined according to the operating condition. For instance, if the CoMoS is close to HDS reaction condition ($\Delta\mu_S$ around -1 eV) or close to the sulfidation condition ($\Delta\mu_S$ around – 0.8 eV), the

shaded region, the proportion of M-edge is close to 50% indicating an hexagonal shape. The composition of the edge is given in Table 9.

Table 9. Composition of M- and S-edge as function of the operating conditions.

Nature of the edge	Sulfidation conditions $\Delta\mu_S$ around – 0.8 eV	HDS reaction conditions $\Delta\mu_S$ around -1 eV
M-edge	Mo non-promoted covered by 50% S or Mo promoted by 50% Co covered by 50% S	Mo non-promoted covered by 37.5% S
S-edge	Mo promoted by 100% Co covered by 50% S	

However, in these DFT studies, calculations are performed without taking into account i) effect of the support on the CoMoS morphology ii) with the effects of size and slab stacking. Moreover, support with high specific area is essential to obtain the higher catalytic activity. Actually, it is important to bear in mind that heterogeneous catalysis deals with reactions on specific surface sites, and hence the catalytic activity is closely linked to the active phase dispersion on the support.

In the next part, the support will be studied especially alumina and silica support. Synthesis, structure and physical characteristics, chemical properties will be detailed.

3 Supports

In this part, two categories of supports will be described, silica and alumina. These supports are the most useful in industrial processes on both economical and practical standpoints.
In the petroleum refinery, transition aluminas are widely used as catalyst support. One of them, the γ-Al_2O_3, is commonly used as support for hydroprocessing catalysts. Indeed, for the specific case of selective HDS catalyst several studies seem to indicate that the HDS/HYDO selectivity of HDS might impact by the nature of the support.

3.1 Alumina support

3.1.1 Generalities

The alumina term gathers transition oxide aluminas with formula Al_2O_3 with various crystallographic structure and theirs precursors namely aluminum trihydroxide with $Al(OH)_3$ formula and aluminum oxihydroxide with AlOOH formula. The most common aluminum trihydroxide is the bayerite or the gibbsite and aluminum oxihydroxide usually refers to Boehmite.[92]
To form the oxide aluminas, the standard method is the formation of these aluminum trihydroxide and oxihydroxide precursors by co-precipitation in aqueous solution of aluminum salts. For instance, the aluminum sulfate acid salt $Al_2(SO_4)_3$ could be with sodium alumina used to obtain boehmite. Then, thermal treatments are performed to obtain the oxide alumina by deshydratation of the desired aluminum oxide precursor. The Figure 11 below presents the formation pathway of the transition oxide alumina from aluminum oxide precursors.[92]
The most frequently encountered transition oxide aluminas are the γ-Al_2O_3 formed by controlled calcination of boehmite as δ-Al_2O_3. Then, θ-Al_2O_3 can be obtained by thermal decomposition of bayerite or boehmite through formation of transition alumina whereas η-Al_2O_3 is only obtained by thermal decomposition of bayerite. α-Al_2O_3 can be formed by controlled calcination regardless the precursors, boehmite, bayerite or gibbsite.

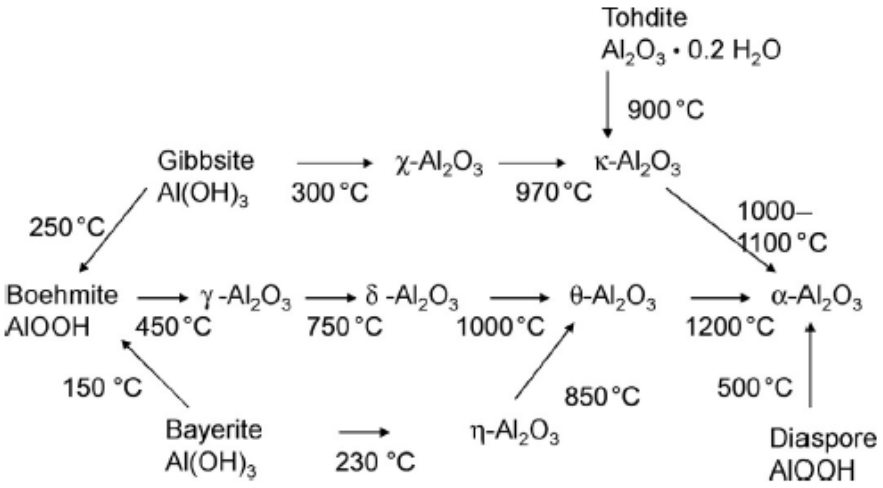

Figure 11. Conversion paths and starting transition temperatures of the different aluminum hydroxide and oxides upon heat treatments.[92]

γ-alumina is one of the most described supports in the literature. Indeed, several processes used it, especially in the HDS process because of the good compromise between the production cost and thermal, mechanical stability and chemical properties.

3.1.2 Structure and physical characteristics of the supports

γ-Al_2O_3 has a pseudo-spinel structure where the face centered cubic (fcc) sublattice of oxygen ions undergoes a quadratic deformation with Al atoms which may occupy both tetrahedral and octahedral sites. [92] Thus, some Al vacancies must be introduced to respect the stoichiometric requirement in the defect spinel structure.[93] Indeed, the cation-to-oxygen ratio between γ-Al_2O_3 and $MgAl_2O_4$ is different (2:3 vs 3:4). Hence, divalent cations are replaced by trivalent cations and Al vacancies to maintain electrical neutrality. [92]

Regarding the aluminum atom positions, from X-ray diffraction it has been found that Al atoms are located mainly on the octahedral sites with the existence of two diffraction peaks related to the (400) and (440) planes.[94] In the same way ^{27}Al MAS NMR[95,96] studies indicate that 25 up to 31% of Al atoms are in tetrahedral sites while 75 down to 69% are in octahedral sites. Figure 12 presents the crystalline structure model of the γ- Al_2O_3.

Besides, the positions of Al vacancies at octahedral or tetrahedral interstices are still under debate even if octahedral position seems to be preferred. Indeed, recent study assumed that the lowest energy configuration of γ-Al_2O_3 occurs when all the aluminum vacancies are in octahedral sites with the largest possible inter-distances.[97,98]

Moreover, Lippens and co-workers[99] have shown that γ-Al_2O_3 crystallographic phase by XRD in the (100), (110) et (111) direction of the cubic spinel unit cell structure in relation with the quadratic alumina structure (a = b ≠ c with a=b=7.97 Å, c= 7.82 Å). Regarding the proportion of each of them, the (100) surface exhibits the predominant area around 80% and the (110) surface around 20%.[100] The (111) surface may be present but its proportion depends on the synthesis conditions.[100] The Figure 12 represents the primitive faced centered cubic cell, one eighth of the alumina spinel structure, where crystallographic surface are presented by the shaded surface.

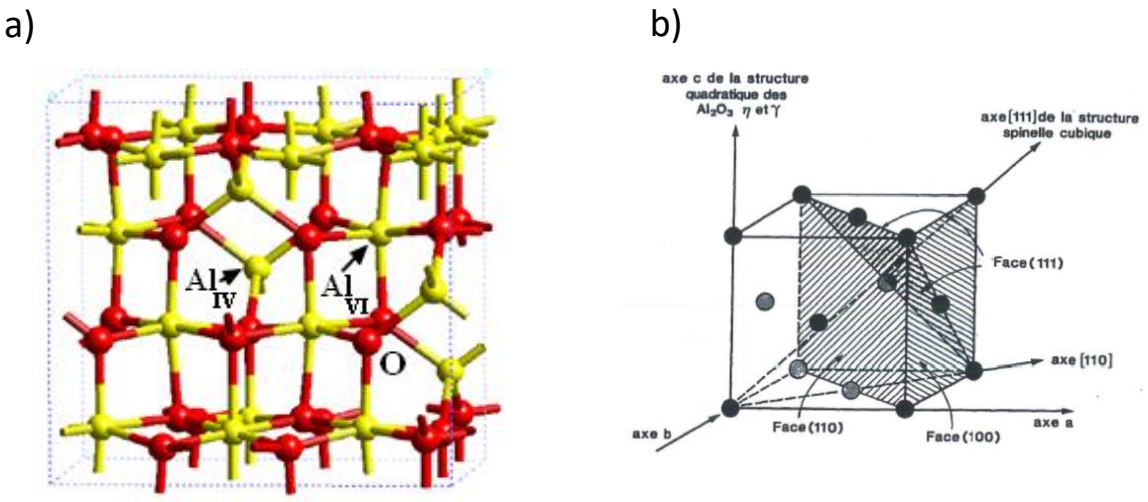

Figure 12. (a) Crystalline structure model of the γ- Al_2O_3.(Yellow balls: aluminum atoms, Red balls: Oxygen atoms).[101,102] (b) γ-Al_2O_3 crystallographic primitive cell with the three main surfaces represented.[103]

However, in order to describe and understand respectively the structure and transformation of the γ-Al_2O_3, structure of boehmite need to be introduced. Boehmite has an orthorhombic structure made up of three crystallographic planes: one basal surface (010) and three types of edge surfaces (100), (001) and (101). To form γ-Al_2O_3 particle from the boehmite, a topotactic transformation[104] occurs (Figure 13). [101]

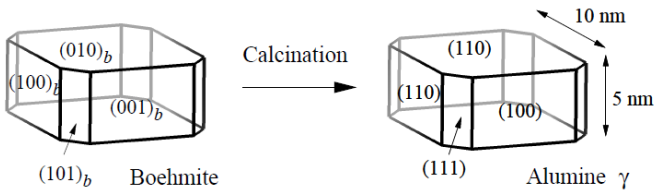

Figure 13. Morphologic model of γ-alumina crystallite.[101]

Thus, according to the pseudo-morphism rules, the (010) basal surface and the (100) edge surface of boehmite yield the same type of surfaces, indexed as (110) in *γ*-alumina. The lateral (001) and (101) surfaces of boehmite correspond to the (100) and (111) surface *γ*-alumina. Moreover, during this transformation to γ-Al_2O_3 from boehmite, the relative areas of the different surfaces remain almost unchanged. Only a strong contraction of volume around 30 % in the (010) direction is significant.

Formation of transition alumina occurs according to a dehydration mechanism well-established confirmed by both experimental[105] and theoretical[106] studies (Figure 14). Formation and elimination of H_2O molecules occurs in the interlayer between tow hydroxyl groups interacting by hydrogen bond. Next or simultaneously with the formation and elimination of H_2O, layers contraction and translation by each of them occurs to form alumina γ-Al_2O_3, and then δ-, θ-Al_2O_3 with the increase of the layers contraction and translation.

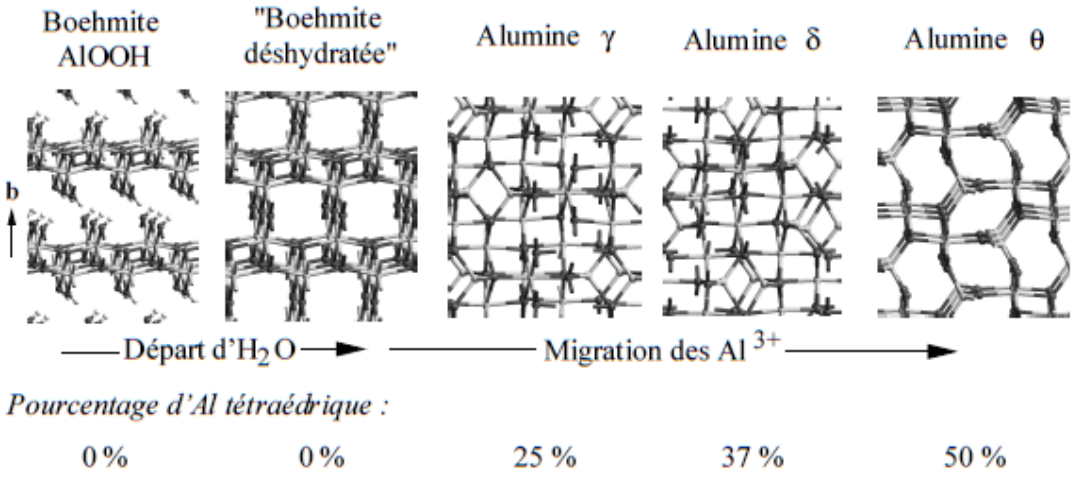

Figure 14. Representation of the formation of Alumina from dehydration of boehmite through the migration of Al^{3+} in the fcc sublattice of oxygen ions.[107]

Surface properties will be directly according to transition alumina considered.

Table 10 presents the δ-Al_2O_3, θ-Al_2O_3, α-Al_2O_3 compared to the γ-Al_2O_3 especially the percentage of different aluminum atoms.

Table 10. Structural data of δ-Al_2O_3, θ-Al_2O_3, α-Al_2O_3, γ-Al_2O_3. [108]

Alumina	Space group	Lattice parameters a (A) b (A)	Lattice parameters c (A)	Structure type	Al_{IV} (%)	Al_{VI} (%)	Al_V (%)
γ-Al_2O_3 [93]	Fd3m	7.90	7.90	Cubic disordered non-stoichiometric spinel	30–60	70–40	1–2
δ-Al_2O_3 [109]	P4m2	7.93	23.50	Tetragonal spinel superstructure	30–45	70-55	
θ-Al_2O_3 [110]	C2/m	5.62 2.91	11.79 β 103.8	Monoclinic β-Ga_2O_3 structure, ordered spinel-related structure	50	50	
α-Al_2O_3 [111,112]	R-3c	4.76	12.99	Hexagonal–rhombohedral, corundum structure		100	

Previously, the focus was on γ-Al_2O_3, but others transition alumina could be used as catalyst support or by confrontation would help to understand the interaction with the TMS active phase of the HDS catalyst.

Alumina support is one of the most commonly used in catalysis for immobilization and dispersion of metallic species. Nevertheless, the surface properties exhibited by the support are not without impact in catalysis and may play an important role.

3.1.3 Surface properties of alumina

As mentioned above, bulk alumina is composed of oxygen and aluminum atoms in tetrahedral or octahedral coordination which are not accessible to reactants. However, alumina also displays surface atoms which exhibit drastically different properties than those present in the bulk structure. Indeed, hydroxyl groups can be exposed to the alumina surface (in order to get the electro-neutrality of the support) and may display an acidic or basic character. The acid-base properties of the alumina are directly related to the hydroxyl groups which are linked to its local charge density. Description of hydroxyl environment and metal cation location on its surface are therefore primordial. For Brønsted acidity, an acid site is a proton donor (i.e. an hydroxyl group), whereas for Lewis acidity it is an electron pair acceptor (i.e. a cation like coordinatively unsaturated Al^{3+} cations).[113] Brønsted acid site and Lewis acid sites will be hereafter referred as BAS and LAS respectively.

Thus, several models have been proposed to help and understand the surface hydroxyls speciation on alumina.

First, focus will be done on the surface hydroxyls of alumina characterized by infrared spectroscopy. Indeed, position of the stretching vibrational bands of the O-H bond in the IR spectrum allows the distinction of hydroxyl groups according the coordination and number of surrounding metal atoms.

Figure 15 presents a typical infrared spectrum of γ-Al_2O_3. Strength of the Hydroxyl groups increases with the increase of the wavenumbers.

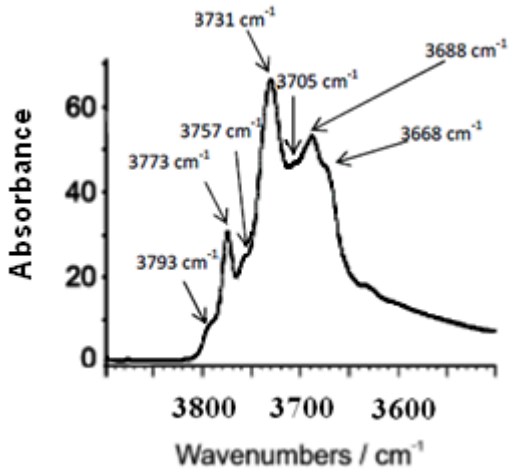

Figure 15. Infrared spectrum of γ-Al_2O_3 (Rhône Poulenc, 200 m^2g^{-1}) calcined at 773K for 16 h under air, then treated at 773K under high vacuum(10^{-5} torr) for 16 h. [114]

Several models have been developed during the last five decade to describe the alumina surface. Peri's Model, Tsyganenko and Filimonov's Model [115], Knözinger's Model [116] have been developed first.

3.1.4 Alumina models

3.1.4.1 Peri's Model[117]

The first model was established by J.B. Peri. This model is based on the local charge density impacted by the nearest neighbor configurations either oxygen atom or vacancies. In this model, some hypotheses are assumed. First, an "ideal" dried alumina with a top layer which contains only oxide ions and only one surface, (100) assumed to be exposed. Moreover, only Al in octahedral sites are considered. Finally, this study does not make any distinction between the different oxidation states of the aluminum atoms, only Al^{3+} is considered.

By this consideration, five infrared bands between 3700 and 3800 cm^{-1} are attributed to five types of hydroxyl ion sites as presented in Figure 16. They differ in local charge density because of their nearest neighbor configurations as view previously. The hydroxyl site with the lower local charge density (A-site) has four oxide ions nearest neighbors attributed to higher IR frequencies. The hydroxyl ion site with local charge density (C-site) has four immediately adjacent vacant sites attributed to lower IR frequencies. Figure 16 presents the assignments to hydroxyl ions on the five types of sites described previously.

a)

Site	Wavenumber cm^{-1}	No, of oxide nearest neighbors
A	3800	4
D	3780	3
B	3744	2
E	3733	1
C	3700	0

b)

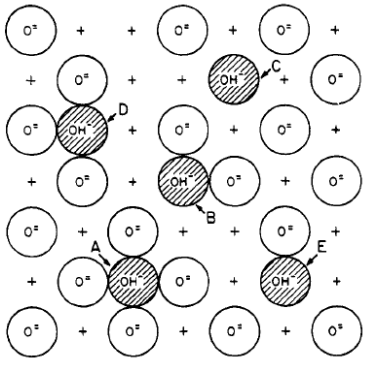

Figure 16. (a) Assignments to hydroxyl ions on the five types of sites. (b)Types of isolated hydroxyl ions (+ denotes Al^{3+}).

The acid-base properties are directly connected to the hydroxyl group environment. For instance, the OH_A site is surrounded by 4 anions oxygen, so most negative site i.e. the most basic. The A surrounded by 4 vacancies is an electron-deficient site, so the most acid.
Regarding the reactivity properties, Peri suggests that the OH group associated to a threefold vacancy may have a stronger Lewis acidity which could adsorb electon-donating guests as olefins or ammoniac.

3.1.4.2 Tsyganenko and Filimonov's Model [115]

Tsyganenko model suggests different type and configurations of hydroxyl groups bonded to metal atom(s) as reported in the Table 11. Type II and III hydroxyls groups can be considered as hydroxyls of the type I with one or two coordinate bonds to adjacent metal atoms. M-O bonds are equivalent to each other. Each OH configurations is attributed to the wavenumber of the stretching vibrational band of the experimental OH bond which vary proportionally with the strength of the OH hydroxyl bond. This strength decreases with increasing the oxygen atoms coordination with the Al atoms.

Table 11. OH hydroxyl configurations according to the Tsyganenko and Filimonov's Model.

Type	I	II	III
OH configurations		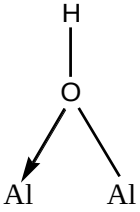	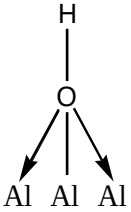
Wavenumbers (cm^{-1})	3800	3740	3700

The presence of two additional bands around 3780 and 3733 cm^{-1} observed by Peri is explained by the fact that the surface OH groups may differ in their coordination of surrounding metal atoms.

3.1.4.3 Knözinger's Model [116]

This model highlights similarly five OH hydroxyl group configurations on the surface of aluminas. Different configurations of hydroxyl group and their characteristics are described

in the Table 12 but in this model the crucial difference is the consideration of the three (111), (100) and (110) crystallographic surfaces. However, crystallographic surface do not have necessarily the five O-H configurations. For instance, the (110) surface may have three configuration Ia, Ib, IIb. For each OH group configurations, the net charge at OH are calculated as the sum of the negative charge of the anion and the strengths of electrostatic bonds to the anions from adjacent cations.

Table 12. OH hydroxyl configurations according to Knözinger's model.[116]

OH configurations	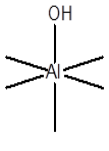		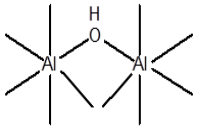	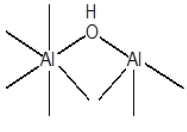	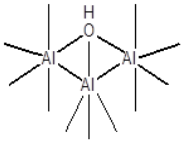
	Ib	Ia	IIb	IIa	III

Coordination	HO-μ_1-Al_{VI}	HO-μ_1-Al_{IV}	HO-μ_2-Al_{VI}	HO-μ_2-(Al_{IV}, Al_{VI})	HO-μ_2-Al_{VI}
Localization (crystallographic surface)	(111) (110) (100)	(111) (100)	(111) (100)	(111)	(111)
Net charge at OH	-0,5	-0,25	0	0,25	0,5
υ_{exp}	3800-3785	3780-3760	3745-3740	3735-3730	3710-3690

Acidic and basic properties are characterized as function of the evolution of these net charges. Indeed, according to the Pauling's electrostatic rule [118], the net charge at OH reflects the ionic bond character i.e. the strength of the OH bond. Thus, higher is the net charge at OH and higher is the protonic acidity.

Moreover, the lower wavenumber of the stretching vibration band of the OH bond match to the most acidic sites. However, this attribution does not take into account the fact that the aluminum vacancy could affect the OH bond frequency.

Moreover, Lewis sites have been described. The condensation of two neighbor hydroxyl groups, one electron-donor and the other electron-acceptor create coordinately unsaturated oxygen sites, CUS oxygen (Basic Lewis sites), and coordinately unsaturated Al^{3+} sites, CUS Al^{3+} (Acid Lewis sites). A CUS Al^{3+} can be fivefold or threefold coordinate located respectively on tetrahedral or octahedral site. These sites are unlikely to form under 573K. Thus, their reactivity is lower.

Knözinger and coworkers suggest also the presence of a specific site responsible of the molecule adsorption especially the chemisorption of different molecule as H_2, CO, olefins and aromatics and of the formation of carbonate from CO_2[119]. This site is supposed implied Ia OH type in interaction with an bulk oxygen atom or with one or two fivefold coordinate CUS Al^{3+}.

3.1.4.4 Busca's Model

Busca and coworkers[120,121] attempt to attribute each hydroxyl vibrational band taking into consideration the number and coordination of surrounding metal atoms and the crystallographic surfaces of alumina. Thus, this model incorporates the vacancy concept owing to the structure of an alumina defect spinel. IR frequencies attributions of the hydroxyl groups are presented in the Table 13.

Table 13. OH hydroxyl configurations according to Busca's model. [120,121]

υ_{exp} (cm^{-1})	3800-3785	3780-3760	3745-3740	3735-3730	3710-3690
Busca attribution	HO-μ_1-Al_{IV}	HO-μ_1-Al_{IV}-lac	HO-μ_2-Al_{VI}	HO-μ_2-Al_{VI}-lac	HO-μ_3-Al

Busca suggests that all of the bands above 3710 cm^{-1} arise from terminal species. The main interpretation is that terminal OH groups on Al_{IV} sites absorb at a higher frequency than terminal OH groups on Al_{VI} sites.[108]

3.1.4.5 Digne's Model

Digne's model[101,122] is based on the density functional theory (DFT) calculations and proposes the assignment of the OH groups as function of the different surface faces of alumina considered, (100) (110) (111) and of the nature of Al. Digne and coworkers[101,122] give a configuration description of these different alumina surfaces as function of the hydratation degree i.e. the hydroxyl surface coverage θ.

Figure 17 presents some relaxed configurations of γ-Al_2O_3 surface. For $\theta_{(100)}$=0, the relaxation of the (100) surface shows that only unsaturated octahedral aluminum Al_V atoms are stable (Figure 17 a)). The hydration of this surface implies a change from Al_V to Al_{VI} atoms. For $\theta_{(110)}$=0, the (110) surface exhibits two kinds of unsaturated aluminum surface sites: 75% of twofold unsaturated octahedral aluminum atoms Al_{IV} and 25% of onefold unsaturated tetrahedral aluminum atoms Al_{III} (Figure 17 c)) Al_{III}. The hydration of this surface causes the formation of onefold, twofold Al_V and onefold Al_{IV}. Finally, for the (111) alumina hydrated surface, onefold and twofold octahedral aluminum atoms are presents Figure 17 b).

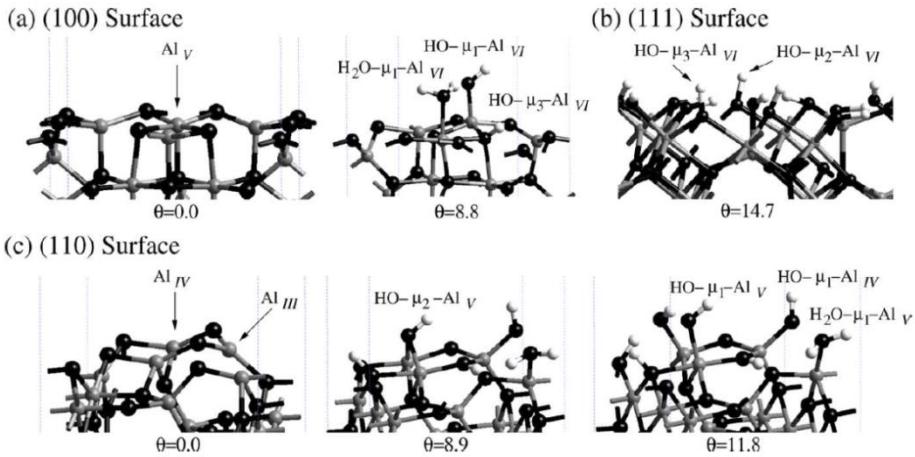

Figure 17. Relaxed configurations of (a) γ-Al_2O_3(100), (b) γ-Al_2O_3(111), and (c) γ-Al_2O_3(110) surfaces for different hydroxyl coverage (θ in $OH.nm^{-2}$). The most relevant surface sites are quoted: Al_n stands for aluminum atoms surrounded by n oxygen atoms, and HO–μ_m for OH groups linked to m aluminum atoms. (Black balls: oxygen atoms, gray balls: aluminum atoms, white balls: hydrogen atoms).[101]

Moreover, the DFT calculations have allowed to determine the hydroxylation coverage θ_{OH} ($OH.nm^{-2}$) on each alumina surface as function of the temperature as seen in the Figure 18.

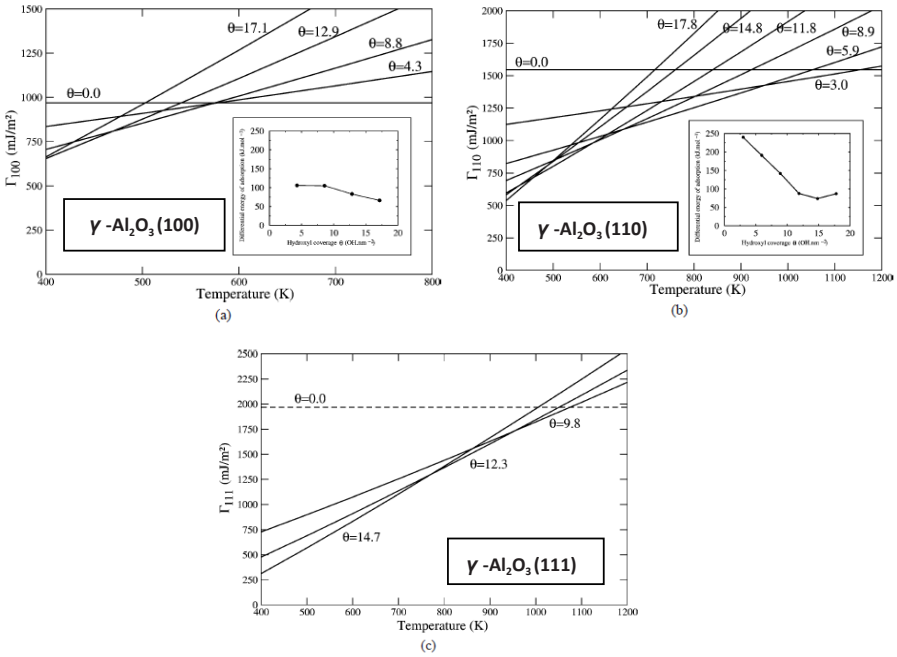

Figure 18. Surface energy of the (a) γ-Al_2O_3 (100), (b) γ-Al_2O_3(110), and(c) γ-Al_2O_3(111) surface as a function of temperature for different hydroxyl coverages (θ in $OH.nm^{-2}$). [101]

For instance, in the sulfidation condition around 623K and under HDS reaction conditions around 473K and if we assumed that the TMS active phase doesn't influence the hydroxyl surface (which is not true), the theoritical maximum hydroxyl coverage should be:

At 623K: (100): $\theta_{OH}= 0$ at.nm^{-2} (110):$\theta_{OH}= 5.9$ at.nm^{-2} (111): $\theta_{OH}= 14.7$ at.nm^{-2}

At 473K: (100): $\theta_{OH}= 8.8 - 12.9$ at.nm^{-2} (110):$\theta_{OH}= 11.8$ at.nm^{-2} (111): $\theta_{OH}= 14.7$ at.nm^{-2}

At 623K, the contribution of the hydroxyl of the (100) surface which represents 80% of the total alumina surface is not significant, while at 473K the proportion of hydroxyl of the (100) is dominating. However, this theoretical model considers that γ-Al_2O_3 exist for a temperature higher than 1000K which normally associated to δ-Al_2O_3.

Finally, Digne and coworkers [101,122] described the assignment of the OH groups of aluminas using the non-spinel model for the γ-Al_2O_3. The bands around 3790, 3770, and 3730 cm^{-1} are assigned to three different terminal hydroxyl groups that are bonded to Al atoms on different surface (Table 14). The hydroxyl group on the (111) surface is assumed to exist.

Table 14. OH hydroxyl configurations according to Digne's model by considering the alumina surface exposed compare with the Busca-s model.

ν_{exp} (cm^{-1})	Digne's model			Busca attribution
	Surface	Attribution	ν_{calc} (cm^{-1})	
3800-3785	110	HO-μ_1-Al_{IV}	3842	HO-μ_1-Al_{IV}
3780-3760	100	HO-μ_1-Al_{VI}	3777	HO-μ_1-Al_{IV}-lac
3755-3740	111	HO-μ_3-Al_{VI}	3757	HO-μ_2-Al_{VI}
3735-3730	110	HO-μ_1-Al_{V}	3736	HO-μ_2-Al_{VI}-lac
	111	HO-μ_2-Al_{V}	3732	
	111	HO-μ_1-Al_{VI}	3713	
	110	HO-μ_2-Al_{VI}	3707	
3710-3690	111	HO-μ_2-Al_{VI}	3690	HO-μ_3-Al
	111	HO-μ_2-Al_{VI}	3640	
3650-3590	100	HO-μ_3-Al_{VI}	3589	

The main difference in these two models appears for the OH group attributed to the 3780-3760 cm^{-1} frequency. Busca attributes it to an Al_{IV} with one vacancy neighbor. Morterra and Magnacca[123] arrived to the same conclusion from infrared observations with CO and pyridine probe molecules. They observe that this OH group is the most reactive and accessible, with weak bases like CO[124] and strong bases like pyridine[125]. Thus, they concluded that this hydroxyl site, which has a great interaction with probe molecules, is located in crystallographic defects such as ridges and corners. Therefore, this hydroxyl group is surrounded by three oxide ions i.e. Al_{IV}. The consideration of the crystallographically defective configuration, corners and ridges, have not previously accounted for.

Méthivier and coworkers[126] have been particularly interested in the comparison between γ-Al_2O_3 and δ-Al_2O_3 by FTIR study. Consistent with the higher crystalline order reported for

δ-Al_2O_3 than for γ-Al_2O_3, the infrared contains lower amounts of hydroxyl groups on the surface. Moreover, the inversion of the intensity for the vibrational band of the hydroxyl group around 3800 and 3775 cm^{-1} between the γ-Al_2O_3 than for δ-Al_2O_3 are observed. Previously, the frequency at 3775 cm^{-1} was attributed to the most reactive hydroxyl group. Thus, the reactivity of δ-Al_2O_3 could be modified compared to the γ-Al_2O_3.

3.2 Silica

3.2.1 Generalities

Silica used as support, with SiO_2 formula, is generally amorphous and has a 3D network of silicon and oxygen atoms. Generally, Silicon atoms are at the centers of tetrahedral of oxygen atoms, [SiO_4], i.e. a silicon atom is bound to four oxygen atoms and each oxygen is surrounded by two silicon atoms. The [SiO_4] tetrahedron unit represents the building block of almost all silica polymorphs. Thus, silica only differs in the structure which depends of the connectivity of the tetrahedral SiO_4 framework. Regarding the specific surface area, it can vary from 30 to 1000 m^2/g, depending on the preparation step [127]. Moreover, silica has a weak surface acidity (both LAS and BAS) which rarely affects the catalytic reactions directly[128,129]compare with alumina support. Moreover, interactions of metal ions are strong and in some cases irreversible held by forces in addition to ionic attraction.

3.2.2 Structure and physical characteristics

Similarly to external surfaces of alumina, the silica surface structure terminates in either siloxane group with the oxygen on the surface, or silanol groups. The silanols are subdivided into different classes: isolated free groups (single silanols), geminal silanol where two hydroxyl groups are attached to one silicon atom. Finally, a third type of silanols, vicinal or bridged silanols, consist of two single silanol groups, attached to different silicon atoms, close enough to hydrogen bond. For geminal and isolated silanols no hydrogen bond can be made since respectively silanols are either too close each other or too far separated respectively [130,131]. Figure 19 presents the silica surface structure with siloxane and silanol groups [131].

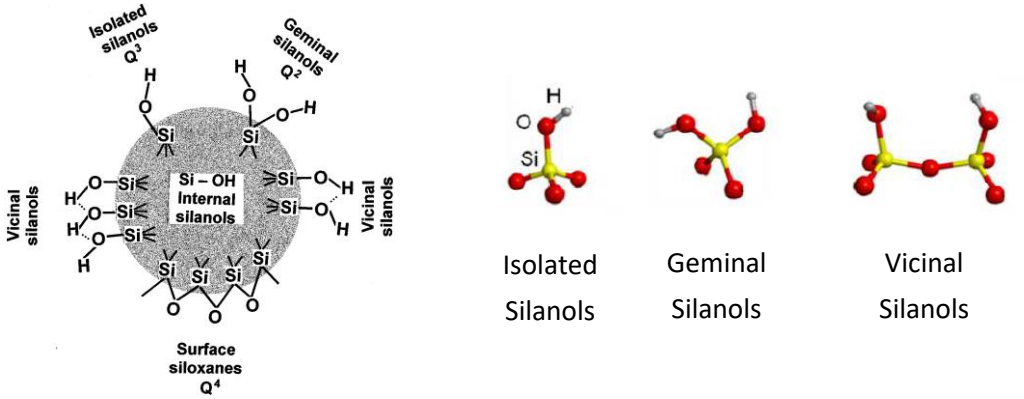

Figure 19. Types of silanol groups and siloxane bridges on the silica surface.[131]

Composition of the surface, silanol type and concentration depends on silica nature and also on the hydroxylation state i.e. of the thermal treatments applied such as calcination or drying step under vacuum. Generally, starting with a fully hydroxylated surface, there are about 5 $OH.nm^{-2}$ at 150 °C and about 1 $OH.nm^{-2}$ at 800 °C. This hydroxyl coverage is around two times lower than on γ-Al_2O_3 at 150°C and an hydroxyl coverage similar at 800°C.

Moreover, a detailed description of the surface state is important in order to understand the part of support involved in the catalyst reactivity or to describe with more details the MSI and synergy between active phase and support.

Thus, Zhuravlev's model [131] has been developed on the basis of experimental and theoretical data in order to predict the concentration and distribution of the silanol and siloxane surface groups as a function of the treatment temperature of SiO_2 (Figure 20).

In order to differentiate each silanol and therefore quantified them, NMR with the deuterium exchange method and IR experiments have been commonly used and for more than 50 years.

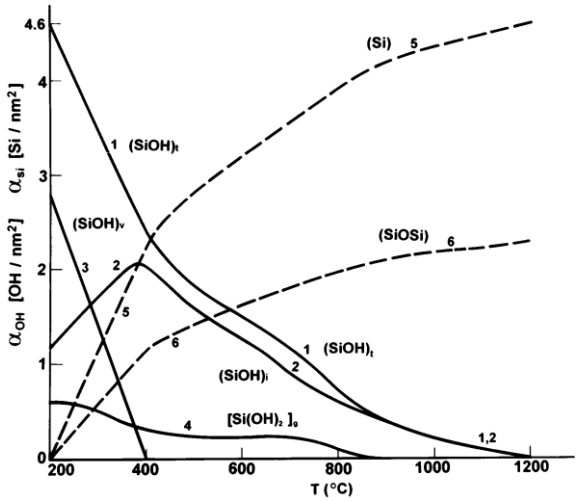

Curves	Description
1	**(SiOH)t**: Average concentration of the total OH groups
2	**(SiOH)i**: Average concentration of the free isolated OH groups
3	**(SiOH)v**: Average concentration of vicinal OH groups bound through the hydrogen bonds
4	**(SiOH)g**: Average concentration of geminal OH groups
5	**Si**: Average concentration of surface Si atoms that are part of the siloxane bridges and free of OH groups
6	**SiOSi**: Average concentration of surface SiOSi bridges, which are free of OH groups

Figure 20. Zhuravlev's model. Distribution of the surface groups as a function of the temperature treatment of SiO_2 in vacuo. (SiOH)t, (SiOH)i, (SiOH)v, (SiOH)g and $(Si)_4$ are respectively the total groups, isolated, vicinal, germinal silanol and siloxane group.[131]

IR studies performed on SiO_2 have provided a detailed description of the surface silanol groups as function of the different vibrational bands observed. Figure 21.a) presents the IR spectras of SiO_2 to different treatment temperature and Figure 21.b) presents attributions of the OH stretching vibrations on SiO_2.

a)

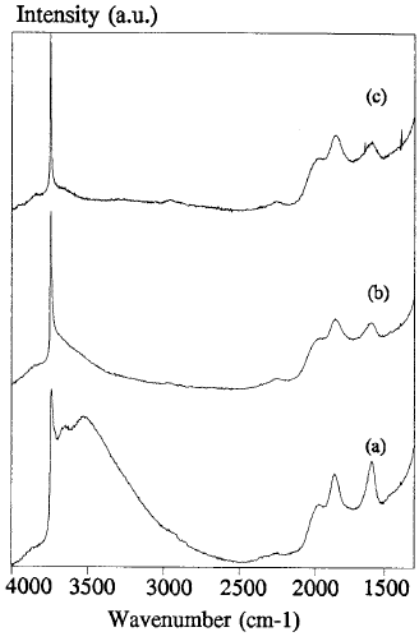

b)

Wavenumber (cm^{-1})	Species
3746	Free OH (isolated)
3742	Geminal OH
3730-3720	Vicinal OH (Hydrogen perturbed OH by H of neighboring SiOH)
3650-3670	Internal OH
3520	Oxygen perturbed OH by O of neighboring SiOH
3500-3400	Molecular adsorbed H_2O

Figure 21. (a) Typical FTIR spectra of silica with treated for 17h at (a) 373 K; (b) 673 K and (c) 973 K. The Y-scales of the three spectra are not comparable.[130] (b)Conventional attributions of the OH stretching vibrations on SiO_2.[130]

The region 3740 – 3400 cm^{-1} relates on the characteristic stretching vibrational modes of SiOH hydroxyl group. The vibrations at 3730 - 3720 cm^{-1} and 3520 cm^{-1} have not been directly assigned to a specific silanol but to the interaction of the oxygen of the hydroxyl group with the hydrogen of a neighboring hydroxyl group.[130]

In a general manner, the relative acidity of silanol sites is greatest for vicinal silanols and geminal silanols are more acidic than isolated or unassociated sites (Hooke law).[132]

Two other regions are attributed to an overtone structure vibration (Contribution falling at 2000 – 1870 cm^{-1}) and the fingerprint region. However, these regions are less characteristic and significant of the silanol groups (Table 15).

Table 15. Attribution of the OH vibrations on SiO_2 in the fingerprint and the overtone structure vibration region.

Wavenumber (cm^{-1})	Species
2000-1870	skeleton (overtone) vibrations
1625	bending O-H (molecular water)
1250-1020	asymmetrical Si-O-Si stretching
970	Si-O-(H...$H_2$0) bending
870	bending O-H (silanal)
800	in-plane bending (geminal)
600	in-plane bending (geminal)
148	out-of-plane bending (geminal)
127	out-of-plane bending (vicinol)

This region could be used as internal reference in diffuse reflectance infrared spectroscopy (DRIFTS) and may allow quantitative data treatment after normalization.

In the same way, NMR spectroscopy studies[130,133,134] have been performed in order to describe the surface silanol group. Figure 22 shows ^{29}Si CP MAS NMR spectrum of silica Aerosil. The main band at – 101 ppm refers to the isolated silanols or vicinal silanols. Two

shoulders at -91 and -110 ppm reflect respectively the presence of geminal silanols and siloxane groups.

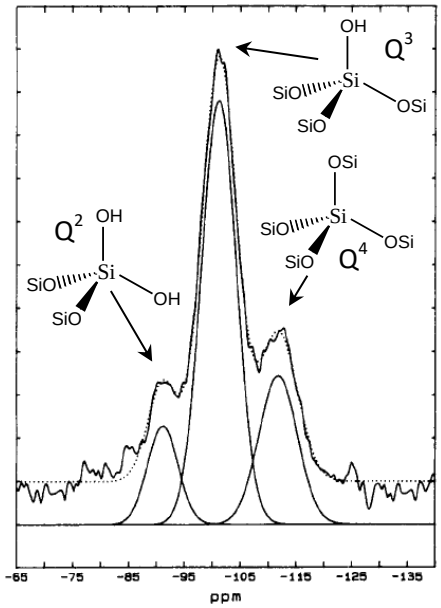

Figure 22. 59.6-MHz ^{29}Si CP/MAS NMR spectra of silica Aerosil. [134]

However, the - 92 ppm band attribution is still under debate. Indeed, while ^{29}Si MAS NMR spectra attributes this band to Si-atoms of geminal silanols, ^{1}H-NMR does not seem able to distinguish between isolated and geminal silanols. Moreover, it was assumed that this band could be explained by changes in the coordination of the surface Si atoms and electronical interactions between silanols.[135]

Infrared studies have suggested that the acidity of the geminal and isolated silanols may be different but quantum mechanical calculations reveal that Q^2 and Q^3 sites have almost the same Brønsted acidity. Indeed, these two sites develop the same aptitude to H-bond with adsorbed water molecules. In other words, it is difficult to conceive differences in reactivity with respect to the same molecule.[128,129,133]

4 Influence of catalytic properties on selective HDS

4.1 Hydrodesulfurization and hydrogenation reactions

As noted above in the part 1.2 olefins are necessary present in the FCC gasoline cut as well as undesirable sulfur compounds especially sulfide heterocyclic compounds as thiophene and alkylthiophene derivatives.

4.1.1 Thiophene and derivative compounds: reactivity and HDS mechanism

Thiophene and derivatives belong to the aromatic heterocycle compounds with a planar conformation. The sulfur atom has a lone pair electrons located on the sp^2 hybrid orbital in the plane of the ring (Figure 23). Regarding the aromaticity, resonance energy of thiophene (120 $kJ.mol^{-1}$) is close to the benzene (153 $kJ.mol^{-1}$) even if it is lower. Thus, thiophene presents a similar aromatic character as benzene. However, the reactivity is directly impacted because the p orbital of the lone pair of electrons on sulfur that conjugates with the ring is a 3p orbital, so the overlap with the 2p orbitals on the neighbor carbon is reduced. Thus, the energy of the Lowest Unoccupied Molecular Orbital (LUMO) of thiophene is significant.[136,137] Moreover, reactivity of thiophene can be reduced by the presence of electron donor substituent in position 2, 3, 4, 5. It increases the electronic density of the ring and so the overlap between the sulfur and carbon atoms.

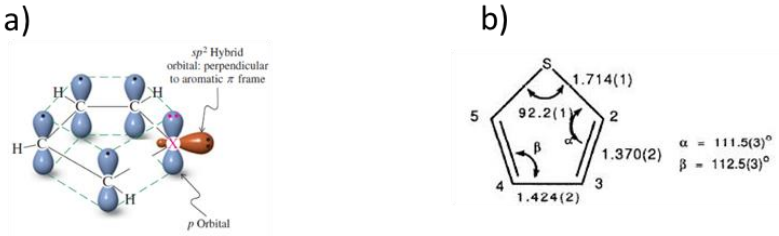

Figure 23. (a) Orbital pictures of (X = S). The heteroatom is sp^2 hybridized and bears one delocalized lone electron pair.[138] (b) A detailed structure of thiophene.[139,140]

Besides, sulfur atom could be also involved in the reactivity with the presence of one delocalized lone electron pair. As for benzene, the electrophilic aromatic substitution may occur and take place preferentially on position 2. Polymerization of alkylation reaction can appear.[136]

In catalysis, the thiophene is adsorbed on the surface before to react. Studies have been carried out to review the various modes of thiophene coordination over transition metal complexes (Figure 24).[140–142]

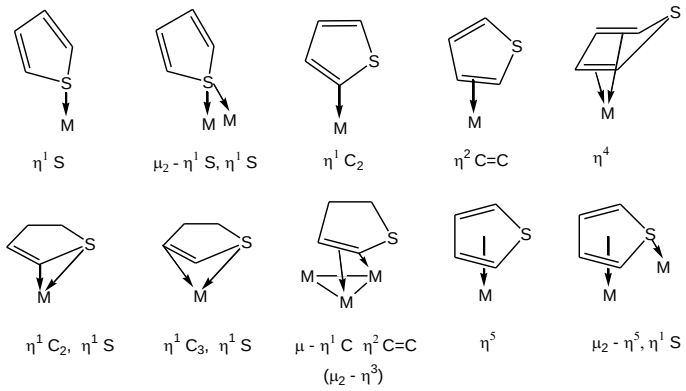

Figure 24. Different coordination modes of thiophene adapted from [140–142].

Tarbuk et al. [143] reported specific coordination modes of thiophene over non promoted MoS_2 phase from IR experiments: η^1(S)-bonded, η^2-bonded, η^1-bonded and η^5-bonded to the catalyst surface. Vibrational mode assignments for thiophene adsorbed on γ-Al_2O_3, sulfided Mo/Al_2O_3 is given in Table 16 from FT-IR experimental studies.[144] The vibrational frequency of the symmetric C=C mode seems shifted to higher wavenumbers (from 1406 to 1429 cm^{-1}) when thiophene is η^1(S)-bonded to a metal center (or surface) and should be shifted to lower wavenumbers when thiophene is □-bonded to a metal center (or surface) but it is not observed. [140,143,145]

Table 16. Vibrational mode assignments for thiophene liquid, adsorbed on γ-Al_2O_3, and sulfided Mo/Al_2O_3 (all values in cm^{-1}).[144]

C_4H_4S(l)	C_4H_4S on γ-Al_2O_3	C_4H_4S on Sulfided Mo/Al_2O_3	Assignment
1250	1253	1252	δ_{CH} (in plane)
1358	1362	1360	ν_R (ring stretch)
	1400	1401	ν_{CC} (symmetric)
1406	1408	1408	ν_{CC} (symmetric)
		1429	ν_{CC} (symmetric)
1504	1504	1502	ν_{CC} (asymmetric)
1575	1576		Combination band
1586	1616	1601	Combination band
3072	3073	3073	ν_{CH}
	3089	3089	ν_{CH}
3107	3104	3104	ν_{CH}

No infrared data of thiophene or its associated derivatives adsorbed on promoted MoS_2 is known in the literature to date.

However, recent DFT studies on Co promoted MoS_2 [142] show that different adsorption configurations of thiophene are stable for the adsorption of 2-methylthiophene (2MT) as function of the percentage and location of the promoter at the edge and of the sulfur coverage. 2MT could be μ_2-η^3-bonded on two neighboring Co atoms in the M-edge (from C to I structures) of the CoMoS phase and according to other way as presented in the Figure 25.

a)

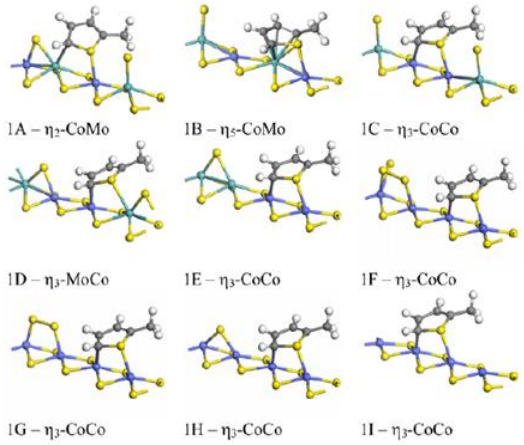

b)

Promoter (%)	S (%)	Adsorption configuration	ΔE_{ads} (eV)
50% alt	25.0%	η_2-CoMo 1A	−0.54
	12.5%	η_5-CoMo 1B	−2.31
50% pair	25.0%	η_3-CoCo 1C	−0.97
		η_3-MoCo 1D	−0.90
	12.5%	η_3-CoCo 1E	−1.19
100%	37.5%	η_3-CoCo 1F	−0.37
	25.0%	η_3-CoCo 1G	−1.12
	12.5%	η_3-CoCo 1H	−1.21
	0.0%	η_3-CoCo 1I	−1.30

Figure 25. a) Stable 2MT adsorption configurations and b) Adsorption energies of the stable 2MT configuration on CoMoS M-edge ((yellow balls: S, green balls: Mo, blue balls: Co or Ni, gray balls: C, white balls: H).[142]

Regarding the S-edge of the CoMoS phase, thiophene could be only η^1-bonded η^5-bonded trough the S atom as presented in the Figure 26.

a)

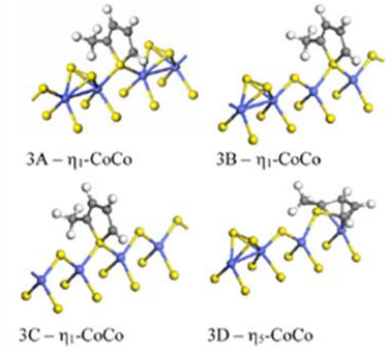

b)

Promoter (%)	S (%)	Adsorption configuration	ΔE_{ads} (eV)
100%	62.5%	η_1-CoCo 3A	−0.22
	50.0%	η_1-CoCo 3B	−0.24
	37.5%	η_1-CoCo 3C	−1.39
		η_5-CoCo 3D	−1.37

Figure 26. a) Stable 2MT adsorption configurations and b) Adsorption energies of stable 2MT configuration on CoMoS S-edge (Same legend color as in Figure 25). b on the CoMoS S-edge. [142]

Thus, in HDS reaction condition, the more stable adsorption configuration of 3MT should be on the S-edge (Figure 25) (S-edge composed to Mo promoted by 100% Co covered by 50% (Figure 26), adsorption of 3MT is favored). If the M-edge is decorated by Co, the adsorption will occur according to 1A or 1D adsorption configuration (Figure 26), (M-edge promoted is composed of Mo promoted by 50%Co covered by 50% S, (Table 9).

However, DFT calculation does not considered the adsorption of thiophene on the support and effect of H_2 coverage.

Once adsorbed, thiophene may follow different hydrodesulfurization routes (Figure 27). In the literature, two relevant pathways for the hydrodesulfurization of thiophenic compounds can be supposed. The Direct Desulfurization route (DDS) consists in a pre-hydrogenation followed by a ring-opening step through diolefinic intermediate, and Hydrogenation (HYD) consists in the total hydrogenation of the sulfur heterocycle followed by C–S bond cleavage. Dos Santos et al.[146] proposed a complete a reaction scheme for the HDS of 3MT (Figure 27). Considering adsorption modes of olefins and thiophene compounds, reaction pathways can be precised. Indeed, if the HYD route is considered, the pre-hydrogenation of thiophene may be favored when flatwise adsorption would occur by π-bonding, on the basis of the similar behavior to aromatics hydrogenation [147], while the DDS route would take place through adsorption of thiophene via its S atom and perpendicularly on the vacant sites.[147]

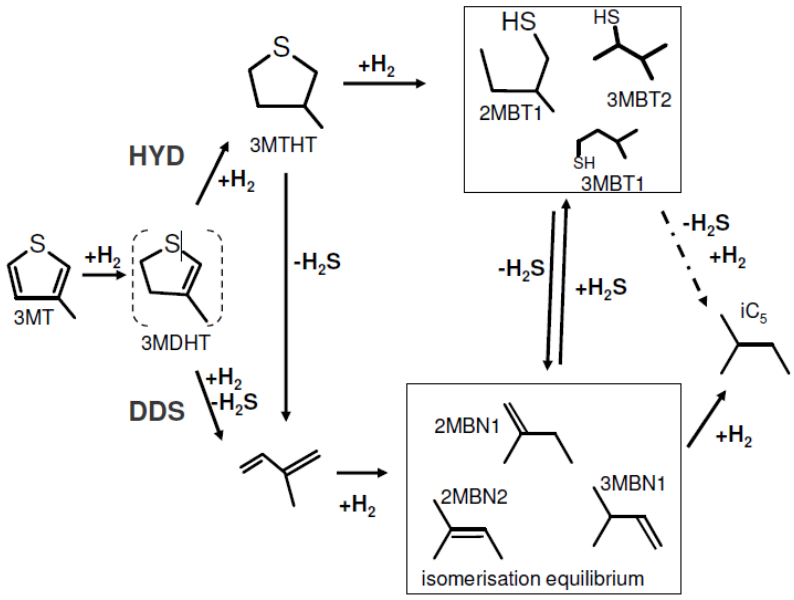

Figure 27. Reaction pathways for 3-methylthiophene HDS.[146]

Moreover, in these reaction pathways, the isomerization equilibrium is not considered. Indeed, 2MT, isomer of 3MT, are not observed which may indicate that the isomerization kinetic is too low compared to the HDS kinetic of 3MT. However, independently of the kinetic, thermodynamic equilibrium between isomer can be considered. The equilibrium of the methylthiophene (2MT/3MT) as function of the temperature is given in Figure 28.

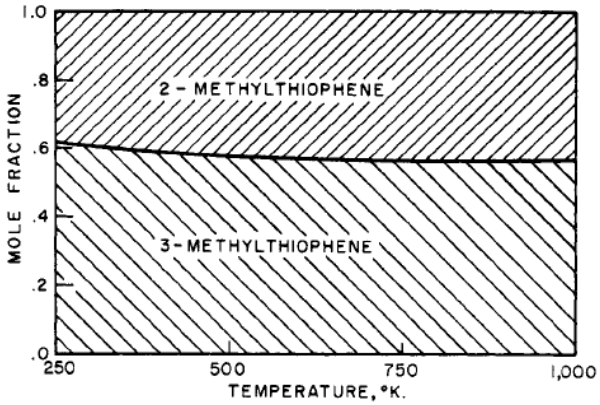

Figure 28. Equilibrium concentrations of methylthiophenes. Reference compound (gas) = isomeric compound (gas), values of equilibrium mole fraction are applicable only in the range from zero pressure up to that pressure at which the ratio of fugacity to pressure still does not differ significantly for the several isomers.[148]

When the HDS of thiophene occurs during the HDS process of FCC gasoline, an undesirable reaction takes place: the olefins hydrogenation. Thus, the understanding of the olefins hydrogenation process over HDS catalyst is necessary in order to drive the selectivity.

4.1.2 Olefins: reactivity and hydrogenation mechanism

Olefin is an unsaturated hydrocarbon with at least one carbon–carbon double bond. The planar double bond incorporating trigonal carbon atoms confers a special electronic and structural feature. Indeed, reactivity is attributed to a strong C-C σ-bond, 450 kJ.mol^{-1}, and a relatively weaker π bond, 270 kJ.mol^{-1}, related to the carbon hybridization. Thus, alkenes can undergo addition reactions by cleavage of the C-C π-bond.[137]

In catalysis as for thiophene, an adsorption step of olefins needs to be considered. Indeed, olefins can be adsorbed on the metal surface in two predominant adsorption modes: the

σ- and π-adsorption modes. In the σ-mode, olefins are adsorbed by formation of two direct σ-bonds with two different surface atoms by the rehybridization of the orbitals on the carbons atoms. In the π adsorption mode, ethylene is coordinated to a single metal atom donative and back-donative interaction of the π_{CO} and π^*_{CO} respectively. Both can be observed, depending on the olefins and surface coverage associated. At lower coverage, the σ-mode is mainly described whereas at higher coverage the π-mode becomes favorable. For instance, DFT calculation indicates by considering Pd(111) surface that on the σ-mode the adsorption of a single hydrogen atom occurs with overall activation energy of 88 $kJ.mol^{-1}$ whereas the hydrogen addition to a π-bonded occurs with an activation energy of 36 $kJ.mol^{-1}$.

Recently, *ab initio* studies have been performed and highlighted the possible adsorption modes of 2,3-dimethylbut-1-ene (23DMB1N) on metal of the Co-promoted MoS_2. Figure 29 gives a representation of these adsorption modes.

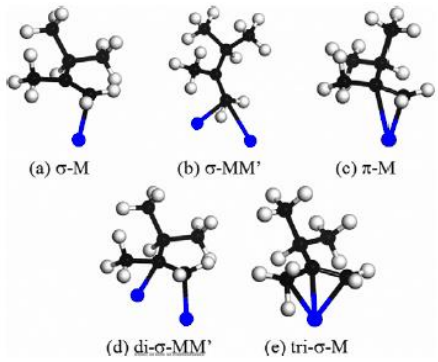

Figure 29. Simplified representation of the adsorption modes of 23DMB1N. (Black balls: C, White balls: H, Blue balls: edge sites (Mo, Co or Ni)).[142]

In this study, authors demonstrated that on the M-edge and the S-edge of the CoMoS phase, most stable adsorption modes of olefin are preferentially those that imply Co atoms as reported in Figure 30 and Figure 31.

a)

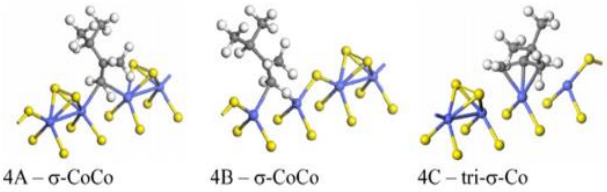

b)

Promoter (%)	S (%)	Adsorption configuration	ΔE_{ads} (eV)
100%	62.5%	σ-CoCo 4A	+0.68
	50.0%	σ-CoCo 4B	+0.72
	37.5%	tri-σ-Co 4C	−0.51

Figure 30. a) Stable 23DMB1N adsorption configurations and b) adsorption energies of the stable 23DMB1N configuration on CoMoS S-edge. (yellow balls: S, green balls: Me = Mo, blue balls: Co or Ni, gray balls: C, white balls: H).[142]

a)

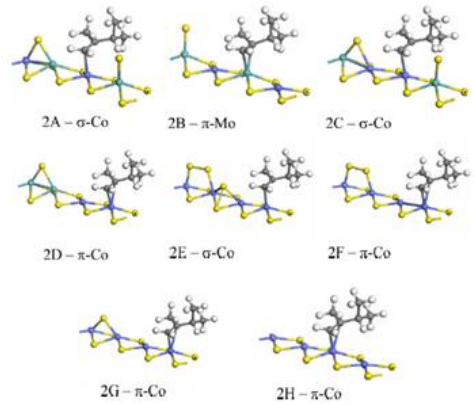

b)

Promoter (%)	S (%)	Adsorption configuration	ΔE_{ads} (eV)
50% alt	25.0%	σ-Co 2A	−0.08
	12.5%	π-Mo 2B	−1.54
50% pair	25.0%	σ-Co 2C	−0.43
	12.5%	π-Co 2D	−0.72
100%	37.5%	σ-Co 2E	−0.19
	25.0%	π-Co 2F	−0.73
	12.5%	π-Co 2G	−0.74
	0.0%	π-Co 2H	−0.79

Figure 31. a) Stable 23DMB1N adsorption configurations and b) adsorption energies of the stable 23DMB1N configuration on CoMoS M-edge. (Same legend color as in the Figure 30). [142]

Thus, in HDS reaction condition, the most stable adsorption configuration of 23DMDBT should be on the M-edge.

At this time, no literature has been found on infrared data of olefins adsorbed on the promoted o unpromoted HDS catalyst.

Once it has been adsorbed on HDS catalyst, reactions may occur depending on the active phase and support of the catalyst but also of the reaction conditions. The two reactions which imply only olefins are the hydrogenation and isomerization reactions. In the case of isomerization reaction, Brønsted acidity of support, especially for Al_2O_3, could participate to this reaction. Indeed, in addition to direct hydrogenation of the olefins to form the related alkane various hydrogenated products are formed. Isomerization of the reactant olefin needs to be considered in order to explain it. For instance, Mey et al.[149] study the hydrogenation of the 2,3dimethylbut-2-ene is presented in Figure 32.

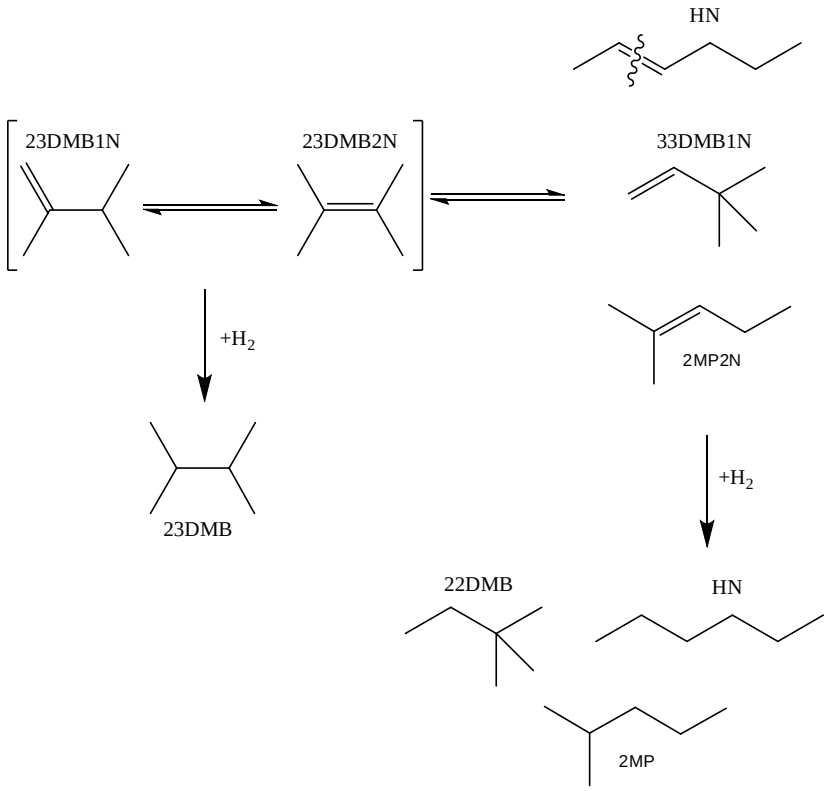

Figure 32. Simplified scheme of the transformation of the 2,3DMB2N.(Adapted from Mey *et al*.[149])

Moreover, during the HDS of sulfur-containing molecules, Mey et al.[149] demonstrate that side reactions can occurs in presence of model FCC mixture feedstock composed of 2methyltiophene and 23DMB2N. Formation of thiols (for instance pentanethiol), alkylation of 2MT by olefins (for instance C5-methylthiophenes) of even craking products from intermediate olefins can appear. Figure 33 presents a scheme of 2MT transformation and the reaction way different possible. [149] According to us, formation of the products involves the Brønsted acidity of the support.

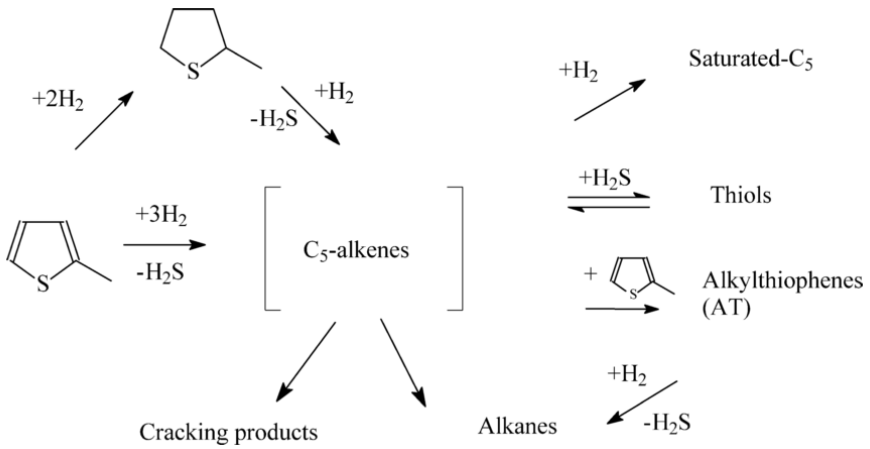

Figure 33. Schematic representation of 2MT transformation. [149]

As it was presented, both reaction HDS and HYDO take place on HDS catalyst. Therefore, the study of active sites implied in these reactions is a real key factor in the understanding of the selectivity of the HDS process.

4.1.3 Nature of the sites involved

Several studies have been conducted in the past in order to highlight the active site of HDS catalyst involved in both competitive reactions of olefins hydrogenation and sulfur compounds hydrodesulfurization. Nevertheless, nature and a detailed description of the catalytic sites involved in hydrogenation and hydrodesulfurization is not yet definitely settled.

C.N. Satterfield and G. W. Roberts[150] show by kinetic study of thiophene reaction, based on Langmuir-Hinshelwood model of both reactions butene hydrogenation and thiophene hydrodesulfurization, that olefins is not hydrogenated at the original desulfurization site. Other studies have confirmed the existence of two types of active sites.[151,152]

Indeed, they assumed that sulfided CoMo catalysts surface has two types of sites. This assumption is consistent with a previous study made by P. Desikan and C.H. Amberg[153] who shown, by pyridine poisoning, that the sites involved in both reactions differed in acid strength. Moreover, authors assume that the presence of H_2S have little or no effect on the hydrogenation of butene suggesting that HDS and HYDO occur on different sites[152,154].

Regarding the HDS reaction, they suggest that thiophene and hydrogen sulfide are expected to react with each other for one type and hydrogen adsorbs on the second type. According to this study, the rate limiting step is the combination of adsorbed thiophene with adsorbed hydrogen because of thiophene adsorption (in two-point) involving a steric hindrance to the adsorption of other molecules.[150]

In 1981, Ramachandran *et al.*[155] assumed that both HDS and HYDO reactions occur on different active sites. Indeed, by variation of the partial pressure of H_2S during the dibenzothiophene HDS test, they demonstrated that H_2S has no effect on the hydrogenation function but increases the cracking function of sulfided CoMo catalysts. However, the H_2S depresses the hydrogenolysis function. Thus, hydrogenation and HDS sites could occur on the active site.

In the same way, in 1994, S. Kasztelan and D. Guillaume[156], assuming that the reaction occurs on a surface containing two sites, described their chemical nature from a detailed kinetic analysis of the effect of a large range of H_2S partial pressure on toluene hydrogenation activity of a model MoS_2/Al_2O_3 catalyst.

One is an unsaturated Mo ion, and the other one is a stable sulfur ion host of the proton generated by the heterolytic dissociative adsorption of hydrogen and hydrogen sulfide. Hydrogenation is assumed to proceed by addition of a hydride ion followed by addition of a proton to the aromatic molecule. However, this hypothesis is based on the hydrogenation of aromatics compounds. Some studies suggest that two different types of sites participate depending on the reaction, olefins or aromatics hydrogenation because of the stronger deactivating effect of H_2S on aromatic hydrogenation compared to olefins hydrogenation.

On the other hand, somes studies indicate that both reactions occurred on the same center [157] or that three types of active sites would be involved[158]. The first is active in HDS and n- and iso-olefins adsorption, the second is active in n-olefin hydrogenation and the third is active in iso-olefin hydrogenation. Others authors also supposed that a synergy between both hydrogenation and hydrodesulfurization sites might exist.[159]

More recently, the presence of sulfur vacancy sites also called coordinatively unsatured sites (CUS sites) have been reported as the most relevant active site in HDS and HYDO reactions. The existence of these CUS sites on the Co-promoted MoS_2 active phase was highlighted by EXAFS experiment.[88,160] Indeed, it was observed a reversible modification in the sulfur coordination sphere around the cobalt in the CoMoS phase upon changing between reducing and sulfiding condition. The adsorption of a molecule within heteroatom directly to the promoter atoms is consistent. [64,160] Moreover, from DFT calculation and labeled [^{35}S]DBT HDS method, Dumeignil and coworkers[161] have proposed a mechanism of formation of a CUS on MoS_2 (Figure 34). Mechanism consists in the dissociative adsorption of an H_2 molecule on the metallic edge of a MoS_2 crystallite surface with further creation of a CUS by release of one H_2S molecule in the gas phase. Moreover, Prodhomme et al.[162] have investigated all the possible pathways for activating H_2 on the M- and S-edges and they show that the process depends on the type of edge and also on the sulfur coverage of each edge.

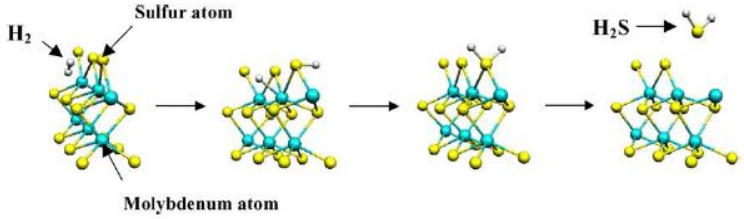

Figure 34. Mechanism of formation of a CUS on non-promoted MoS_2 determined by *ab initio* calculations.[161]

Besides, different research teams work in the same way to demonstrate that binding energy of sulfur to the transition metal is a key parameter to describe the promotional effect. Nørskov et al.[163] used a model based on the *ab initio* calculation to describe the binding energy and show a decrease of metal-sulfur binding energy when the cobalt is added to the MoS_2 catalyst. In addition, Toulhoat et al.[164] showed that the experimental activities can be correlated to the sulfur-metal bond energy through a volcano master curve. Optimal catalysts such as CoMoS exhibit an intermediate M-S bond energy in line with the Sabatier principle.[161,165]

Dumeignil *et al.*[161] by using ^{35}S DBT HDS experiments have recently confirmed the previous results exposed. Indeed a difference of 3 kcal.mol^{-1} is observed regarding the activation energy of the H_2S release reaction between un- and promoted catalysts. Co promoting effect increases the number of active sites with an enhanced activity due to higher sulfur mobility in contrast with the non-promoted catalyst.

In a different way, Lauritsen *et al.*[166,167] have highlighted by STM a new type of sites of high electron state density, i.e. high ability to donate and accept electrons, located on the fully sulfur-saturated Mo edges (Figure 35) These so-called “brim” sites (bright rim) with metallic character could bind S-containing molecules such as thiophene and were observed to be involved in hydrogenation reactions and partial hydrogenolysis of the sulfur-containing molecules in the presence of hydrogen. Hydrogen would be available in neighboring edge sites in the form of SH groups and its transfer would allow the HYD reactions to take place.[168] However, operating conditions of the STM analysis are different of HDS reaction conditions which could be implied a structural modification of the TMS phase of the catalyst.

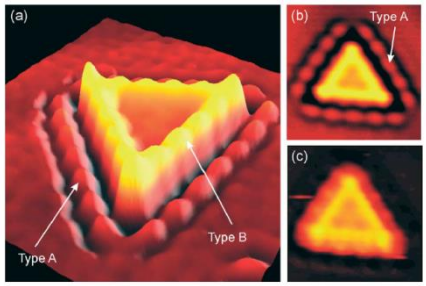

Figure 35. STM images of a triangular single-layer MoS_2 nanocluster illustrating the bonding of thiophene at low temperatures. The images are listed in the order of increasing substrate temperature (T). (a) When T is below 200 K thiophene adsorbs molecularly in two different configurations. The 3D rendering of the STM image shows thiophene molecules adsorbed in positions on top of the bright brim associated with an edge state (type B), and additionally thiophene decorates the perimeter of the cluster (type A). (b) STM image representative for the temperatures in the interval 200 K < T < 240 K, where thiophene molecules on top of the brim have desorbed, whereas the perimeter decoration is retained. (c) At temperatures T >240 K no indication of adsorbed thiophene was observed with STM. [167]

A few years later, Moses and coworkers[169,170] give a further description of the HDS route reaction by considering the active sites of the TMS phase, Brim and CUS sites, involved for the un- and promoted MoS_2 catalysts. Indeed, they highlight the possible HDS mechanism of the thiophene considering the different edges, M- and S-edges, of the active phase.

Regarding to the non-promoted MoS_2 catalyst with the edge configuration which is thermodynamically most stable under HDS conditions (Figure 36b)), the HYD and DDS routes seem promoted first on the M-edge and in second time on the S-edge. Figure 36 a) present a general scheme of the reaction pathways at the two edges on MoS_2 (only the full and dotted black arrows have to be considered for the non-promoted MoS_2 catalyst).

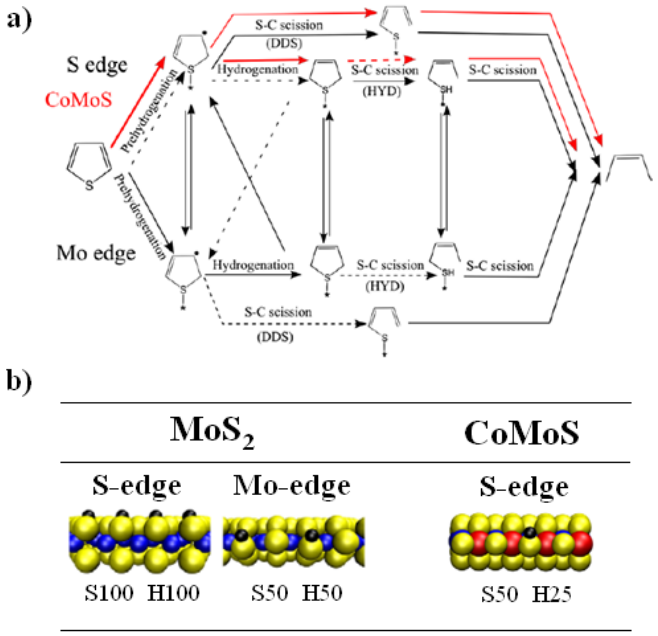

Figure 36. a) Schematic overview over the reactions and structures involved in the HDS of thiophene. The schematic overview includes the reactions at the Co-promoted MoS_2 with the Co promoted S-edge marked with red lines. The non-promoted MoS_2 with both S- and M-edge marked with black lines respectively in the upper and in the lower part. In the middle the possible interactions between the two coexisting edges. The dotted arrows denote reactions found to be slow. b) Structure of the edge of the un- and promoted MoS_2 in the realistic HDS conditions.[169–171]

Indeed, H_2 adsorption and hydrogenation reactions have lower barriers at the M-edge brim site than those at the S-edge vacancy site. Moreover, in the equilibrium state the S-edge has a full S-coordination which requires the creation of vacancies in the first step of the catalytic cycle. Thus, thiophene would be preferentially adsorbed on the M-edge and hydrogenation step is energetically unfavorable at the S-edge.

For the HYD route, the hydrogenation of the thiophene occurs to form the hydrogenated product (2,5-dihydrothiophene). For the DDS route, only a partial hydrogenation of the thiophene occurs.

Then, they suggest that the edges can catalyze the reaction in interplay between sites. A migration of these hydrogenated products occurs since their adsorptions at the S-edge vacancy sites are favored. Indeed, on these sites the binding is stronger than at the M-edge brim site.

Finally, for both DDS and HYD pathways the subsequent S–C scission step occurs at the S-edge. Authors indicate that DDS pathway is favored relatively to the HYD pathway. Indeed,

while hydrogenation of thiophene can occur easily at the Mo edge, S–C bond scission has a very high barrier and is therefore not likely to happen at this edge.

Regarding the Co-promoted catalysts, Moses et al.[171] show that both HYD and DDS pathways occurs preferentially on the promoted S-edge as view in the Figure 36 a) marked with the red lines.

The promoter incorporation involved the formation of the CoMoS phase with promoted S-edge as view in the part 2.2.2. Regarding the edge of the MoS_2, an important difference appears. Indeed, in contrast to the non-promoted, CUS sites are directly present in equilibrium conditions and the catalysis does not require vacancy formation in the first step.

Thus, adsorption of thiophene occurs on the S-edge of the CoMoS phase following by the pre- or hydrogenation occurring directly on it. Then, HYD and DDS routes occur on the S-edge. However, authors indicate, as for the non-promoted, that while hydrogenation of thiophene can occur easily at the Mo edge, S–C bond scission has a very high barrier and is therefore not likely to happen at this edge. Thus, the DDS may be favored compared to HYD pathway.

Studies have been performed by Lauritsen et al.[172] with STM analysis. They assumed that both edge terminations, S- and M-edges, is present but only the S-edge would be promoted consistent with DFT calculation[173] and EXAFS experiments[174]. However, the use of specific support and specific STM conditions probably impact the morphology of the promoted MoS_2 described of the MoS_2 expected to realistic HDS conditions.

However, it is still under debate. Indeed, controversial DFT study has been performed by Krebs and coworkers[142] As previously present in the part 2.2.2 , they have shown that both S-edge and M-edge could be promoted (Table 9) and may thus impact the reactivity.

4.2 Reactivity and HDS/HYDO selectivity

Researchers have developed various approaches to make meaningful connections between HDS selectivity and/or activity and the structural, physical or chemical properties of the catalyst.

4.2.1 Active phase and promoter effects

As it was mentioned previously, the decoration of MoS_2 by Co atoms enhances the HDS reactivity and HDS/HYDO selectivity compare with un-promoted catalyst. Miller et al.[21] suggest that the higher HDS activity and the HYDO/HDS selectivity observed for the Co-Mo catalyst is correlated with the formation of the CoMoS phase. They mentioned a preferential adsorption of sulfur compounds at the active site, thereby limiting adsorption and saturation/hydrogenation of olefins.

An EXAFS characterization have been performed by Leliveld *et al.*[175]. They show that cobalt promotion favored the formation of sulfur vacancies, and thereby increases the number of active CUS sites.

More recently, Daudin et al.[165] have revealed that a volcano curve correlates HDS and HYDO activities with the sulfur-metal bon energy. In addition, the selectivity itself may follow such a trend. Using such a volcano curve, Krebs et al. reveals that the CoMoS phase should be the most selective according to its sulfur-metal bond energy value. CoMoS catalyst enhances the HDS/HYDO selectivity i.e. a decrease of the hydrogenation activity versus an increase of the HDS activity a directly correlated with a lower M-S bonding energy.

Nikulshin *et al.* [176] have been conducted a nano-scale description of the promoted MoS_2 to explain the HDS/HYDO selectivity. They follow the Co/Mo ratio at the MoS_2 edge (XPS analysis) and the slab length as function of the HDS/HYDO selectivity. They underlined an increase of this selectivity when the average length of the active phase increases and (Co/Mo) edge ratio value rises.

Regarding the impact of the cobalt added on the morphology especially the shape of the slab, it is commonly assumed that the almost triangular shape of non-promoted MoS_2 moves to hexagonal one for the promoted catalyst. High-Angle Annular Dark-field Scanning experiment (HAADF-STEM)[57] and DFT calculation[71] are both consistent with this trend. Moreover, as reported previously, DFT shows that the S-edge fraction increases which

indicates that the promoted S-edge is most stable. Regarding the size and slab stacking of MoS_2 crystallite obtained in TEM experiments, two different trends are reported in the literature: an increase[177] or decrease [178,179] when the cobalt is present in decoration. However, the length obtained in TEM depends also on the shape of the slab and cannot give direct information regarding the geometric size.

In the same way, DFT studies have been performed to obtain a detailed description of the slab at the nano-scale especially focus on the structures and properties of the edges, especially by further differentiating the edge of the slab, M- or S-edge, with their atomic composition between molybdenum, sulfur and cobalt atoms.

The DFT study by Schweiger *et al.*[180] indicate that the S-edge energy becomes significantly lower than that of the Mo edge in presence of cobalt. Thus, the affinity of Co for the S-edge is predominant in the slab.

Following this, recent DFT calculations have been undertaken by Krebs and coworkers[142] in order to discriminate if one type of CoMoS active edge sites, between M- or S-edge could be specific to the HDS or HYDO reaction or at least specific to the adsorption step on the active phase.

First, adsorption of thiophene is favored on both M- and S-edge compare with olefins adsorption. Consequently, olefins is inhibited by the adsorption of sulfur compounds regardless the edges. So, competitive reactant adsorption could occur. The second one is that the adsorption energy of the alkylthiophene on the S-edges would be thermodynamically favored comparatively to the olefins adsorption (Figure 37): S-edge is more selective than M-edge based on adsorption consideration which counterbalances the kinetic aspect. [142]

According to this study, by considering preferentially the cobalt decoration of S-edge first, M-edge/S-edge ratio is a key descriptor of the HDS/HYDO selectivity. More recently, Baubet *et al.*[181] confirmed this trend experimentally by proposing a DFT based microkinetic model depending on the edge sites and by analyzing the 2D morphology by HR HAADF-STEM. For CoMoS, they show that the increase of HDS/HYDO selectivity is directly related to the increased S-edge fraction.

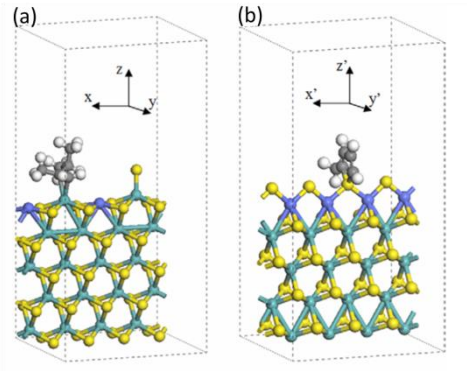

Figure 37. Part of slabs used to simulate molecules adsorption on M- and S-edges of a promoted CoMoS nano-crystallite (a) with various promoter (Me) contents a partially promoted M-edge with an adsorbed 23DMB1N; (b) a fully promoted S-edge with an adsorbed 2MT; (yellow balls: S, green balls: Me = Mo, blue balls: Co or Ni, gray balls: C, white balls: H.).[142]

An *in situ* IR spectroscopy using CO as probe molecule of the TMS phase (IR/CO) and TEM characterization conducted by Chen et al.[182] on the non-promoted catalyst confirm DFT result. Indeed by using a chelating agent to control the S-edge/M-edge ratio, they showed that an increase of the HDS activity is directly correlated with an increase of this S-edge/M-edge ratio.

In this part, the discussion was focused on the most relevant model proposed in the literature to understand the HDS activity and the HDS/HYDO. In the following discussion, support effect will be study.

4.2.2 Supports effects

Most of the literature deals with the physical and chemical properties of TMS phase to understand the origin of the HDS and HYDO activity and selectivity. Nevertheless, this active phase is dispersed on a support where metal support interactions (MSI) are present and cannot be neglected especially for well dispersed TMS phase. Understanding of the support role, regarding its effect on the active phase and on the HDS or HYDO reaction, has been investigated. Support may play significant roles – direct or indirect – respectively by impacting the hydrogenation reaction kinetic (isomerization side reaction) or the reactant adsorption or by modifying the MoS_2 active phase properties: length, stacking, $(Co/Mo)_{edge}$ ratio, Cobalt decoration degree of the slab edges.

Thus, Table 17 and Table 18 summarize some of the proposed assumption existing in the literature regarding the direct and indirect support effect on the HDS/HYDO selectivity.

Table 17. Support effect on the HDS/HYDO selectivity: un-/or direct role.

Supports	HDS/HYDO selectivity trend	Assumptions	Refs.
Al_2O_3	$S_{HDS/HYDO}$ is linked to the presence of interfacial sites.	**Support has a direct effect** on the $S_{HDS/HYDO}$. - HYDO is impacted by interfacial sites, consisting of support OH groups H-bonded with the sulfide phase.	[183]
γ-Al_2O_3 Al_2O_3-SiO_2	CoMoS on Al_2O_3-SiO_2>γ-Al_2O_3	**Support has a direct impact** on the effect is direct and indirect effect on $S_{HDS/HYDO.}$ ISZ reaction became the predominant reaction and the HYDO conversion is decreasing when support acidity increases HDS conversion is kept constant	[184] [185]

Table 18. Support effect on the HDS/HYDO selectivity: un-/or direct role.

Supports	HDS/HYDO selectivity trend	Assumptions	Refs.
γ-Al_2O_3 η-Al_2O_3 SiO_2 TiO_2 SiO_2–$Al2O_3$ SiO2–MgO	$S_{HDS/HYDO}$ decrease regarding the following the support order : SiO_2>η-Al_2O_3> SiO_2–Al_2O_3>TiO_2 >SiO_2-MgO	**Support has an direct and indirect on the $S_{HDS/HYDO}$.** -Acidic support property is implied: Hydrocracking appears in presence of SiO_2 more than Al_2O_3 which could engage in HYDO reaction. -Different catalytic sites of the active phase is associated to HDS and HYDO reaction	[186] [187]
SiO_2 $Al2O_3$ TiO_2 ZrO_2	CoMoS on SiO_2>TiO_2=ZrO_2>h-Al_2O_3	**Support has an direct and indirect,** respectively on the HYDO reaction and on the HDS reaction with CoMoS modification morphology. CoMoS Type II is formed on SiO_2 (CoMoS and support interaction are assumed weaker) whereas Type I is formed on the other support as for the non-promoted catalyst.	[188,189]
γ-Al_2O_3 $\delta\gamma$-Al_2O_3 SiO_2	CoMoS on SiO_2 > $\delta\gamma$-Al_2O_3 > γ-Al_2O_3	**Support has an indirect effect on the $S_{HDS/HYDO}$.** Slab length (edge/corner ratio) of the active phase are impacted by the support. Slab length is higher on SiO_2 than γ-Al_2O_3.	[190]

Al_2O_3	Selectivity is optimal for a support which give the better compromise between stacking and dispersion	**Support has an indirect effect on the $S_{HDS/HYDO}$.** Stacking and dispersion of the active phase are impacted by the support. (Rim/edge model)	[191]

4.2.2.1 Indirect effect of the support

First, studies of indirect role of the support which explain the HDS/HYDO selectivity are presented.

In the literature, M. Daage and R. R. Chianelli[192] proposed an interesting model to described the experimental observations regarding the $S_{HDS/HYDO}$ (selectivity HDS over HYDO) and the reactivity of the HDS catalyst. This model - called Rim-Edges - highlighting a relation between bulk MoS_2 morphology and catalytic HDS/HYDO selectivity with a detailed description at the macro-scale.

In this model, the TMS phase is described as a stack of several disks. Each disk corresponds to a MoS_2 layer (one slab). The top and bottom disks are associated to the Rim sites while “sandwiched” disks between the top and the bottom are associated with the Edge sites. The top surface of the Rim disks is the basal plane. A scheme of this model is indicated Figure 38 (a).

To explain the HDS/HYDO selectivity experimentally observed, two kind of sites presented above have been suggested. The Edge sites where the HDS reaction solely occurs and the Rim and Basal sites where occur both HYDO and HDS reactions. In this way, the selectivity of the HDS versus HYDO depends on the ratio of number of layer with exposed basal planes to the number of layers which have basal planes covered by adjacent layers of MoS_2.

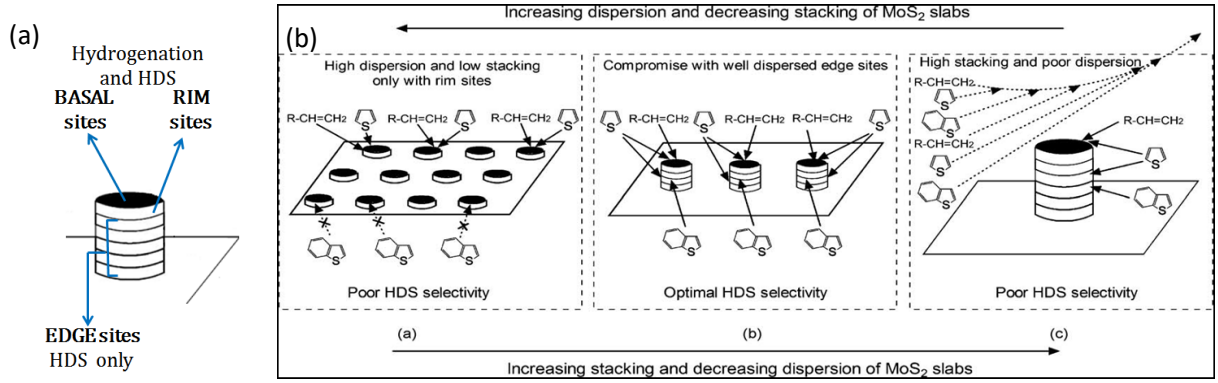

Figure 38. (a) Rim-edge model of an MoS_2 catalytic particle[192], (b) Schematic representation for optimizing the Rim-edge model i.e. the dispersion and the stacking of supported MoS_2 slabs for the selective HDS of FCC gasoline.[191]

Nevertheless, it has to be kept in mind that this model has been developed based on the study of MoS_2 single crystals with well-defined morphology and planes. In this case, no complexities of the MoS_2 phase in regard to morphology phase, coexistence of different planes, differentiation of the corner and edge sites and cobalt decoration, no interactions between support and active phase and reactivity of the support are taken into account.

This model was then enhancing by Y. Fan and coworkers[191] by considering an additional parameter: dispersion on the active phase on the support (Figure 38 (b)). By preparing various support (mixing two alumina in different proportion with surface area and pore volume different), they shown that stacking and dispersion of the active phase is directly impacted.

Figure 39 presents the HDS/HYDO selectivity observed has function of these two parameters.

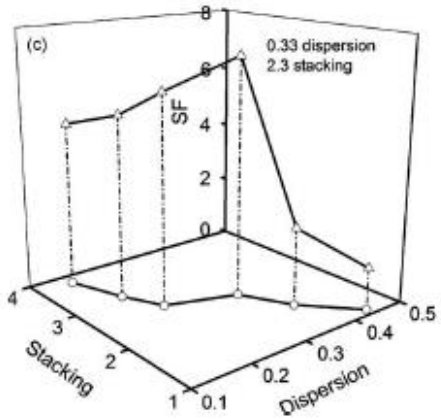

Figure 39. HDS/HYDO selectivity (SF factor) is plotted as function of active phase dispersion and stacking.

Thus, for an ideal catalyst that can selectively desulfurize FCC gasoline, support must allow a compromise between the dispersion and the stacking of supported MoS_2 slabs which is crucial to enhance the HDS/HYDO selectivity. Indeed, high dispersion and low stacking of supported MoS_2 slabs increased the number of active adsorption sites for olefins and thus promoted the catalyst olefin hydrogenation activity, leading to a low HDS selectivity. High stacking and low dispersion of supported MoS_2 slabs decreased the number of olefin adsorption sites, but the poor accessibility of the sulfur adsorption sites gave the corresponding catalyst unsatisfactory HDS activity and selectivity.

M.Li et al.[190] demonstrate that support impact indirectly HDS/HYDO selectivity by modifying the ratio between atoms at the edge and the corner of promoted MoS_2 slab. So, the slab length is directly link to this edge/corner atoms ratio. Figure 40 presents the HDS selectivity versus the slab length.

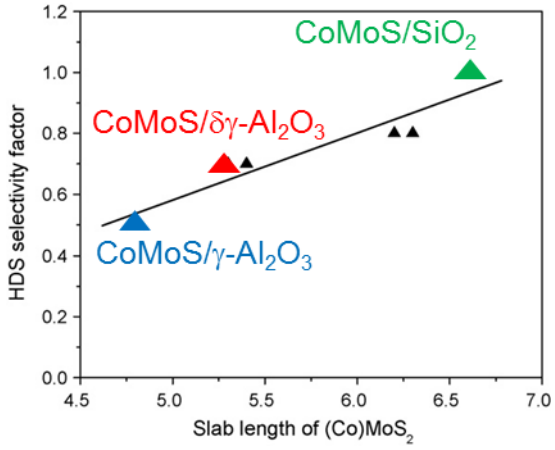

Figure 40. Correlation of HDS selectivity factor with slab length of CoMoS/ support.

Thus, it has been shown that support enhanced the HDS/HYDO selectivity in the following order: CoMoS on γ-Al_2O_3 < $\gamma\delta$-Al_2O_3 < SiO_2.

Finally, some studies deal with the orientation of the CoMoS slab at the support surface. Perpendicular and parallel orientations of the slab over the support are assumed in different study. The orientation may be driven by the Mo-O-Al bonding between support and active phase. According to the orientation, the adsorption of the reactants at the active phase surface would appear different. Especially in the parallel orientation, the access of the reactants to the active sites which are located on the edge MoS_2 slab is hampered. Thus, the HDS/HYDO selectivity could be affected. [62,193]

Nevertheless, these models give a description at the macro and microscopic scale. Model at the nano-scale have been also developed to rationalize the HDS activity and $S_{HDS/HYDO}$.
DFT calculation performed by Hinnemann et al.[189] indicate that the CoMoS(I) or (II), presented in the part 2.2.2, could impact the HDS/HYDO selectivity. CoMoS(I) or (II) is formed depending on the interaction of metals with support respectively weak and strong. Indeed, they observed that the molybdenum–sulfur binding energy at the MoS_2 edge increases upon formation of Mo–O linkages to the support. Thus, the CoMoS phase (II) is more reactive than (I) because of S vacancies considered as the active site are expected easily formed. Okamoto et al.[188] assumed the behavior in order to demonstrate the HDS/HYDO selectivity observed. CoMoS Type II is formed on SiO_2 (CoMoS and support interaction are assumed weaker) whereas Type I is formed on the other support as for the non-promoted catalyst.

4.2.2.2 Direct effect of the support

Some authors reveal that support could also play a direct role on the HDS or HYDO reaction by these own properties especially its acidity. Choi[183] and coworkers reported the presence of interfacial sites, observed by FT-IR, which could impact the HDS/HYDO selectivity. The presence of interfacial sites, consisting of support OH group H-bonded with the SH of the TMS phase, has been mentioned. These sites are assumed engaged in the olefin HYDO reaction while no evident correlation can be found with CUS, free OH groups or Al^{3+} sites for olefin HYD.

Qiherima et al. [194]compared two CoMoS catalysts supported on two different alumina (Same Mo and Co loading) and demonstrated that support could modify morphology and amount the CoMoS species formation. In this study, Lewis acid sites (LAS) are assumed to be a key parameter driving the interaction between CoMoS phase and support. Lower are the LAS and weaker is this interaction. However, the number of LAS by nm² of support is similar between both alumina (0.06 µmol.nm^{-2} of support). Thus, the LAS cannot explain a difference of interaction. Moreover, the molybdenum surface density is different between both supports and increase of slab stacking and length on alumina is observed for the higher dMo. Thus, dMo could impact the slab length and stacking. Moreover, XPS and CO FT-IR show both an increase of MoS_2 promotion by cobalt atoms. This observation could be related to

XRD results where they observed crystalized $CoMoO_4$ phase for the higher dMo. Thus, proximity between Co and Mo atoms could enhance the formation of a well promoted MoS_2 phase improving directly the selectivity and activity rate.

Studies have been also performed by Pérez-Martínez[185] to evaluate the acidic properties of the support which could impact the HDS and HYDO reaction and the respective conversion. Activity of both reactions have been evaluated over a CoMoS catalyst supported on an alumino-silicate support less and more acidic compare to a CoMoS/γ-Al_2O_3. In addition to these two reactions, only olefin isomerization reactions (ISZ) and alkylation of the alkylthiophene must be taken in account. In a conventional catalyst, olefin conversion is converted in ISZ product and HYDO product with the same yield and alkyl thiophene is converted in HDS product and partial hydrogenated products. Then, it has been shown that when the acidity of the support increases, the ISZ reaction became the predominant reaction and the HYDO conversion is decreasing whereas the HDS conversion is kept constant. Thus, the HDS/HYDO selectivity is enhanced by the support acidic properties according to this study. Shi *et al.*[184] confirm the last study mentioned. Indeed, they underlined a possible competition between olefin hydrogenation and isomerization reaction and show that HYDO is lower when ISZ is higher by the fact that branched olefins is formed and so less reactive to the HYDO reaction. Moreover, isomerization of the olefins before the hydrogenation could impact the HDS/HYDO selectivity.

In this last part, an overview of the various parameters which could influence the reactivity and HDS/HYDO selectivity of the HDS catalyst has been presented. Active phase, working-used conditions and support have been studied in detailed but separately. Indeed, no study takes into account a possible cooperative or even synergetic effect between some of these parameters. For instance DFT calculations presented previously does not consider the possible interaction between support and active phase. Experimentally, the Rim-edge model by definition is devoted to highly unpromoted bulk systems, and thus focused only on the active phase properties (stacking, length), and did not take into account a possible support effect. By contrast, when the support is considered experimentally, the impact on the active phase is only described in term of stacking or length of the MoS_2 slab, whereas the edge structure is not considered.

5 Strategy and methodology of the thesis

5.1 Strategy

The key industrial challenge to develop ever more efficient catalysts in the selective HDS of sulfur compounds of FCC gasolines will be reach only if we address the scientific challenge based on an ever better understanding of the supported CoMoS catalyst.

As presented previously, with the aims to elucidate which driving forces control HDS catalyst activity and selectivity, some parameters of the CoMoS active phase have been studied and identified as relevant such as the 2D morphology, stacking, size, promoter/molybdenum ratio. Moreover, the literature focused more recently on the description of the support which may play a key role (either direct, taking part to the reaction mechanisms or indirectly, by modifying CoMoS properties.) in respect of the HDS activity and HDS/HYDO selectivity.

However, most of these parameters exposed are generally investigated independently without considering and exploring in much details a possible interplay between each of them. As a consequence, the understanding of the HDS activity and selectivity is generally restrictive or limited only to the dedicated study. Thus, key questions regarding the active phase, the support and the interplay between both of them remain open.

The main objective of this project is to explore the possible cooperative and/or synergistic effect between various properties of the CoMoS active phase and its support by considering and evaluating the contribution of most of the relevant parameters together which could, directly or indirectly, affect the catalytic performances of the HDS catalysts.

The strategy adopted for the thesis consists of combining fundamental spectroscopic surface phenomena with the simultaneous measurement of catalytic performances (activity and selectivity). Different approaches will be undertaken to achieve this purpose.

The first and widespread direct approach will consist to correlate ex-situ catalyst spectroscopic characterizations and catalytic performances. Common spectroscopic analysis such as High Resolution Transmission Electron Microscopy (HRTEM), High-Resolution Scanning Transmission Electron Microscopy (HRSTEM), Fourier-Transform Infrared

Spectroscopy (FTIR) and X-ray Photoelectron Spectroscopy (XPS) will be combined to obtain a detail description of the HDS catalyst features (CoMoS phase and support).

Indirect spectroscopic approach will also be employed in order to investigate the nature of the active sites of the CoMoS phase which could be engaged in the catalytic properties of the HDS catalysts. The use of specific probe molecule of the active sites of the CoMoS phase followed by Fourier-transform infrared spectroscopy (FTIR) will be combined dedicated DFT calculations.

Finally, an in situ spectroscopic approach will be engaged in the description of the structure-activity relationships of the catalytic system to present a new insight on the most relevant parameters and a clearer interpretation of selectivity trend on the FCC gasoline. To realize this innovative approach, a Gas Chromatography coupled with Diffuse Reflectance InfraRed Fourier Transformed Spectroscopy (GC-DRIFTS) and coupled with Attenuated Total Reflectance (GC-ATR) methodology have been chosen with the aims to analyze the interactions of the HDS model reactants and key intermediates with the CoMoS active phase and support at the catalytic interface in conditions close to the working conditions. Dedicated GC-DRIFT and GC-ATR has been built on purpose within this research project. Such an in situ spectroscopic study represents a promising challenge, since a direct insight on the adsorption and reaction mechanisms occurring on the surface of HDS catalyst (support and sulfide phase) in 'real' HDS conditions was never undertaken before and should lead to the description and understanding of the main catalyst properties which drive HDS activity and selectivity.

5.2 General methodology

The general methodology adopted for the thesis is described in the following.

1- Well defined HDS catalysts containing Molybdenum, Cobalt and Phosphorus elements will be prepared on three supports in order to control precisely their surface concentration per nm^2 and evaluate consistently their impact and those of the support on the HDS activity and selectivity.

To study the support effect, three supports have been selected to disperse the CoMoS active phase: γ-Al_2O_3, $\delta\theta$-Al_2O_3 and SiO_2. These supports have been chosen according to their

intrinsic acido-basic properties and their already known impacts on the HDS selectivity.[23,160,178,186,188,190,195]

To study the molybdenum surface density effect, four well-chosen molybdenum surface densities normalized by nm² of support (from 1 to 4.8) have been selected.

To study the Co-promoter effect, unpromoted MoS_2 supported on $\delta\theta$-Al_2O_3 and SiO_2 have been selected as well as CoMoS/$\delta\theta$-Al_2O_3 catalyst series with various Co/Mo atomic ratio (from 0 to 0.4).

2- All the catalysts will be characterized from the oxide and sulfided state by ex-situ analysis: XRF, Castaing micro-probe, XRD, HRTEM, HRSTEM and XPS analysis.

3- HDS catalytic test in the fixed bed reactor will be performed in presence of model molecules feedstocks alone or in mixture: 3-methylthiophene (3MT), 2,3-dimethylbut-2-ene (23DMB2N) under heptane solvent.

4- Interpretation of catalytic performances and ex-situ characterizations will be proposed by means of attempted structure-activity relationships.

5- NO-FTIR experiment will be carried out and combined with DFT calculations so as to explore the nature of the active sites of the HDS catalysts.

6- Finally, the GC-DRIFT and ATR-DRIFT unit will be set up to perform analysis of the HDS surface catalysts under realistic HDS conditions in presence of model HDS molecule, the 3MT molecule.

In the following of the report, the experimental part will describe the targeted catalysts and their preparation protocols as well as characterization of the oxides materials. Other specific characterization techniques performed on the sulfided catalysts will be presented in each subsequent chapter together with the obtained results.

6 References

[1] Official Journal of the European Union, **2009**, *L 140/88*, 88–113.

[2] *US Environ. Prot. Agency "EPA Propos. Tier 3 Mot. Veh. Emiss. Fuel Stand. march* **2013***.*

[3] *Int. Counc. Clean Transp. "China Announc. Breakthr. timeline Implement. ultra-low sulfur fuel Stand. march* **2013.**

[4] *Key World Energy Statistics*, **2014**.

[5] P. Grange, X. Vanhaeren, *Catal. Today* **1997**, *36*, 375–391.

[6] H. Toulhoat, P. Raybaud, *Catalysis by Transition Metal Sulphides*, Editions TECHNIP, Paris, **2013**.

[7] *J. Off. l'Union Eur. L 140/88* **2009**, *5.6*, 88–113.

[8] M. Guisnet, *Catalyse Acido-Basique*, **2005**.

[9] C. Song, *Catal. Today* **2003**, *86*, 211–263.

[10] T. G. Kaufmann, A. Kaldor, G. F. Stuntz, M. C. Kerby, L. L. Ansell, *Catal. Today* **2000**, *62*, 77–90.

[11] C. Marcilly, *Stud. Surf. Sci. Catal.* **2001**, *135*, 37–60.

[12] I. V Babich, J. A. Moulijn, *Fuel* **2003**, *82*, 607–631.

[13] S. Brunet, D. Mey, G. Pérot, C. Bouchy, F. Diehl, *Appl. Catal. A Gen.* **2005**, *278*, 143–172.

[14] L. L. Upson, M. W. Schnaith, *Oil Gas J.* **1997**.

[15] S. Hatanaka, M. Yamada, *Ind. Eng. Chem. Res.* **1998**, *37*, 1748–1754.

[16] B. Liu, Y. Chai, Y. Li, A. Wang, Y. Liu, C. Liu, *Fuel* **2014**, *123*, 43–51.

[17] S. Hatanaka, *Catal. Surv. from Asia* **2005**, *9*, 87–93.

[18] C. Yin, G. Zhu, D. Xia, *Fuel Process. Technol.* **2002**, *79*, 135–140.

[19] S. Brunet, D. Mey, G. Pérot, C. Bouchy, F. Diehl, *Appl. Catal. A Gen.* **2005**, *278*, 143–172.

[20] B. Didillon, D. Uzio, N. Marchal, *Procédé de Production D'essences à Faible Teneur En Soufre*, **2001**.

[21] J. T. Miller, W. J. Reagan, J. a. Kaduk, C. L. Marshall, a. J. Kropf, *J. Catal.* **2000**, *193*, 123–131.

[22] J. Wu, *Selective Catalysts Having High Temperature Alumina Support for Naphta Hydrodesulphurization*, **2007**, PCT/US2007/001000.

[23] J. Wu, C. Bai, T. Halbert, S. Soled, S. Miseo, *Selective Catalysts Having Silica Supports for Naphtha Hyddrodesulfurization*, **2007**, WO 2007/084439 A1.

[24] H. Tospoe, B. S. Clausen, F. E. Massoth, *Springer-Verlag Berlin Heidelb. New York* **1996**, *11*, 39.

[25] P. Blanchard, C. Lamonier, a. Griboval, E. Payen, *Appl. Catal. A Gen.* **2007**, *322*, 33–45.

[26] J. Mazurelle, C. Lamonier, C. Lancelot, E. Payen, C. Pichon, D. Guillaume, *Catal. Today* **2008**, *130*, 41–49.

[27] J. M. Lewis, R. A. Kydd, *J. Catal.* **1992**, *136*, 478–486.

[28] P. a. Nikulshin, A. V. Mozhaev, A. a. Pimerzin, V. V. Konovalov, A. a. Pimerzin, *Fuel* **2012**, *100*, 24–33.

[29] C. Kwak, J. Joon, J. Sang, K. Choi, S. Heup, *Appl. Catal. A Gen.* **2000**, *200*, 233–242.

[30] W. Zhang, M. Sun, R. Prins, *J. Phys. Chem. B* **2003**, *107*, 10977–10982.

[31] J. Ramirez, R. Cuevas, L. Gasque, *Appl. Catal.* **1991**, *71*, 351–361.

[32] J. Chen, V. Labruyere, F. Maugé, A.-A. Quoineaud, A. Hugon, L. Oliviero, *J. Phys. Chem. C* **2014**, *118*, 30039–30044.

[33] M. Nagai, Y. Goto, H. Ishii, S. Omi, *Appl. Catal. A Gen.* **2000**, *192*, 189–199.

[34] D. J. Sajkowski, S. T. Oyama, *Appl. Catal. A Gen.* **1996**, *134*, 339–349.

[35] J. A. Mendoza-Nieto, I. Puente-Lee, C. Salcedo-Luna, T. Klimova, *Fuel* **2012**, *100*, 100–109.

[36] D. J. Pérez-Martínez, P. Eloy, E. M. Gaigneaux, S. a. Giraldo, A. Centeno, *Appl. Catal. A Gen.* **2010**, *390*, 59–70.

[37] J. C. Duchet, E. M. Van Oers, V. H. . De Beer, R. Prins, *J. Catal.* **1983**, *80*, 386–402.

[38] D. Laurenti, B. Phung-Ngoc, C. Roukoss, E. Devers, K. Marchand, L. Massin, L. Lemaitre, C. Legens, A.-A. Quoineaud, M. Vrinat, *J. Catal.* **2013**, *297*, 165–175.

[39] O. Y. Gutiérrez, S. Singh, E. Schachtl, J. Kim, E. Kondratieva, J. Hein, J. A. Lercher, *ACS Catal* **2014**, *4*, 1487–1499.

[40] V. Rabarihoela-Rakotovao, S. Brunet, G. Perot, F. Diehl, *Appl. Catal. A Gen.* **2006**, *306*, 34–44.

[41] A.-F. Lamic, A. Daudin, S. Brunet, C. Legens, C. Bouchy, E. Devers, *Appl. Catal. A Gen.*

2008, *344*, 198–204.

[42] H. Topsøe, B. S. Clausen, F. E. Massoth, *Catal. - Sci. Technol.* **1996**, *11*.

[43] M. Lojacono, J. L. Verbeek, G. C. A. Schuit, *J. Catal.* **1973**, *29*, 463–474.

[44] F. E. Massoth, *Adv. Catal.* **1979**, *27*, 265–310.

[45] T. Lim, S. W. Weller, *J. Catal.* **1987**, *108*, 175–184.

[46] V. M. MasTikhin, A. V. Nosov, V. V. Terskikh, K. I. Zamaraev, I. E. Wachs, *J. Phys. Chem.* **1994**, *98*, 13621–13624.

[47] E. R. H. van Eck, A. P. M. Kentgens, H. Kraus, R. Prins, *J. Phys. Chem.* **1995**, *99*, 16080–16086.

[48] T. G. Parham, R. P. Merrill, *J. Catal.* **1984**, *85*, 295–310.

[49] B. S. Clausen, H. Topsoe, R. Candla, B. Lengeler, J. Als-nlelsen, F. Chrlstensen, **1981**, *85*, 3868–3872.

[50] H. Topsøe, F. . Massoth, B. S. Clausen, *Hydrotreating Catalysis*, **1996**.

[51] C. Cheng, G. L. Schrader, *J. Catal.* **1979**, *60*, 276–294.

[52] J. M. Stencel, L. E. Makovsky, T. A. Sarkus, J. De Vries, R. Thomas, J. A. Moulijn, *J. Catal.* **1984**, *90*, 314–322.

[53] J. Medema, C. V. Van Stam, V. H. J. De Beer, A. J. A. Konings, D. C. Koningsberger, *J. Catal.* **1978**, *53*, 386–400.

[54] A. L. Diaz, M. E. Bussell, *J. Phys. Chem.* **1993**, *97*, 470–477.

[55] P. Arnoldy, J. A. M. den Heijkant, G. D. de Bok, J. A. Moulin, *J. Catal.* **1985**, *92*, 35–55.

[56] B. Scheffer, N. J. J. Dekker, P. J. Mangnus, J. A. Moulin, *J. Catal.* **1990**, *121*, 31–46.

[57] M. Brorson, A. Carlsson, H. Topsøe, *Catal. Today* **2007**, *123*, 31–36.

[58] R. M. Stockmann, H. W. Zandbergen, A. D. van Langeveld, J. A. Moulijn, *Jounral Mol. Catal. A Chem.* **1995**, *102*, 147–161.

[59] S. Helveg, J. V Lauritsen, E. Lægsgaard, I. Stensgaard, J. K. Nørskov, B. S. Clausen, H. Topsøe, F. Besenbacher, *Phys. Rev. Lett.* **2000**, *84*, 951–954.

[60] R. Prins, V. H. J. De Beer, G. A. Somorjai, *Catal. Rev.* **1989**, *31*, 1–41.

[61] Y. Sakashita, T. Yoneda, *J. Catal.* **1999**, *185*, 487–495.

[62] T. F. Hayden, J. A. Dumesic, **1987**, *384*, 366–384.

[63] G. C. A. Schuit, B. C. Gates, *J. Rev.* **1973**, *19*, 417–438.

[64] H. Tospoe, B. S. Clausen, F. E. Massoth, *Springer-Verlag Berlin Heidelb. New York* **1996**,

11, 29–35.

[65] S. Kasztelan, H. Toulhoat, J. Grimblot, J. P. Bonnelle, D. Lille, *Appl. Catal.* **1984**, *13*, 127–159.

[66] P. Raybaud, J. Hafner, G. Kresse, S. Kasztelan, H. Toulhoat, *J. Catal.* **2000**, *189*, 129–146.

[67] P. Raybaud, J. Hafner, G. Kresse, S. Kasztelan, H. Toulhoat, *J. Catal.* **2000**, *189*, 129–146.

[68] M. Sun, J. Adjaye, A. E. Nelson, *Appl. Catal. A Gen.* **2004**, *263*, 131–143.

[69] Emmanuel Krebs, Modélisation Moléculaire Ab Initio Des Effets de Morphologie En Catalyse Par Les Sulfures, **2008**.

[70] P. Raybaud, J. Hafner, G. Kresse, H. Toulhoat, *Surf. Sci.* **1998**, *407*, 237–250.

[71] H. Schweiger, P. Raybaud, G. Kresse, H. Toulhoat, *J. Catal.* **2002**, *207*, 76–87.

[72] G. Wulff, *Zeitschrift fur Kryst. und Mineral.* **1901**, *34*, 449–530.

[73] J. V. Lauritsen, M. V. Bollinger, E. Lægsgaard, K. W. Jacobsen, J. K. Nørskov, B. S. Clausen, H. Topsøe, F. Besenbacher, *J. Catal* **2004**, *221*, 510–522.

[74] J.V Lauristen, Atomic-Scale Study of a Hydrodesulfurization Model Catalyst, **2002**.

[75] H. Topsøe, F. . Massoth, B. S. Clausen, *Hydrotreating Catalysis*, **1996**.

[76] C. Wivel, B. S. Clausen, R. Candia, S. Mørup, H. Topsøe, *J. Catal.* **1984**, *87*, 497–513.

[77] Y. Yokoyama, K. Teranishi, A. Nishijima, N. Matsubayashi, H. Shimada, M. Nomura, *Jpn. J. Appl. Phys.* **1992**, *32*, 466–468.

[78] J. A. Rob van Veen, E. Gerkema, A. M. van der Kraan, P. A. J. M. Hendriks, H. Beens, *J. Catal.* **1992**, *133*, 112–123.

[79] Y. Yokoyama, K. Teranishi, *Jpn. J. Appl. Phys.* **1993**, *32*, 466–468.

[80] N.-Y. Topsøe, H. Topsoe, *J. Catal.* **1982**, *75*, 354–374.

[81] R. J. H. Voorhoeve, *J. Catal.* **1971**, *252*, 243–252.

[82] B. Delmon, *Bull. des Sociétés Chim. Belges* **1979**, *88*, 979–987.

[83] H. Tospoe, B. S. Clausen, F. E. Massoth, *Hydrotreating Catalysis*, New York, **1996**.

[84] H. Topsøe, B. S. Clausen, *Appl. Catal.* **1986**, *25*, 273–293.

[85] H. Topsøe, B. S. Clausen, *Catal. Rev. Sci. Eng.* **1984**, *26*, 395–420.

[86] B. S. Clausen, B. Lengeler, R. Candia, J. Als-Nielsen, H. Topsøe, *Bull. des Sociétés Chim. Belges* **1981**, *90*, 1249–1259.

[87] N.-Y. Topsøe, H. Topsøe, *Jounral Catal.* **1983**, *84*, 386–401.

[88] H. Topsøe, B. S. Clausen, N.-Y. Topsøe, P. Zeuthen, *Catalysts in Petroleum Refining 1989, Proceedings of the Conference on Catalysts in Petroleum Refining*, Elsevier, **1989**.

[89] K. S. Chung, F. E. Massoth, *J. Catal.* **1980**, *64*, 320–331.

[90] *Characterization and Chemical Modification of the Silica Surface*, Elsevier, **1995**.

[91] E. Krebs, a. Daudin, P. Raybaud, *Oil Gas Sci. Technol. - Rev. l'IFP* **2009**, *64*, 707–718.

[92] X. Krokidis, P. Euzen, P. Raybaud, H. Toulhoat, J. L. L. Loarer, J. P. Jolivet, C. Froidefond, *Handbook of Porous Materials*, Wiley-VCH Verlag GmbH, Weinheim, Germany, **2002**.

[93] R. S. Zhou, R. L. Snyder, *Acta Crystallogr. Sect. B Struct. Sci.* **1991**, *47*, 617–630.

[94] H. Saalfeld, **1957**, 249–257.

[95] L. Smrcok, V. Langer, J. Krestan, *Acta Crystallogr. C.* **2006**, *62*, i83–4.

[96] C. S. John, N. C. M. Alma, G. R. Hays, *Appl. Catal.* **1983**, *6*, 341–346.

[97] M. Yazdanmehr, S. J. Asadabadi, A. Nourmohammadi, M. Ghasemzadeh, M. Rezvanian, *Nanoscale Res. Lett.* **2012**, *7*, 488.

[98] E. Menéndez-Proupin, G. Gutiérrez, *Phys. Rev. B* **2005**, *72*, 035116.

[99] B. C. Lippens, J. H. de Boer, *Acta Crystallogr.* **1964**, *17*, 1312–1321.

[100] P. Nortier, P. Fourre, a B. Mohammed, J. C. Lavalley, *Appl. Catal.* **1990**, *61*, 141–160.

[101] M. Digne, P. Sautet, P. Raybaud, P. Euzen, H. Toulhoat, *J. Catal.* **2004**, *226*, 54–68.

[102] M. Digne, *Des Hydroxyles D'aluminium Aux Propriétés Chimiques de L'alumine Gamma En Catalyse: Une Étude Théorique Ab Initio*, **2003**.

[103] C. Marcilly, *L'alumine Support de Catalyseurs Acides Ou Bifonctionnels : Synthèse, Structures, Texture et Modèles de Surface*, **1993**.

[104] S. J. Wilson, *Jounral solid state Chem.* **1979**, *30*, 247–255.

[105] S. J. Wilson, *J. Solid State Chem.* **1979**, *30*, 247–255.

[106] X. Krokidis, P. Raybaud, A. Gobichon, B. Rebours, P. Euzen, *J. Phys. Chem. B* **2001**, *105*, 5121–5130.

[107] M. Digne, Des Hydroxyles D'aluminium Aux Propriétés Chimiques de L'alumine Gamma En Catalyse: Une étude Théorique Ab Initio, **2003**.

[108] G. Busca, *Structural , Surface , and Catalytic Properties of Aluminas*, **2014**.

[109] I. Levin, D. Brandon, *J. Am. Ceram. Soc.* **1998**, *81*, 1995–2012.

[110] M. F. Peintinger, M. J. Kratz, T. Bredow, *J. Mater. Chem. A* **2014**, *2*, 13143–13158.

[111] T. Tsuchida, *Solid State Ionics* **1993**, *63-65*, 464–470.

[112] H. J. Kim, T. G. Kim, J. J. Kim, S. S. Park, S. S. Hong, G. D. Lee, *J. Phys. Chem. Solids* **2008**, *69*, 1521–1524.

[113] G. Busca, *Catal. Today* **2014**, *226*, 2–13.

[114] M. Taoufik, K. C. Szeto, N. Merle, D. Rosal, L. Maron, J. Trøbosc, G. Tricot, R. M. Gauvin, L. Delevoye, **2014**, 4038–4046.

[115] A. A. Tsyganenko, V. N. Filimonov, *J. Mol. stucture* **1973**, *19*, 579–589.

[116] H. Knözinger, P. Ratnasamy, *Catal. Rev. Sci. Eng.* **1978**, *17*, 31–70.

[117] J. B. Peri, **1965**, *809*, 220–230.

[118] T. H. E. Nature, A. Of, R. Obtained, F. The, Q. Mechanics, *Nat. Chem. Bond* **1931**, *53*, 1367–1400.

[119] E. Baumgarten, a. Zachos, *Spectrochim. Acta Part A Mol. Spectrosc.* **1981**, *37*, 93–98.

[120] G. Busca, L. Vincenzo, V. Escribano, R. Guidetti, *J. Catal.* **1991**, *131*, 167–177.

[121] G. Busca, V. Lorenzelli, G. Ramis, R. J. Willey, *Langmuir* **1993**, *9*, 1492–1499.

[122] M. Digne, P. Sautet, P. Raybaud, P. Euzen, H. Toulhoat, *J. Catal.* **2002**, *211*, 1–5.

[123] C. Morterra, G. Magnacca, *Catal. Today* **1996**, *27*, 497–532.

[124] G. Della Gatta, B. Fubini, G. Ghiotti, C. Morterra, *J. Catal.* **1976**, *43*, 90–98.

[125] C. Morterra, A. Chiorino, G. Ghiotti, E. Garrone, *J. Chem. Soc., Faraday Trans.* **1979**, *75*, 271–288.

[126] R. Métivier, I. Leray, M. Roy-Auberger, N. Zanier-Szydlowski, B. Valeur, *New J. Chem.* **2002**, *26*, 411–415.

[127] R. K. Iler, *The Chemistry of Silica*, John Wiley & Sons, **1979**.

[128] R. Duchateau, T. W. Dijkstra, R. a. Van Santen, G. P. a Yap, *Chem. - A Eur. J.* **2004**, *10*, 3979–3990.

[129] T. W. Dijkstra, R. Duchateau, R. a Van Santen, A. Meetsma, G. P. a Yap, *Adsorpt. J. Int. Adsorpt. Soc.* **2002**, 9856–9864.

[130] E. F. Vansant, P. Van Der Voort, K. C. Vrancken, *Characterization and Chemical Modification of the Silica Surface*, Elsevier, **1995**.

[131] L. T. Zhuravlev, *Colloids Surfaces A Physicochem. Eng. Asp.* **2000**, *173*, 1–38.

[132] H. E. Bergna, W. O. Roberts, in *Colloid. Silica Fundam. Appl.* (Ed.: C. Press), **2005**, p. 385.

[133] A. Rimola, D. Costa, M. Sodupe, P. Ugliengo, *Am. Chem. Soc.* **2013**, *113*, 4216–4313.

[134] S. Léonardelly, L. Facchini, C. Fretigny, P. Tougne, A. P. Legrand, *J. Am. Chem. Soc.* **1992**, *114*, 6412–6418.

[135] J. E. Roberts, *J. Am. Chem. Soc.* **1988**, *110*, 2023–2026.

[136] R. Milcent, F. Chau, *Chimie Organique Hétérocycle*, **2003**.

[137] J. Clayden, S. Warren, N. Greeves, P. Wothers, *Organic Chemistry*, **2002**.

[138] N. Schore, P. Vollhardt, *Organic Chemistry : Structure and Function*, Clancy Marshall, **2011**.

[139] B. Bak, D. Christensen, L. H.- Ygaard, A. K. D. J. Rastrup-andersen, *Jounral Mol. Spectrosc.* **1961**, *7*, 58–63.

[140] R. J. Angelici, *Coord. Chem. Rev.* **1990**, *105*, 61–76.

[141] T. Rauchfuss, *Prog. Inorg. Chem* **1991**, *39*, 259.

[142] E. Krebs, B. Silvi, a. Daudin, P. Raybaud, *J. Catal.* **2008**, *260*, 276–287.

[143] T. L. Tarbuck, K. R. Mccrea, J. W. Logan, J. L. Heiser, M. E. Bussell, W. Washington, V. Uni, **1998**, *5647*, 7845–7857.

[144] D. Liu, Z. Li, Q. Sun, X. Kong, A. Zhao, Z. Wang, *Fuel* **2012**, *92*, 77–83.

[145] H. Orita, K. Uchida, N. Itoh, *J. Mol. Catal. A Chem.* **2003**, *193*, 197–205.

[146] N. Dos Santos, H. Dulot, N. Marchal, M. Vrinat, *Appl. Catal. A Gen.* **2009**, *352*, 114–123.

[147] H. Tospoe, B. S. Clausen, F. E. Massoth, *Hydrotreating Catalyst*, New York, **1993**.

[148] D. W. Scott, G. B. Guthrie, J. P. Mccullough, G. U. Y. Waddington, *J. Chem. Eng. Data* **1959**, *4*, 246–251.

[149] D. Mey, S. Brunet, C. Canaff, F. Maugé, C. Bouchy, F. Diehl, *J. Catal.* **2004**, *227*, 436–447.

[150] C. N. Satterfield, G. W. Roberts, *AIChE Jounral* **1968**, *14*, 159–164.

[151] I. A. Van Parijs, G. F. Froment, *Ind. Eng. Chem. Res. Dev.* **1986**, *25*, 431–436.

[152] H. C. Lee, J. B. Butt, *J. Catal.* **1977**, *49*, 320–331.

[153] C. H. Amberg, P. Desikan, *Can. J. Chem.* **1964**, *42*, 843.

[154] S. H. YANG, C. N. Satterfield, *J. Catal.* **1983**, *81*, 168–178.

[155] R. Ramachandran, F. E. Massoth, *J. Catal.* **1981**, *67*, 248–249.

[156] S. Kasztelan, D. Guillaume, *Ind. Eng. Chem. Res.* **1994**, *33*, 203–210.

[157] Y. Okamoto, H. Tomioka, S. Teranishi, *J. Catal.* **1980**, *100*, 93–100.

[158] S. Hatanaka, M. Yamada, O. Sadakane, *Ind. Eng. Chem. Res.* **1997**, *36*, 5110–5117.

[159] A. E. Hargreaves, J. R. H. Ross, *Jounral Catal.* **1979**, *56*, 363–376.

[160] W. Niemann, B. S. Clausen, H. Topsøe, *Catal. Letters* **1990**, *4*, 355–364.

[161] F. Dumeignil, J. F. Paul, E. Veilly, E. W. Qian, A. Ishihara, E. Payen, T. Kabe, *Appl. Catal. A Gen.* **2005**, *289*, 51–58.

[162] P. Prodhomme, P. Raybaud, H. Toulhoat, *J. Catal.* **2011**, *280*, 178–195.

[163] J. K. Norskov, B. S. Clausen, H. Topsøe, *Catal. Letters* **1992**, *13*, 1–8.

[164] H. Toulhoat, P. Raybaud, S. Kasztelan, G. Kresse, J. Hafner, *Catal. Today* **1999**, *50*, 629–636.

[165] a. Daudin, a. F. Lamic, G. Pérot, S. Brunet, P. Raybaud, C. Bouchy, *Catal. Today* **2008**, *130*, 221–230.

[166] J. Lauritsen, M. Nyberg, R. Ang, M. V Bollinger, B. Clausen, HTopsøe, KWJacobsen, E. Lægsgaard, JKNørskov, F. Besenbacher, *Nanotechnology* **2003**, *14*, 385–389.

[167] J. V Lauritsen, M. Nyberg, J. K. Nørskov, B. S. Clausen, H. Topsøe, *J. Catal.* **2004**, *224*, 94–106.

[168] P. a. Nikulshin, D. I. Ishutenko, a. a. Mozhaev, K. I. Maslakov, a. a. Pimerzin, *J. Catal.* **2014**, *312*, 152–169.

[169] P. G. Moses, B. Hinnemann, H. Topsøe, J. K. Nørskov, *J. Catal.* **2008**, *248*, 188–203.

[170] P. G. Moses, B. Hinnemann, H. Topsøe, J. K. Nørskov, *J. Catal.* **2007**, *248*, 188–203.

[171] P. G. Moses, B. Hinnemann, H. Topsøe, J. K. Nørskov, *J. Catal.* **2009**, *268*, 201–208.

[172] J. V. Lauritsen, S. Helveg, E. Lægsgaard, I. Stensgaard, B. S. Clausen, H. Topsøe, F. Besenbacher, *J. Catal.* **2001**, *197*, 1–5.

[173] P. Raybaud, J. Hafner, G. Kresse, S. Kasztelan, H. Toulhoat, *J. Catal.* **2000**, *190*, 128–143.

[174] Bjerne S. Clausen, B. Lengelerb, R. Candia, J. Ah-Nielsen, H. Topsøe, *Bull. des Sociétés Chim. Belges* **1981**, *90*, 1249–1259.

[175] B. R. . Leliveld, J. . A. . Van Dillen, J. W. Geus, D. C. Koningsberger, **1997**, *5647*, 11160–11171.

[176] P. A. Nikulshin, V. A. Salnikov, A. V Mozhaev, P. P. Minaev, V. M. Kogan, A. A. Pimerzin, *J. Catal.* **2014**, *309*, 386–396.

[177] G. Berhault, M. Perez, D. Rosa, A. Mehta, M. Jose, *Appl. Catal. A Gen.* **2008**, *345*, 80–88.

[178] D. Laurenti, B. Phung-Ngoc, C. Roukoss, E. Devers, K. Marchand, L. Massin, L. Lemaitre, C. Legens, A.-A. Quoineaud, M. Vrinat, *J. Catal.* **2013**, *297*, 165–175.

[179] C. Fontaine, Y. Romero, A. Daudin, E. Devers, C. Bouchy, S. Brunet, *Appl. Catal. A Gen.* **2010**, *388*, 188–195.

[180] H. Schweiger, P. Raybaud, *Jounral Catal.* **2002**, *38*, 33–38.

[181] B. Baubet, M. Girleanu, A.-S. Gay, A.-L. Taleb, M. Moreaud, F. Wahl, V. Delattre, E. Devers, A. Hugon, O. Ersen, et al., *ACS Catal.* **2016**, *6*, 1081–1092.

[182] W. Chen, F. Maugé, J. Van Gestel, H. Nie, D. Li, X. Long, *J. Catal.* **2013**, *304*, 47–62.

[183] J. Choi, F. Maugé, C. Pichon, J. Olivier-fourcade, J. Jumas, C. Petit-clair, D. Uzio, *Appl. Catal. A Gen.* **2008**, *267*, 203–216.

[184] G. Shi, H. Zhao, L. Song, J. Shen, *Energy & Fuels* **2008**, *22*, 2450–2454.

[185] D. J. Perez-Martinez, P. Eloy, E. M. Gaigneaux, S. A. Giraldo, A. Centeno, *Appl. Catal. A Gen.* **2010**, *390*, 59–70.

[186] G. Muralidhar, F. E. Massoth, J. Shabatai, *Jounral Catal.* **1984**, *85*, 44–52.

[187] H. Shimada, T. Sato, Y. Yoshimura, J. Hiraishi, A. Nishijima, *Jounral Catal.* **1988**, *110*, 275–284.

[188] Y. Okamoto, K. Ochiai, M. Kawano, K. Kobayashi, T. Kubota, **2002**, *226*, 115–127.

[189] B. Hinnemann, J. K. Nørskov, H. Topsøe, *J. Phys. Chem. B* **2005**, *109*, 2245–2253.

[190] M. Li, H. Li, F. Jiang, Y. Chu, H. Nie, *Catal. Today* **2010**, *149*, 35–39.

[191] Y. Fan, G. Shi, H. Liu, X. Bao, *Appl. Catal. B Environ.* **2009**, *91*, 73–82.

[192] M. Daage, R. R. Chianelli, *J. Catal.* **1994**, *149*, 414–427.

[193] J. Van Doorn, J. a Moulijn, G. Djéga-Mariadassou, *Appl. Catal.* **1990**, *63*, 77–90.

[194] Qiherima, L. Huifeng, Y. Hui, Z. Yunhong, X. Guangtong, *Chinese J. Catal.* **2011**, *32*, 240–249.

[195] F. E. Massoth, G. Muralidhar, J. Shabtai, *J. Catal.* **1984**, *85*, 53–62.

- Chapter II -
Experimental methods

Tables of contents

1. Catalysts and preparation 84

1.1 Target promoted catalysts 84

1.2 Experimental protocol 84

2. Oxide phase characterization 86

2.1 X-Ray Fluorescence 86

2.1.1 Principle 86

2.1.2 Results 87

2.2 Electron Micro Probe Analyzer (EPMA or Castaing micro probe) 88

2.2.1 Principle 88

2.2.2 Results 88

2.3 X-ray diffraction analysis 89

2.3.1 Principle 89

2.3.2 Results 90

3. Appendices 91

- Chapter II -
Experimental methods

1. Catalysts and preparation

1.1 Target promoted catalysts

Targeted CoMoS catalysts are prepared by taking into account 3 objectives which are: evaluate support, Mo surface coverage and Co-promotion impact on their catalytic performance, activity and selectivity.

On each support, three molybdenum loadings were selected to obtain surface densities (called dMo in what follows) from 0.9 to 4.8 by nm^{-2} of support. In order to compare catalysts at iso-dMo and iso-support, Co/Mo and P/Mo molar ratios are also kept constant respectively 0.4 and 0.27. CoMoS/$\delta\theta$-Al_2O_3 catalysts have been prepared at iso-dMo of 2.2 $at.nm^{-2}$ at various Co/Mo molar ratio from 0.1 to 0.4 with a P/Mo kept constant at 0.27. MoS_2 and Co_9S_8 supported on $\delta\theta$-Al_2O_3 and SiO_2 reference materials are also prepared in accordance to the CoMoS on $\delta\theta$-Al_2O_3 and SiO_2 at iso-dMo of 2.2 $at.nm^{-2}$ (according to the same preparation steps mentioned above for CoMoS supported catalysts).

1.2 Experimental protocol

The various cobalt promoted MoS_2 phases are prepared on three different supports: γ-Al_2O_3, $\delta\theta$-Al_2O_3 and SiO_2. The alumina supports are used as extrudates (dimensions around 2-4 mm with diameter of 1.6 mm) and the silica support as porous pellets (diameter around 0.315-1 mm). The supports' characteristics are reported in Table 1.

Table 1. Physical properties of the γ-Al_2O_3, $\delta\theta$-Al_2O_3 and SiO_2..

Supports	γ-Al_2O_3	$\delta\theta$-Al_2O_3	SiO_2
S_{BET} ($m^2.g^{-1}$)	285	81	232
$V_{mesopores}$ ($ml.g^{-1}$)	0.65	0.76	0.78
$V_{macropores}$ ($ml.g^{-1}$)	0.01	-	0.21
Pore diameter (nm)	6.8 - 11.0	35.8	14.9

γ-Al_2O_3 and $\delta\theta$-Al_2O_3 are obtained from a thermal treatment of the same boehmite at respectively 450°C and 900°C. Formation of transition alumina occurs according to a well-established dehydration mechanism.[21–23] Simultaneously to the dehydration phenomena (formation and elimination of H_2O), contraction and translation of the individual layers occurs to form γ-Al_2O_3, and then δ-, θ-Al_2O_3 polymorphs.

HDS catalysts were prepared by incipient wetness impregnation. Impregnation solutions were prepared from MoO_3 and $Co(OH)_2$ precursors dissolved in aqueous solution in presence of H_3PO_4. Impregnation was performed on support extrudates (1.6 mm diameter) followed by an ageing step for 12 h to allow metal diffusion throughout the extrudate. Then, solids were dried in an oven at 120°C for 24h and calcined in air at 450°C for 2h15. Finally, oxide catalysts are presulfided ex situ by heating at 5°C.min^{-1} from room temperature to 350°C, at atmospheric pressure in a flow of 15 vol.%H_2S in H_2 (1.5 L.h^{-1}g^{-1} of catalyst). Sulfidation was achieved at 350°C for 2h15. The presulfided catalysts were then flush under argon and isolated under vacuum at 200°C in a sealed ampoule. The presulfided catalysts is then isolated under vacuum at 200°C. Figure 1 summarized the preparation step in order to obtain the oxidic and presulfided catalysts.

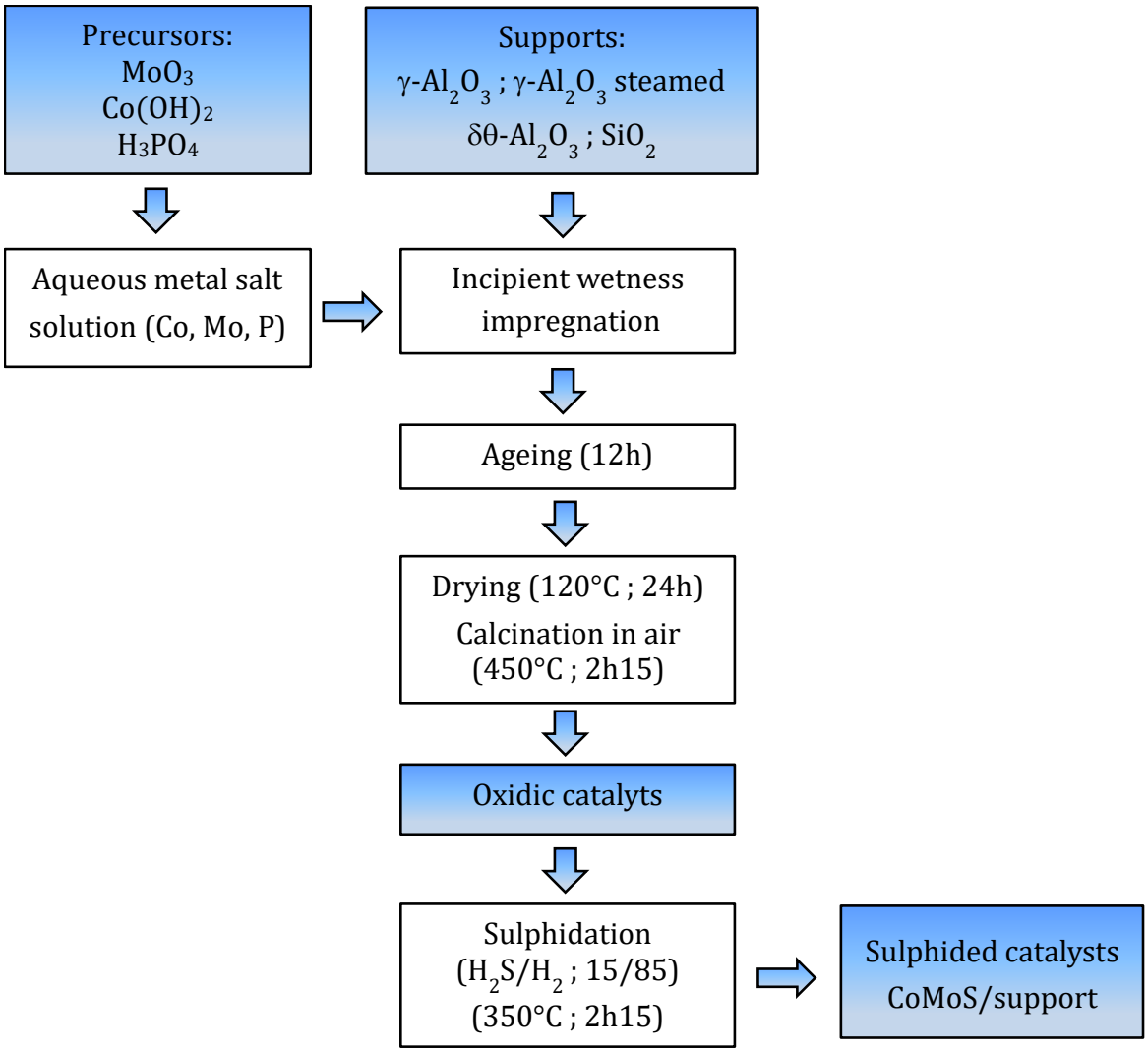

Figure 1. Classical preparation steps of a CoMoS/support synthesis.

2. Oxide phase characterization

Once calcined oxide precursors prepared, their conventional characterizations have been achieved.

2.1 X-Ray Fluorescence

2.1.1 Principle

Sample exposed to the X-ray may lead to the ionization of atoms of its which means the ejection of one or more electrons from a lower energy level (K or L) of the atom considered. The loss of an electron results in the structure electronic instability of the atoms (excited

atoms) that tend to return to the ground state. Thus, the electron ejected is replaced by an outer electron with higher energy leading to a release of energy corresponding to the electronic transition characteristic of the atoms excited.

2.1.2 Results

The element contents of Co, Mo and P deposited on different supports have been analyzed by XRF to ensure that it consistent with the element content target. Table 2 and Table 3 summarize the element contents obtained by XRF.

Table 2. XRF elemental analysis on the calcined oxide CoMo precursors of the CoMoS phase over the three supports.

Supports	dMo (at.nm^{-2} of support)	(Co/Mo)$_{molar}$	(P/Mo)$_{molar}$	% wt Co	% wt Mo	% wt P
γ-Al_2O_3	0.9	0.39	0.29	0.99	4.10	0.38
	2.1	0.38	0.29	1.95	8.40	0.79
	3.9	0.39	0.26	3.19	13.48	1.12
	4.8	0.39	0.27	3.76	15.83	1.39
$\delta\theta$-Al_2O_3	0.9	0.36	0.28	0.28	1.25	0.11
	2.2	0.10	0.26	0.16	2.58	0.22
	2.2	0.20	0.7	0.32	2.60	0.23
	2.2	0.39	0.27	0.71	2.94	0.26
	3.6	0.39	0.27	1.09	4.58	0.39
	4.5	0.39	0.25	1.34	5.63	0.45
SiO_2	0.7	0.32	0.25	0.52	2.67	0.22
	2.4	0.39	0.23	1.86	7.78	0.58
	3.7	0.39	0.23	2.68	11.22	0.83

Table 3. XRF elemental analysis of the calcined oxide precursor of the unpromoted MoS_2 on $\delta\theta$-Al_2O_3 and on SiO_2, and Co_9S_8/$\delta\theta$-Al_2O_3 reference materials.

Sulfided catalysts	dMo (at.nm^{-2} of support)	(Co/Mo)$_{molar}$	(P/Co)$_{molar}$	(P/Mo)$_{molar}$	% wt Co	% wt Mo	% wt P
MoS_2/SiO_2	2.2	-		0.28	-	6.71	0.60
MoS_2/$\delta\theta$-Al_2O_3	2.2	-	-	0.27	-	3.06	0.26
Co_9S_8/$\delta\theta$-Al_2O_3	-	-	2.56	-	0.74	-	0.97

The catalysts prepared are in good agreement with the targeted catalysts except for the SiO_2 supported catalyst at a dMo of 0.74 Mo atoms by nm² of support with Co/Mo ratio around 0.32.

2.2 Electron Micro Probe Analyzer (EPMA or Castaing micro probe)

2.2.1 Principle

Additionally, to obtain local concentration and dispersion of Co, Mo, P element and their distribution profile along the diameter of the support extrudate, Electron Micro Probe Analyzer (EPMA or Castaing micro probe) is performed. For each catalyst, the content and profile distribution of each element Co, M, P are measured.

Extrudate is bombarded by an electron beam, and emitting x-rays from elements deposited at the catalyst surface is analyzed by recording their own signature wavelengths. EMPA allows a quantitative analysis by measuring the intensity measured directly link to the mass concentration of considered element.

Element profile distribution is then recorded with an analysis time of 10s and a step analysis of 50µm. R distribution coefficient is determined to evaluate the element profile distribution is obtained:

- R distribution coefficient value close to 1 matches with an homogeneous dispersion of the probed elements on the extrudate thickness.
- R distribution coefficient lower than 1 matches with a bowl-shaped profile of the probed elements on the extrudate thickness.
- R distribution coefficient higher than 1 matches with a domed profile of the probed elements on the extrudate thickness.

2.2.2 Results

Calcined oxide precursors have been also characterized by the Castaing micro-probe to evaluate the oxide phase repartition within the catalyst particles. For each catalyst, the concentration of each oxide phases and the R distribution coefficient are measured. The R distribution coefficient represents the distribution of the probed elements within the extrudate The R distribution coefficient is plotted as function of the dMo for the

CoMo/$\delta\theta$-Al_2O_3 (Figure 2). Overall, the same trend is observed for the others supported catalysts: homogeneous distribution of the P, Co and Mo species (Appendix 1), except for low phosphorus concentration leading to core-shell distribution (at dMo= 0.9 at/nm²).

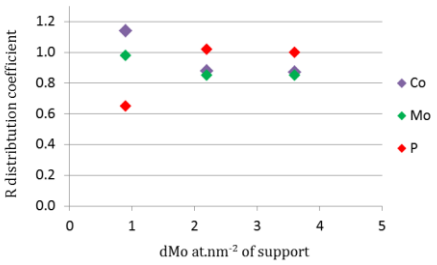

Figure 2. R distribution coefficient of Co, Mo, P elements for the CoMo/$\delta\theta$-Al_2O_3 by Castaing micro-probe.

It is observed that for a dMo higher than 2 at.nm^{-2} of support, the R distribution coefficient for P, Mo and Co species are close to 1: the distribution on the extrudate thickness is homogenous. However, for a dMo of 1 at.nm^{-2} of support, the R distribution coefficient for Mo species are close to 1 but not for the Co and P species (around respectively 1.2 and 0.5). The R distribution coefficient of Co and P presents opposite profiles, respectively higher and lower. It indicates that the phosphorus is preferentially located on the edge of the extrudate and the cobalt is more concentrate in the center.

2.3 X-ray diffraction analysis

Dispersion has been also evaluate by XRD, and crystallize oxide species are identified.

2.3.1 Principle

The X-ray diffraction is a qualitative, macroscopic and non-destructive method for the sample analyzed. X-ray diffractometers is composed of three main elements: an X-ray tube, a sample holder, and an X-ray detector. X-rays are generated in a copper anti-cathode, CuK_α radiation λ=1.5448 A. The electron beam is then accelerated (voltage of 50kV and 35 mA) toward the sample order with a particular. Once the sample bombarded, intensity of the reflected X-rays is recorded. When the angle of the incident X-rays satisfies the Bragg Equation ($2d\sin\theta=n\lambda$ with d, interplanar distance; θ, scattering angle; n, a positive integer; λ, wavelength of incident wave), a constructive interference occurs and a peak in intensity occurs. For typical powder patterns, diffractogram is recorded at 2θ from 5° to 70°.

2.3.2 Results

Regarding the XRD results (Appendix 2), metal elements are well dispersed for a dMo lower than 3.7 at.nm^{-2} of support. As expected, for a dMo of 3.7 at.nm^{-2} of support and higher, a crystallized phases is observed. Indeed, for alumina supported catalysts, mixed-phase metal oxide is observed at higher dMo. The distinct diffraction peaks at a Bragg angle of 2θ= 26.5° and 23.2° reveal the features of a $CoMoO_4$ phase. For γ-Al_2O_3 supported catalysts, the full-width half-maximum of the peak at 2θ=26.5° is narrower than for the $\delta\theta$ that supposed a phase well defined on it. Besides, no MoO_3 or ($Al_2(MoO_3)_4$) oxide phase is observed. However, on silica supported catalyst, the mixed-phase the $CoMoO_4$ is almost undetected, instead the crystallized MoO_3 oxide phase is observed with diffraction peaks at a Bragg angle of 2θ= 27.3° and 33.8 °.

These observations are coherent with the literature which refer to these crystallized oxide phase when the Mo loading (% w/w) reach 12 % [203,204]. Indeed, around this Mo loading, a molybdenum “monolayer” would be reached and then, an additional Mo and Co contents are in favor of these oxide phase formation. [205,206]

3. Appendices

Appendix 1: EPMA profile of CoMo oxide precursors

1. EPMA profile of CoMo/γ-Al_2O_3 oxide precursor

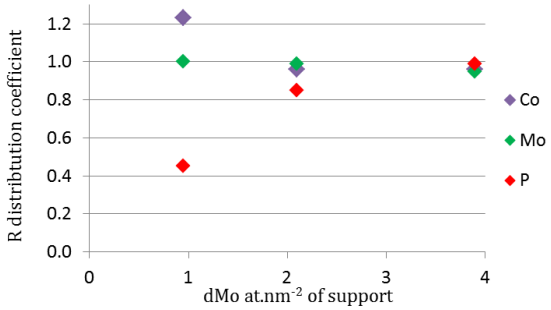

Figure 3. R distribution coefficient of Co, Mo, P elements for the CoMo/γ-Al_2O_3 by Castaing micro-probe.

a)

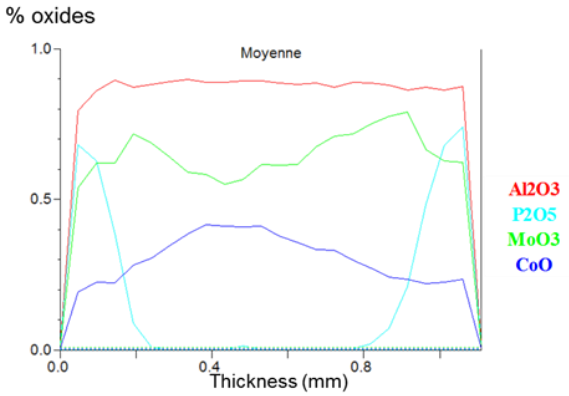

b)

Elt	Conc (% m/m) MS	Ecart type	R	Conc (% m/m) FX
P2O5	0.691	0.153	0.45	0.85
MoO3	6.57	0.467	1.00	5.93
CoO	1.28	0.129	1.23	1.21

Figure 4. a) Average profile concentration of the oxides (wt%) related to the Al, P, Mo and Co atoms. b) Average concentration R distribution coefficient of Co, Mo, P elements for the CoMo/γ-Al_2O_3 at dMo 0.9 at.nm^{-2} of support.

a)

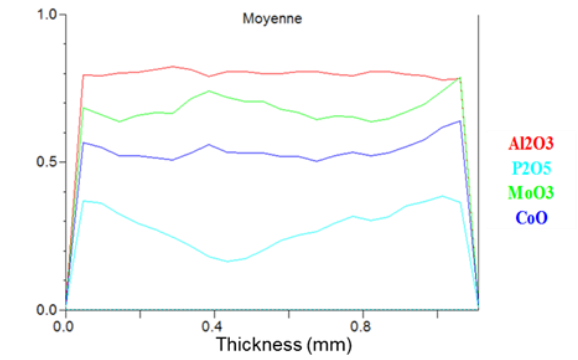

b)

Elt	Conc (%poids)	Ecart type	R
Al2O3	79.8	0.550	1.01
P2O5	1.63	0.122	0.85
MoO3	13.7	0.347	0.99
CoO	2.77	0.0855	0.96

Figure 5. a) Average profile concentration of the oxides (wt%) related to the Al, P, Mo and Co atoms. b) Average concentration R distribution coefficient of Co, Mo, P elements for the CoMo/γ-Al_2O_3 at dMo 2.2 at.nm^{-2} of support.

a)

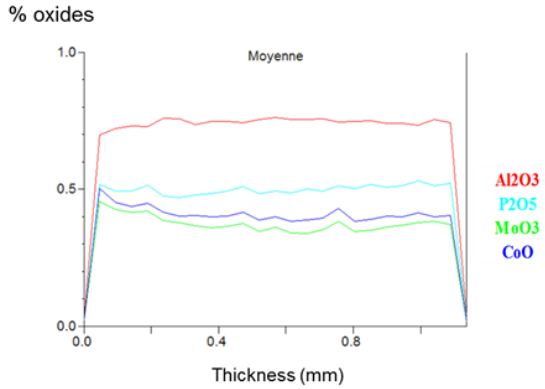

b)

Elt	Conc (%poids)	Ecart type	R
Al2O3	73.6	1.84	1.01
P2O5	2.52	0.0991	0.99
MoO3	19.5	2.21	0.95
CoO	4.22	0.364	0.96

Figure 6. a) Average profile concentration of the oxides (wt%) related to the Al, P, Mo and Co atoms. b) Average concentration R distribution coefficient of Co, Mo, P elements for the CoMo/γ-Al_2O_3 at dMo 3.8 at.nm^{-2} of support.

2. EPMA profile of CoMo/δθ-Al_2O_3 oxide precursor

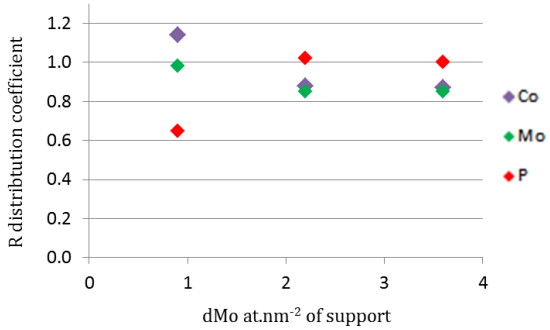

Figure 7. R distribution coefficient of Co, Mo, P elements for the CoMo/δθ-Al_2O_3 by Castaing micro-probe.

a)

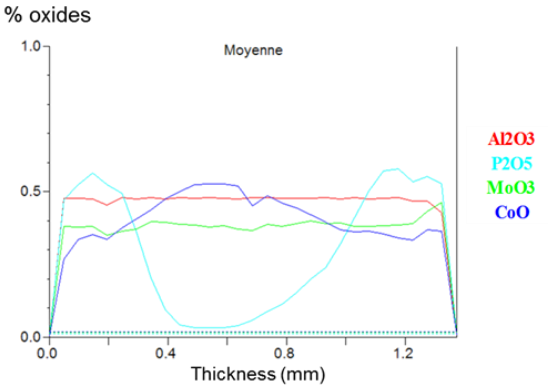

b)

Elt	Conc (%m/m)	R	Ecart type
P2O5	0.224	0.65	0.0293
MoO3	1.95	0.98	0.225
CoO	0.365	1.14	0.0178

Figure 8. a) Average profile concentration of the oxides (wt%) related to the Al, P, Mo and Co atoms. b) Average concentration R distribution coefficient of Co, Mo, P elements for the CoMo/δθ-Al_2O_3 at dMo 0.9 at.nm^{-2} of support.

a)

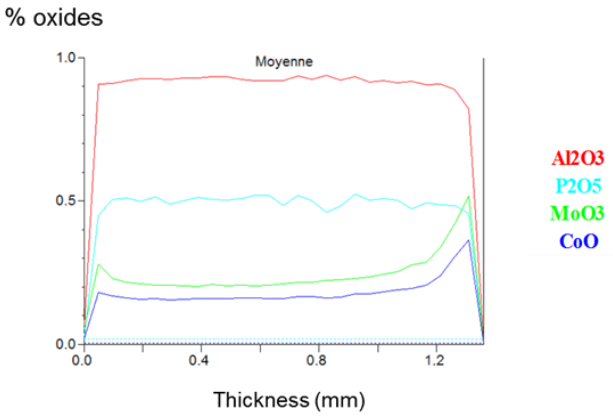

b)

Elt	Conc (%m/m)	R	Ecart type
P2O5	0.490	1.02	0.0531
MoO3	5.56	0.85	0.835
CoO	1.01	0.88	0.132

Figure 9. a) Average profile concentration of the oxides (wt%) related to the Al, P, Mo and Co atoms. b) Average concentration R distribution coefficient of Co, Mo, P elements for the CoMo/δθ-Al_2O_3 at dMo 2.2 at.nm^{-2} of support.

a)

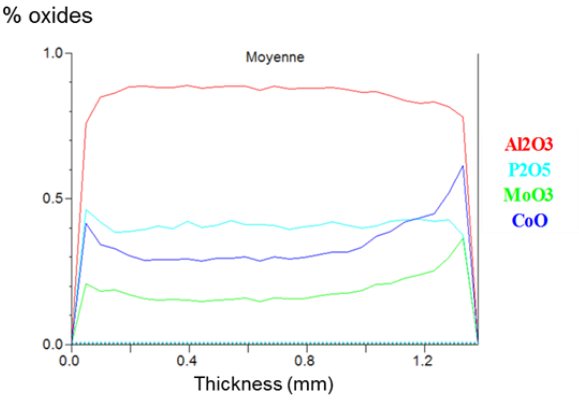

b)

Elt	Conc (%m/m)	R	Ecart type
P2O5	0.823	1.00	0.0365
MoO3	10.7	0.85	1.29
CoO	1.94	0.87	0.204

Figure 10. a) Average profile concentration of the oxides (wt%) related to the Al, P, Mo and Co atoms. b) Average concentration R distribution coefficient of Co, Mo, P elements for the CoMo/$\delta\theta$-Al_2O_3 at dMo 3.8 at.nm^{-2} of support.

Appendix 2: XRD patterns of CoMo oxide precursors

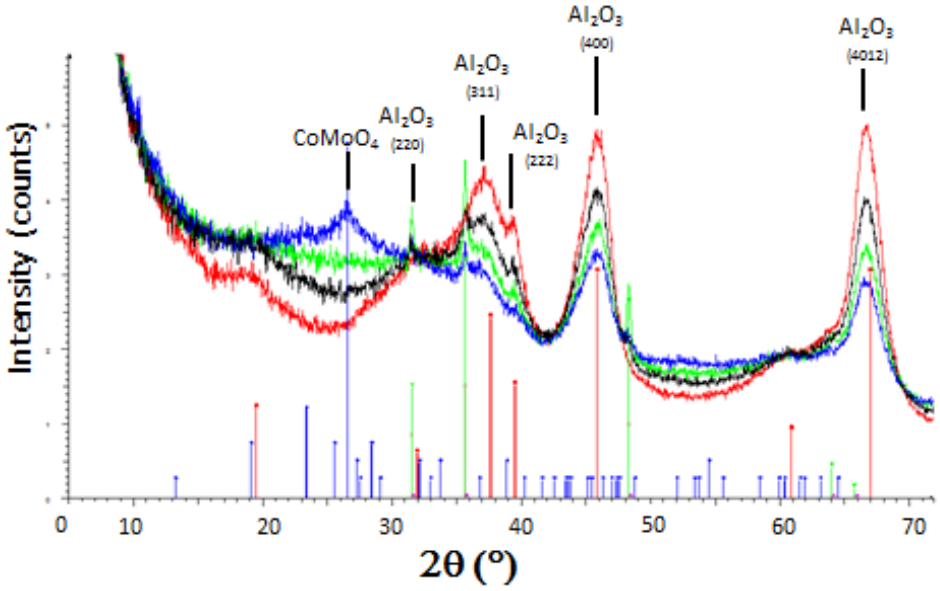

Figure 11. XRD pattern of γ-Al_2O_3 (red) and of CoMo on γ-Al_2O_3 at dMo of 0.9 (black), 2.2 (green) and 3.8 (blue) at.nm^{-2} of support.

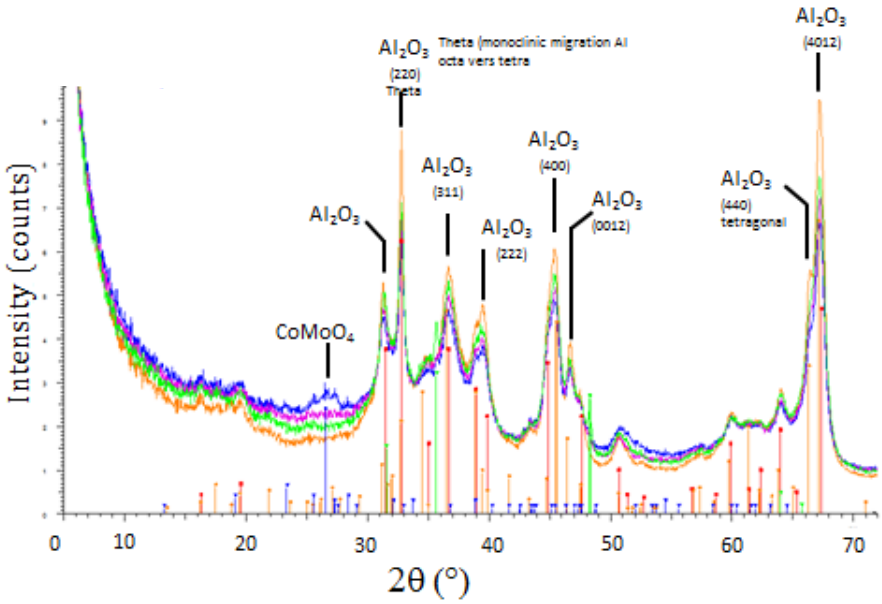

Figure 12. XRD pattern of δθ-Al_2O_3 (orange) and of CoMo on δθ-Al_2O_3 at dMo of 0.9 (green), 2.2 (purple) and 3.8 (blue) at.nm^{-2} of support.

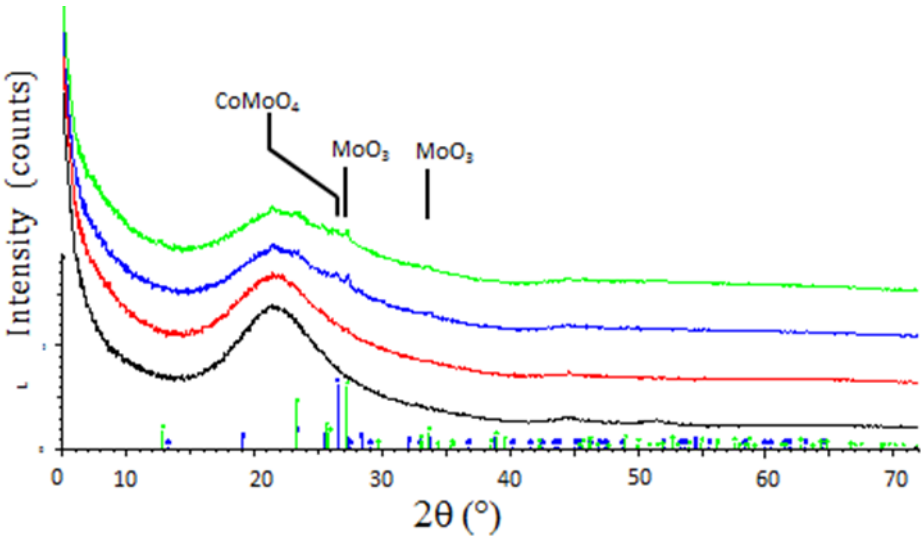

Figure 13. XRD pattern of SiO_2 (black) and of CoMo on SiO_2 at dMo of 0.9 (red), 2.2 (blue) and 3.8 (green) at.nm^{-2} of support.

- Chapter III -
Catalytic performances of the alumina and silica supported catalysts

Table of contents

1 Introduction 101

2 Experimental 102

2.1 Catalysts preparation 102

2.2 High pressure catalytic tests 103

2.2.1 Catalytic test conditions 103

2.2.2 GC analysis system 104

2.2.3 Transformation of 3MT and 23DMB2N 108

2.2.4 Conversion, yield and selectivity calculations 111

2.2.5 Activity calculation 112

3 Results and discussion 114

3.1 Co/Mo ratio effect 114

3.1.1 Evolution of 3MT and (23DMB2N+23DMB1N) conversions 114

3.1.1 Product distributions 116

3.1.1.1 Products from 3MT transformation 116

3.1.1.2 Products from 23DMB2N transformation 120

3.1.2 HDS/HYDO selectivity 123

3.2 Support effect 123

3.2.1 Evolution of 3MT and (23DMB2N+23DMB1N) conversions 124

3.2.2 Product distributions 127

3.2.2.1 Products from 3MT transformation 127

3.2.2.2 Products from 23DMB2N transformation 131

3.2.3 HDS/HYDO selectivity 134

3.3 Mo coverage effects 136

3.3.1 3MT and (23DMB2N+23DMB1N) conversion 137

3.3.2 Products distribution 138

3.3.2.1 Products from 3MT transformation 138

3.3.2.2 Products from (23DMB2N+23DMB1N) transformation 140

3.3.3 HDS/HYDO selectivity 142

4 Conclusions 144

5 Appendixes 146

6 References 171

- Chapter III -
Catalytic performances
of the alumina and silica supported catalysts

1 Introduction

One of the key steps to ensure a deep HDS of sulphur compounds of FCC gasolines while avoiding the loss of octane number is to develop more efficient supported CoMoS catalysts thanks to a better understanding of the HDS catalyst selectivity (HDS/HYDO). Catalysts based on the Co, Mo and P atoms have been prepared in order to evaluate the promotor effect (Co/Mo ratio), the support effect and the impact of the molybdenum surface density by nm^2 of support (labelled dMo in what follows) on the HDS activity and selectivity.

To study the support effect, three supports have been selected to disperse the CoMoS active phase: γ-Al_2O_3, $\delta\theta$-Al_2O_3, SiO_2. These supports have been chosen according to the literature reported previously:

- different transition aluminas, such as γ, δ, and θ have revealed an impact on the HDS selectivity,
- silica has been chosen for the significantly different acid-base properties compare with alumina supports and according to their higher selectivies previously reported.

However it should be stressed that the simultaneous impact of the molybdenum surface density (dMo) has been far less investigated in consistent way with the nature of the support.

For these reasons, in this chapter, it is reported a set of experimental data on the various catalysts prepared on purpose to quantify and compare a set of hydrodesulfurization, hydrogenation activities and selectivity as a function of the support and the Co-promoter and the Mo surface density used.

2 Experimental

2.1 Catalysts preparation

The various transition metal sulfides phases were prepared on three different supports: γ-Al_2O_3, $\delta\theta$-Al_2O_3 and SiO_2. Catalyst preparation is reported in the previous chapter II (1. Catalysts and preparation).

CoMoS supported catalysts have been prepared in order to study the support and the dMo effect. Thus, three supports have been selected to disperse the CoMoS active phase: γ-Al_2O_3, $\delta\theta$-Al_2O_3, SiO_2 and three well-chosen molybdenum surface densities by nm² of support. Over $\delta\theta$-Al_2O_3, catalysts at Co/Mo variable (from 0 to 0.4) at iso-dMo of 2.2at.nm^{-2} have been also prepared (Table 1).

The catalysts prepared are all in good agreement with the targeted catalysts except for the SiO_2 supported catalyst at a dMo of 0.73 Mo at.nm.² where the Co/Mo ratio is around 0.32.

Table 1. XRF elemental analysis on the calcined oxide CoMo three supports.

Supports	dMo (at.nm^{-2} of support)	(Co/Mo) molar	(P/Mo) molar	% wt Co	% wt Mo
γ-Al_2O_3	0.9	0.39	0.29	0.99	4.10
	2.1	0.38	0.29	1.95	8.40
	3.9	0.39	0.26	3.19	13.48
$\delta\theta$-Al_2O_3	0.9	0.36	0.28	0.28	1.25
	2.3	0.00	0.27	-	3.06
	2.2	0.10	0.26	0.16	2.58
	2.2	0.20	0.7	0.32	2.60
	2.2	0.39	0.27	0.71	2.94
	3.6	0.39	0.27	1.09	4.58
SiO_2	2.2	0.00	0.28	-	6.71
	0.7	0.32	0.25	0.52	2.67
	2.4	0.39	0.23	1.86	7.78
	3.7	0.39	0.23	2.68	11.22

2.2 High pressure catalytic tests

2.2.1 Catalytic test conditions

Catalytic activity measurements were carried out in fixed bed high throughput reactors (16 in parallel) at various temperatures from 453 to 513 K under a total pressure of 1.5 MPa with a H_2/feed volumic ratio of 300 NL/L, close to industrial operating conditions of the FCC gasoline hydroprocessing. The feed was injected in the reactor by a JASCO pump (307 series, pump's head: 5cm^3). The mass of catalyst varied from 30 to 400 mg. The flow of the liquid feed and the H_2 is kept constant respectively at 0.3 ml.min^{-1} and 9 ml.min^{-1}. Three model feedstocks are studied:

(i) a thiophenic feed containing 0.33 wt% of 3-methylthiophene, labelled 3MT, (corresponding to 1000 wt ppm of sulfur) diluted in n-heptane.

(ii) an olefinic feed containing 10 wt% of 2,3-dimethylbut-2-ene, labelled 23DMB2N, diluted in n-heptane

(iii) a model FCC gasoline feed containing 0.33 wt% of 3MT (corresponding to 0.33 %mol) and 10 wt% of 23DMB2N (11.6 %mol), diluted in n-heptane (Molar composition).

Measurements of conversion and yield related to the 3MT and 23DMB2N transformations have been performed as function of the contact time, labelled $\tau_{Mo,reactant}$. This contact time is calculated as the reverse of the weight hourly space velocity (WHSV). As specific surface area of each support is different, to obtain the same dMo between each catalyst, different loading of Molybdenum have to be used. As a consequence, in order to compare the properties of CoMoS supported catalysts each other and to evaluate the support and dMo effect on the catalytic properties, WHSV is defined by the ratio between the mass gas flow rate of the reactant of the considered reaction (3MT or 23DMB2N) and the mass of the molybdenum deposited on the support. To reach variation of conversion (between 0 and 100%), the contact time, $\tau_{Mo,reactant,}$ has been modified by changing the amount of catalyst used (between 33 and 400 mg) or the reactant flow. Thus, $\tau_{Mo,reactant}$ varies from 0.24 to 14 h and from 0.5 to 29.5 min for 3MT and 23DMB2N respectively.

Finally, support references have been tested in the same operatory conditions and results will be reported and discussed in Appendix 1.

2.2.2 GC analysis system

The reaction products have been identified on-line by means of an automatic sampling valve of an Agilent 7890 gas chromatograph equipped with two columns (one polar column and one column with intermediate polarity) with a dean switch device and a flame ionization detector. Figure 1 represents a scheme of the gas chromatographic detection system used. Hence, 3MT and 23DMB2N conversions, product selectivities and the HDS and HYDO yields have been then deduced.

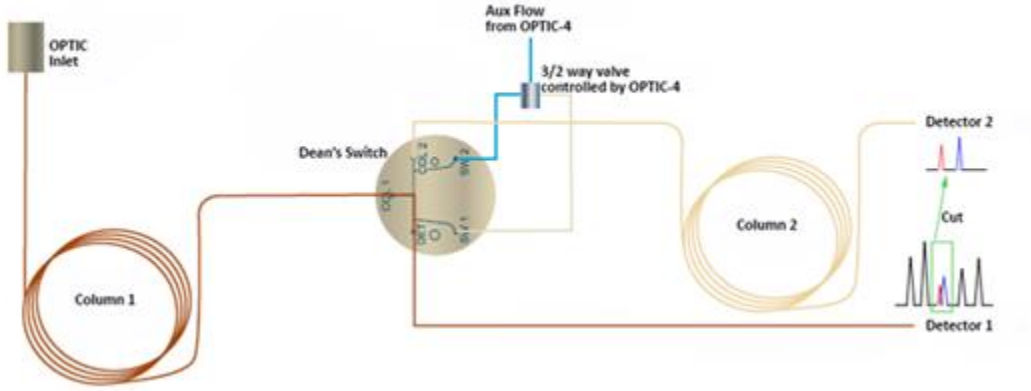

Figure 1. Schematic representation of the gas chromatographic detection system used.

Two columns have been selected for this chromatographic method, connected by a Deans Switching System in order to separate products with closed retention time and to obtain the associated chromatogram pic. Computer interface EZChrom allow to record chromatograms. Thus, two FID detectors have been used. A non-polar column (Agilent J&W DB-1) and an intermediate polarity column (Rtx®-1701) are used. Details of the method are given in Table 2.

Table 2. Details of the gas chromatographic method used.

Split injector	Temperature	280°C	
	carrier gas	H_2	
	Constant pressure	42.5 Psi	
	Injection volume	Injection loop :Avantium	
	Split ratio	500/1	
auxiliary PCM	Constant pressure	3.6 Psi	
power cut duration	cut 1	5-6 min	
DB-1 column	L: 20m	d: 100µm	e: 0.4µm
Rtx-1701 column	L: 30m	d: 320µm	e: 1.0µm
restrictor insert	L: 35m	d: 100 µm	
Oven	Programmation (°C/min)	T(°C)	Plateau (min)
		35	3.35
	15.5	130	3
Detector	Temperature	280°C	
	H_2	35ml/min	
	Air	400ml/min	
	Make-up	30ml/min	

An example of chromatogram from a catalytic test is in presence of the model FCC gasoline feedstock for $CoMoS/SiO_2$ is presented in Figure 2.

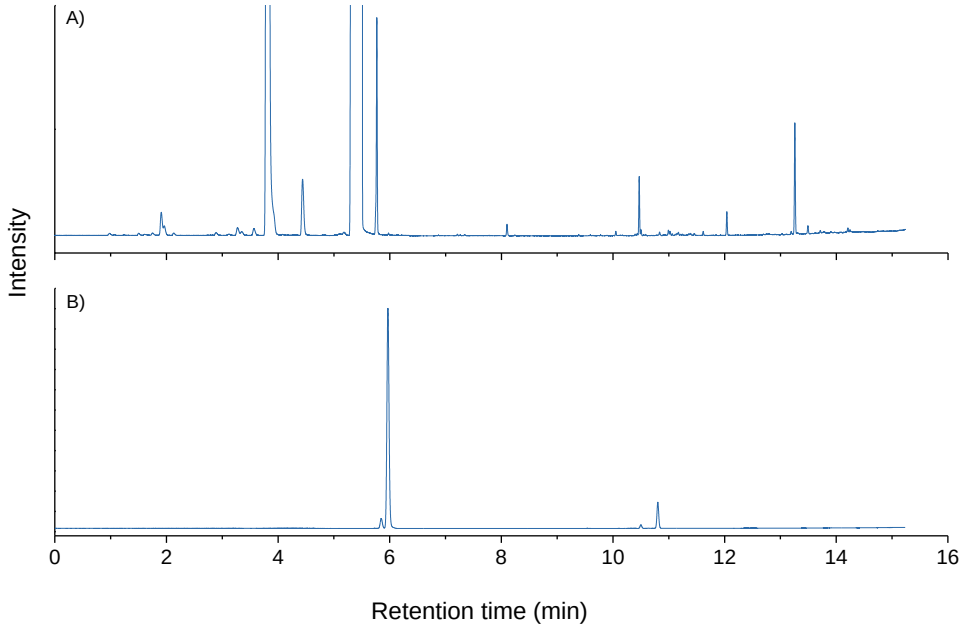

Figure 2. Chromatogram obtained on (A) the front detector and on (B) the back detector for a HDS catalytic test in presence of 3MT, 23DMB2N in n-heptane (respectively 0.33%, 10% and 89.67%) of $CoMoS/SiO_2$ at dMo of 2.2at.nm^{-2} of support at 210°C and a mass loaded of 117 mg.

Identification of the products from the 3MT and 23DMB2N transformation is based on the literature[1–3] and based on an additional GC/MS analysis carried out at IFPEN. Product identification is performed on catalytic test with the three model feedstocks presented previously. Table 3 presents 3MT and 23DMB2N products, their retention times and response factors.

It is important to note that all products are not identified which induced uncertainties on conversions or yields reported in what follows. However, the amount of unknown products is very low and ensures a good material balance as reported Figure 3. Material balances related to 3MT and 23DMB2N products have been calculated considering the response factor of each compound.

Table 3. Retention times, Tr, and response factor of analyzed compounds formed during the 3MT and 23DMB2N reactions.

Tr (min)		Attributions	Response factor
	Front detector		
1.08 , 1.18 , 1.25	*Unknown*	*Products from the 23DMB2N transformation*	1.1
1.50	Pentene and isomers	PN	1.1
1.61	2methybutane	2MB	1.1
1.75	2methylbut-1-ene	2MB1N	1.1
1.90	3,3dimethylbut-1-ene	33DMB1N	1.1
1.96	2methylbut-2-ene	2MB2N	1.1
2.13	2,2dimethylbutane	22DMB	1.1
2.60	*Unknown*	*Products from the 23DMB2N transformation*	1.1
2.89, 3.12, 3.28	Hexene and isomers	HN	1.1
3.4	2methylpent-2-ene	2MP2N	1.1
3.80	2,3dimethylbut-2-ene	23DMB2N	1.1
7.26	Octene	C8H14	1.1
7.78	C6-thiol	C6H14S	1.1
8.10	3-methyltetrahydrothiophene	3MTHT	1.15
8.24	C6-thiol	C6H14S	1.1
9.88	*decene*	$C_{10}H_{20}$	1.1
10.05	Undecene	C11H22	1.1
10.3-11.7	Dodecene	C12H24	1.1
12.04	Dodecene	C12H24	1.1
12.69 - 12.79	*Unknown*	*Products from* model FCC gasoline feedstock	1.1
13.19	*Unknown*	*Products from* model FCC gasoline feedstock	1.1
13.26	Alkylthiophene	C11H18S	1.15
13.49	*Unknown*	*Products from* model FCC gasoline feedstock	1.1
13.7-14	*Unknown*	*Products from* model FCC gasoline feedstock	1.1
14.21	Alkyltetrahydrothiophene	C11H22S	1.15
14.25	Alkyltetrahydrothiophene	C11H22S	1.15
14.28	Alkyltetrahydrothiophene	C11H22S	1.15
14.94	*Unknown*	*Products from* model FCC gasoline feedstock	1.15
	Back detector		
5.5	2,3dimethylbutane	23DMB	1.1
6.0	2,3dimethylbut-1-ene	23DMB1N	1.1
10.8	3methylthiophene	3MT	1.2

Figure 3 presents the molar material balance related for the CoMoS/δθ-Al_2O_3 at dMo of 0.9 at.nm^{-2} of support at 220°C for a model FCC gasoline feed. Empty reactor is used to obtain the blank of the feedstock composition. Thus uncertainties relative to the global system (analysis system and reactor system) can be determined. For alumina supported catalysts, absolute uncertainties related to the conversion of 3MT and 23DMB2N is around +/- 5%. However, for silica supported catalysts, material balance is matching at +/- 8% related to the 3MT and +/- 3% related to the 23DMB2N. For the 3MT molar material balance for silica supported catalysts, uncertainties are higher (Appendix 2). It could be explained by the fact that the response factor of the sulphided derivative compounds is taken equal to the response of the 3MT.

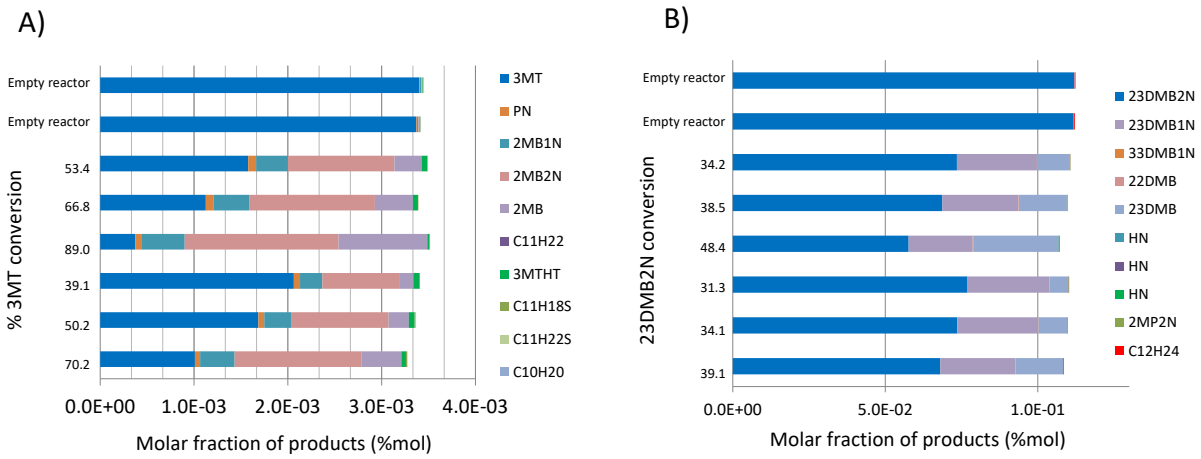

Figure 3. Molar material balance related to (A) the 3MT product and (B) the 23DMB2N products for the CoMoS/δθ-Al_2O_3 at dMo of 0.9 at.nm^{-2} of support at 220°C.

2.2.3 Transformation of 3MT and 23DMB2N

Products observed in GC analysis are related to the 3MT transformation and the 23DMB2N transformation but also to the reaction between 3MT and 23DMB2N and its isomers.

3MT can react and form different products according different pathways. First, 3MT can be totally desulfurized to form alkene and alkane products. Desulfurized products are designated as HDS products. The main desulfurized products are 2-methylbutane (2MB), 2-methylbut-1-ene (2MB1N) and 2-methylbut-2-ene (2MB2N) according to the reaction scheme described in Figure 4.

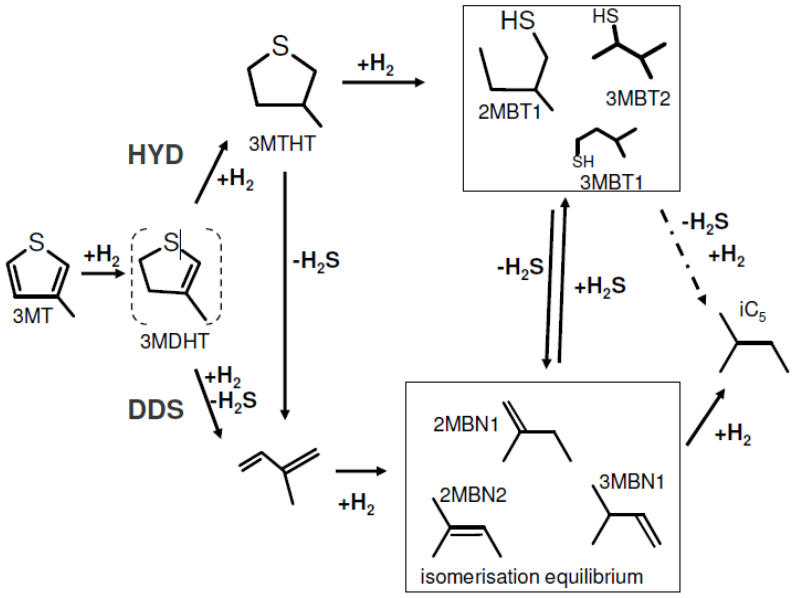

Figure 4. Reaction pathways for 3-methylthiophene HDS.[2]

However, 3MT can be partially hydrogenated to form 3-methyltetrahydrothiophene (3MTHT). Moreover, side reactions occur between 3MT and 23DMB2N (and its C_6 isomers) to form alkylthiophene and derivatives ($C_{11}H_{18}S$, $C_{11}H_{22}S$, $C_{11}H_{22}$). (see bibliographic part 3.1.2).

The transformation of the 23DMB2N leads to the formation of isomerization products (mainly

2,3-dimethylbut-1-ene, 23DMB1N) and small amounts of corresponding skeletal isomers: 3,3-dimethylbut-1-ene (33DMB1N), hexene (HN), 2-methylpent-2-ene (2MP2N) and hydrogenation products (mainly 2,3-dimethylbutane, 23DMB and small amounts of hydrogenated skeletal isomers, 2,2-dimethylbutane, 22DMB). Simplified scheme of the transformation of the 23DMB2N is reported Figure 5.

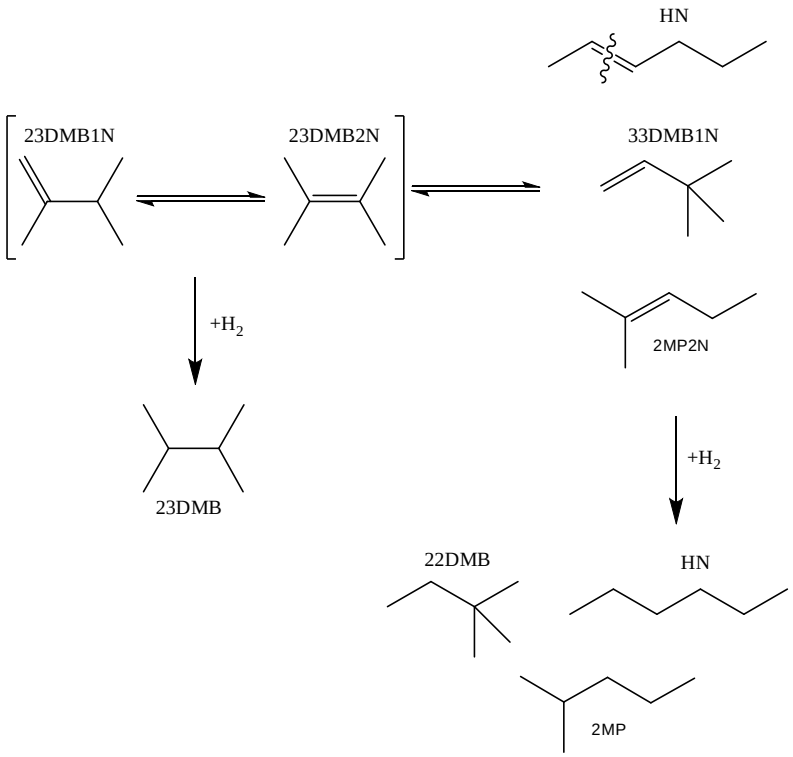

Figure 5. Simplified scheme of the transformation of the (23DMB2N+23DMB1N).
(Adapted from Mey *et al*.[4])

The isomerization of 23DMB2N into 23DMB1N is known to be very fast over CoMoS supported catalysts.[3] This assumption was verified our operatory conditions and it was noted that isomerization reaction reaches rapidly the thermodynamic equilibrium (Appendix 3). Thus, the mixture composed of 23DMB2N:23DMB1N in molar proportion %67:%23 (%mol:%mol) is considered present from the initial state to react with the catalyst. Thus for the following, 23DMB2N and 23DMB1N will be considered as a single initial reactant.

Moreover, side reaction is observed and need to be considered. Indeed, as previously mentioned, 23DMB2N and isomers react with 3MT to form alkylthiophene and its derivatives ($C_{11}H_{18}HS$, $C_{11}H_{22}S$ and $C_{11}H_{22}$). Additionally, reaction between C_6 olefins and H_2S occurs to form C_6-thiol compounds. Finally, C_6 olefins react with themselves to form a mixture dodecene and its isomers ($C_{12}H_{24}$).

All products observed in experimental catalytic test conditions, related to the 3MT and 23DMB2N transformation, will be described in the following section.

2.2.4 Conversion, yield and selectivity calculations

Conversions and yields have been calculated by considering a constant volume, because of the high H_2/HC volume ratio equal to 300. Thus, molar flow rate of reactant can be assimilated to the concentration. The 3MT and (23DMB2N+23DMB1N) conversions and HDS and HYDO yields are determined in molar percent.

Conversions are calculated from chromatograms obtained for the model feedstock considered. Absolute uncertainty is evaluated at +/- 5% on the 3MT and (23DMB2N+23DMB1N) conversion. 3MT and (23DMB2N+23DMB1N) conversions are calculated as below (%mol):

$$\%\text{Conversion 3MT} = \frac{\left(\text{S}\right)_{t_0} - \left(\text{S}\right)_{t}}{\left(\text{S}\right)_{t_0}} \times 100$$

$$\%\text{Conversion (23DMB2N+23DMB1N)} = \frac{\left(\text{C}_6\text{H}_{12}\right)_{t0} - \left(\text{C}_6\text{H}_{12}\right)_{t}}{\left(\text{C}_6\text{H}_{12}\right)_{t0}} \times 100$$

HDS and HYDO yields are calculated from chromatograms obtained for the model feedstock considered. For alumina supported catalysts, absolute uncertainties related to the HDS of 3MT and the HYDO of (23DMB2N+23DMB1N) is around +/- 5%. However, for silica supported catalysts, material balance is matching at +/- 8% related to the 3MT and +/- 3% related to the (23DMB2N+23DMB1N).

HDS yield is calculated according to the sulfided products formed from the 3MT partial hydrogenation or from the side reaction between 3MT and (23DMB2N+23DMB1N) leading to alkylthiophenes as below (%mol):

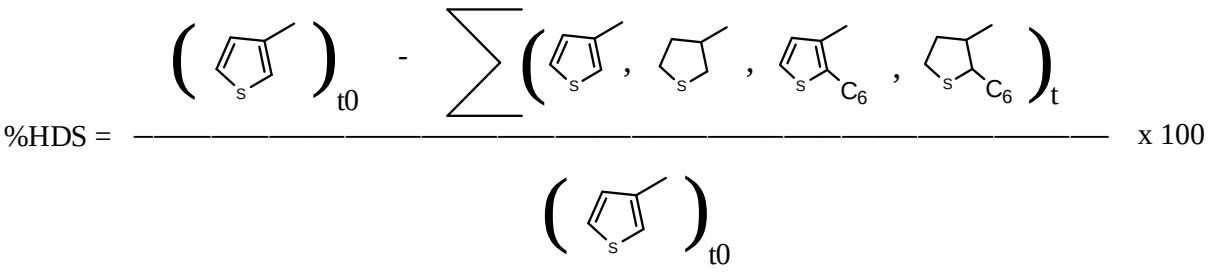

HYDO yield is calculated according to the alkane products formed from the hydrogenation of (23DMB2N+23DMB1N) and its isomers (23DMB and 22DMB) as below (%mol). Skeletal isomers of 23DMB were not take into account because they were not observed or not clearly identified by GC analysis

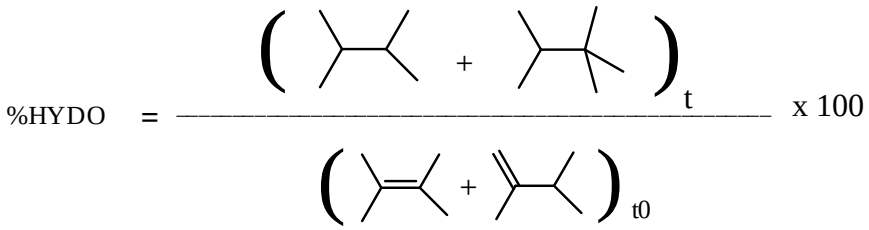

Finally, in order to study more precisely the catalyst features of the CoMoS supported catalyst, product selectivity of 3MT and (23DMB2N+23DMB1N) transformation have been calculated.

Selectivity S_i of the product i, is calculated as followed (%mol),

$$S_i = \left[\frac{P_i}{\sum_j P_j} \right] \times 100$$

Where P_j represents products related to reactant transformation considered (either 3MT or (23DMB2N+23DMB1N)).

2.2.5 Activity calculation

Initial rate (or initial activity) of the reaction related to the 3MT and (23DMB2N+23DMB1N) conversions, a_{3MT} and $a_{(23DMB2N+23DMB1N)}$, is determined by plotting the 3MT and (23DMB2N+23DMB1N) conversions (%mol) as function of the contact time, $\tau_{Mo,reactant}$,

reverse of the WHSV. WHSV is defined by the ratio between the mass gas flow rate of the reactant of the considered reaction (3MT or (23DMB2N+23DMB1N)) and the mass of the molybdenum deposited on the support.

In the same way, initial activity of the reaction related to the HDS and HYDO yields, a_{HDS} and a_{HYDO}, is determined by plotting the HDS and HYDO yields (%mol) as function of the contact time, $\tau_{Mo,reactant}$, reverse of the WHSV.

Then, the gradient of the tangent at the initial time of the 3MT or (23DMB2N+23DMB1N) conversions or HDS and HYDO yields are determined to obtain the initial activity by mol of reactant (3MT or (23DMB2N+23DMB1N)) by mol of Mo by unit of times.

Relative uncertainties related to the determination of the initial activity of 3MT ((23DMB2N+23DMB1N)) conversion or HDS (HYDO) is estimated at 20%. Uncertainties calculated depend on the experimental point obtained as well as the mathematic model used to plot the conversion or yield as function of the contact time.

Finally, the selectivity between the 3MT and (23DMB2N+23DMB1N) conversion, $S_{3MT/(23DMB2N+23DMB1N)}$, will be given by the ratio between a_{3MT} and $a_{(23DMB2N+23DMB1N)}$ initial activities.

$$S_{3\mathrm{MT}/23\mathrm{DMB2N}} = \left[\frac{a_{3MT}}{a_{23DMB2N}}\right] \times 100$$

And, the selectivity between the HDS and HYDO yields, $S_{HDS/HYDO}$, will be given by the ratio between a_{HDS} and a_{HYDO} initial activities.

$$S_{HDS/HYDO} = \left[\frac{a_{HDS}}{a_{HYDO}}\right] \times 100$$

3 Results and discussion

3.1 Co/Mo ratio effect

The Co/Mo ratio effect has been evaluated on CoMoS/$\delta\theta$-Al_2O_3 at iso-dMo of 2.2 at.nm^{-2} of support at Co/Mo ratio variable, from 0 to 0.4, with a feedstock composed of 3MT (0.33 %wt) and 23DMB2N (10 %wt) in n-heptane. In order to evaluate Co/Mo ratio effect on the 3MT and (23DMB2N+23DMB1N) conversion as well as on the HDS and HYDO reactions and on the associated selectivity, i.e experimental points obtained in the same HDS and HYDO ranges, comparison of each CoMoS catalyst has been performed at 210°C (483K).

3.1.1 Evolution of 3MT and (23DMB2N+23DMB1N) conversions

Table 4 presents the 3MT and (23DMB2N+23DMB1N) conversions at iso-contact time ($\tau_{Mo/}$3MT) of MoS_2 and CoMoS on $\delta\theta$-Al_2O_3 and SiO_2 at iso-dMo of 2.2 at.nm^{-2} of support at Co/Mo ratio from 0 to 0.4. 3MT and (23DMB2N+23DMB1N) conversions vs. the contact time, $\tau_{Mo/reactant,}$ have been reported in Appendix 4 and Appendix 5. It is observed at iso-contact time that the 3MT conversion increases with the increase of the Co/Mo, as expected due to the formation of mixed CoMoS crystallites. Indeed, the 3MT conversion increases by a factor 1.1 to 2.4 from the MoS_2/$\delta\theta$-Al_2O_3 to the CoMoS/$\delta\theta$-Al_2O_3 with respectively a Co/Mo ratio equal to 0.1 and 0.4 whereas the (23DMB2N+23DMB1N) conversion decrease and then increase slightly by a factor 1.6, respectively. It can be noticed that the hydrogenation activity of unpromoted catalyst is relatively high compared to low Co/Mo catalysts. These results are in line with the literature which shows that the presence of the Co-promoter increase significantly the 3MT conversion more than (23DMB2N+23DMB1N) conversion.[5]

Table 4: 3MT and (23DMB2N+23DMB1N) conversions at iso-contact time ($\tau_{Mo/}$3MT) of MoS_2 and CoMoS on $\delta\theta$-Al_2O_3 and SiO_2 at iso-dMo of 2.2 at.nm^{-2} of support at Co/Mo ratio from 0 to 0.4 at 210°C.

	Co/Mo	$\theta_{Mo,\ 3MT}$ (h)	Conversion 3MT	Conversion (23DMB2N+23DMB1N)
$MoS_2/\delta\theta$-Al_2O_3	0	1.4	21	10
	0.1	1.7	24	6
CoMoS/$\delta\theta$-Al_2O_3	0.2	1.7	34	9
	0.4	1.7	51	17
MoS_2/SiO_2	0	11	56	20
CoMoS/SiO_2	0.4	11	56	6

Regarding the silica supported catalysts, the promoting effect is very low and only a slightly increase of 3MT conversion is obtained at iso-$\tau_{Mo/3MT}$ between the unpromoted and Co promoted MoS_2 catalyst at iso-dMo of 2.2 at.nm^{-2} at 210°C. However, the (23DMB2N+23DMB1N) conversion is divided by a factor 4.2 in presence on Co-promoted MoS_2 compare with MoS_2/SiO_2 which is an opposite trends compared with the results obtained for $\delta\theta$-Al_2O_3 supported catalyst.

Moreover, whereas 3MT and (23DMB2N+23DMB1N) conversion plotted as function of the contact time conducted to classify the catalyst in term of activity, it is interesting to study the selectivity between both reaction of conversion of 3MT and 23DMB2N, $S_{3MT/(23DMB2N+23DMB1N)}$. Thus, the (23DMB2N+23DMB1N) conversion is plotted as a function of the 3MT conversion for CoMoS/$\delta\theta$-Al_2O_3 at iso-dMo of 2.2 at.nm^{-2} and Co/Mo variable at 210°C (Figure 6).

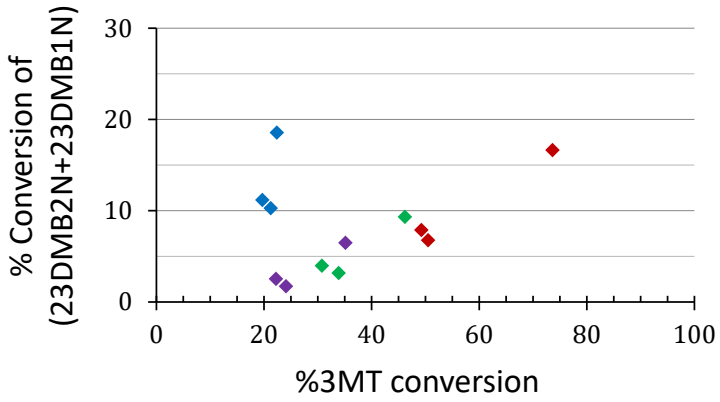

Figure 6. Selectivity between the 3MT and the (23DMB2N+23DMB1N) conversions of $MoS_2/\delta\theta$-Al_2O_3 (blue) and CoMoS/$\delta\theta$-Al_2O_3 at iso-dMo of 2.2 at.nm^{-2} of support, Co/Mo=0.1 (purple), Co/Mo=0.2 (green) and Co/Mo=0.4 (red), at 210 °C.

It can be noted that the $MoS_2/\delta\theta$-Al_2O_3 exhibits a 3MT/ 23DMB2N selectivity significantly lower compared with $CoMoS/\delta\theta$-Al_2O_3 regardless the Co/Mo ratio. Moreover, the 3MT/ 23DMB2N selectivity increases slightly with the increase of the Co/Mo ratio from 0.1 to 0.4.

For the silica supported catalysts, MoS_2/SiO_2 exhibits a 3MT/23DMB2N selectivity significantly lower compared with $CoMoS/SiO_2$ (Appendix 5).

3.1.1 Product distributions

3.1.1.1 Products from 3MT transformation

Products formed from 3MT transformation have been identified by GC/MS. Three compound families were identified:

- Products corresponding to the complete 3MT desulfurization leading to the formation of alkenes and alkanes (Table 5):
  2-methylbut-2-ene (2MB2N), 2-methylbut-1-ene (2MB1N), pentene and isomers (PN) and 2-metylbutane (2MB)

Table 5. Alkene and alkane identified from the 3MT transformation.

Products			
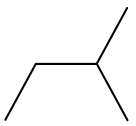	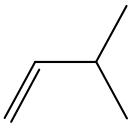	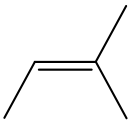	
2MB	2MB1N	2MB2N	PN and isomers

- Intermediate products corresponding to hydrogenation of 3MT, (Table 6):
- 3-methyltetrahydrothiophene (3MTHT)

Table 6. 3-methylthiophene hydrogenated identified from the 3MT transformation.

Products
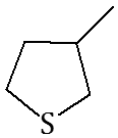
3MTHT

- Side-products corresponding to the reaction of 3MT or 3MTHT with alkenes (23DMB2N and isomers) leading to heavier alkylthiophenes (Table 7): Alkylthiophenes ($C_{11}H_{18}S$), alkylthiophenes tetrahydrogenated ($C_{11}H_{22}S$) and $C_{11}H_{22}$

Table 7. Heavy alkylthiophenes identified from the 3MT reaction with olefins.

Products		
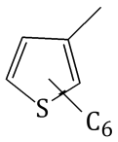	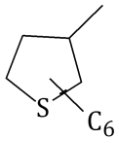	$C_{11}H_{22}$
$C_{11}H_{18}S$	$C_{11}H_{22}S$	$C_{11}H_{22}$

Figure 7 presents the selectivity of the main transformation products of 3MT over CoMoS/δθ-Al_2O_3 at iso-dMo of 2.2 at.nm^{-2} of support and at various Co/Mo ratio. Over all catalysts, HDS products (2MB, 2MB2N and 2MB1N) are the major products observed regardless the 3MT conversion excepted for unpromoted catalyst MoS_2/δθ-Al_2O_3. Indeed, in addition to the HDS products, the selectivity of 3MTHT appears to be significant (~30%) compared with Co-promoted MoS_2/δθ-Al_2O_3 (~8-10%). These results are in compliance with the literature regarding the Co-promoter effect which is known to enhance the conversion of 3MT in HDS product.[4,6]

Regarding the Co/Mo ratio effect from 0.1 to 0.4, it can be noted that the products selectivity is closed at iso-conversion of the 3MT.

Besides, for unpromoted and promoted MoS_2/δθ-Al_2O_3, it is observed that the product selectivity is not in favor of the formation $C_{11}H_{18}S$ alkylthiophene (< 2%) and its resulting hydrogenating and desulfurization products, $C_{11}H_{22}S$ and $C_{11}H_{22}$ (< 1%). (noted that hydrogenated alkylthiophene could also be formed from the reaction of 23DMB2N (or its isomers) with 3MTHT).

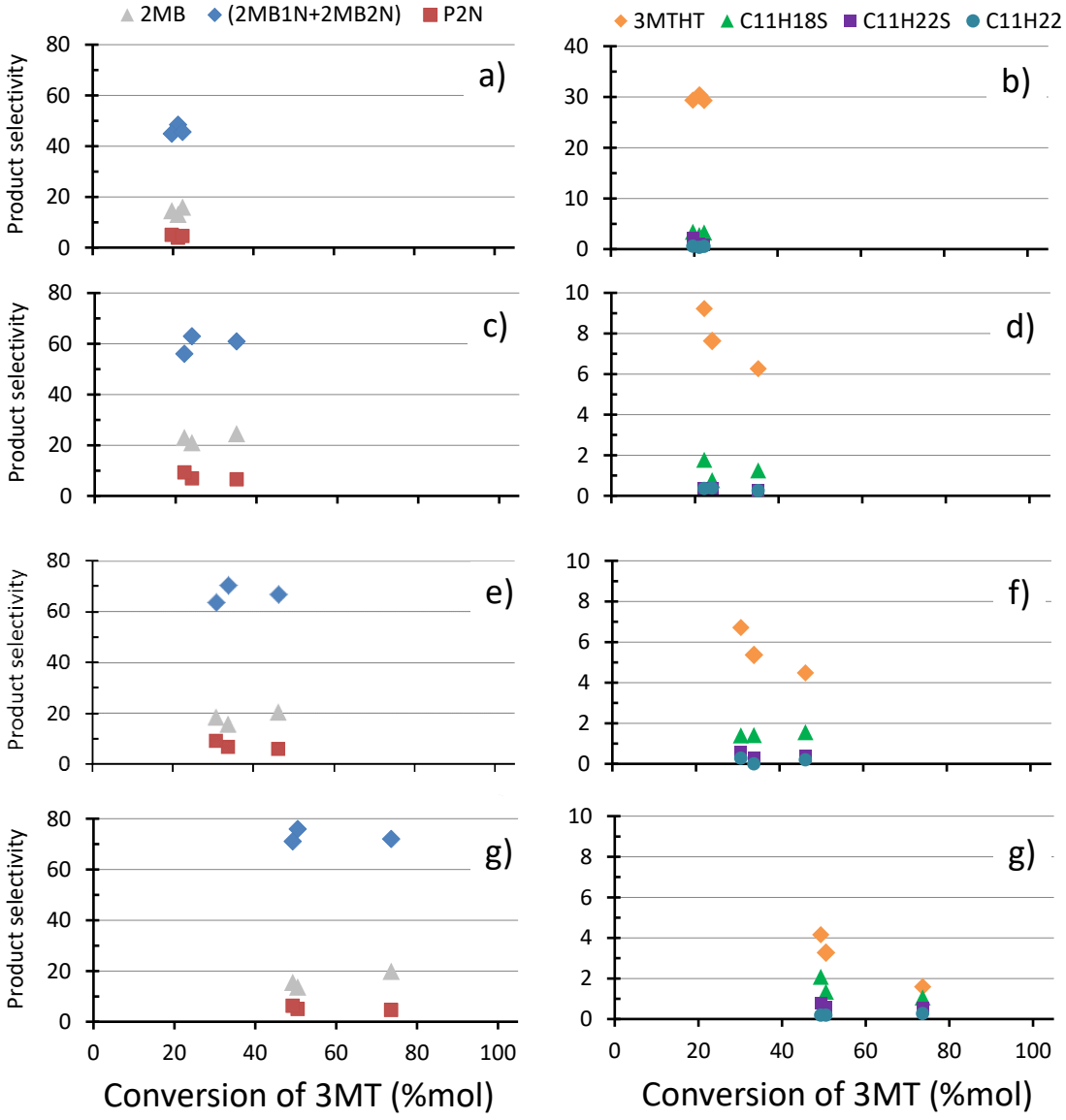

Figure 7. Selectivity of 3MT products of MoS_2 (a,b) and CoMoS/δθ-Al_2O_3 at iso-dMo of 2.2 at.nm^{-2} of support, (c,d) Co/Mo=0.1, (e,f) Co/Mo=0.2, (g,h) Co/Mo=0.4 at 210 °C. Graphs on the left represent the product distribution of alkanes and alkene from the complete desulfurization of 3MT. Graphs on the right represent the product distribution of 3MTHT from the hydrogenation of 3MT and alkylthiophene from 3MT side reaction with (23DMB2N+23DMB1N) olefins.

Regarding the silica supported catalysts, it can be noticed a similar evolution of the 3MT product selectivity compare with δθ-Al_2O_3 supported catalysts with however more pronounced differences (Appendix 6). Indeed, the 3MTHT selectivity appears to be more significant in presence of MoS_2/SiO_2 (~50%) whereas the selectivity towards the alkane (2MB) and alkenes (2MB2N, 2MB1N, PN) is lower. Moreover, on the contrary of δθ-Al_2O_3

supported catalysts, the presence of Co as promoter on MoS_2/SiO_2 leads to a decrease of the 3MTHT selectivity and a notable increase of the selectivity towards $C_{11}H_{18}S$.

One of the main catalytic parameter concerning the transformation of 3MT is the hydrodesulfurization activity. For each catalyst, HDS yield, corresponding to the amount of 3MT transformed in desulfurized product (i.e. alkanes and alkenes), can be determined as function of the contact time, $\tau_{Mo/3MT}$ (Table 8). Plots associated are reported in the Appendix 7 and Appendix 8. This more correct analysis takes now into account the amount of residual sulfided compounds identified in Figure 7, which was not the case in our previous analysis of the 3MT conversion.

Table 8. HDS yields at iso-contact time ($\tau_{Mo/}$3MT) of MoS_2 and CoMoS on $\delta\theta$-Al_2O_3 and SiO_2 at iso-dMo of 2.2 at.nm^{-2} of support at Co/Mo ratio from 0 to 0.4 at 210°C.

	Co/Mo	$\tau_{Mo,\ 3MT}$ (h)	HDS (%mol)
$MoS_2/\delta\theta$-Al_2O_3	0	1.4	13
CoMoS/$\delta\theta$-Al_2O_3	0.1	1.7	32
	0.2	1.7	43
	0.4	1.7	71
MoS_2/SiO_2	0	11.0	30
$CoMoS/SiO_2$	0.4	11.0	39

As expected and previously observed for the 3MT conversion, at iso-$\tau_{Mo/3MT}$, the HDS yield increases but more significantly by a factor 2.5 and 5.5 from the $MoS_2/\delta\theta$-Al_2O_3 to the CoMoS/$\delta\theta$-Al_2O_3 with respectively a Co/Mo ratio equal to 0.1 and 0.4 whereas the (23DMB2N+23DMB1N) conversion decrease and increase slightly by a factor 1.4 and 1.5 respectively.

However, Similar behavior is observed between both unpromoted and Co-promoted silica catalysts for the HDS yield compare with the 3MT conversion with an increase by a factor 1.3 for a Co/Mo from 0 to 0.4 (Appendix 8).

3.1.1.2 Products from 23DMB2N transformation

Products related to 23DMB2N transformation have been identified by GC/MS. Four compound families can be identified:

- Products corresponding to the isomerization of 23DMB2N (Table 9):
  2,3-dimethylbut-2-ene (23DMB2N), 2,3-dimethylbut-1-ene (23DMB1N), 3,3-dimethylbut-1-ene (33DMB1N), hexene and its isomers and 2methylpent-2-ene (HN) and its isomers (2MP2N)

Table 9. 23DMB2N isomers identified from the 23DMB2N transformation.

Products				
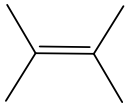	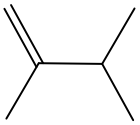	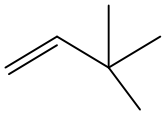	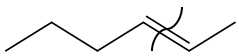	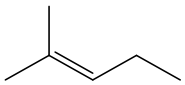
23DMB2N	23DMB1N	33DMB1N	nH	2MP2N

- Products corresponding to oligomerization of 23DMB2N (and isomers) leading to $C_{12}H_{24}$ alkenes
- Products corresponding to hydrogenation of 23DMB2N (and isomers) leading to alkanes (Table 10)
  2,3-dimethylbutane (23DMB), 2,2-dimethylbutane (22DMB), n-hexane (nH)and 2methylpentane (2MP)

Table 10. Alkane products identified from the hydrogenation of 23DMB2N ad isomers.

Products			
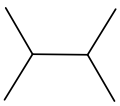	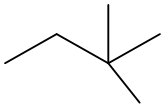	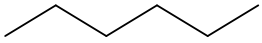	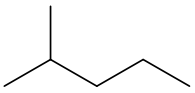
23DMB	22DMB	nC_6	2MP

- Products corresponding to the reaction of 3MT with 23DMB2N (and isomers) leading to alkythiophene compounds (Table 7):
  Alkylthiophene ($C_{11}H_{18}S$), Alkylthiophene tetrahydrogenated ($C_{11}H_{22}S$) and alkene $C_{11}H_{22}$
- Products corresponding to the reaction of 23DMB2N or isomers with H_2S leading to C6-thiols, $C_6H_{14}S$.

Figure 8 presents the selectivity of the main transformation products of (23DMB2N+23DMB1N). At iso-conversion of the 23DMB2N, it can be noted that a similar product selectivity distribution. Regardless the Co/Mo ratio and 3MT conversion, HYDO products (23DMB) is the major product observed. Formation of isomers compounds (33DMB1N, HN, 2MP2N) of (23DMB2N+23DMB1N), is approximatively 30-50 times lower than the formation of 23DMB.

Moreover, side reactions occur leading to $C_{12}H_{24}$ products from oligomerization of 23DMB2N (or 23DMB1N), alkylthiophene $C_{11}H_{18}S$ and its resulting products ($C_{11}H_{22}S$, $C_{11}H_{22}$), with respectively a selectivity less than 5% and 0.5%.

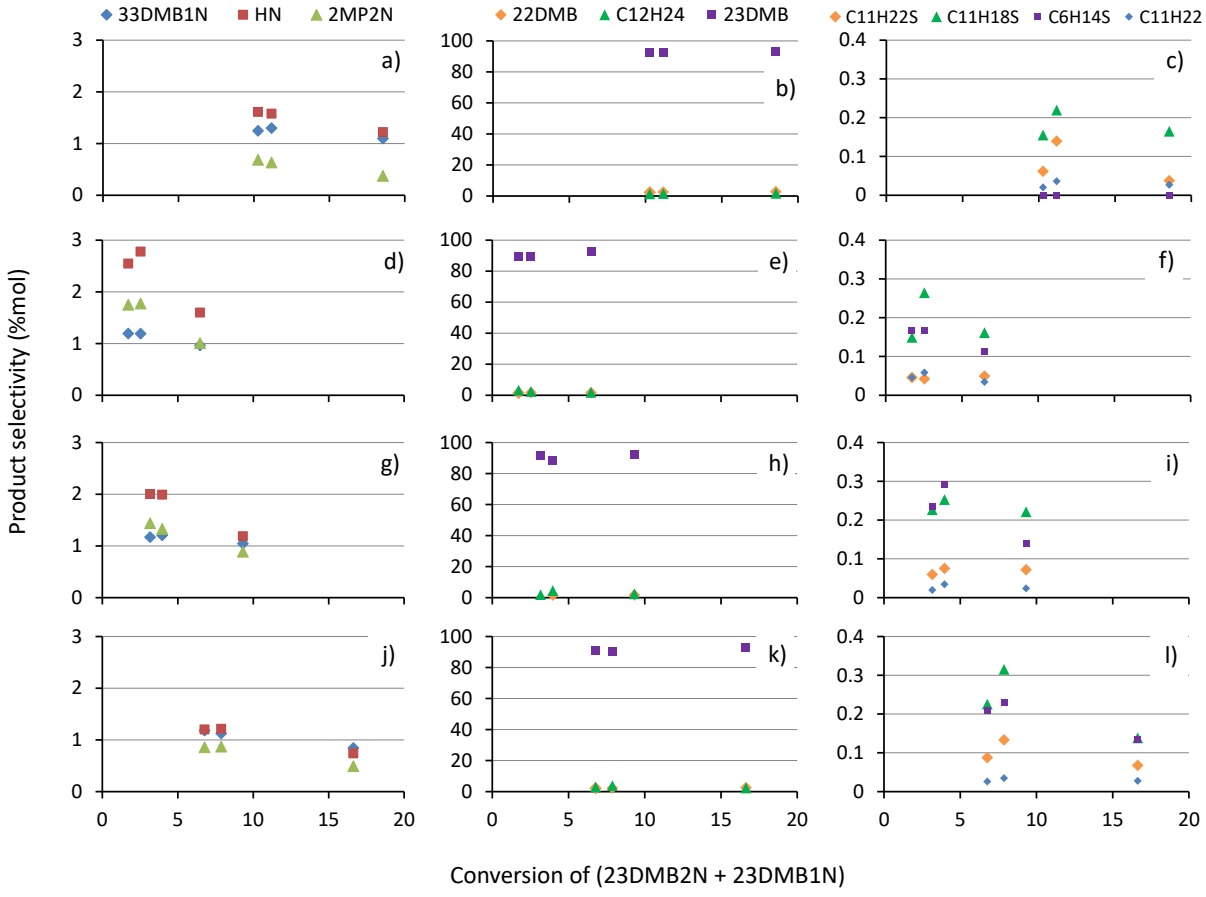

Figure 8. Selectivity of 3MT products of MoS_2 (a,b,c) and CoMoS/$\delta\theta$-Al_2O_3 at iso-dMo of 2.2 at.nm^{-2} of support, (d,e,f) Co/Mo=0.1, (g,h,i) Co/Mo=0.2, (j,k,l) Co/Mo=0.4 at 210 °C. Graphs in the center represent the product distribution of alkane from hydrogenation reaction of (23DMB2N+23DMB1N). Graphs on the right represent the product distribution heavy alkylthiophenes and hydrogenated products from 3MT side reaction with (23DMB2N+23DMB1N) olefins.

Over silica supported catalyst (Appendix 9), the selectivity is towards to the major HYDO products, 23DMB (~80%) for the $MoS_2/\delta\theta$-SiO_2 whereas the selectivity is lower for CoMoS/$\delta\theta$-SiO_2 at Co/Mo=0.4 (~60%). Moreover, the increase of the Co/Mo ratio (from 0 to 0.4) leads to the formation of $C_{12}H_{24}$ compounds whereas the alkene selectivity is almost constants (33DMB1N, HN).

Thus, HYDrOgenation (HYDO) yield corresponding to the amount of (23DMB2N+23DMB1N) and isomers (33DMB1N, HN or 2MP2N) transformed in alkanes can be determined as function of the contact time. (Table 11). Plots associated are reported in the Appendix 7 and Appendix 8.

Table 11. HYDO yields at iso-contact time (τ_{Mo}/3MT) of MoS_2 and CoMoS on $\delta\theta$-Al_2O_3 and SiO_2 at iso-dMo of 2.2 at.nm^{-2} of support at Co/Mo ratio from 0 to 0.4 at 210°C.

	Co/Mo	$\tau_{Mo,\ 3MT}$ (h)	HYDO (%mol)
$MoS_2/\delta\theta$-Al_2O_3	0	1.4	13
CoMoS/$\delta\theta$-Al_2O_3	0.1	1.7	9
	0.2	1.7	11
	0.4	1.7	18
MoS_2/SiO_2	0	11.0	18
CoMoS/SiO_2	0.4	11.0	4

As previously observed for the (23DMB2N+23DMB1N) conversion at iso-$\tau_{Mo/23DMB2N}$, the HYDO yields decreases slightly from unpromoted to low Co/Mo ratio (by a factor 1.4) following by a slight increase of HYDO yields at the highest Co/Mo ratio equal to 0.4 (by a factor 1.5) .

For silica supported catalyst, the increase of the Co/Mo ratio from 0 to 0.4 leads to a decrease of the HYDO (by a factor 4.2) essentially due to the formation $C_{12}H_{24}$ product at the expanse of the 23DMB formation, major HYDO products (Appendix 8).

3.1.2 HDS/HYDO selectivity

In the field of FCC gasoline hydroprocessing, not only HDS activity is one parameter of prior importance but HDS/HYDO selectivity, $S_{HDS/HYDO}$, is also a key parameter. The HYDO yield is plotted as a function of the HDS yield for alumina and silica supported catalysts at each dMo at 220°C and various contact times (respectively Figure 9 and Appendix 8). Thus, the HDS/HYDO selectivity can be evaluated. The highest the HDS yield and the lowest the HYDO yield is, the highest will be the HDS/HYDO selectivity of the CoMoS supported catalysts.

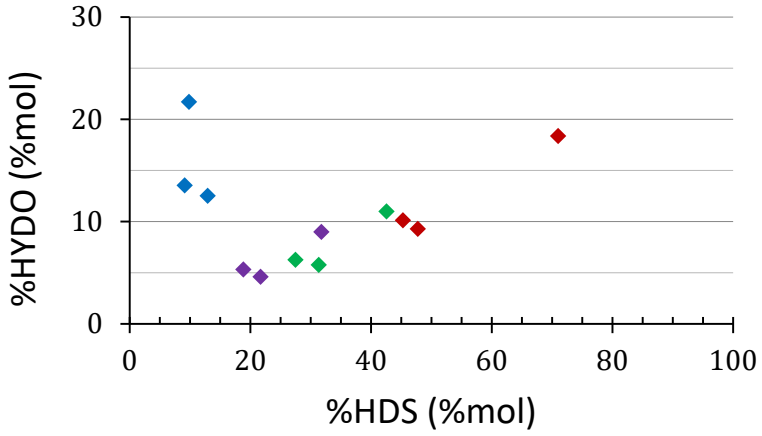

Figure 9. Selectivity between the HDS and the HYDO reactions of $MoS_2/\delta\theta\text{-}Al_2O_3$ (blue) and $CoMoS/\delta\theta\text{-}Al_2O_3$ at iso-dMo of 2.2 at.nm^{-2} of support, Co/Mo=0.1 (purple), Co/Mo=0.2 (green) and Co/Mo=0.4 (red), at 210 °C.

Thus, it can be noted that the $MoS_2/\delta\theta\text{-}Al_2O_3$ exhibits a HDS/ HYDO selectivity significantly lower compared with $CoMoS/\delta\theta\text{-}Al_2O_3$ regardless the Co/Mo ratio. Moreover, the HDS/ HYDO selectivity is constant or increases slightly with the increase of the Co/Mo ratio from 0.1 to 0.4.

Regarding the MoS_2/SiO_2 and $CoMoS/SiO_2$, same evolution of the selectivity is observed than for $\delta\theta\text{-}Al_2O_3$ supported catalyst with the Co/Mo ratio variation. (Appendix 8).

3.2 Support effect

The support effect has been evaluated on CoMoS active phase for $\gamma\text{-}Al_2O_3$, $\delta\theta\text{-}Al_2O_3$, SiO_2 at various dMo of 0.9, 2.2 and 3.8 at.nm^{-2} of support with a feedstock composed of 3MT (0.33 %wt) and 23DMB2N (10 %wt) in n-heptane at 220°C. In order to evaluate the support effect on the 3MT and (23DMB2N+23DMB1N) conversion as well as on the HDS and HYDO

reactions and on the associated selectivity, i.e experimental points obtained in the same HDS and HYDO ranges, comparison of each CoMoS catalyst has been performed at 220°C (493K). For sake of clarity, experimental results of the CoMoS catalysts at iso-dMo 2.2 at.nm^{-2} will be presented in what follows while the cases of other dMo will be discussed and corresponding figures will be reported in Appendix 10-14.

3.2.1 Evolution of 3MT and (23DMB2N+23DMB1N) conversions

3MT and (23DMB2N+23DMB1N) conversions of CoMoS/support at dMo 2.2 at 220 °C have been plotted as function of the contact time, $\tau_{Mo/reactant,}$ in Figure 10. It is observed at iso-$\tau_{Mo/reactant}$ similar conversions for a γ- and $\delta\theta$-Al_2O_3 supported CoMoS catalysts with a slightly higher conversion for CoMoS on $\delta\theta$-Al_2O_3. Silica supported CoMoS catalyst exhibits much lower 3MT and (23DMB2N+23DMB1N) conversions compared with γ- and $\delta\theta$-Al_2O_3 supported CoMoS catalysts.

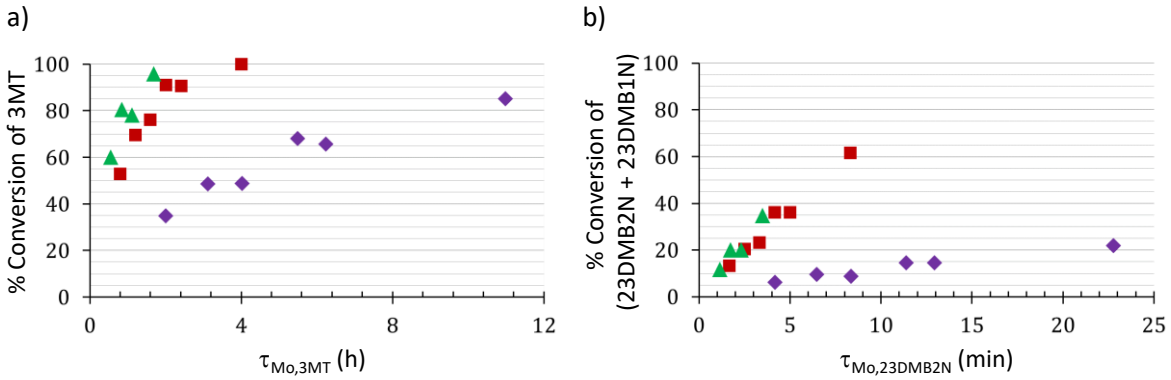

Figure 10. a) 3MT and b) (23DMB2N+23DMB1N) conversions vs. $\tau_{Mo/reactant}$ of CoMoS on γ-Al_2O_3 (red), $\delta\theta$-Al_2O_3 (green) and SiO_2 (purple) at dMo 2.2 at 220 °C.

These results can be also analyzed in terms of initial activities related to the 3MT (a_{3MT}) and (23DMB2N+23DMB1N) ($a_{(23DMB2N+23DMB1N)}$) in order to attempt to correlate catalytic performances and catalyst features in the next chapter IV. Initial activities are expressed as the number of consumed moles of 3MT (or (23DMB2N+23DMB1N)) by mole of Mo and by second. Initial activities (mol$_{(3MT\ or\ (23DMB2N+23DMB1N))}$. mol of Mo^{-1}.s^{-1}) are reported in the Table 12. For all catalysts, it can be first noticed that the reactivity of (23DMB2N+23DMB1N) is much more important than the one of 3MT. Over silica-based catalysts, reactivity of both reactants decrease around one order magnitude compared to alumina-based catalysts. Thus, activities of the catalysts related to 3MT and (23DMB2N+23DMB1N) conversions are increasing at iso-$\tau_{Mo/reactant}$ in the following order:

$$CoMoS/SiO_2 < CoMoS/\gamma\text{-}Al_2O_3\ CoMoS/\gamma\text{-}Al_2O_3 \leq CoMoS/\delta\theta\text{-}Al_2O_3$$

Same trend is observed for the 3MT and (23DMB2N+23DMB1N) conversions at dMo equal to 0.9 and 3.8 at.nm^{-2} of support (Appendix 10).

Table 12. Initial activities related to the 3MT and (23DMB2N+23DMB1N) conversions respectively a_{3MT} and $a_{(23DMB2N+23DMB1N)}$. Relative uncertainties to consider for the initial activity, a_{3MT} and $a_{(23DMB2N+23DMB1N)}$ values are ±20%.

dMo (at.nm^{-2} of support)	Supports	a_{3MT} (mol $_{3MT}$. mol of Mo $^{-1}$.s^{-1})	$a_{(23DMB2N+23DMB1N)}$ (mol $_{(23DMB2N+23DMB1N)}$. mol of Mo $^{-1}$.s^{-1})	$S_{3MT/(23DMB2N+23DMB1N)}$ ($a_{3MT}/a_{(23DMB2N+23DMB1N)}$)
0.9	γ-Al_2O_3	0.044	0.255	0.17
	$\delta\theta$-Al_2O_3	0.052	0.284	0.18
	SiO_2	0.007	0.025	0.26
2.2	γ-Al_2O_3	0.023	0.165	0.14
	$\delta\theta$-Al_2O_3	0.035	0.214	0.16
	SiO_2	0.006	0.021	0.26
3.8	γ-Al_2O_3	0.016	0.108	0.15
	$\delta\theta$-Al_2O_3	0.028	0.167	0.17
	SiO_2	0.004	0.014	0.26

As previously mentioned, it is interesting to study the selectivity between both reaction of conversion of 3MT and 23DMB2N. Thus, The (23DMB2N+23DMB1N) conversion is plotted as a function of the 3MT conversion for γ-, $\delta\theta$- alumina and silica catalysts at each dMo at 220°C and various contact times (Figure 11). It can be noted that at low an high dMo, the experimental points lay on the same curve regardless the support with perhaps a selectivity slightly higher towards the 3MT conversion for silica-based catalysts. However, at intermediate dMo, 3MT/(23DMB2N+23DMB1N) selectivity is slightly higher for a silica and $\delta\theta$-Al_2O_3 supported catalysts compare with CoMoS/γ-Al_2O_3.

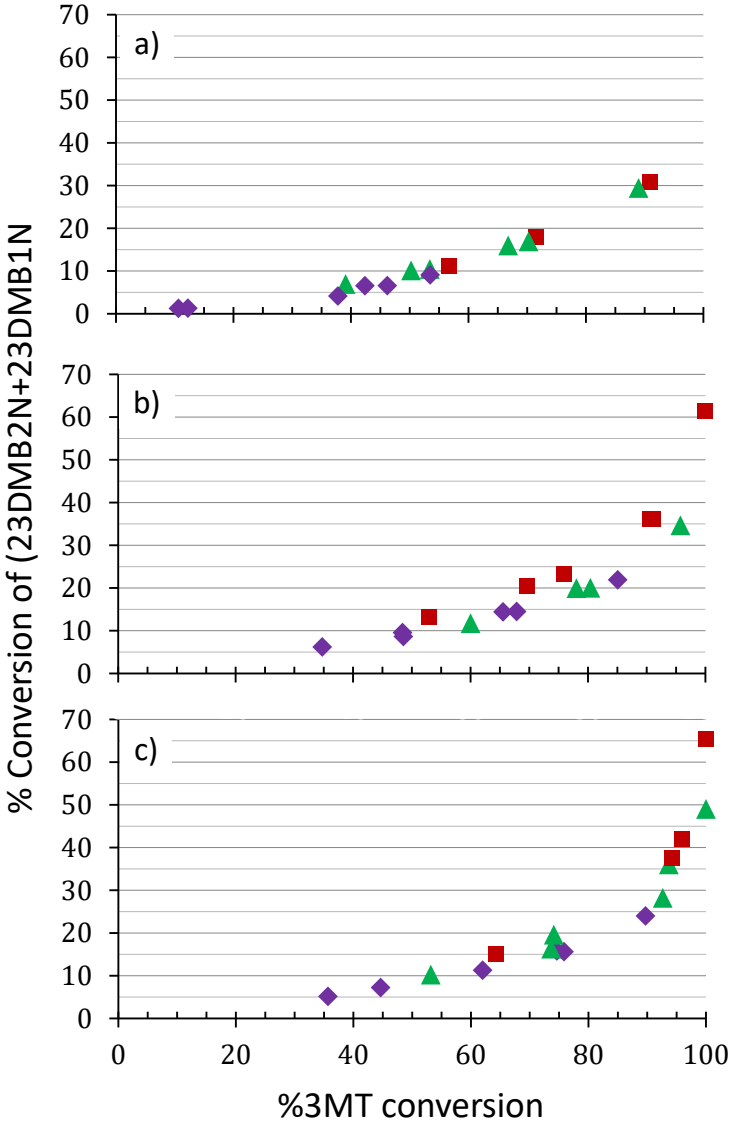

Figure 11. Selectivity between the 3MT and (23DMB2N+23DMB1N) conversions of CoMoS on γ-Al_2O_3 (in red), δθ-Al_2O_3 (in green) and SiO_2 (in purple) at iso-dMo of (a) 0.9, (b) 2.2 and (c) 3.8 at.nm^{-2} of support.

The $S_{3MT/(23DMB2N+23DMB1N)}$ as is reported Table 12. It can be noted, silica-based catalyst reach higher relative $S_{3MT/(23DMB2N+23DMB1N)}$ toward 3MT conversion compared with alumina-based catalysts.

However, even if the calculated $S_{3MT/(23DMB2N+23DMB1N)}$ of silica-based catalyst is significantly higher compared with alumina-based catalysts, it has to be borne in mind that these initial selectivity and activity calculations are based on an extrapolation of the experimental points which could introduce an important error if the activities are not calculated with experimental points in the same range of conversion. Thus, the orders of selectivity between

catalysts need to be considered carefully in respect of the experimental curves ((23DMB2N+23DMB1N) vs 3MT conversions).

In the next section, we will address more insights into the transformation of 3MT and (23DMB2N+23DMB1N) and the products distribution observed as a function of the catalytic support and Mo loading.

3.2.2 Product distributions

3.2.2.1 Products from 3MT transformation

Figure 12 (and Appendix 11) presents the selectivity of the main transformation products of 3MT for CoMoS on γ-, δθ-Al_2O_3 and SiO_2 at dMo 2.2 at 220°C. Over all catalyst, HDS products (2MB, 2MB2N and 2MB1N) are the major products observed regardless the 3MT conversion. Two important differences appear in the product selectivity of the 3MT transformation between alumina and silica supported catalysts. First, on silica supported catalysts, the amount of heavy alkylthiophenes (such as $C_{11}H_{18}S$) is significant compared with alumina supported catalysts, mostly at low conversion (4 times higher regardless the 3MT conversion between 50-90%). Moreover, regarding aluminas-based catalysts, products selectivity shows that

CoMoS/δθ-Al_2O_3 is less likely to form the $C_{11}H_{18}S$ alkylthiophene and its resulting hydrogenating and desulfurization products ($C_{11}H_{22}S$, $C_{11}H_{22}$) than CoMoS/γ-Al_2O_3. (noted that hydrogenated alkylthiophene could also be formed from the reaction of 23DMB2N (or its isomers) with 3MTHT).

The second important experimental result is related to alkane/alkene proportion on HDS products (2MB/(2MB1N+2MB2N)) which is decreasing at higher conversion for CoMoS/SiO_2 whereas it is increasing for CoMoS/γ, δθ-Al_2O_3. This difference points out the lower hydrogenation ability of silica-supported catalyst compared to alumina supported ones. Thus, different features of the catalyst (acidity of the support: Brønsted and Lewis sites, morphology of the CoMoS phase, edge nature) may be invoked to be at the origin of these different catalytic properties, although it remains difficult to identify the single one which is responsible. Nevertheless, it could be suggested that HDS of 3MT is similar on silica and alumina supported catalyst due to the presence of the CoMoS phase as it is well known but

once the alkene formed, difference of acidity of the support could play a key role. Indeed, Brunet et al.[7] suggest that higher is the acidity of the support and higher is expected the hydrogenation activity of alkene.

More specifically focused on the alumina-based catalysts, it can be observed that at iso-conversion the alkene/alkane selectivity is higher on CoMoS/$\delta\theta$-Al_2O_3 than on CoMoS/γ-Al_2O_3. Thus, for alumina supported catalysts, it may suggest that support (difference of Brønsted and Lewis sites) could impact the reactant adsorption, especially adsorption of alkene intermediate; adsorption properties being related to the different hydroxyl features of the two alumina supports. As a consequence of the formation of $\delta\theta$-Al_2O_3 suspected to be the result from the sintering of γ-Al_2O_3 particles, nature and distribution of the hydroxyl are different between both aluminas. This difference will be discussed in more details in the chapter IV on the basis of the IR analysis of the two supports. It will be shown in particular that γ-Al_2O_3 exhibit more acidic hydroxyl groups than θ-Al_2O_3 where neutral hydroxyls are predominant. If so, the olefin adsorption is lower on CoMoS/$\delta\theta$-Al_2O_3 than on CoMoS/γ-Al_2O_3, which may explain the higher selectivity observed in olefin products on $\delta\theta$-Al_2O_3. Specific experiments and discussions will be provided in chapter IV and VI. Regarding the other sulphided products, the selectivity is comparable between alumina and silica supported catalysts.

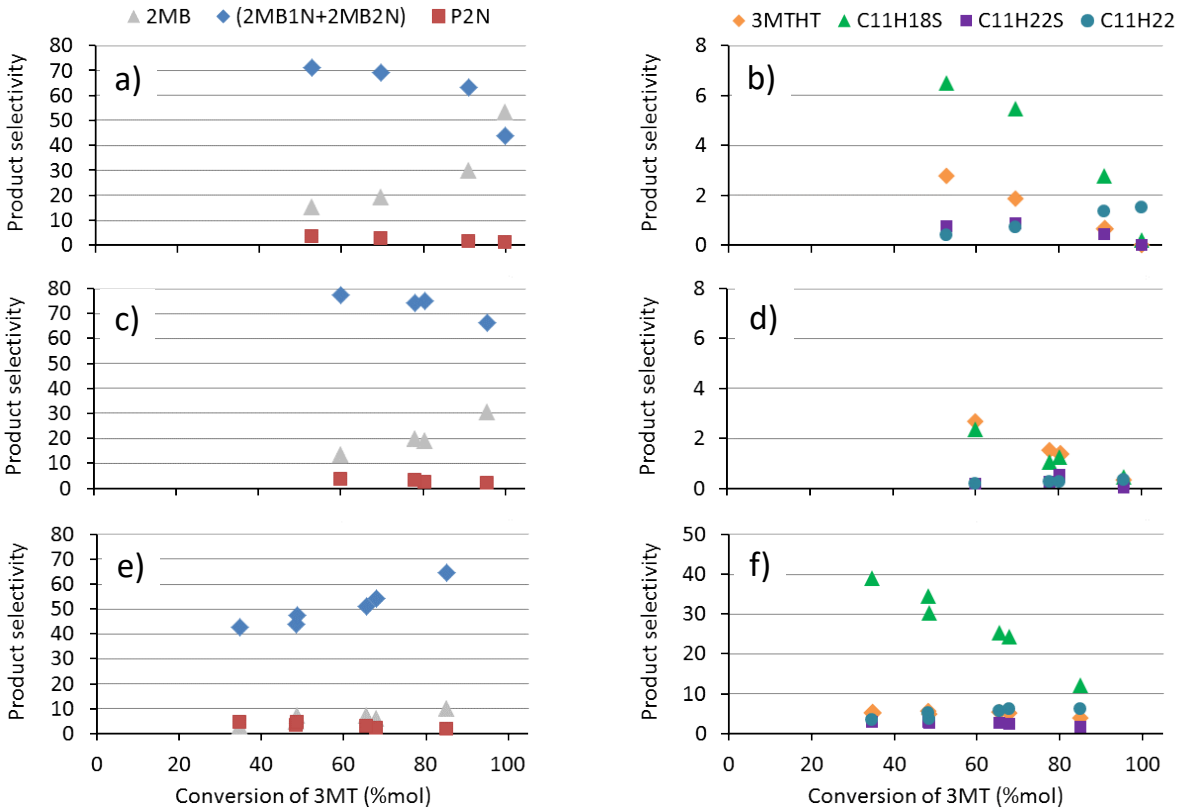

Figure 12. Product selectivity of the 3MT transformation for CoMoS on (a,b) γ-Al_2O_3, (c,d) δθ-Al_2O_3, (e,f) SiO_2 at iso-dMo of 2.2 at.nm^{-2} of support (T=220°C). Graphs on the left represent the product distribution of alkanes and alkene from the complete desulfurization of 3MT. Graphs on the right represent the product distribution of 3MTHT from the hydrogenation of 3MT and alkylthiophene from 3MT side reaction with (23DMB2N+23DMB1N) olefins.

As previously mentioned, HDS yield can be determined and plotted as function of the contact time, $\tau_{Mo/3MT}$ (Figure 13 and Appendix 12). This more correct analysis takes now into account the amount of residual sulfided compounds identified in Figure 12, which was not the case in our previous analysis of the 3MT conversion.

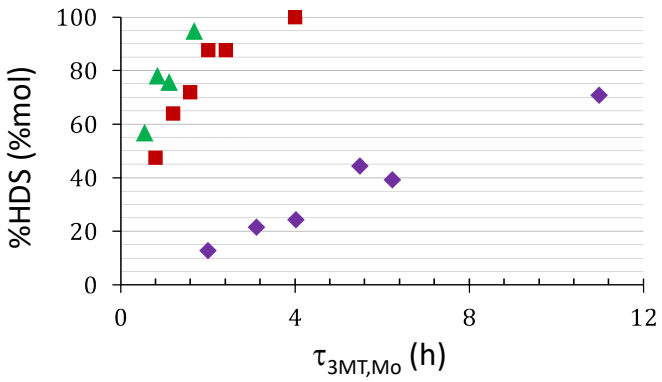

Figure 13. HDS yield as function of the contact time for CoMoS on γ-Al_2O_3 (red), δθ-Al_2O_3 (green), SiO_2 (purple) at iso-dMo of 2.2 at.nm^{-2} of support at 220°C.

As previously observed for the 3MT conversion, it is observed at iso-$\tau_{Mo/3MT}$ similar HDS yield for γ- and $\delta\theta$-Al_2O_3 supported CoMoS catalysts with a slightly higher HDS for CoMoS on $\delta\theta$-Al_2O_3. Silica supported CoMoS catalyst exhibits a much lower HDS yield than γ- and $\delta\theta$-Al_2O_3 supported CoMoS catalysts. Thus, HDS is increasing at iso-$\tau_{Mo/reactant}$ in the following order:

$$CoMoS/SiO_2 << CoMoS/\gamma\text{-}Al_2O_3 < CoMoS/\delta\theta\text{-}Al_2O_3.$$

As previously shown, these results can be understood in term of HDS initial activity, $a_{HDS,}$ expressed as consumed mole of 3MT converted in desulfurized products by mole of Mo and by second. Table 13 presents a_{HDS} for each catalyst at dMo of 0.9, 2.2 and 3.8 at.nm^{-2} of support.

Table 13. Activities related to 3MT converted into desulfurized products, a_{HDS}. Relative uncertainties to be considered for the HDS initial activity values are ±20%.

dMo (at.nm^{-2} of support)	Supports	a_{HDS} (mol $_{3MT}$. mol of Mo $^{-1}$.s^{-1})
0.9	γ-Al_2O_3	0.044
	$\delta\theta$-Al_2O_3	0.048
	SiO_2	0.003
2.2	γ-Al_2O_3	0.020
	$\delta\theta$-Al_2O_3	0.032
	SiO_2	0.002
3.8	γ-Al_2O_3	0.014
	$\delta\theta$-Al_2O_3	0.026
	SiO_2	0.002

Regardless the dMo, the HDS initial activity of CoMoS/SiO_2 is approximatively 10 times lower than the alumina supported catalysts. Moreover, CoMoS/$\delta\theta$-Al_2O_3 shows a higher HDS initial activity than CoMoS/γ-Al_2O_3 when the dMo is higher whereas at low dMo the HDS initial activity is almost identical. Indeed, HDS initial activity is about 2 times higher on $\delta\theta$-Al_2O_3 than on γ-Al_2O_3 for the higher dMo. Moreover, this highest intrinsic HDS initial activity of CoMoS catalyst over low surface area alumina is scarcely reported in the literature and our results confirm the observation made by Laurenti et al[8]

3.2.2.2 Products from 23DMB2N transformation

Figure 14 (and Appendix 13) presents the selectivity of the main transformation products of (23DMB2N+23DMB1N). Two important differences appear in the product selectivity of the (23DMB2N+23DMB1N) between alumina and silica supported catalysts. As already observed for products distribution of 3MT, the amount of $C_{11}H_{18}S$ is significant higher on silica than on alumina supported catalysts (between 10 and 2 times higher as function of the (23DMB2N + 23DMB1N) conversion from 0 to 20% respectively). Moreover, $C_{12}H_{24}$ products from oligomerization of 23DMB2N (or 23DMB1N) exhibit a selectivity around 25% for $CoMoS/SiO_2$ whereas the selectivity is less than 5% for alumina supported catalysts regardless the (23DMB2N + 23DMB1N) conversion.

Regarding the hydrogenated products, it can be noted that the selectivity in 23DMB is higher for CoMoS/γ, $\delta\theta$-Al_2O_3 than for silica supported catalyst. However, formation of isomers compounds of (23DMB2N+23DMB1N) (33DMB1N, HN, 2MP2N) is approximatively 10 times higher for $CoMoS/SiO_2$ compare with CoMoS/γ, $\delta\theta$-Al_2O_3.

Thus, all these observations suggest again that different features of the catalyst is engaged (Brønsted, Lewis acidity, morphology of the CoMoS phase, edge nature) leading to catalytic properties significantly different as previously mentioned in the section 3.2.2.1, product from 3MT transformation.

For alumina supported catalysts, products selectivity shows that CoMoS/$\delta\theta$-Al_2O_3 is less likely to form the alkylthiophene $C_{11}H_{18}S$ and its resulting products ($C_{11}H_{22}S$, $C_{11}H_{22}$) than CoMoS/γ-Al_2O_3 as already mentioned. Moreover, it can be observed that the selectivity in 23DMB2N isomers (33DMB1N, HN) is higher for CoMoS/γ-Al_2O_3 but the selectivity of 23DMB is slightly lower than for CoMoS/$\delta\theta$-Al_2O_3. Thus, for alumina supported catalyst, it may suggest that the support could impact the reactant adsorption, especially adsorption of alkene intermediate. Adsorption properties could be thus related to the different hydroxyl features of the alumina supports. The support by interacting differently with the CoMoS phase could also modulate its properties.

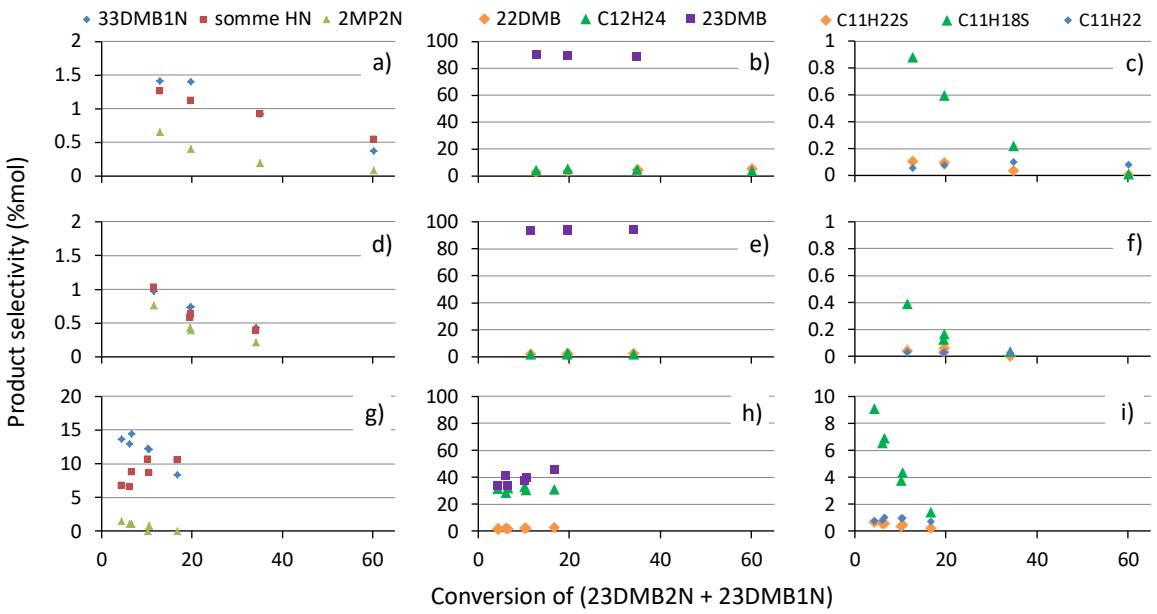

Figure 14. Products selectivity of the (23DMB2N+23DMB1N) transformation for CoMoS on (a,b,c) γ-Al_2O_3, (d,e,f) δθ-Al_2O_3, (g,h,i) SiO_2 at iso-dMo of 2.2 at.nm^{-2} of support at 220°C. Graphs on the left represent the product distribution of isomers of 23DMB2N. Graphs in the center represent the product distribution of alkane from hydrogenation reaction of (23DMB2N+23DMB1N). Graphs on the right represent the product distribution heavy alkylthiophenes and hydrogenated products from 3MT side reaction with (23DMB2N+23DMB1N) olefins.

Thus, HYDO yield corresponding to the amount of (23DMB2N+23DMB1N) and isomers (33DMB1N, HN or 2MP2N) transformed in alkanes can be determined and plotted as function of the contact time, $\tau_{Mo/23DMB2N}$ (Figure 15 and Appendix 14).

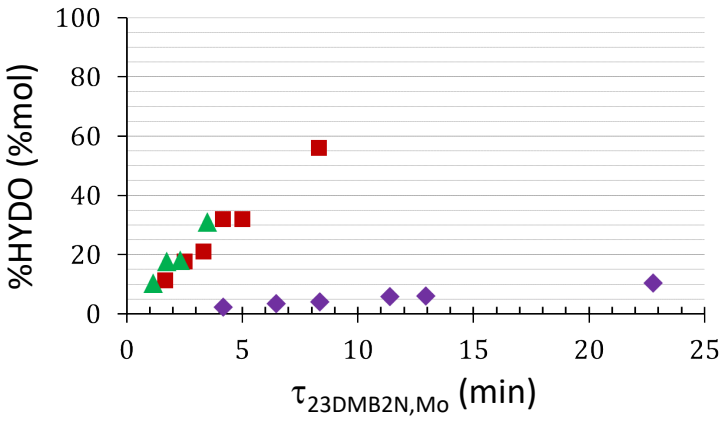

Figure 15. HYDO yield as function of the contact time for CoMoS on γ-Al_2O_3 (red), δθ-Al_2O_3 (green), SiO_2 (purple) at iso-dMo of 2.2 at.nm^{-2} of support at 220°C.

As previously observed for the (23DMB2N+23DMB1N) conversion, it is observed at iso-$\tau_{Mo/23DMB2N}$ similar HYDO yield for γ- and $\delta\theta$-Al_2O_3 supported CoMoS catalysts with a slightly higher HYDO for CoMoS on $\delta\theta$-Al_2O_3. Silica supported CoMoS catalyst exhibits a much lower HYDO yield compare with γ- and $\delta\theta$-Al_2O_3 supported CoMoS catalysts. Thus, the HYDO is increasing at iso-$\tau_{Mo/reactant}$ in the following order:

$$CoMoS/SiO_2 << CoMoS/\gamma\text{-}Al_2O_3 = CoMoS/\delta\theta\text{-}Al_2O_3.$$

Again, these results can be understood in term of HYDO activities, a_{HYDO}, expressed as consumed mole of 23DM2N converted in alkane products (23DMB and 22DMB) by mole of Mo and by time unit (second). Table 14 presents a_{HYDO} for each catalyst at dMo of 0.9, 2.2 and 3.8 at.nm^{-2} of support on various supports.

Table 14. Activities related to the (23DMB2N+23DMB1N) convert in hydrogenated products, a_{HYDO}. Relative uncertainties to consider for the HYDO initial activity values are ±20%.

dMo (at.nm^{-2} of support)	Supports	a_{HYDO} (mol $_{23DMB2N + 23DMB1N}$. mol of Mo $^{-1}$.s^{-1})
0.9	γ-Al_2O_3	0.215
	$\delta\theta$-Al_2O_3	0.215
	SiO_2	0.013
2.2	γ-Al_2O_3	0.141
	$\delta\theta$-Al_2O_3	0.191
	SiO_2	0.009
3.8	γ-Al_2O_3	0.092
	$\delta\theta$-Al_2O_3	0.139
	SiO_2	0.010

As reported previously for the HDS initial activity, regardless the iso-dMo, the HYDO initial activity of $CoMoS/SiO_2$ is approximatively 10-20 times lower than the alumina supported catalysts. Moreover, as reported previously for HDS reaction, whereas at low iso-dMo the HYDO intrinsic initial activity is similar for both alumina-based catalysts, $CoMoS/\delta\theta$-Al_2O_3 shows a higher HYDO initial activity than $CoMoS/\gamma$-Al_2O_3 at higher iso-dMo. This means that the impact of the loading is more pronounced on γ-Al_2O_3 than on /$\delta\theta$-Al_2O_3.

3.2.3 HDS/HYDO selectivity

The HYDO yield is plotted as a function of the HDS yield for alumina and silica supported catalysts at each dMo at 220°C and various contact times (Figure 16).

It is observed that the experimental points lay on the same curve at iso-dMo of 0.9 at.nm^{-2} regardless the support. Indeed, at 40% of HDS, CoMoS/SiO_2 and CoMoS/$\delta\theta$-Al_2O_3 show a similar HDS/HDO selectivity. Between 40 and 90% of HDS, γ- and $\delta\theta$-Al_2O_3 supported catalysts have also a similar HDS/ HYDO selectivity. It indicates no significant support effect on the selectivity between CoMoS on γ - $\delta\theta$ and SiO_2 at low molybdenum loading.

At higher dMo, HDS/HYDO selectivity is similar in the [0-40]% HDS range. However, CoMoS/SiO_2 exhibits an improvement of the HDS/HYDO selectivity at 70-75% of HDS compare with alumina supported catalyst (%HDS $\sim$ 10% at 70%). Due to the low activity of silica based catalysts, higher HDS yield have not been reached in these operatory conditions. Between alumina supported catalysts, CoMoS/$\delta\theta$-Al_2O_3 shows a slight enhancement (5-7%) compared with CoMoS/γ-Al_2O_3 at high HDS yield (≥ 80%).

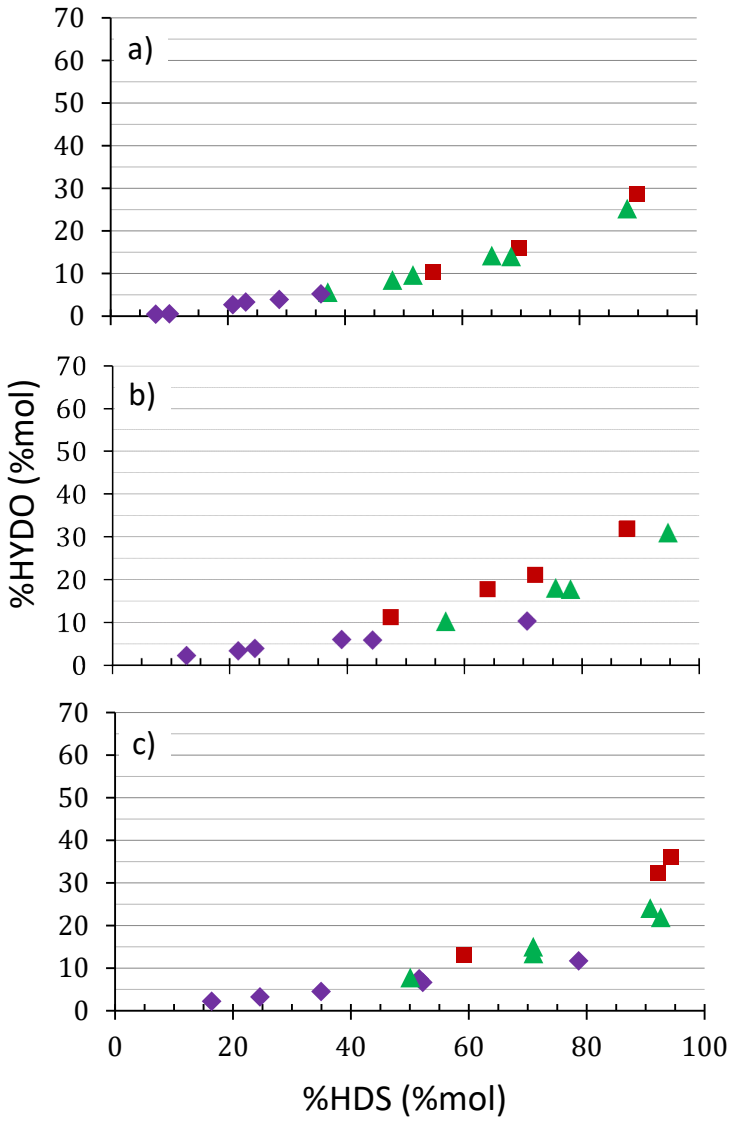

Figure 16. Selectivity between the HDS and the HYDO reactions of CoMoS on γ-Al_2O_3 (in red), δθ-Al_2O_3 (in green) and SiO_2 (in purple) at iso-dMo of (a) 0.9, (b) 2.2 and (c) 3.8 at.nm^{-2} of support.

For industrial application purpose, HDS/HYDO selectivity must be evaluated over the required range of HDS conversion especially between 75 and 100%. In these conditions, it appears the HDS/HYDO selectivity of CoMoS catalysts at 220°C evolves in the following order, depending on the support: SiO_2 ≥ δθ-Al_2O_3 ≥ γ-Al_2O_3. These results confirm literature observation on the high selectivity of silica-based catalyst compared to alumina ones at high HDS .[9,10] Moreover, this higher HDS/HYDO selectivity on silica support can be interpreted according the literature. Indeed, it is well known that 3MT has a strong inhibitor effect on the 23DMB2N reactant adsorption over alumina supported catalyst and so on the HYDO reaction (i.e. $E_{ads,3MT} > E_{ads,23DMB2N}$ [11,12]). However, this inhibition effect is seems to be less pronounced for CoMoS on SiO_2 as shown by the adsorption competition between 3MT and

23DMB2N reported in Appendix 19. Thus, due to the lower adsorption of alkene on silica, a lower level of HYDO is observed with respect to alumina supported catalyst.

As previously presented, HDS/HYDO selectivity can be expressed as the ratio of the HDS and HYDO initial activity (Table 15), a_{HDS}/a_{HYDO} in order to make the link with the features of the catalyst, especially of the CoMoS phase in the following chapter IV. As previously, similar conclusion can be formulated regarding the order of selectivity as function of the support.

Table 15. HDS/HYDO selectivity, a_{HDS}/a_{HYDO}, for CoMoS on γ-Al_2O_3, $\delta\theta$-Al_2O_3, SiO_2 at each dMo at 220°C. Relative uncertainties to consider for the HYDO initial activity values are ±40%.

dMo (at.nm^{-2} of support)	Supports	a_{HDS}/a_{HYDO}
0.9	γ-Al_2O_3	0.20
	$\delta\theta$-Al_2O_3	0.22
	SiO_2	0.23
2.2	γ-Al_2O_3	0.14
	$\delta\theta$-Al_2O_3	0.17
	SiO_2	0.22
3.8	γ-Al_2O_3	0.15
	$\delta\theta$-Al_2O_3	0.19
	SiO_2	0.20

3.3 Mo coverage effects

The dMo effect has been evaluated on CoMoS active phase for γ-Al_2O_3, $\delta\theta$-Al_2O_3, SiO_2 at various dMo of 0.9, 2.2 and 3.8 at.nm^{-2} of support with a feedstock composed of 3MT (0.33 %wt) and 23DMB2N (10 %wt) in n-heptane. In order to evaluate the dMo effect on the 3MT and (23DMB2N+23DMB1N) conversion as well as HDS and HYDO activities and on the associated selectivity, i.e experimental points obtained in the same HDS and HYDO range, comparison of each CoMoS catalyst has been performed at 220°C (493K).

Experimental results of CoMoS/γ-Al_2O_3 at variable dMo will be presented in the next section and experimental of CoMoS on $\delta\theta$-Al_2O_3 and SiO_2 results will be discussed and report in the Appendix 15-18.

3.3.1 3MT and (23DMB2N+23DMB1N) conversion

3MT and (23DMB2N+23DMB1N) conversions of CoMoS/support at dMo 2.2 at 220 °C have been plotted as function of the contact time, $\tau_{Mo/reactant,}$ in Figure 17. It is observed at iso-$\tau_{Mo/reactant}$ an increase of the conversion with the increase of the dMo for a γ-Al_2O_3 supported CoMoS catalysts. The same trend is observed for $\delta\theta$-Al_2O_3 and SiO_2 supported CoMoS catalysts, but in a less extent. So, over gamma alumina catalyst, the efficiency regarding the 3MT and 23DMBN conversions is more sensitive to the dMo variation between 0,9 and 3,8 at/nm² of support than $\delta\theta$-Al_2O_3 and SiO_2 supported catalysts.

As for the support effect, These results can be understood in term of activities related to the 3MT and (23DMB2N+23DMB1N) conversions. Initial activities, (a_{3MT}) and ($a_{(23DMB2N+23DMB1N)}$), expressed in $mol_{(3MT\ or\ (23DMB2N+23DMB1N))}$.mol of $Mo^{-1}.s^{-1}$ are reported in the Table 12 previously presents in 3.2.1. Regarding the dMo effect on supports, it is noticed a decrease of the intrinsic initial activity for the transformation of both reactants without modification on $a_{3MT}/a_{(23DMB2N+23DMB1N)}$. Moreover, in more details it is revealed that as a function of the increase of the dMo, the intrinsic 3MT initial activity decreases more abruptly on γ-Al_2O_3 (by a factor of ~ 2.7) than on $\delta\theta$-Al_2O_3 and SiO_2 (factor of ~1.8) leading to the difference of HDS activities.

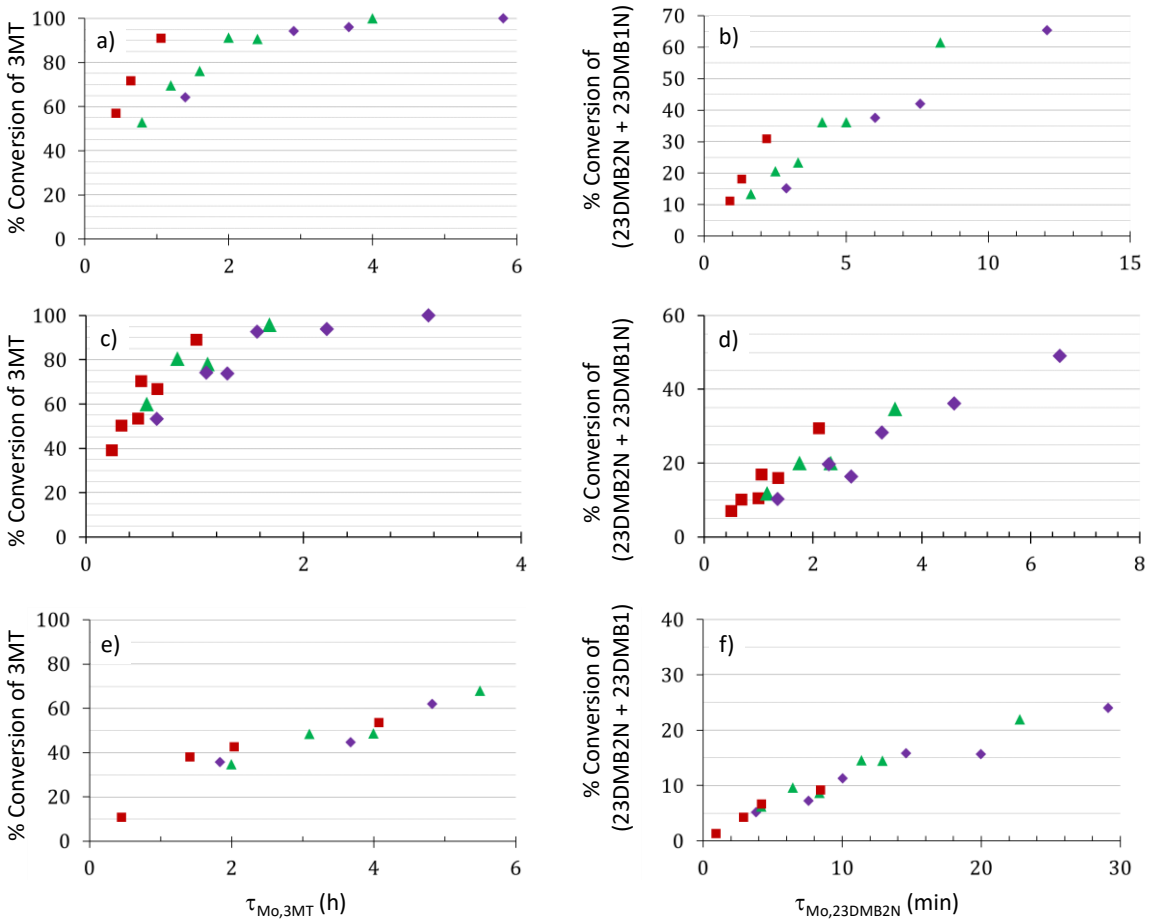

Figure 17. 3MT and (23DMB2N+23DMB1N) conversion vs. $\tau_{Mo/reactant}$ of CoMoS on (a,b) γ-Al_2O_3 (c,d) $\delta\theta$-Al_2O_3 and (e,f) SiO_2 at dMo of 0.9 (red), 2.2 (green) and 3.8 (purple) at.nm^{-2} at 220 °C.

3.3.2 Products distribution

In this section, only the results obtained from gamma alumina-based catalyst are reported due to the highest sensitivity on the Mo loading (or dMo) for these catalyst compared to the two other supports.

3.3.2.1 Products from 3MT transformation

Products formed from 3MT transformation have been already presented in the section 3.2.1. Figure 18 presents the selectivity of the main transformation products of 3MT for CoMoS/γ-Al_2O_3. Regardless the dMo, HDS products (2MB, 2MB1N and 2MB2N) are the major products observed regardless the 3MT conversion as already mentioned in the part 3.2.1. The amount of heavy alkylthiophenes (such as $C_{11}H_{18}S$) is significant for dMo higher than 2.2 whereas at lower dMo alkylthiophene is not present. The increase of the dMo appears to be not significant on the amount of 3MTHT. Regarding the other sulphided products, selectivity is comparable between low and high dMo for alumina and silica supported catalysts. More

specifically on HDS products, at low dMo it can be noticed that the proportion (2MB1N+2MB2N) is higher than at low dMo. Same behavior of products selectivity is observed for CoMoS/δθ-Al_2O_3 (Appendix 15, Figure 48). According to these experimental results, two different hypotheses can be formulated. It may suggest that support could impact the reactant adsorption which could modulate the alkane/alkene. Due to a support proportion higher at low dMo, adsorption properties could be related to the different hydroxyl features of the alumina supports. Otherwise, it cannot be neglected that the properties of the active CoMoS phase could be modified with the dMo change (length, stacking, Co-promotion level on the M- and S-edges). Chapter IV will give a more detail description of the support and active CoMoS phase features.

For silica supported catalysts, the dMo has no significant effect on the 3MTproduct selectivity (Appendix 15, Figure 49).

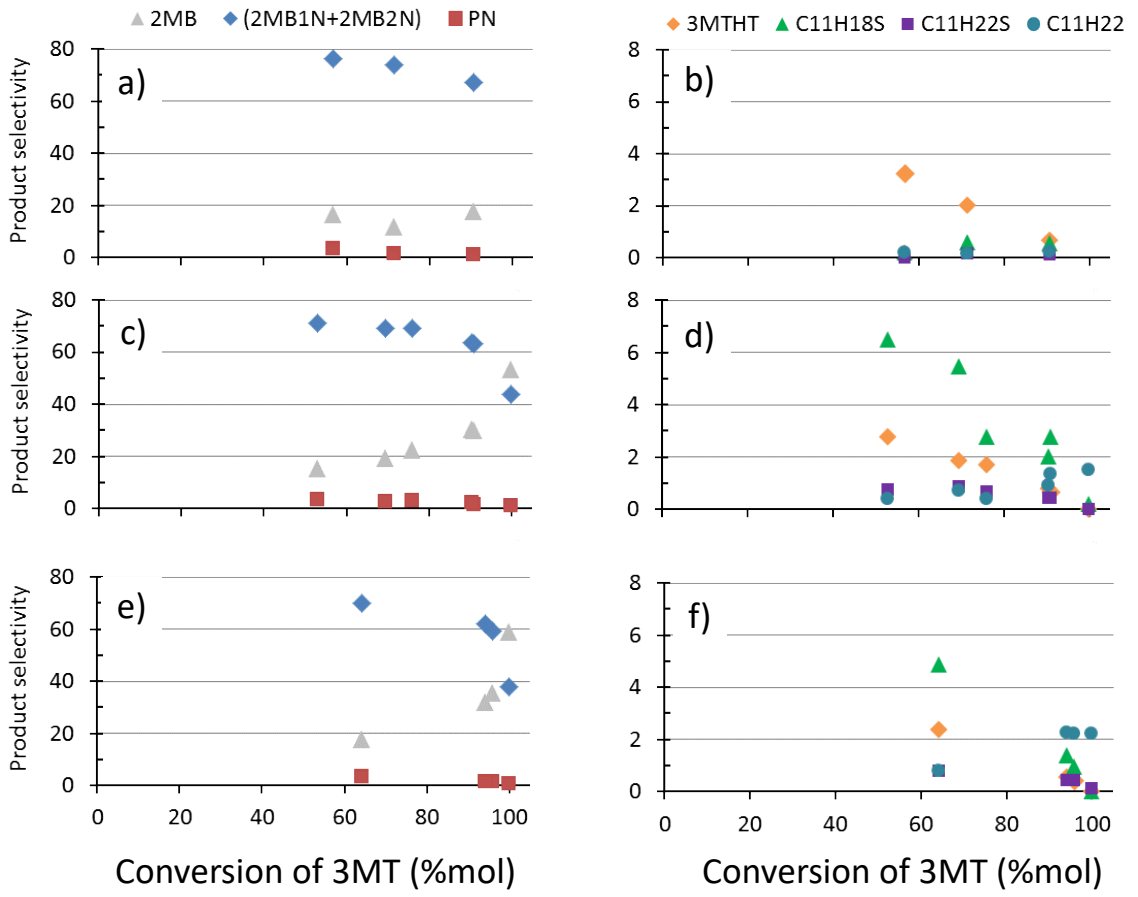

Figure 18. Selectivity of 3MT products for CoMoS/γ-Al_2O_3 at dMo of (a,b) 0.9, (c,d) 2.2, (e,f) 3.8 at.nm^{-2} at 220°C. Graphs on the left represent the product distribution of alkanes and alkene from the complete desulfurization of 3MT. Graphs on the right represent the product distribution of 3MTHT from the hydrogenation of 3MT and alkylthiophene from 3MT side reaction with (23DMB2N+23DMB1N) olefins.

One of the main catalytic parameter concerning the transformation of 3MT is the hydrodesulfurization initial activity. For each dMo, HDS yield, corresponding to the amount of 3MT transformed in product desulfurized (i.e. alkanes and alkenes), can be determined and plotted as function of the contact time, $\tau_{Mo/3MT}$ (Figure 19).

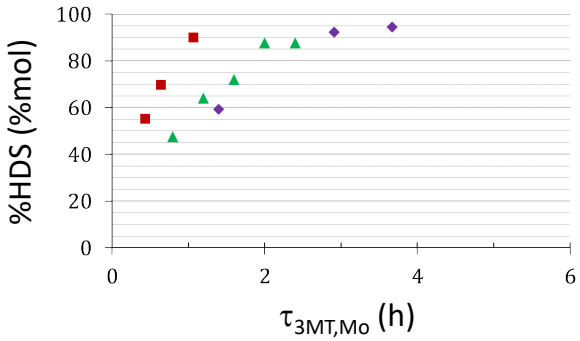

Figure 19. HDS yield as function of the contact time for CoMoS/γ-Al_2O_3 at dMo variable, 0.9 (red), 2.2 (green) and 3.8 (purple) at.nm^{-2} of support at 220°C.

As previously observed for the 3MT conversion, CoMoS/γ-Al_2O_3 shows at iso-$\tau_{Mo/3MT}$ similar HDS yield for the two higher dMo whereas at low dMo, HDS is significantly higher. For CoMoS/γ-Al_2O_3 and for CoMoS/SiO_2, the HDS is nearly constant at iso-$\tau_{Mo/3MT}$ regardless the dMo (Appendix 16, Figure 51, Figure 52).

As already proposed before, these results can be analyzed in term of HDS activities, a_{HDS}, expressed as consumed mole of 3MT converted in desulfurized products by mole of Mo and by second). Table 13 present a_{HDS} for each catalyst at dMo of 0.9, 2.2 and 3.8 at.nm^{-2} of support. It can be noticed that the intrinsic HDS initial activity decreases more abruptly on γ-Al_2O_3 (by a factor of ~ 3.1) than on $\delta\theta$-Al_2O_3 (factor of ~1.8) from the lower to the higher dMo. For silica supported catalysts, the HDS initial activity decreases slightly with the increase of the dMo.

3.3.2.2 Products from (23DMB2N+23DMB1N) transformation

Products formed from (23DMB2N+23DMB1N) transformation have been already presented in the section 3.2.1. Figure 20 presents the selectivity of the main transformation products of (23DMB2N+23DMB1N) for CoMoS/γ-Al_2O at various dMo at 220°C. As already observed for the 3MT product distribution, the amount of $C_{11}H_{18}S$ is low at low dMo and more important at higher dMo. Moreover, at dMo of 0.9, the amount of 23DMB is higher and the selectivity

for the (23DMB2N+23DMB1N) isomers (33DMB1N, HN, 2MP2N) whereas at higher dMo, the selectivity for 23DMB is decreasing and the selectivity for the C_6 alkenes is increasing.

Thus, all these observations suggest that properties of the support and/or the active CoMoS phase are combined at low dMo as previously mentioned in the section 3.3.2.1. Same behavior of products selectivity is observed for CoMoS/$\delta\theta$-Al_2O_3 (Appendix 17, Figure 53). For silica supported catalysts, the dMo has no significant effect on the 3MTproduct selectivity (Appendix 17, Figure 54).

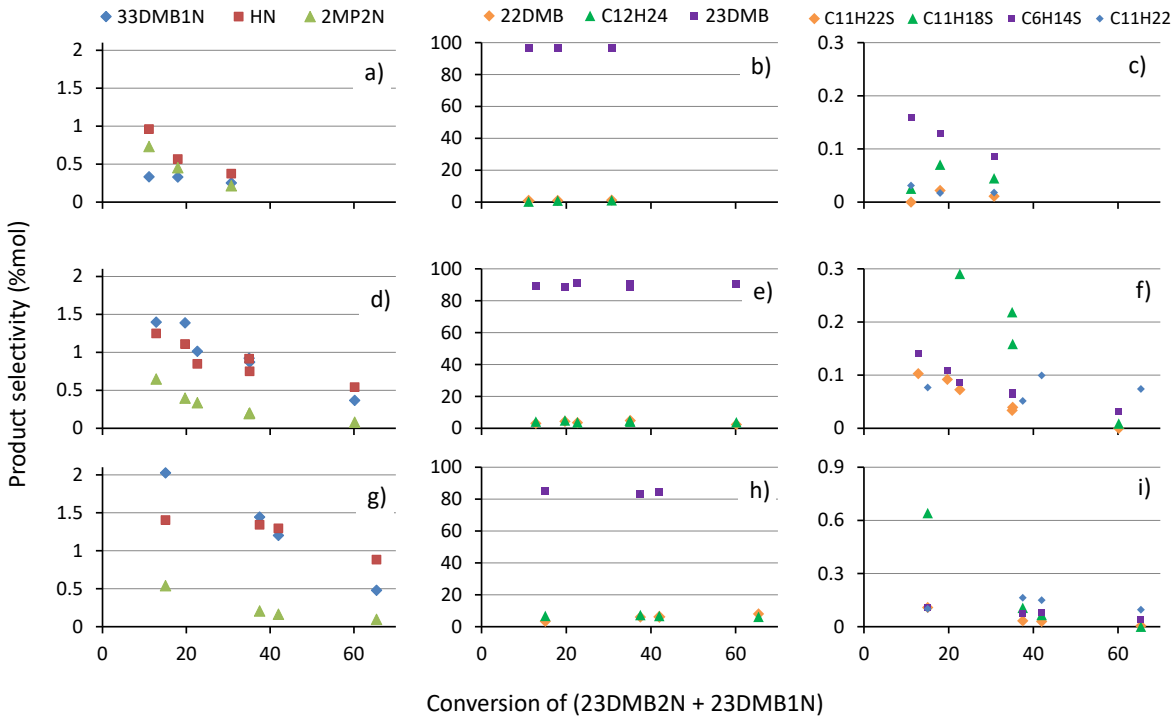

Figure 20. Selectivity of (23DMB2N+23DMB1N) products for CoMoS/γ-Al_2O_3 at dMo of (a,b,c) 0.9, (d,e,f) 2.2, (g,h,i) 3.8 at.nm^{-2} at 220°C. Graphs in the center represent the product distribution of alkane from hydrogenation reaction of (23DMB2N+23DMB1N). Graphs on the right represent the product distribution heavy alkylthiophenes and hydrogenated products from 3MT side reaction with (23DMB2N+23DMB1N) olefins.

HYDO yield corresponding to the amount of (23DMB2N+23DMB1N) and isomers (33DMB1N, HN or 2MP2N) transformed in alkanes can be determined and plotted as function of the contact time, $\tau_{Mo/23DMB2N}$ (Figure 21).

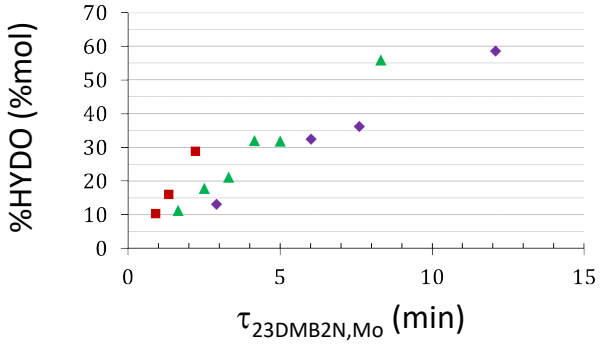

Figure 21. HYDO yield as function of the contact time for CoMoS/γ-Al_2O_3 at dMo variable, 0.9 (red), 2.2 (green) and 3.8 (purple) at.nm^{-2} of support at 220°C.

As previously observed for the (23DMB2N+23DMB1N) conversion, CoMoS/γ-Al_2O_3 shows at iso-$\tau_{Mo/3MT}$ closed HYDO yield for the two higher dMo whereas at low dMo, HYDO is significantly higher. For CoMoS/δθ-Al_2O_3 and for CoMoS/SiO_2, the same trend is observed but in a less extent (Appendix 18, Figure 56,Figure 57).

Table 14 presents a_{HYDO} for each catalyst at dMo of 0.9, 2.2 and 3.8 at.nm^{-2} of support on various supports. As reported previously for the HDS initial activity, for δθ and γ alumina supported catalysts, a decrease of the HYDO initial activity is observed with the increase of the dMo. For silica supported catalysts, the HDS initial activity decrease slightly with the increase of the dMo.

3.3.3 HDS/HYDO selectivity

In Figure 22, the HYDO yield is plotted as a function of the HDS yield for alumina and silica supported catalysts at each dMo at 220°C and various contact time (Figure 16). It is observed that the experimental points lay on the same curve at iso-support regardless the dMo. Indeed, at the HDS considered between 30 and 90%, the dMo seems have no impact the HDS/HYDO selectivity excepted may be for the CoMoS/γ-Al_2O_3 which could be slightly more selective at the higher dMo than at lower dMo. However, within our margin of errors, each graph reveals a universal trend whatever the dMo. This means that the dMo is not an experimental parameter critical for controlling the selectivity.

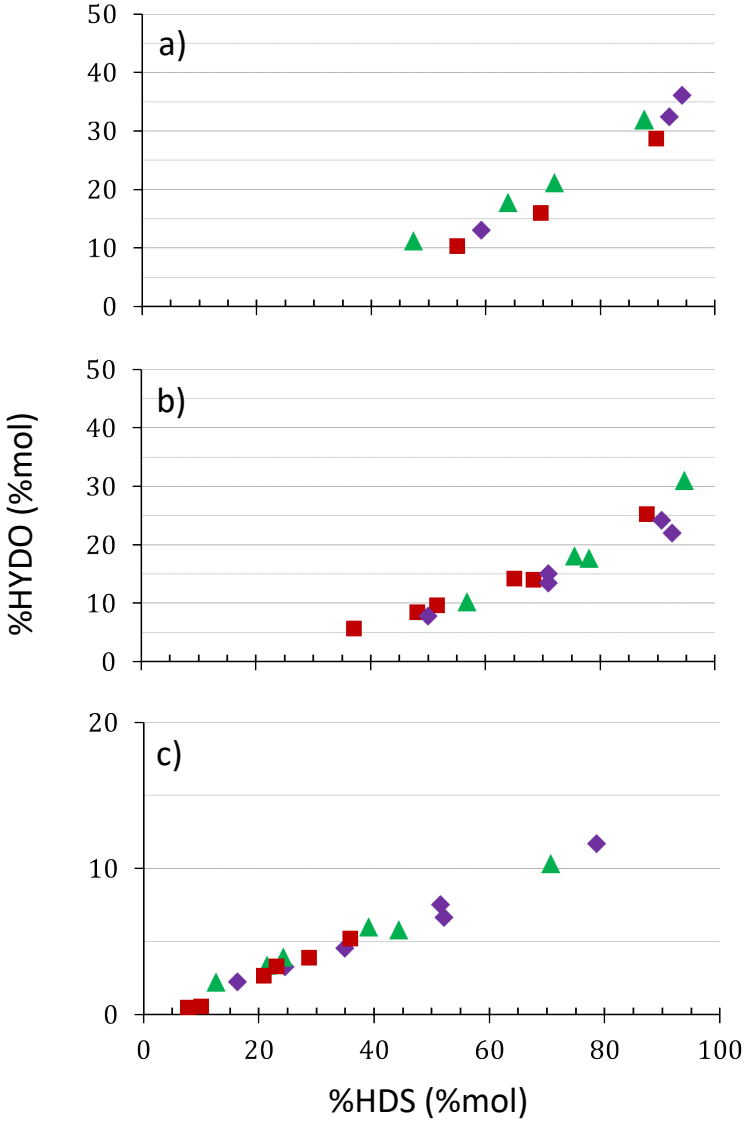

Figure 22. selectivity between the HDS vs HYDO reactions of CoMoS on (a) γ-Al_2O_3, (b) $\delta\theta$-Al_2O_3 and (c) SiO_2 for the three dMo 0.9 (red), 2.2 (green) and 3.8 (purple) at.nm^{-2}.

4 Conclusions

Catalysts based on the Co, Mo and P atoms have been prepared in order to evaluate the promotor effect, the support effect (γ-Al_2O_3, $\delta\theta$-Al_2O_3, SiO_2) and the impact of the molybdenum surface density by nm² of support (labelled dMo in what follows) on the HDS, HYDO activities and HDS/HYDO selectivity.

As expected, it is reported report the well-known promoting effet of Co on MoS_2 supported on $\delta\theta$-Al_2O_3 and SiO_2 for HDS activity but also for HDS/HYDO selectivity. Indeed, for the unpromoted MoS_2 catalysts, the 3MT transformation leads to simultaneously formation of HDS products (2MB) but also a high concentration of hydrogenated 3MT products, 3MTHT (~30-50%), resulting in a lower HDS yields compared to promoted ones (3MTHT < 10%). Regarding the selectivity products of the 23DMB2N, no significant difference appears for $\delta\theta$-Al_2O_3-based catalyst whereas the Co-promoter presence for the MoS_2/SiO_2 leads to a higher selectivity toward the $C_{12}H_{24}$ formation. Additionally, it can be noted that the HDS and HYDO activities are significantly improved in presence of Co-promoter, with a_{HDS} more than the a_{HYDO}, leading as well to HDS/HYDO selectivity increase, as expected.

Regarding the support effect on CoMoS catalysts, alumina supported catalysts have demonstrated a higher activity than silica supported catalysts. However, whereas the HDS/HYDO selectivity reported is shown to be quasi-equivalent at low HDS regardless the support, selectivity difference are revealed for higher HDS reaction progress (except for the lower dMo). Following order of selectivity is demonstrated at high HDS reaction progress: CoMoS/SiO_2 ≥ CoMoS/$\delta\theta$-Al_2O_3 > CoMoS/γ-Al_2O_3. Regarding the products selectivity from the 3MT transformation, it is observed that the alkene selectivity is higher at low and moderate 3MT conversion (<70%) and decreases at higher 3MT conversion for alumina supported catalysts whereas on silica supported catalysts the opposite trend is observed with an increase of the olefins selectivity. These results could be rationalized by adsorption competition phenomena. Indeed, adsorption competition between 3MT and 23DMB2N has been shown in Appendix 19. Thiophenic molecule (3MT) is a strong inhibitor for the hydrogenation reaction of 23DMB2N on alumina supported catalyst considered and regardless the dMo. However, this inhibition effect has been less pronounced on CoMoS on SiO_2. Moreover, over silica supported catalysts, the products selectivity from the

(23DMB2N+23DMB21N) transformation shows higher product selectivity (~10 times) towards the isomers of (23DMB2N+23DMB2N). These results could be related to an olefin adsorptions lower on silica than on alumina support or related to olefin adsorptions lower on the CoMoS phase supported on silica due to modification of the electronic properties compare with CoMoS phase supported on alumina.

Finally, dMo effect (increase of the Mo loading) has reveal no significant impact on the HDS/HYDO selectivity whereas the HDS activity is higher (γ-Al_2O_3) and slightly higher ($\delta\theta$-Al_2O_3 and SiO_2) when dMo is lower. However, regarding HDS and HYDO activities, the lower the dMo (or Mo loading) the higher the activities per molybdenum atoms on each support. Indeed, it can be noted that the product selectivity of 3MT and (23DMB2N+23DMB1N) transformations is almost unchanged with the increase the dMo.

In the following chapters, we will investigate various physico-chemical properties obtained by various characterization and simulation techniques of the active phases and the supports in order to better understand the previous catalytic results. Moreover, the catalytic properties especially the activities related to the HDS and HYDO reactions will be discussed according the catalysts features exposed so far. To achieve that, qualitative (relative order of activity and selectivity) and quantitative analysis (initial activities calculated for each catalyst) will be used.

5 Appendixes

Appendix 1. Reference materials: Support.

γ-Al_2O_3, $\delta\theta$-Al_2O_3 and SiO_2 supports have been evaluated with a feedstock composed of 3MT (0.33 %wt) and 23DMB2N (10 %wt) in n-heptane at 210°c. Measurements of conversion related to the 3MT and 23DMB2N reactions have been performed as function of the contact time, labeled $\tau_{g\ of\ catalyst,\ reactant}$. This contact time is calculated as the reverse of the weight hourly space velocity (WHSV). Here, WHSV is defined by the ratio between the mass gas flow rate of the reactant of the considered reaction (3MT or 23DMB2N) and the mass of the catalyst deposited on the support. However, it is important to remember that the pecific area of each support is different. The contact time, $\tau_{g\ of\ catalyst,reactant,}$ has been modified by changing the flow of the feedstock (between $1.6.10^{-10}$ and 5.10^{-10} $m^3.s^{-1}$) with a mass of material equal to 200mg. Thus, $\tau_{g\ of\ catalyst,reactant}$ varies from 45 to 150h and from 1 to 5 min for 3MT and 23DMB2N respectively.

1. Evolution of 3MT and (23DMB2N+23DMB1N) conversions

3MT and (23DMB2N+23DMB1N) conversions of γ-, $\delta\theta$-Al_2O_3 and SiO_2 have been plotted as function of the contact time, $\tau_{Mo/reactant,}$ at 210°C in Figure 23 a) and b). It is observed at iso-$\tau_{Mo/reactant}$ the 3MT conversion is closed to 0 (< 5%) and the (23DMB2N+23DMB1N) conversion is zero for the three supports. However, whereas the 23DMB2N conversion is nil for $\delta\theta$-Al_2O_3 and SiO_2 i.e no isomerization reaction of 23DMB2N in 23DMB1N, it can be noted that the 23DMB2N conversion only is not nil γ-Al_2O_3 (Figure 23 c). This result shows that the isomerization reaction of 23DMB2N in 23DMB1N occurs on γ-Al_2O_3 but not until the thermodynamic equilibrium as it was shown in the Appendix 3 even if it may converge towards it with the increase of the contact time.

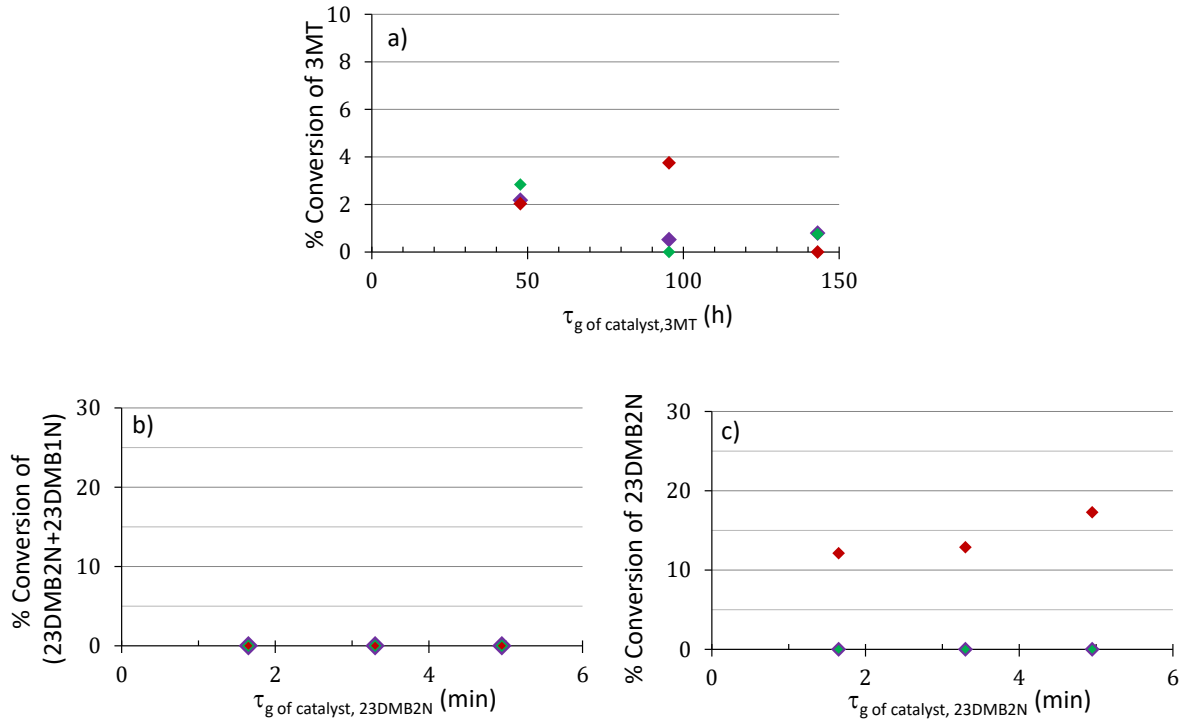

Figure 23. (a) 3MT, (b) (23DMB2N+23DMB1N) and (c) 23DMB2N conversions vs. $\tau_{g\ of\ catalyst/reactant}$ of γ-Al_2O_3 (red), $\delta\theta$-Al_2O_3 (green) and SiO_2 (purple) at 210 °C.

Appendix 2. Molar material balance of 3MT and (23DMB2N+23DMB1N) products for $CoMoS/SiO_2$.

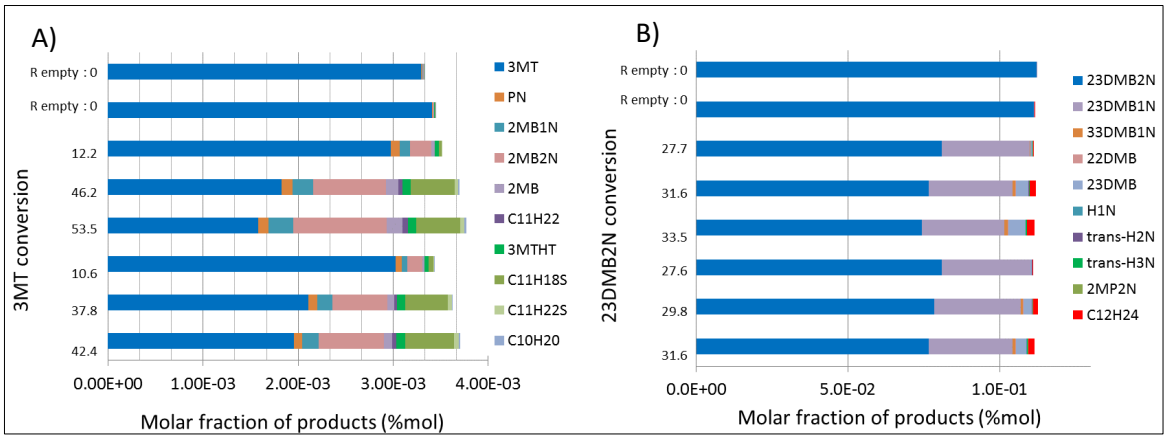

Figure 24. Molar material balance related to (A) the 3MT product and (B) the (23DMB2N+23DMB1N) products for the $CoMoS/SiO_2$ at dMo of 0.9 at.nm^{-2} of support at 220°C.

Appendix 3. Thermodynamic equilibrium of the 23DMB2N/23DMB1N isomerization reaction evaluates on the CoMoS on γ- δθ-Al_2O_3 and SiO_2 at iso-dMo of 2.2 at.nm^{-2} of support (Co/Mo ratio equal to 0.4) at 220°C.

Regardless the support, it can be noted over CoMoS/support a steady state is reached rapidly between the 23DMB2N and 23DMB1N reactant leading to the 23DMB2N:23DMB1N molar proportion of %73/%27 (Figure 25).

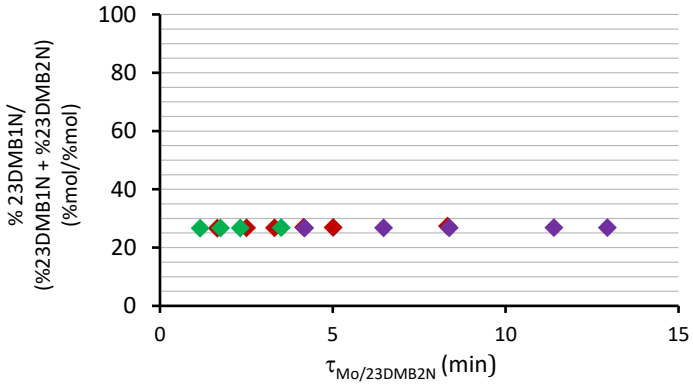

Figure 25. Equilibrium between 23DMB2N and 23DMB1N as function of the contact time for CoMoS on γ-Al_2O_3 (red), δθ-Al_2O_3 (green) and SiO_2 (purple) at iso-dMo of 2.2 at.nm^{-2} of support (Co/Mo ratio equal to 0.4) at 220°C.

Appendix 4. 3MT and (23DMB2N + 23DMB1N) as function of the contact time, $\tau_{Mo,3MT}$ and $\tau_{Mo,23DB2N}$ for $MoS_2/\delta\theta Al_2O_3$ (Co/Mo=0) and $CoMoS/\delta\theta$-Al_2O_3 (Co/Mo=0.4) at iso-dMo of 2.2 at.nm^{-2} of support for the transformation of model FCC gasoline feedstock

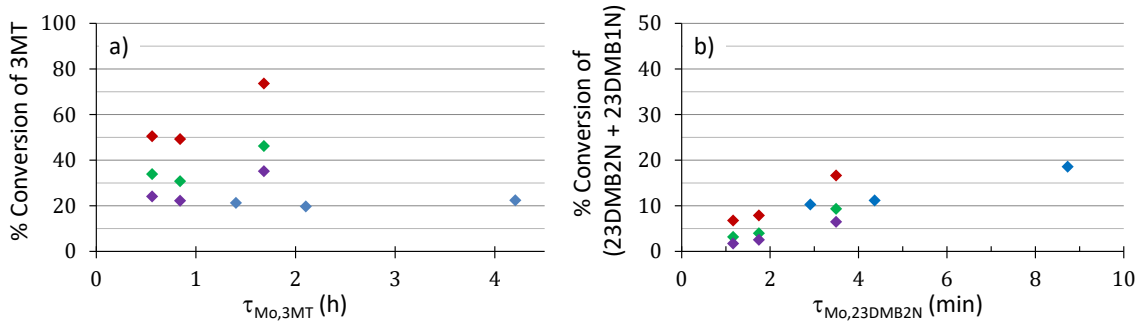

Figure 26. (a) 3MT and (b) (23DMB2N+23DMB1N) conversions vs. $\tau_{Mo/reactant}$ of $MoS_2/\delta\theta$-Al_2O_3 (blue) and $CoMoS/\delta\theta$-Al_2O_3 at iso-dMo of 2.2 at.nm^{-2} of support, Co/Mo=0.1 (purple), Co/Mo=0.2 (green) and Co/Mo=0.4 (red), at 210 °C. *noted that probably one of the two first points at lower contact time is not valid.

Appendix 5. 3MT and (23DMB2N + 23DMB1N) as function of the contact time, $\tau_{Mo,3MT}$ and $\tau_{Mo,23DB2N}$ for MoS_2/SiO_2 (Co/Mo=0) and $CoMoS/SiO_2$ (Co/Mo=0.4) at iso-dMo of 2.2 at.nm^{-2} of support for the transformation of model FCC gasoline feedstock.

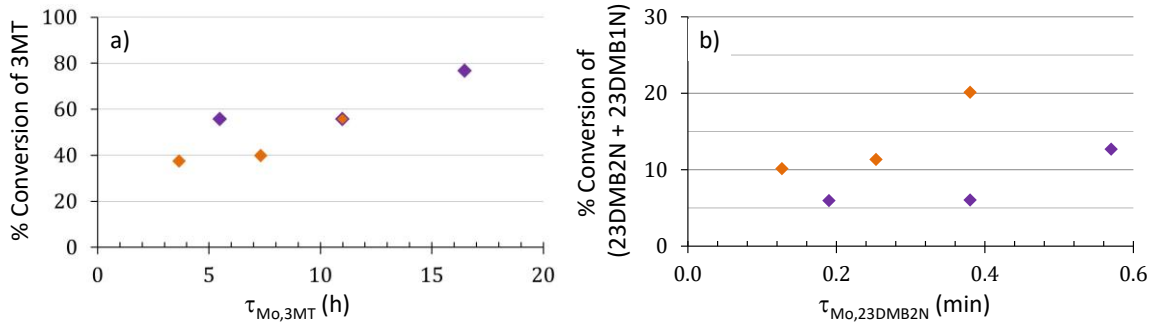

Figure 27. (a) 3MT and (b) (23DMB2N+23DMB1N) conversions vs. $\tau_{Mo/reactant}$ of MoS_2/SiO_2 and $CoMoS/SiO_2$ at iso-dMo of 2.2 at.nm^{-2} of support and respectively a Co/Mo ratio equal to 0 (orange), 0.4 (purple) at 210 °C. *noted that probably one of the two first points at lower contact time is not valid.

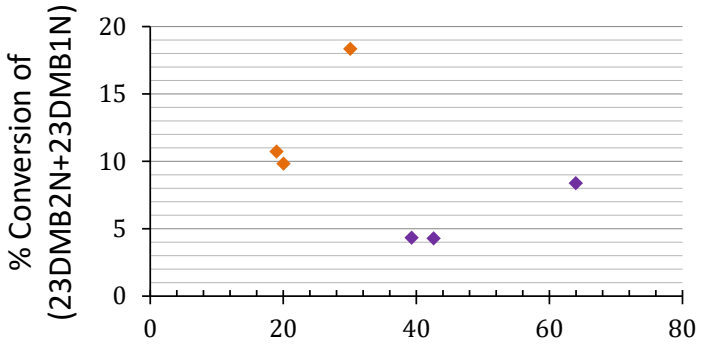

Figure 28. Selectivity between the 3MT and (23DMB2N+23DMB1N) conversions of MoS_2/SiO_2 and $CoMoS/SiO_2$ at iso-dMo of 2.2 at.nm^{-2} of support and respectively a Co/Mo ratio equal to 0 (orange), 0.4 (purple) at 210 °C.

Appendix 6. 3MT product distribution as function of 3MT conversion for MoS_2/SiO_2 and $CoMoS/SiO_2$ at iso-dMo of 2.2 at.nm^{-2} and respectively a Co/Mo ratio equal to 0 (orange), 0.4 (purple) at 210 °C for the transformation of model FCC gasoline feedstock.

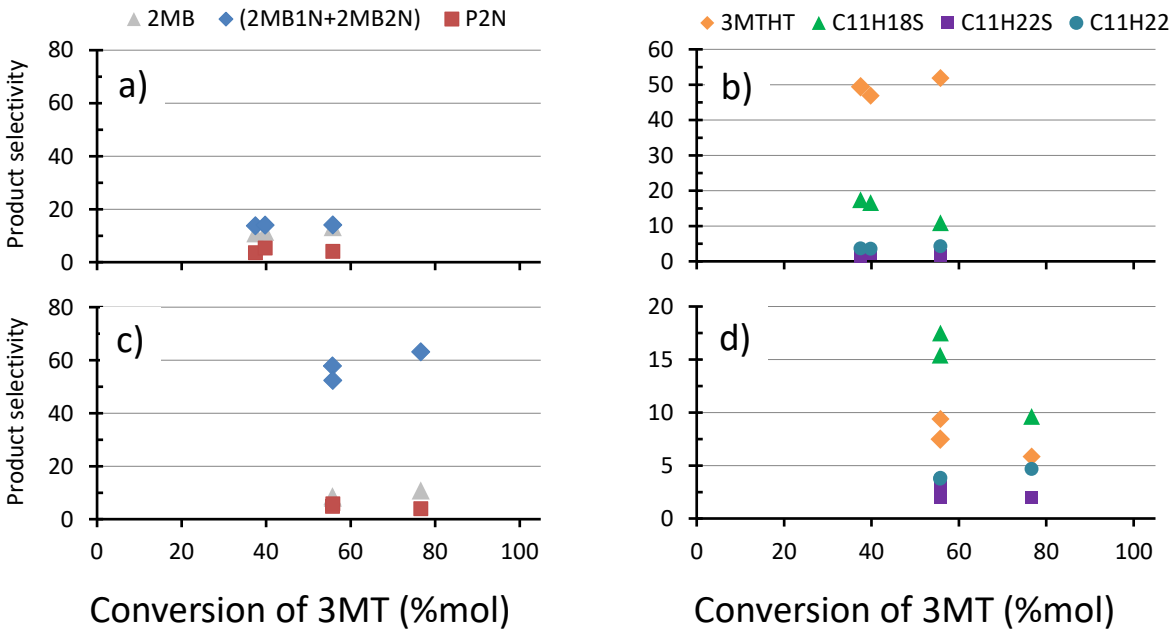

Figure 29. Product selectivity of the 3MT transformation for (a,b) MoS_2/SiO_2 and (c,d) $CoMoS/SiO_2$ at iso-dMo of 2.2 at.nm^{-2} and respectively a Co/Mo ratio equal to 0 (orange), 0.4 (purple) at 210 °C. Graphs on the left represent the product distribution of alkanes and alkene from the complete desulfurization of 3MT. Graphs on the right represent the product distribution of 3MTHT from the hydrogenation of 3MT and alkylthiophene from 3MT side reaction with (23DMB2N+23DMB1N) olefins.

Appendix 7. HDS and HYDO yield as function of the contact time, $\tau_{Mo,3MT}$ and $\tau_{Mo,23DB2N}$ for $MoS_2/\delta\theta$-Al_2O_3 (Co/Mo=0) and $CoMoS/\delta\theta$-Al_2O_3 (Co/Mo=0.4) at iso-dMo of 2.2 at.nm^{-2} of support for the transformation of model FCC gasoline feedstock.

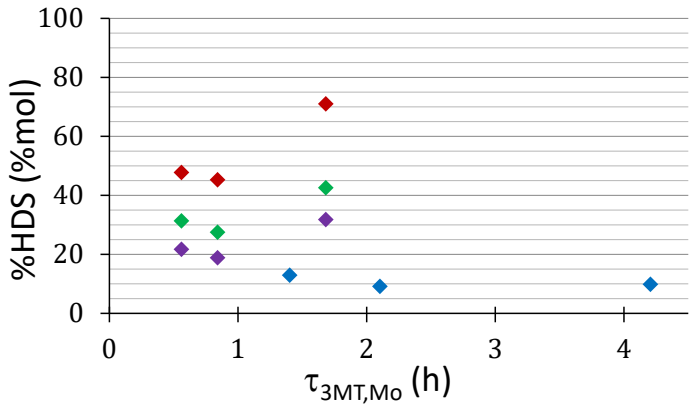

Figure 30. HDS yield vs. $\tau_{3MT,Mo}$ of MoS_2 (blue) and $CoMoS/\delta\theta$-Al_2O_3 at iso-dMo of 2.2 at.nm^{-2} of support: Co/Mo=0.1 (purple), Co/Mo=0.2 (green) and Co/Mo=0.4 (red), at 210 °C. *noted that probably one of the two first points at lower contact time is not valid.

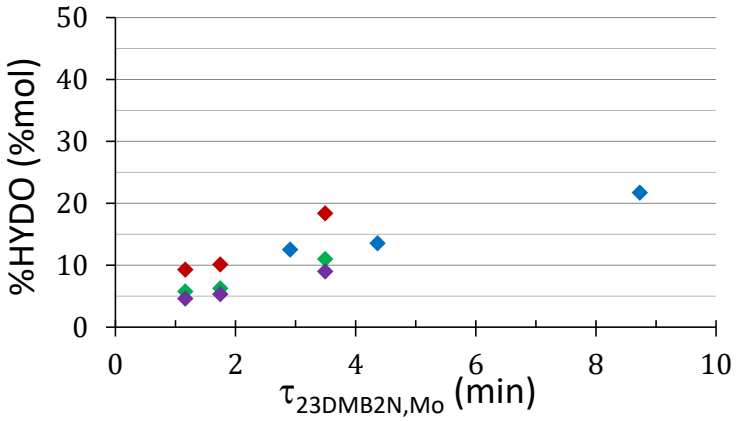

Figure 31. HYDO yield vs. $\tau_{23DMB2N,Mo}$ of MoS_2 (blue) and $CoMoS/\delta\theta$-Al_2O_3 at iso-dMo of 2.2 at.nm^{-2} of support, Co/Mo=0.1 (purple), Co/Mo=0.2 (green) and Co/Mo=0.4 (red), at 210 °C. *noted that probably one of the two first points at lower contact time is not valid.

Appendix 8. HDS and HYDO yield as function of the contact time, $\tau_{Mo,3MT}$ and $\tau_{Mo,23DB2N}$ for MoS_2/SiO_2 (Co/Mo=0) and $CoMoS/SiO_2$ (Co/Mo=0.4) at iso-dMo of 2.2 at.nm^{-2} of support for the transformation of model FCC gasoline feedstock.

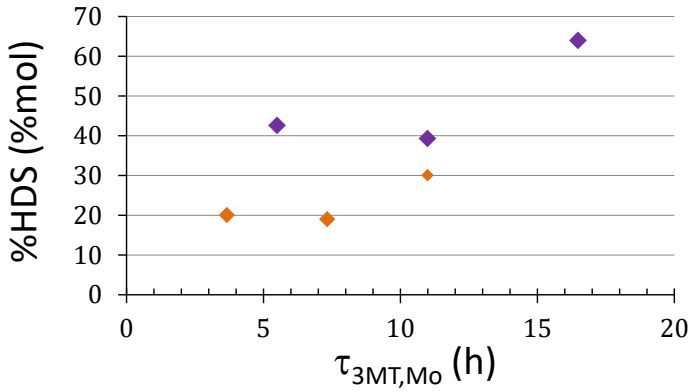

Figure 32. HDS yield as function of the contact time of MoS_2/SiO_2 and $CoMoS/SiO_2$ at iso-dMo of 2.2 at.nm^{-2} and respectively a Co/Mo ratio equal to 0 (orange), 0.4 (purple) at 210 °C.

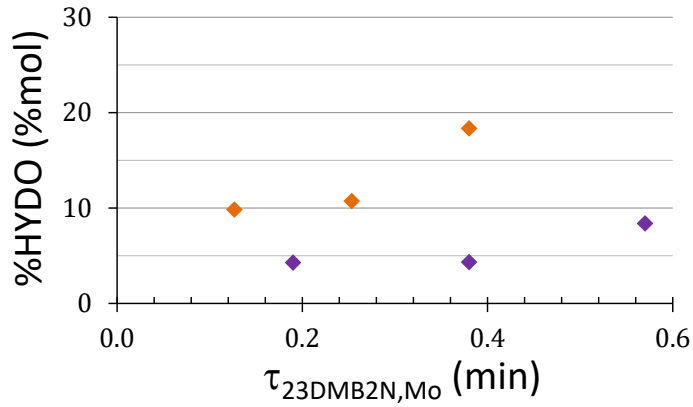

Figure 33. HYDO yield as function of the contact time of MoS_2/SiO_2 and $CoMoS/SiO_2$ at iso-dMo of 2.2 at.nm^{-2} and respectively a Co/Mo ratio equal to 0 (orange), 0.4 (purple) at 210 °C.

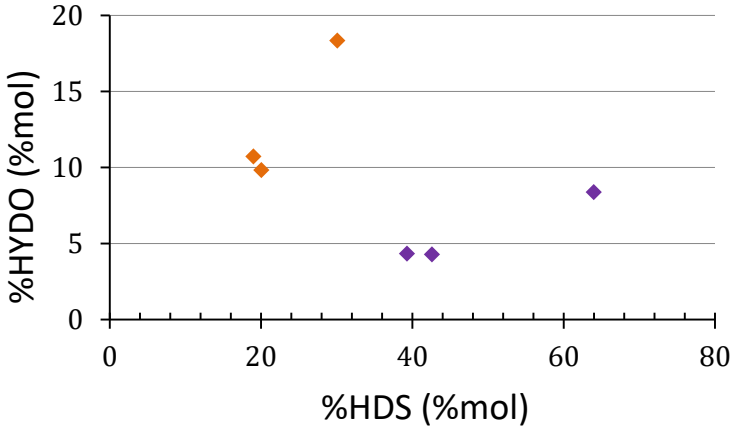

Figure 34. Selectivity between the HDS and the HYDO reactions of MoS_2/SiO_2 and $CoMoS/SiO_2$ at iso-dMo of 2.2 at.nm^{-2} and respectively a Co/Mo ratio equal to 0 (orange), 0.4 (purple) at 210 °C.

Appendix 9. (23DMB2N+23DMB1N) product distribution as function of (23DMB2N + 23DMB1N) conversion for MoS_2/SiO_2 and $CoMoS/SiO_2$ at iso-dMo of 2.2 at.nm^{-2} and respectively a Co/Mo ratio equal to 0 (orange), 0.4 (purple) at 210 °C for the transformation of model FCC gasoline feedstock.

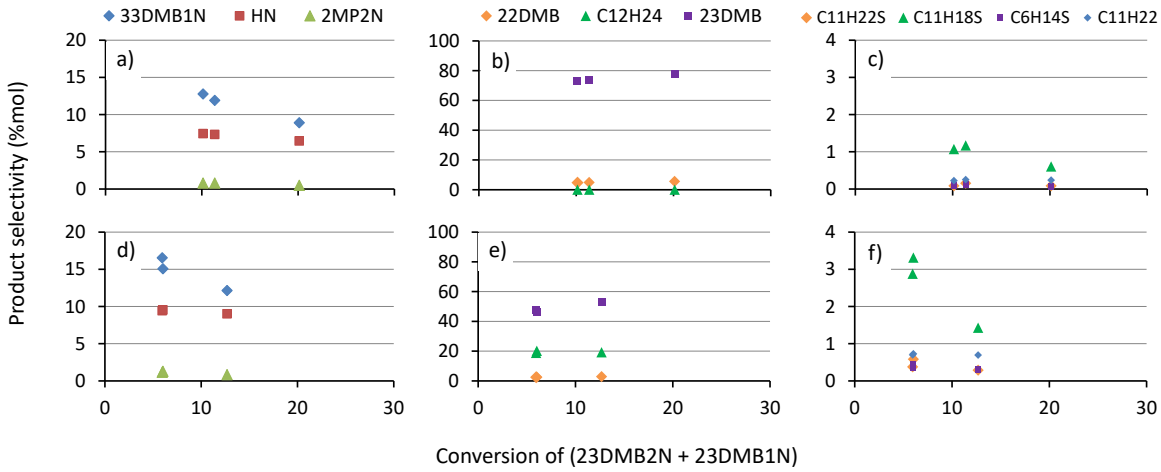

Figure 35. Products selectivity of the (23DMB2N+23DMB1N) transformation for (a,b,c) MoS_2/SiO_2 and (d,e,f) $CoMoS/SiO_2$ at iso-dMo of 2.2 at.nm^{-2} and respectively a Co/Mo ratio equal to 0 (orange), 0.4 (purple) at 210 °C. Graphs on the left represent the product distribution of isomers of 23DMB2N. Graphs in the center represent the product distribution of alkane from hydrogenation reaction of (23DMB2N+23DMB1N). Graphs on the right represent the product distribution heavy alkylthiophenes and hydrogenated products from 3MT side reaction with (23DMB2N+23DMB1N) olefins.

Appendix 10. 3MT and (23DMB2N+23DMB1N) conversion as function of the contact time for CoMoS catalysts at 220°C for each dMo for the transformation of model FCC gasoline feedstock.

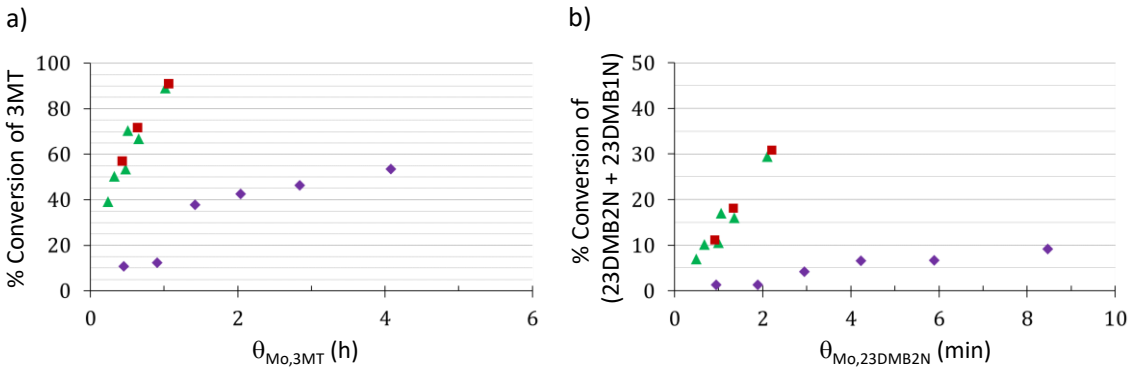

Figure 36. a) 3MT and b) (23DMB2N+23DMB1N) conversions vs. $\tau_{Mo/reactant}$ of CoMoS on γ-Al_2O_3 (red), $\delta\theta$-Al_2O_3 (green) and SiO_2 (purple) at dMo 0.9 at 220 °C.

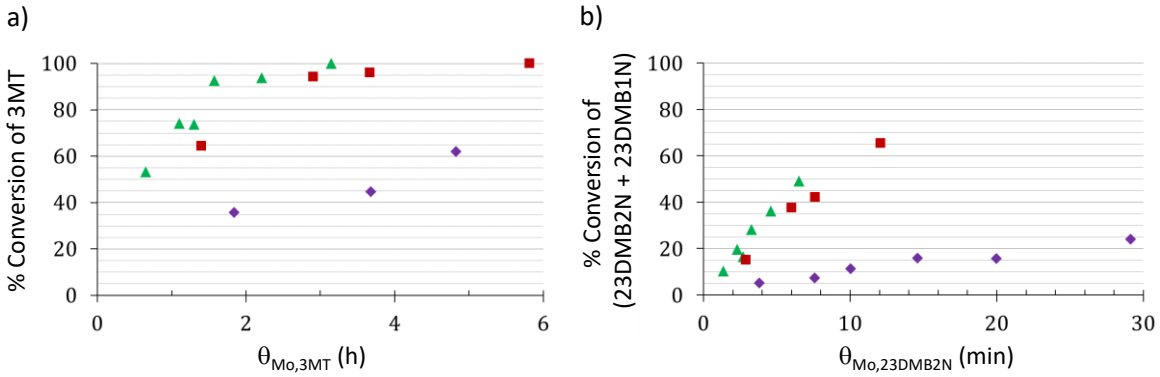

Figure 37. a) 3MT and b) (23DMB2N+23DMB1N) conversions vs. $\tau_{Mo/reactant}$ of CoMoS on γ-Al_2O_3 (red), $\delta\theta$-Al_2O_3 (green) and SiO_2 (purple) at dMo 3.8 at 220 °C.

Appendix 11. 3MT product distribution as function of 3MT conversion, for CoMoS catalysts at 220°C for each dMo for the transformation of model FCC gasoline feedstock.

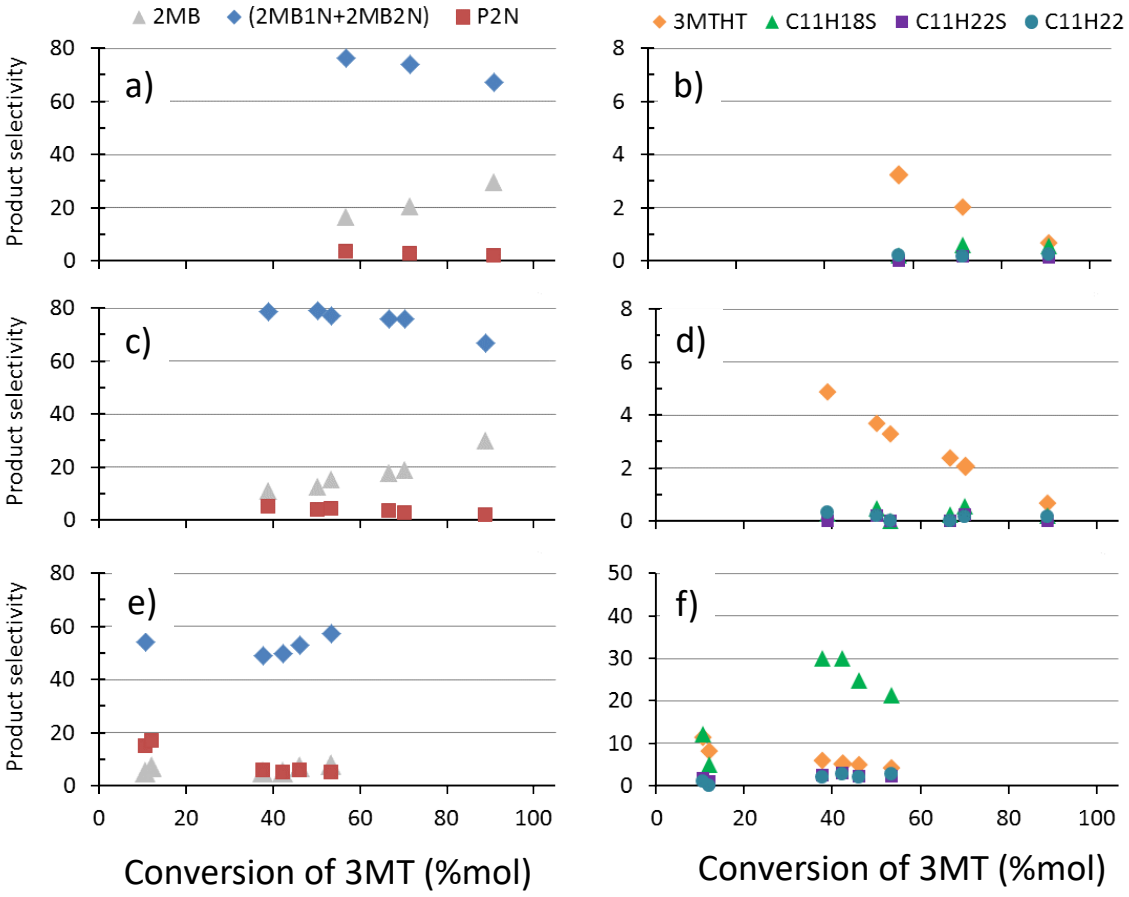

Figure 38. Product selectivity of the 3MT transformation for CoMoS on (a,b) γ-Al_2O_3, (c,d) $\delta\theta$-Al_2O_3, (e,f) SiO_2 at iso-dMo of 0.9 at.nm^{-2} of support (T=220°C). Graphs on the left represent the product distribution of alkanes and alkene from the complete desulfurization of 3MT. Graphs on the right represent the product distribution of 3MTHT from the hydrogenation of 3MT and alkylthiophene from 3MT side reaction with (23DMB2N+23DMB1N) olefins.

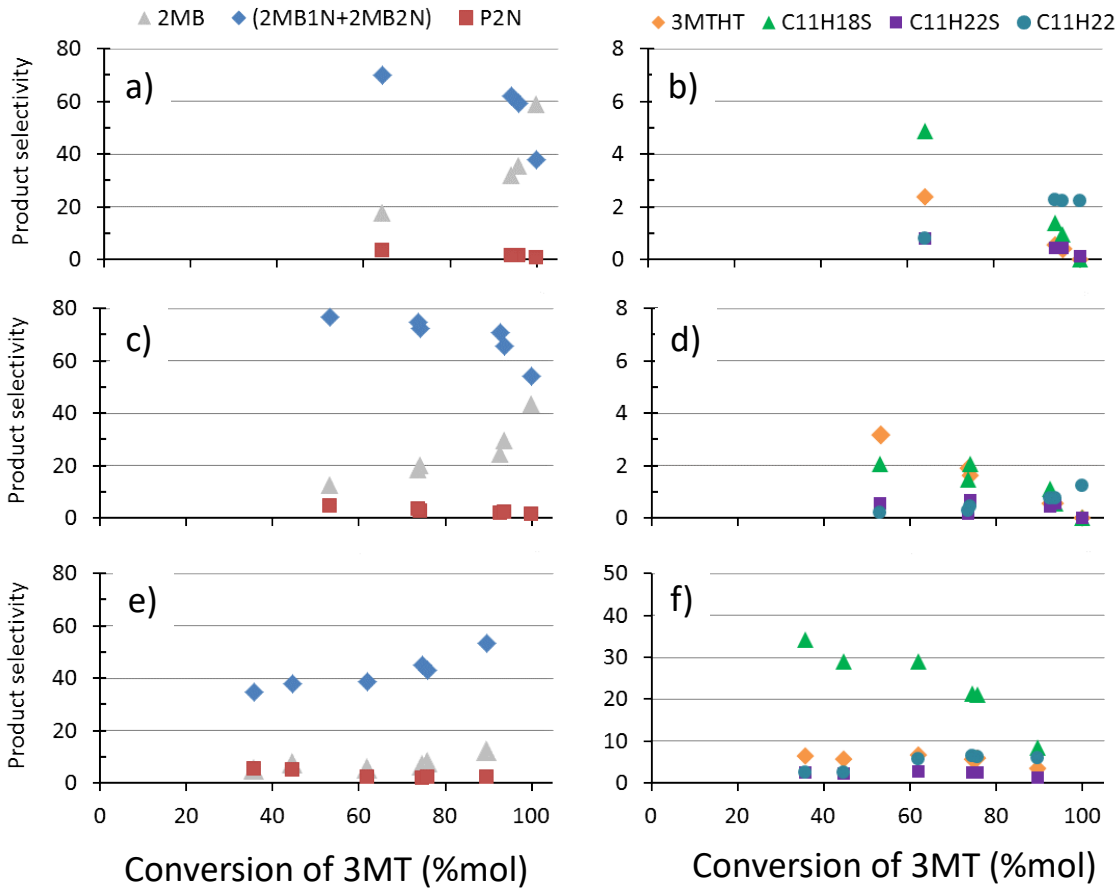

Figure 39. Product selectivity of the 3MT transformation for CoMoS on (a,b) γ-Al_2O_3, (c,d) δθ-Al_2O_3, (e,f) SiO_2 at iso-dMo of 3.8 at.nm^{-2} of support (T=220°C). Graphs on the left represent the product distribution of alkanes and alkene from the complete desulfurization of 3MT. Graphs on the right represent the product distribution of 3MTHT from the hydrogenation of 3MT and alkylthiophene from 3MT side reaction with (23DMB2N+23DMB1N) olefins.

Appendix 12. HDS yield as function of the contact time, $\tau_{Mo,3MT}$, for CoMoS catalysts at 220°C for each dMo for the transformation of model FCC gasoline feedstock.

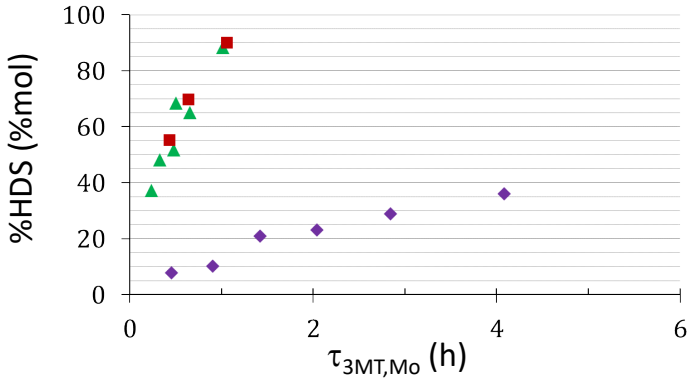

Figure 40. HDS yield as function of the contact time for CoMoS on γ-Al_2O_3 (red), δθ-Al_2O_3 (green) and SiO_2 (purple) at iso-dMo of 0.9 at.nm^{-2} of support at 220°C.

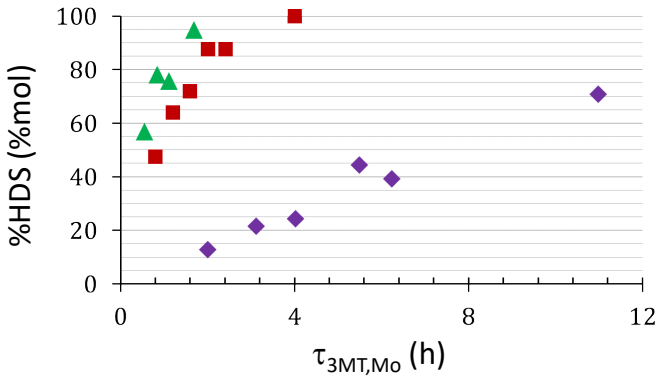

Figure 41. HDS yield as function of the contact time for CoMoS on γ-Al_2O_3 (red), δθ-Al_2O_3 (green) and SiO_2 (purple) at iso-dMo of 2.2 at.nm^{-2} of support at 220°C.

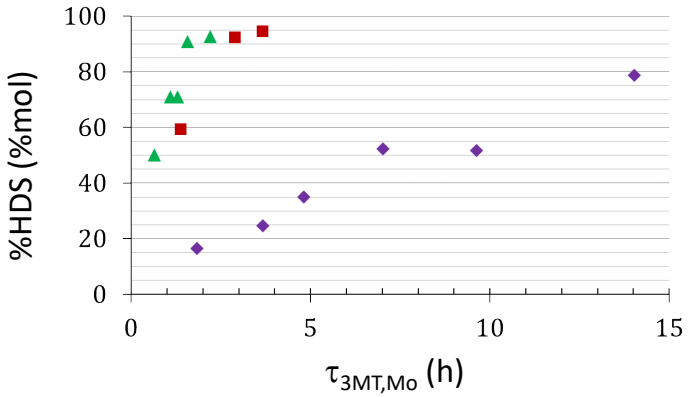

Figure 42. HDS yield as function of the contact time for CoMoS on on γ-Al_2O_3 (red), δθ-Al_2O_3 (green) and SiO_2 (purple) at iso-dMo of 3.8 at.nm^{-2} of support at 220°C.

Appendix 13. (23DMB2N+23DMB1N) product distribution as function of (23DMB2N + 23DMB1N) conversion, for CoMoS catalysts at 220°C for each dMo for the transformation of model FCC gasoline feedstock.

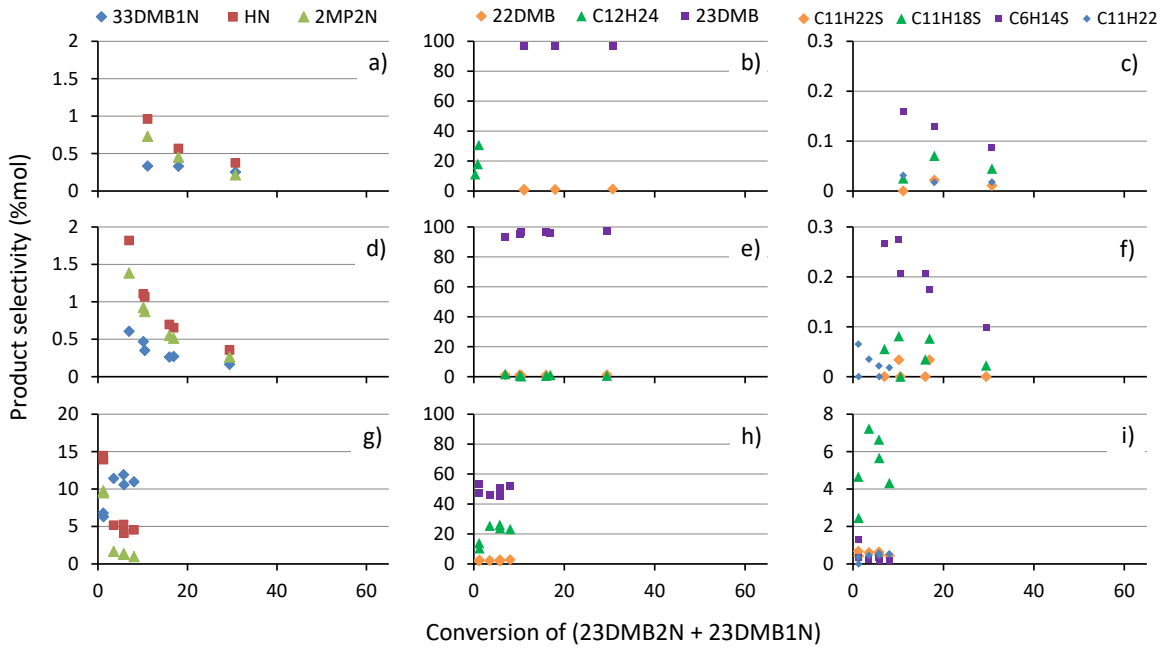

Figure 43. Products selectivity of the (23DMB2N+23DMB1N) transformation for CoMoS on (a,b,c) γ-Al_2O_3, (d,e,f) δθ-Al_2O_3, (g,h,i) SiO_2 at iso-dMo of 0.9 at.nm^{-2} of support at 220°C. Graphs on the left represent the product distribution of isomers of 23DMB2N. Graphs in the center represent the product distribution of alkane from hydrogenation reaction of (23DMB2N+23DMB1N). Graphs on the right represent the product distribution heavy alkylthiophenes and hydrogenated products from 3MT side reaction with (23DMB2N+23DMB1N) olefins.

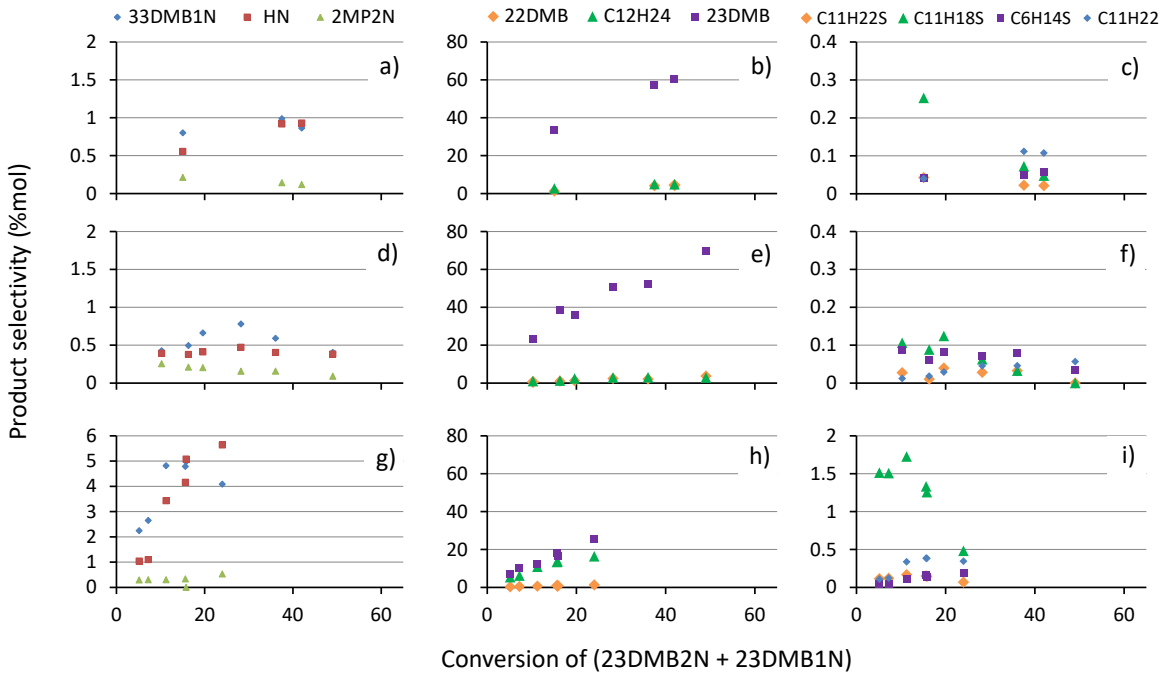

Figure 44. Products selectivity of the (23DMB2N+23DMB1N) transformation for CoMoS on (a,b,c) γ-Al_2O_3, (d,e,f) $\delta\theta$-Al_2O_3, (g,h,i) SiO_2 at iso-dMo of 3.8 at.nm^{-2} of support at 220°C. Graphs on the left represent the product distribution of isomers of 23DMB2N. Graphs in the center represent the product distribution of alkane from hydrogenation reaction of (23DMB2N+23DMB1N). Graphs on the right represent the product distribution heavy alkylthiophenes and hydrogenated products from 3MT side reaction with (23DMB2N+23DMB1N) olefins.

Appendix 14. HYDO yield as function of the contact time, $\tau_{Mo,23DMB2N}$, for CoMoS catalysts at 220°C for each dMo for the transformation of model FCC gasoline feedstock.

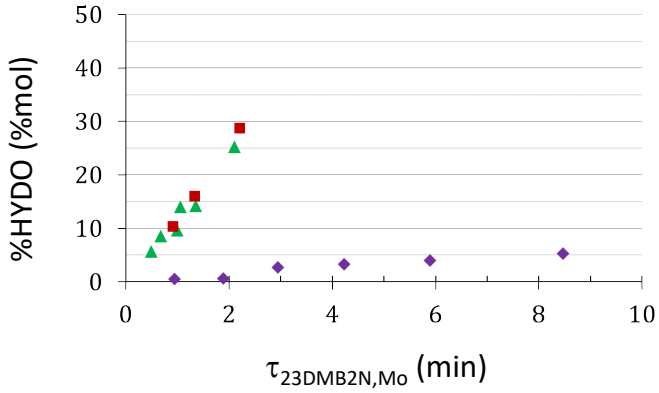

Figure 45. HYDO yield as function of the contact time for CoMoS on γ-Al_2O_3 (red), δθ-Al_2O_3 (green), SiO_2 (purple) at iso-dMo of 0.9 at.nm^{-2} of support at 220°C.

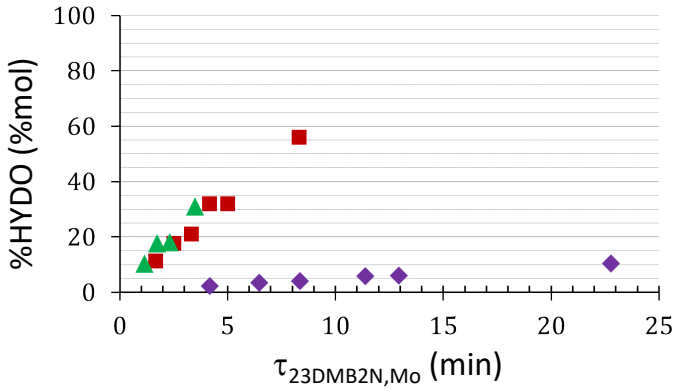

Figure 46. HYDO yield as function of the contact time for CoMoS on γ-Al_2O_3 (red), δθ-Al_2O_3 (green), SiO_2 (purple) at iso-dMo of 2.2 at.nm^{-2} of support at 220°C.

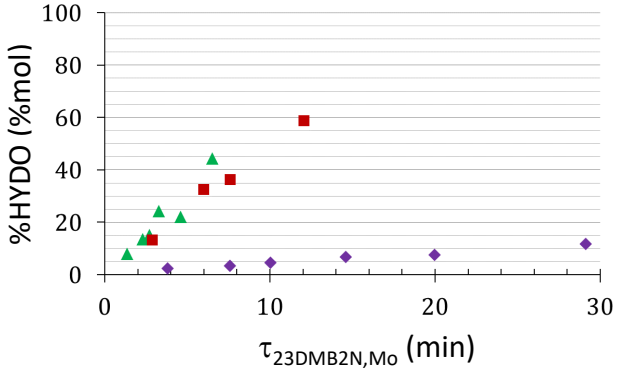

Figure 47. HYDO yield as function of the contact time for CoMoS on γ-Al_2O_3 (red), δθ-Al_2O_3 (green), SiO_2 (purple) at iso-dMo of 3.8 at.nm^{-2} of support at 220°C.

Appendix 15. 3MT product distribution as function of 3MT conversion, for CoMoS catalysts at 220°C as function of the dMo for each catalyst the transformation of model FCC gasoline feedstock.

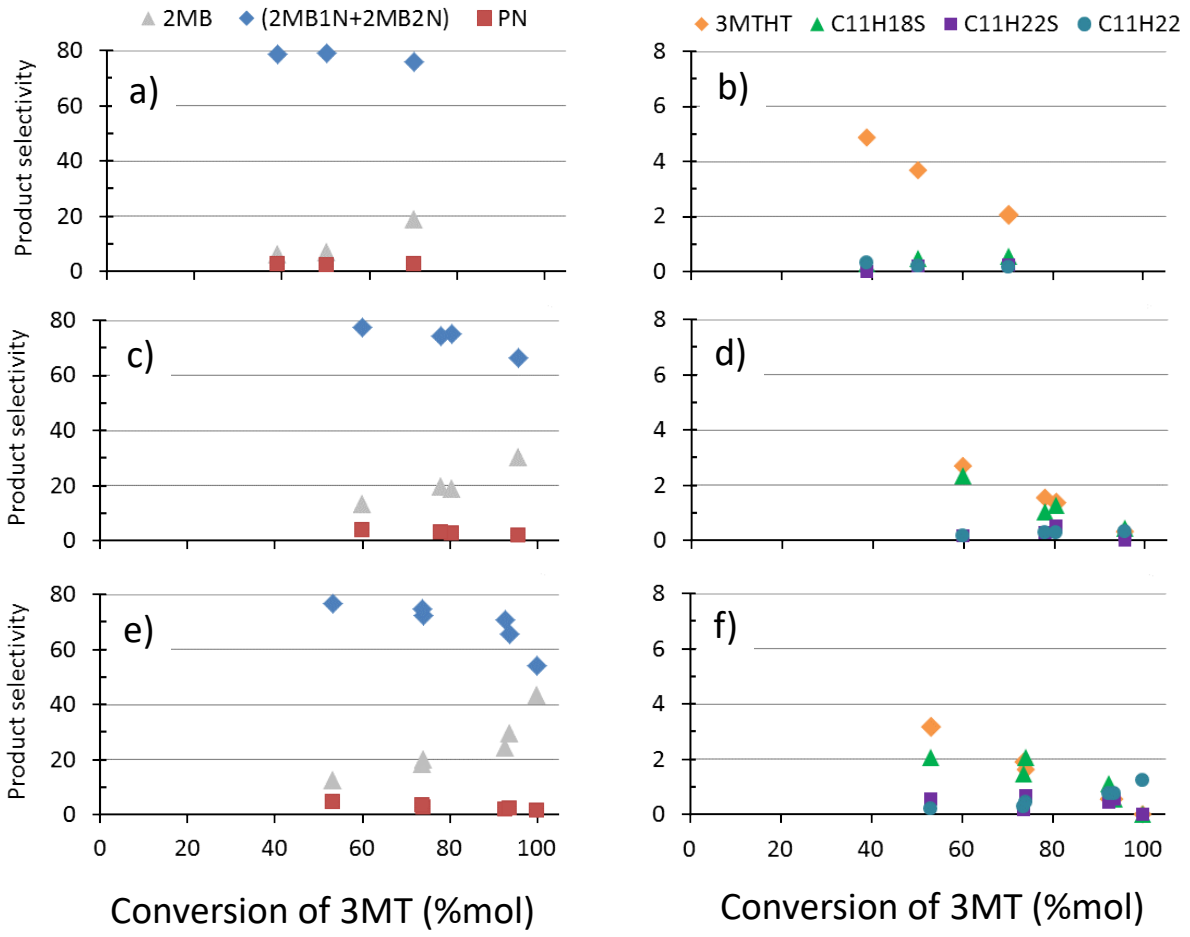

Figure 48. Selectivity of 3MT products for CoMoS/δθ-Al_2O_3 at dMo of (a,b) 0.9, (c,d) 2.2, (e,f) 3.8 at.nm^{-2} at 220°C. Graphs on the left represent the product distribution of alkanes and alkene from the complete desulfurization of 3MT. Graphs on the right represent the product distribution of 3MTHT from the hydrogenation of 3MT and alkylthiophene from 3MT side reaction with (23DMB2N+23DMB1N) olefins.

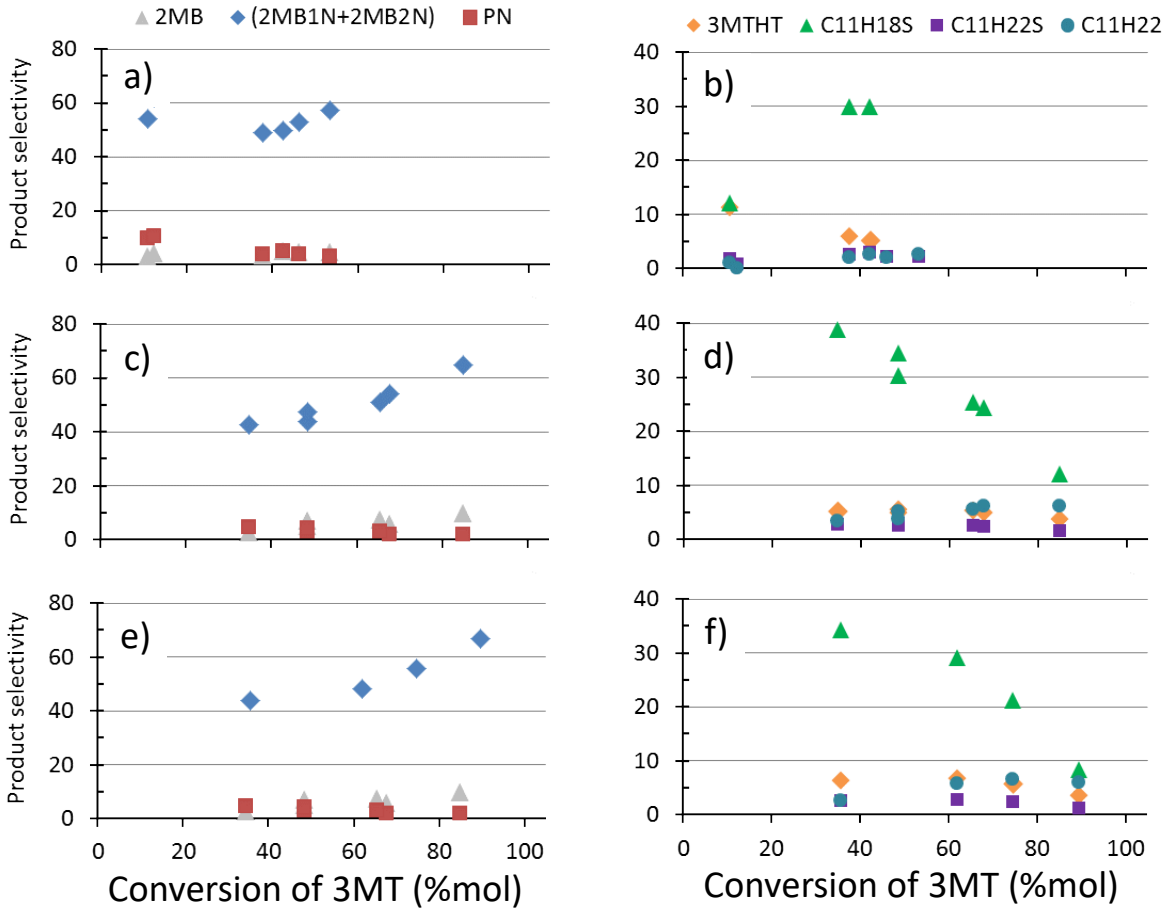

Figure 49. Selectivity of 3MT products for $CoMoS/SiO_2$ at dMo of (a,b) 0.9, (c,d) 2.2, (e,f) 3.8 at.nm^{-2} at 220°C. Graphs on the left represent the product distribution of alkanes and alkene from the complete desulfurization of 3MT. Graphs on the right represent the product distribution of 3MTHT from the hydrogenation of 3MT and alkylthiophene from 3MT side reaction with (23DMB2N+23DMB1N) olefins.

Appendix 16. HDS yield as function of the contact time, $\tau_{Mo,3MT}$, for CoMoS catalysts at 220°C for each dMo for the transformation of model FCC gasoline feedstock.

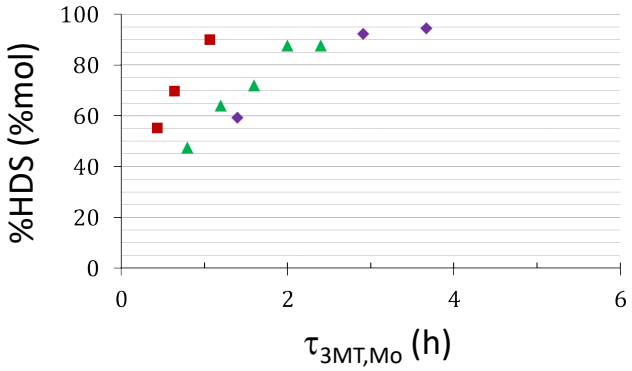

Figure 50. HDS yield as function of the contact time for CoMoS/γ-Al_2O_3 at dMo variable, 0.9 (red), 2.2 (green) and 3.8 (purple) at.nm^{-2} of support at 220°C.

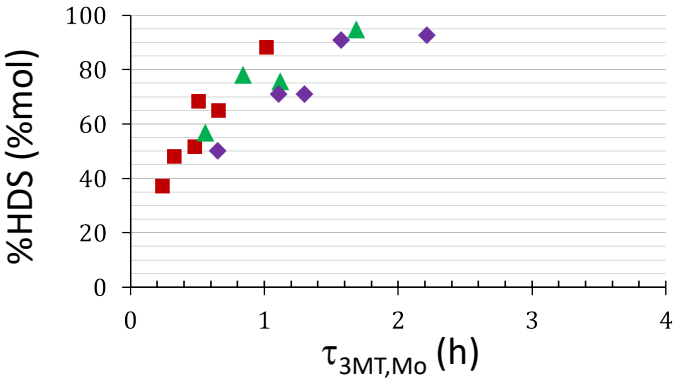

Figure 51. HDS yield as function of the contact time for CoMoS/δθ-Al_2O_3 at dMo variable, 0.9 (red), 2.2 (green) and 3.8 (purple) at.nm^{-2} of support at 220°C.

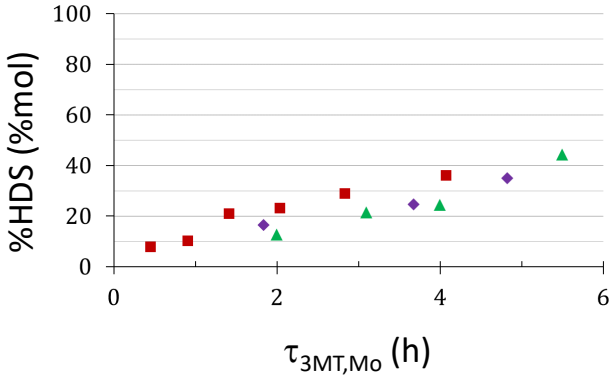

Figure 52. HDS yield as function of the contact time for CoMoS/SiO_2 at dMo variable, 0.9 (red), 2.2 (green) and 3.8 (purple) at.nm^{-2} of support at 220°C.

Appendix 17. (23DMB2N+23DMB1N) product distribution as function of (23DMB2N + 23DMB1N) conversion, for CoMoS catalysts at 220°C as a function of the dMo for the transformation of model FCC gasoline feedstock.

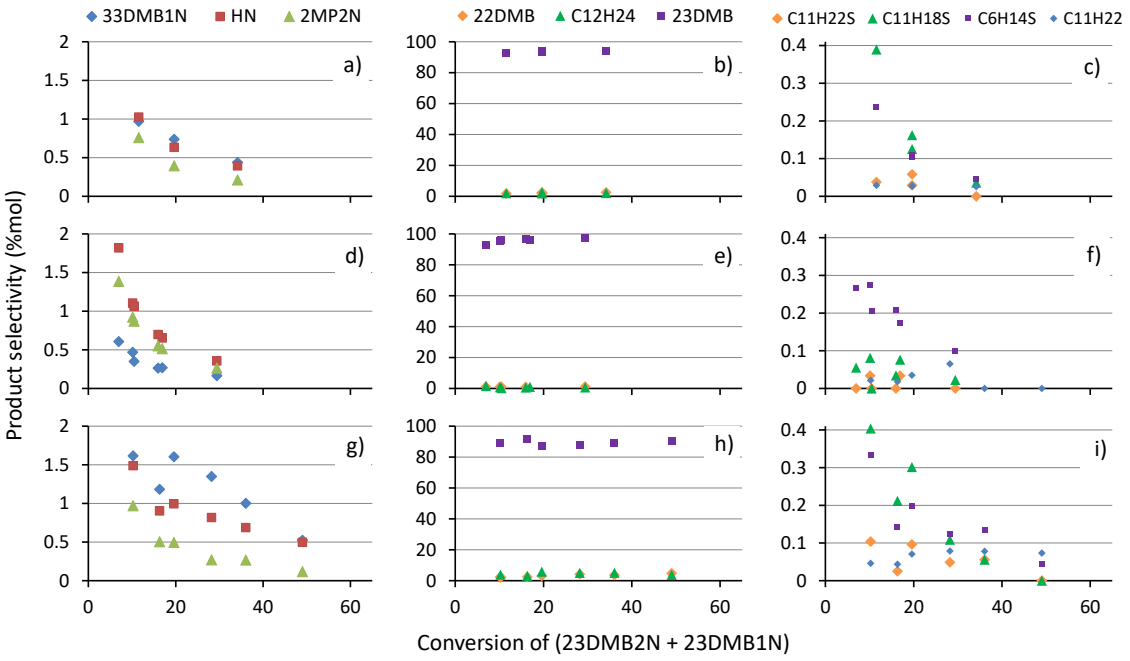

Figure 53. Selectivity of (23DMB2N+23DMB1N) products for CoMoS/δθ-Al_2O_3 at dMo of (a,b,c) 0.9, (d,e,f) 2.2, (g,h,i) 3.8 at.nm^{-2} at 220°C. Graphs in the center represent the product distribution of alkane from hydrogenation reaction of (23DMB2N+23DMB1N). Graphs on the right represent the product distribution heavy alkylthiophenes and hydrogenated products from 3MT side reaction with (23DMB2N+23DMB1N) olefins.

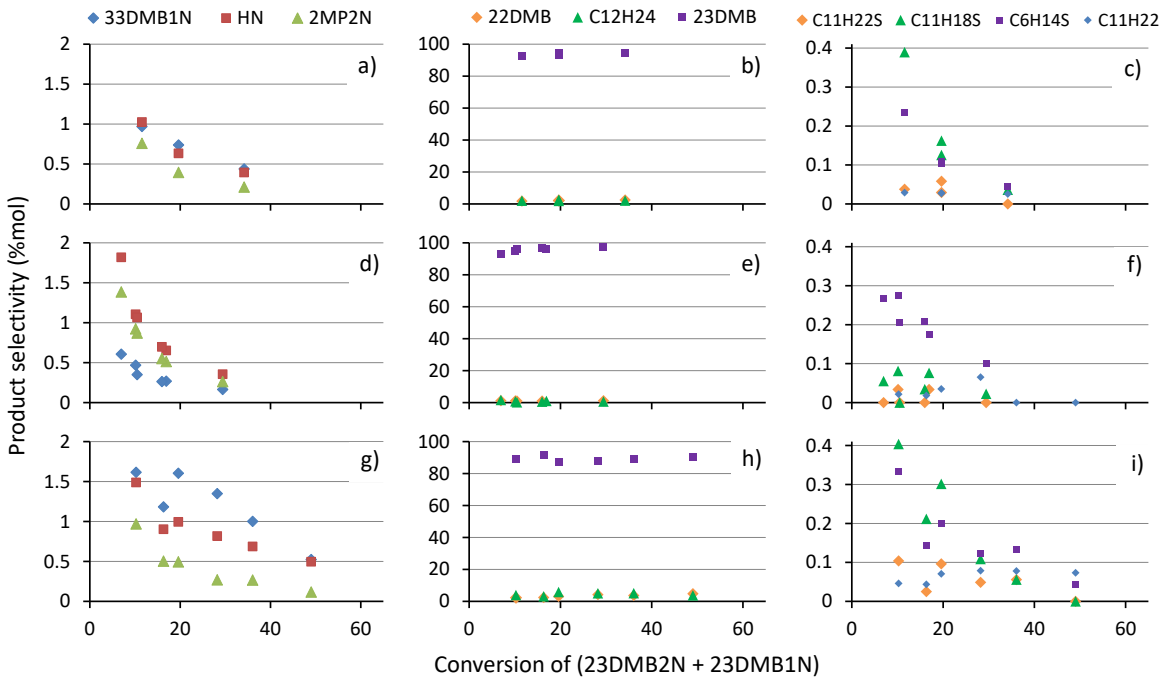

Figure 54. Selectivity of (23DMB2N+23DMB1N) products for $CoMoS/SiO_2$ at dMo of (a,b,c) 0.9, (d,e,f) 2.2, (g,h,i) 3.8 at.nm^{-2} at 220°C. Graphs in the center represent the product distribution of alkane from hydrogenation reaction of (23DMB2N+23DMB1N). Graphs on the right represent the product distribution heavy alkylthiophenes and hydrogenated products from 3MT side reaction with (23DMB2N+23DMB1N) olefins.

Appendix 18. HYDO yield as function of the contact time, $\tau_{Mo,23DMB2N}$, for CoMoS catalysts at 220°C for each dMo for the transformation of model FCC gasoline feedstock.

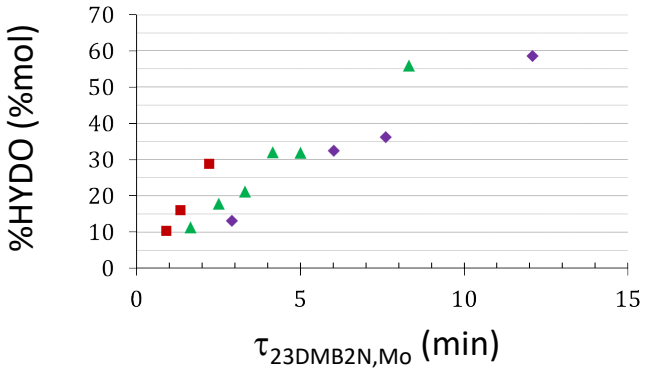

Figure 55. HYDO yield as function of the contact time for CoMoS/γ-Al_2O_3 at dMo variable, 0.9 (red), 2.2 (green) and 3.8 (purple) at.nm^{-2} of support at 220°C.

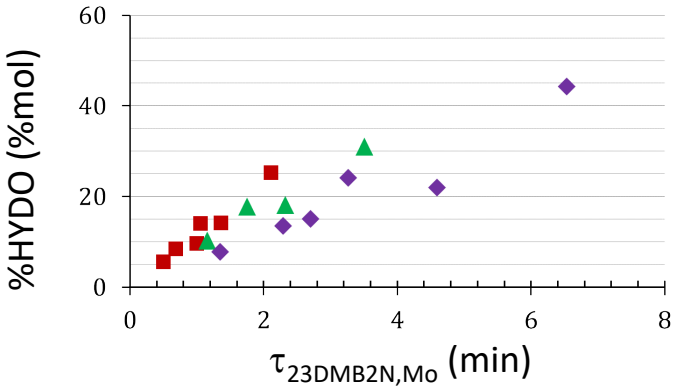

Figure 56. HYDO yield as function of the contact time for CoMoS/δθ-Al_2O_3 at dMo variable, 0.9 (red), 2.2 (green) and 3.8 (purple) at.nm^{-2} of support at 220°C.

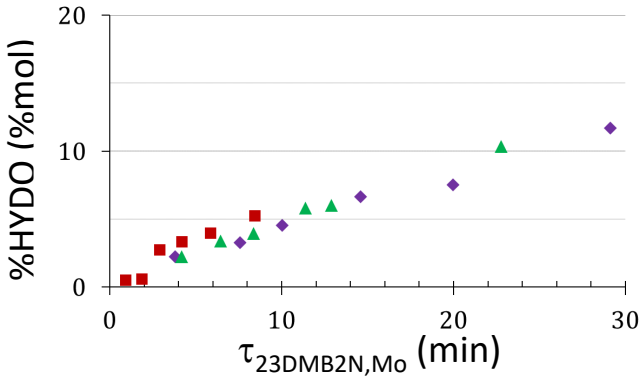

Figure 57. HYDO yield as function of the contact time for CoMoS/SiO_2 at dMo variable, 0.9 (red), 2.2 (green) and 3.8 (purple) at.nm^{-2} of support at 220°C.

Appendix 19. HDS catalytic tests with thiophenic or olefinic feedstocks.

In order to point out mutual inhibition between 3MT and alkenes during the transformation of FCC gasoline model feed reported in the previous section, we carried out catalytic activity measurements with feeds containing both families of reactants but also only the thiophenic molecule or olefin molecule alone in heptane. 3MT and (23DMB2N+23DMB1N) concentrations have been kept constant compare with the mixture model FCC gasoline feed, as well as operating conditions. CoMoS on γ, $\delta\theta$-Al_2O_3 and on SiO_2 at iso-dMo of 2.2 at.nm^{-2} of support have been tested.

Figure 58 presents the 3MT and (23DMB2N+23DMB1N) conversion for CoMoS at iso-support at dMo around 2.2 at.nm^{-2} in presence of mixture, thiophenic and olefin feed.

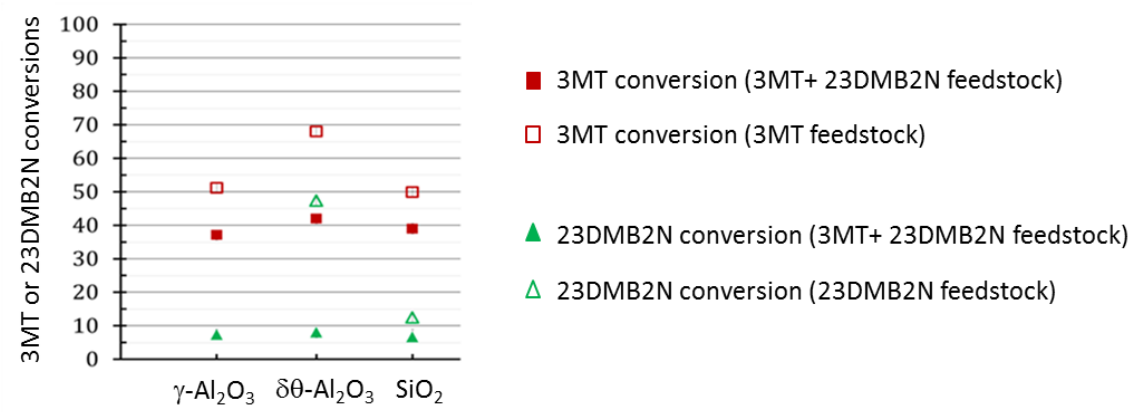

Figure 58. 3MT and HDS conversions for CoMoS on γ-, $\delta\theta$-Al_2O_3 and on SiO_2 at dMo around 2.2 at.nm^{-2} of support at respectively 180, 200 and 220°C (catalyst mass= 0.198g, 0.174g and 0.131g for respectively CoMoS on γ-, $\delta\theta$-Al_2O_3 and on SiO_2) to reach similar conversions. 3MT and (23DMB2N+23DMB1N) conversions obtained on the mixture model FCC gasoline feed correspond to squares and triangles respectively. HDS and HYDO conversions obtained from the thiophenic feed only or the olefinic feed only correspond to empty symbols. *noted that ideally the temperature should be the same but here it is considered that temperature variation is not sufficient to impact the order of the experimental observation.

It can be noticed that the thiophenic molecule is a strong inhibitor for the hydrogenation reaction of alkenes (2DMB2N+23DMB1N) for the $\delta\theta$-Al_2O_3 supported catalysts. HYDO conversion with the pure alkene feed is ~7 times higher than HYDO conversion measured on the mixture model FCC gasoline feed. Regarding CoMoS/SiO_2, the inhibitor effect of 3MT on the HYDO reaction is significantly less important (< 2 times higher).

However, (23DMB2N+23DMB1N) has also an inhibitor effect on the HDS reaction of 3MT though more moderate. Indeed, HDS conversion is around 1.5 times higher when only 3MT is present in the feed. Such inhibiting effects have been already reported in previous experimental works[7] and can be explained by the stronger adsorption energies of thiophenic molecules than olefinic ones on the edges of a CoMoS active phase, as earlier reported by Krebs et al [12]. Although the adsorption energies of olefin are less exothermic than the thiophene, the significantly higher concentration of olefin in the feed counterbalances it in part, which also explains its inhibiting effect on thiophene.

Thus, these results could mean that the inhibiting effect depends on the nature of the support: in particular the inhibiting effect of 3MT on olefin is apparently lower on the silica support than on the delta/theta alumina one.

6 References

[1] N. Dos Santos, Contrôle de La Sélectivité Des Réactions D'hydrodésulfuration et D'hydrogénation En Hydrotraitement: Étude Cinétique Sur Des Essences Craquées Modèles, **2008**.

[2] N. Dos Santos, H. Dulot, N. Marchal, M. Vrinat, *Appl. Catal. A Gen.* **2009**, *352*, 114–123.

[3] D. Mey, Hydrodesulfuration Poussée Des Essences. Influence Des Propriétés Acido-Basiques Des Catalyseurs Sur La Sélectvitité En Hydrodesulfuration Par Rapport à L'ydrogénation Des Oléfines, **2002**.

[4] D. Mey, S. Brunet, C. Canaff, F. Maugé, C. Bouchy, F. Diehl, *J. Catal.* **2004**, *227*, 436–447.

[5] C. Fontaine, Y. Romero, A. Daudin, E. Devers, C. Bouchy, S. Brunet, *Appl. Catal. A Gen.* **2010**, *388*, 188–195.

[6] C. Fontaine, Y. Romero, A. Daudin, E. Devers, C. Bouchy, S. Brunet, *Appl. Catal. A Gen.* **2010**, *388*, 188–195.

[7] S. Brunet, D. Mey, G. Pérot, C. Bouchy, F. Diehl, *Appl. Catal. A Gen.* **2005**, *278*, 143–172.

[8] D. Laurenti, B. Phung-Ngoc, C. Roukoss, E. Devers, K. Marchand, L. Massin, L. Lemaitre, C. Legens, A.-A. Quoineaud, M. Vrinat, *J. Catal.* **2013**, *297*, 165–175.

[9] T. Mochizuki, H. Itou, M. Toba, Y. Miki, Y. Yoshimura, **2008**, 1456–1462.

[10] M. Li, H. Li, F. Jiang, Y. Chu, H. Nie, *Catal. Today* **2010**, *149*, 35–39.

[11] P. Raybaud, *Appl. Catal. A Gen.* **2007**, *322*, 76–91.

[12] E. Krebs, B. Silvi, a. Daudin, P. Raybaud, *J. Catal.* **2008**, *260*, 276–287.

- Chapter IV -
Support's effects on the physico-chemical properties of the Co promoted MoS_2 phase

Table of contents

1 Introduction 175

2 Experiments 178

2.1 Catalysts preparation 178

2.2 Catalysts characterization 182

2.2.1 X-ray photoelectron spectroscopy (XPS) 182

2.2.2 High resolution transmission electron microscopy (HRTEM) 183

2.2.3 2D morphology model of CoMoS slabs 184

3 Results and discussion 187

3.1 Morphology and size analysis the CoMoS nano-crystallites 187

3.1.1 Analysis of mean sizes and stacking number by HRTEM 187

3.1.2 HR HAADF STEM analysis 190

3.1.2.1 2D and 3D morphology analysis 190

3.1.2.2 Effect of $\delta\theta$-Al_2O_3 facets on the CoMoS crystallites' sizes 193

3.1.2.3 Role of hydroxyls groups as function of the exposed facets 195

3.1.3 Impact on the catalytic activity and genesis of the active phase 197

3.1.4 Possible role of the corners and edges of γ-Al_2O_3 crystallites 199

3.2 Molybdenum and cobalt surface speciation 200

3.2.1 Analysis of Mo 3d levels BE by XPS and DFT 202

3.2.1.1 Case of dMo=2.2 at.nm^{-2} 202

3.2.1.2 Electronic effect of the support 204

3.2.1.3 Size effect correlated with low coordination edge sites 205

3.2.1.4 Promoter effect on Mo binding energy 207

3.2.1.5 Effect of Mo surface coverages 208

3.2.1.6 Mo species quantification 210

3.2.2 Analysis of Co 2p levels BE by XPS 211

3.2.2.1 Co species quantification 213

3.2.2.2 $(Co/Mo)_{slab}$ atomic ratio 215

3.3 2D morphology model of the CoMoS slab 216

3.3.1 Distribution of Co and Mo atoms at M-edge and S-edge 216

3.3.2 2D morphology model of the CoMoS slab vs catalytic activity of the HDS catalysts 220

4 Conclusion 222

5 Appendices 226

6 References 250

1 Introduction

Many European environmental regulations aimed at decreasing toxic compound contents, especially sulfur-based ones, in the gasoline formulation as well as in diesel.[1–3] So, the hydrodesulfurization (HDS) is a key industrial process to reach these targeted specifications on clean fuels. Focusing on the gasoline produced from the fluid catalytic cracking (FCC) unit, HDS is specifically used to remove undesirable sulfur compounds while maintaining the combustion quality (octane number) owed to olefins. Industrial catalysts involved in the HDS process are based on an transition metal sulfides (TMS) active phases, usually MoS_2 phase supported on alumina where the MoS_2 nano-slabs are decorated at the edges by cobalt atoms to form the mixed CoMoS phase.[4–10] So research has to address a threefold challenge which is to selectively desulfurize sulfur compounds while the olefins hydrogenation (HYDO) must be avoided in order to keep a high octane number of the gasoline product. Thus, the design of more efficient selective HDS catalysts has become a major concern for research in order to understand the catalytic behavior of the CoMoS active phase and also the important direct or indirect roles played by the support.

Regarding the active phase itself, several studies were conducted to establish which relevant parameters are impacting the properties of the MoS_2 based active phase with the aim of designing new selective HDS catalysts. Indeed, Daage and Chianelli[11] proposed the so-called rim-edge model for the unsupported MoS_2 phase which highlights the potential role of stacking on the selective desulfurization *vs* hydrogenation pathways of dibenzothiophene compounds and could be extended to HDS/HYDO selectivity. More recently, combining experimental and computational studies on several unsupported transition metal sulfides, some authors reveal that the HYDO, HDS activities and HDS/HYDO selectivity depends on the sulfur-metal bond energy of the active phase according to a volcano curve relationships.[12,13] Density functional theory (DFT) calculations on promoted MoS_2 phases further highlighted that the nature of the promoter (Co or Ni) and the type of promoted edge (S-edge *vs* M-edge) directly modifies the adsorption energies of the 2-methyl-thiophene and 2,3-dimethylbut-2-ene which may explain catalytic trends observed in HDS/HYDO selectivity as a function of the nature of the active phases.[13] In line with this theoretical analysis, Baubet et al.[14] showed that the experimental selectivities correlate with the

two-dimensional shapes (ratio of S-edge/M-edge) of the CoMoS nano-crystallites supported on δ-alumina: the analysis was provided by High Resolution High-Angle Annular Dark Field Scanning Transmission Electron Microscopy (HR HAADF-STEM).

Regarding support effects, Fan and coworkers[15] showed that, depending on the nature and properties of the support (alumina or silica), the stacking of the active phase as well as its dispersion can be directly modified. They demonstrate that a compromise between the dispersion and the stacking of supported CoMoS slabs is crucial in order to reach the highest ratio between sulfur and olefins adsorption sites leading to the higher HDS/HYDO selectivity. Li et al.[16] proposed that the support impacts the CoMoS phase by modifying the slab length and consequently the ratio between atoms located at the edge and the corner of promoted MoS_2 slabs. They showed that silica supported catalyst which has the CoMoS slabs with the higher length and so the higher edge/corner ratio, induces the higher HDS/HYDO selectivity. Thus, it was suggested that support enhanced indirectly the HDS/HYDO selectivity, by modifying the CoMoS length slab, in the following order: CoMoS on γ-Al_2O_3 < $\gamma\delta$-Al_2O_3 < SiO_2. Qiherima et al.[17] compared two CoMoS catalysts supported on two different aluminas and show that the Mo loading could modify the morphology in term of length and stacking of the slab and also the concentration of promoted CoMoS species. Laurenti et al.[18] suggest that the nature of the support could affect the cobalt promotion of the MoS_2 slab at the edge. They show in particular that on the silica support, the amount of CoMoS sites, determined by XPS and ICP experiments, are more than twice lower than on γ-Al_2O_3 for a similar Mo density (dMo) and Co/Mo ratio. An in-depth study combining XPS, TEM and AFM experiments and DFT calculation, focus on the orientation of MoS_2 slabs as function of the crystallographic planes of the alumina support was conducted by Bara et al.[19]. It was shown a dependence between support surface exposed and the strength of the metal/support interactions leading to a change of the length, stacking, sulfidation degree, and orientation of the MoS_2 slabs by edge or basal-bonding of the CoMoS slab.

Considering the results previously exposed, it is obvious that several physico-chemical properties and atomic scale features (Cobalt edge contents, 2D shape, 3D-stacking, crystallite's length) of the CoMoS active phase may impact the catalytic selectivity. However, it is still not clear how these physico-chemical properties can be modulated by the support itself. In addition, for a given support, another important parameter which may influence the

resulting physico-chemical properties is the molybdenum loading which directly changes the surface concentration of the MoS_2 nano-crystallites on the support.

Thus, the objective of the present work is to elucidate how the physico-chemical properties and morphologies of the CoMoS phase are modified according to relevant parameters such as the nature of support, metal content and promoter/active phase ratio, slab stacking and to quantify the impact of each parameter on the resulting CoMoS phase. For that purpose, we propose a multi-technique approach combining XPS, TEM and HR-STEM to better characterize the physico-chemical properties and atomic scale features of the CoMoS active phases as a function of the Mo coverage (dMo), the Co/Mo ratio on three different supports, γ- and $\delta\theta$- aluminas and silica. Moreover, HR HAADF-STEM experiments were undertaken to identify the morphology of the CoMoS slab as a function of the support effect for the most relevant systems. Finally, a 2D morphology model of the CoMoS nano-crystallites is proposed with quantifications of S or M-edge promoted (or not) by the Co atoms, by using insights taken from previous DFT calculations.[20]

2 Experiments

2.1 Catalysts preparation

The various cobalt promoted MoS_2 phases were prepared on three different supports: γ-Al_2O_3, $\delta\theta$-Al_2O_3 and SiO_2. The alumina supports were used as extrudates (dimensions around 2-4 mm with diameter of 1.6 mm) and the silica support as porous pellets (diameter around 0.315-1mm). The supports' characteristics are reported in Table 1.

Table 1. Physical properties of the γ-Al_2O_3, $\delta\theta$-Al_2O_3 and SiO_2.

Supports	γ-Al_2O_3	$\delta\theta$-Al_2O_3	SiO_2
S_{BET} ($m^2.g^{-1}$)	285	81	232
$V_{mesopores}$ ($ml.g^{-1}$)	0.65	0.76	0.78
$V_{macropores}$ ($ml.g^{-1}$)	0.01	-	0.21
Pore diameter (nm)	6.8 - 11.0	35.8	14.9

γ-Al_2O_3 and $\delta\theta$-Al_2O_3 are obtained from a thermal treatment of the same boehmite at respectively 450°C and 900°C. Formation of transition alumina occurs according to a well-established dehydration mechanism.[21–23] Simultaneously to the dehydration phenomena (formation and elimination of H_2O), contraction and translation of the individual layers occurs to form γ-Al_2O_3, and then δ-, θ-Al_2O_3 polymorphs (Figure 1). Transformation from γ-Al_2O_3, to δ-, θ-Al_2O_3 leads to an increase of the Al^{4+} at the expense of Al^{6+}.[24]

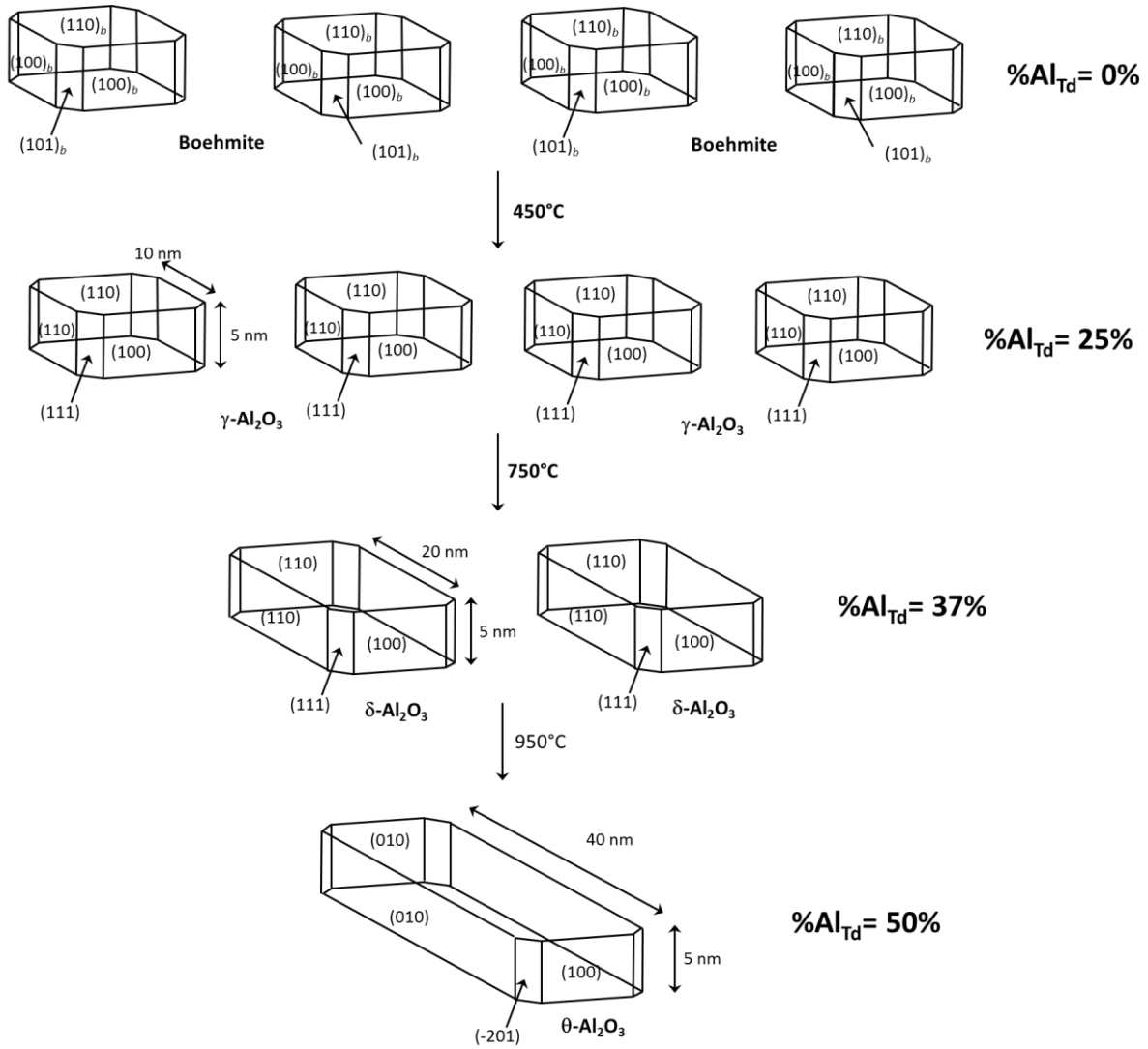

Figure 1. Morphologic model of γ-, δ- and θ-Al_2O_3 crystallites formed respectively from boehmite dehydration and γ-Al_2O_3 sintering. Adapted from[23,25]

By Scanning Electron Microscopy, alumina platelets sizes were observed to be as high as 50-100 nm and 200-250 nm for the γ-Al_2O_3 and δθ-Al_2O_3, respectively (Appendix 1). However, due to the resolution of the SEM analysis we cannot distinguish that these observed objects are made of individual platelet or that they are not made of aggregates of several platelets. Indeed as it will be shown by HR STEM analysis (section 3.1.2), we will be able to identify nano-crystallites down to 30 nm for δθ-Al_2O_3, whereas the γ-Al_2O_3 nano-sizes could even be smaller. Figure 2 presents the XRD pattern of the γ-Al_2O_3 (black) and δθ-Al_2O_3(blue) support. δθ-Al_2O_3 differs from γ-Al_2O_3 diffractogram by the refinement and the increase of the intensity of the diffractogram along with the splitting of two peaks corresponding to (400) and (440) diffraction plans (respectively identified at about 46.8° and 67° 2θ). The existence of these 2 peaks at higher scattering angle is specific of alumina with a

tetragonal structure, δ-Al_2O_3 phase.[26] Moreover, the existence of an additional strong and narrow peak at about 33, 46.8° 2θ confirms the presence of θ-Al_2O_3 phase which corresponds more specifically to the migration of the aluminum atoms in octahedral to tetrahedral geometric environment.[23] These results attest the denomination give to the $\delta\theta$-Al_2O_3.

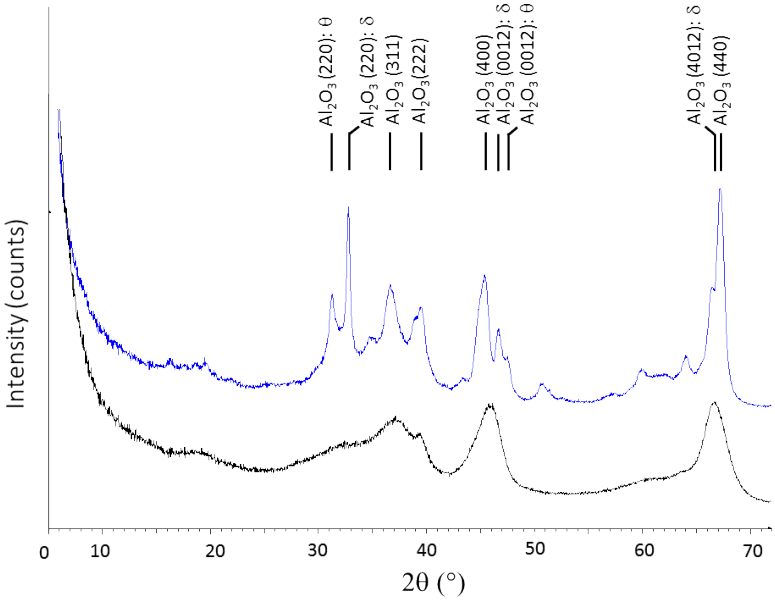

Figure 2. XRD pattern of γ-Al_2O_3 (black) and $\delta\theta$-Al_2O_3(blue).

HDS catalysts were prepared by incipient wetness impregnation. Impregnation solutions were prepared from MoO_3 and $Co(OH)_2$ precursors dissolved in aqueous solution in presence of H_3PO_4. Impregnation was performed on support extrudates (1.6 mm diameter) followed by an ageing step at RT for 12 h to allow metal diffusion throughout the extrudate. Then, solids were dried in an oven at 120°C for 24h and calcined in air at 450°C for 2h15. Finally, oxide catalysts are presulfided ex situ by heating at 5°C.min^{-1} from room temperature to 350°C at atmospheric pressure in a flow of 15 vol.%H_2S in H_2 (1.5 L.h^{-1}g^{-1} of catalyst). Sulfidation was achieved at 350°C for 2h15. The presulfided catalysts were then flush under argon and isolated under vacuum at 200°C in a sealed ampoule.

On each support, three molybdenum loadings were introduced to obtain surface densities (called dMo in what follows) from 0.9 to 4.8 by nm.² of support. In order to compare catalysts at iso-dMo and iso-support, Co/Mo and P/Mo molar ratios are also kept constant respectively 0.4 and 0.27 (Table 2). CoMoS/$\delta\theta$-Al_2O_3 catalysts have been prepared at iso-dMo of 2.2 at.nm^{-2} at Co/Mo molar ratio variable from 0.1 to 0.4 with a P/Mo kept

constant at 0.27. MoS_2 and Co_9S_8 supported on $\delta\theta$-Al_2O_3 and SiO_2 reference materials are also prepared in accordance to the CoMoS on $\delta\theta$-Al_2O_3 and SiO_2 at iso-dMo of 2.2 at.nm^{-2} (according to the same preparation steps mentioned above for CoMoS supported catalysts).

The XRF elemental analysis of Co, Mo and P on different supports ensures the consistency with the targeted elemental contents for the Tables 2 and 3).

Table 2. XRF elemental analysis on the calcined oxide CoMo precursors of the CoMoS phase over the three supports.

Supports	dMo (at.nm^{-2} of support)	(Co/Mo) $_{molar}$	(P/Mo) $_{molar}$	% wt Co	% wt Mo	% wt P
γ-Al_2O_3	0.9	0.39	0.29	0.99	4.10	0.38
	2.1	0.38	0.29	1.95	8.40	0.79
	3.8	0.39	0.26	3.19	13.48	1.12
	4.8	0.39	0.27	3.76	15.83	1.39
$\delta\theta$-Al_2O_3	0.9	0.36	0.28	0.28	1.25	0.11
	2.2	0.10	0.26	0.16	2.58	0.22
	2.2	0.20	0.70	0.32	2.60	0.23
	2.2	0.39	0.27	0.71	2.94	0.26
	3.6	0.39	0.27	1.09	4.58	0.39
	4.5	0.39	0.25	1.34	5.63	0.45
SiO_2	0.7	0.32	0.25	0.52	2.67	0.22
	2.3	0.39	0.23	1.86	7.78	0.58
	3.7	0.39	0.23	2.68	11.22	0.83

Table 3. XRF elemental analysis of the calcined oxide precursors of the unpromoted MoS_2 on $\delta\theta$-Al_2O_3 and MoS_2 on SiO_2, and Co_9S_8/$\delta\theta$-Al_2O_3 reference materials

Sulfided catalysts	dMo (at.nm^{-2} of support)	(Co/Mo) $_{molar}$	(P/Co) $_{molar}$	(P/Mo) $_{molar}$	% wt Co	% wt Mo	% wt P
MoS_2/SiO_2	2.2	-		0.28	-	6.71	0.60
Co_9S_8/SiO_2	-	-	2.70		1.75	-	2.61
MoS_2/$\delta\theta$-Al_2O_3	2.3	-	-	0.27	-	3.06	0.26
Co_9S_8/$\delta\theta$-Al_2O_3	-	-	2.56	-	0.74	-	0.97

The catalysts prepared are all in good agreement with the targeted catalysts except for the SiO_2 supported catalyst at a dMo of 0.7 Mo at.nm^{-2} with a Co/Mo ratio around 0.32 whereas the expected dMo was 0.9 Mo at.nm^{-2} and the Co/Mo ratio was 0.4.

2.2 Catalysts characterization

2.2.1 X-ray photoelectron spectroscopy (XPS)

X-ray photoelectron spectroscopy (XPS), (Appendix 2), analyses of the catalysts were performed using a Kratos Axis Ultra spectrometer equipped with a monochromatic Al Kα source (1486,6 eV) and a hemispherical analyzer. Measurements were carried out at room temperature under high vacuum 10^{-9} Torr in the analysis chamber with 40 eV pass energy. Sulfided samples were prepared in a glovebox directly connected to the analysis chamber (under controlled atmosphere), ground, pressed in indium foil and stuck on the sample bar with a double side carbon scotch. XPS spectra were fitted with Casa XPS software (version 2.0.71). A Shirley background subtraction was applied and Gaussian-Lorentzian (70%-30%) curves were used.

The measurements were done at 0.05 eV intervals for the Cobalt and 0.1 eV intervals for molybdenum, phosphorus, sulfur, aluminum and carbon. The binding energy of each element is referenced to the binding energy of the C1s level of the contamination carbon at 284.6 eV.

Quantification of Mo and Co species are performed based on the work of Gandubert et al.[27] The identified Mo species correspond to Mo(+IV) attributed to MoS_2 species, to Mo(+V) oxidation state attributed to oxysulfide species (MoS_xO_y) and to Mo(+VI) oxidation state attributed to the Mo oxide phase. The identified Co species correspond to three distinguished species: Co(+II) species attributed to a Co oxide phase (such as CoO), a Co species attributed to a Co sulfided species (as Co_9S_8) and a Co sulfided species present in the mixed CoMoS phase. In order to validate the stoichiometry of the MoS_2 phase between the Mo and S atoms engaged on it, the S/Mo ratio has been determined.

$$\frac{S}{Mo} = \frac{[S]_{sulphided} - [Co]_{sulphided} \times 8/9}{[MoS_2]_{sulphided}}$$

Where $[S]_{sulfided}$ is the atomic concentration of S engaged in the sulfided phase, $[Co]_{sulfided}$ is the atomic concentration of Co engaged in the Co_xS_y phase with the following stoichiometry considered x=9, y=8 and $[MoS_2]$ is the atomic concentration of Mo engaged in the MoS_2 phase.

When the decomposition of the Co XPS spectra is performed, a binding energy difference of 549.95 eV +/- 0.1 eV between Co $2p_{3/2}$ and Mo(+IV) $3d_{5/2}$, corresponding to the identified

CoMoS mixed phase, is fixed. Relative uncertainty on the global amount of Mo or Co (%wt) is evaluated at ±10%. Relative uncertainty on the amount of Mo engaged in each phase (Mo oxide, MoS_xO_y and MoS_2) and Co engaged each phase is evaluated at ±10%. Thus, the uncertainties $(Co/Mo)_{slab}$ is evaluated at ±20%. An example of the decomposition of Mo 3d and Co 2p spectra is shown in Figure 3 according to Gandubert et al.[27]

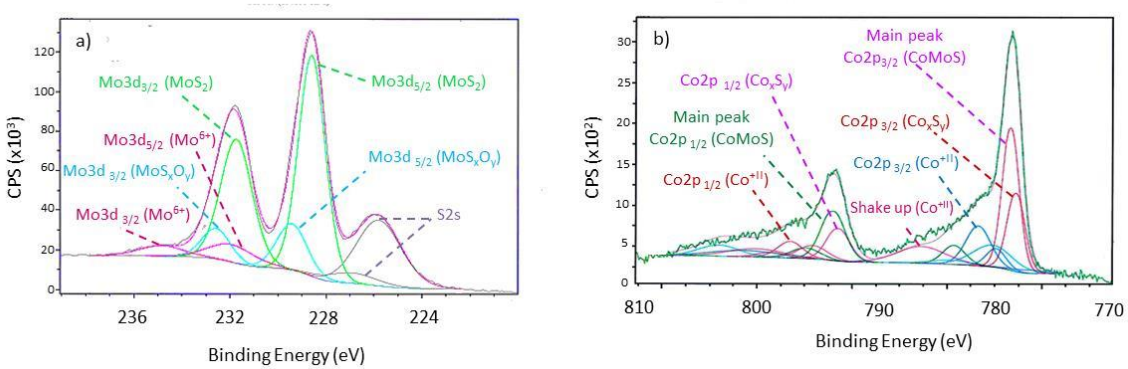

Figure 3. Example of decomposition of XPS spectra of CoMoS/γ-Al_2O_3 at dMo of 3.8 at.nm^{-2} of support according the ref.[27] a) XPS Mo3d spectrum (in pink: Mo^{VI+} oxide contributions; in blue: MoS_xO_y oxysulfide contributions; in green: MoS_2 contributions). b) Co2p spectrum (in blue: Co^{+II} oxide contributions; in red: Co_xS_y contributions; in pink: CoMoS mixed phase contributions).

2.2.2 High resolution transmission electron microscopy (HRTEM)

High resolution transmission electron microscopy (HRTEM) observations were performed using a JEOL 2100F FEG TEM, operated at 200 kV. Sulfided catalysts, kept in sealed ampoules, were crushed in ethanol and sonicated. A drop of the suspension was deposited on a Cu grid covered by a holey carbon membrane. Ethanol is evaporated and TEM analysis is performed. By HRTEM, MoS_2 nano-layers can be observed only when their basal planes are oriented parallel to the electron beam axis. The mean length and stacking number of MoS_2 nano-layers were calculated by analyzing at least 200 nano-layers, using an in-house image processing software: the image is pre-processed in order to stretch contrast, and then a region growing algorithm and active contour techniques are used to obtain slab contours. MoS_2 nano-layers with sizes lower than 1 nm are not detected. Relative uncertainties on the slab length and on the stacking number are evaluated at ±10% and ±15% respectively.

High resolution high-angle annular dark-field scanning transmission electron microscopy (HR HAADF-STEM) analyses were performed using a FEG TEM/STEM system (JEOL, Model 2100 F) that was operated at 200 kV and equipped with a probe Cs corrector. For HAADF acquisition, the camera length was 10 cm, corresponding to the inner and outer diameters of annular

detector of ~60 and 160 mrad. The samples were prepared in the same way as for HRTEM analysis. Three selected catalysts have been investigated using this technique.

2.2.3 2D morphology model of CoMoS slabs

Results of characterization (TEM analysis, FX analysis and XPS experiments) and previously published DFT calculations can be correlated in order to obtain the two dimensional (2D) morphology of the CoMoS slab.

First, as mentioned in the chapter I, part 2.2.1, Krebs and coworkers[28] have studied the equilibrium morphology of the CoMoS crystallites. In our HDS reaction conditions, a hexagonal shape was found to be stable for the CoMoS crystallite, which means that the M-edge sites and S-edge sites represent both 50% of the total edge. This hexagonal shape with a (50%/50%) M-edge/S-edge ratio will be considered as representative in the following study.

But it is important to keep in mind that this approach based on DFT results will lead to one plausible model representation of unsupported MoS_2 slabs for each catalyst and it does not necessarily correspond to a complete view of CoMoS slabs supported on alumina or silica.

This approach is also compatible with the earlier Kasztelan's geometrical model[29] proposing the hexagonal shape as being one of the most relevant 2D morphologies for MoS_2 based active phases. Thus, by considering a hexagonal shape and considering the slab length obtained in TEM analysis, the quantification of the Mo atoms contained in each slab, at the edges and in the basal plane will be determined for each individual crystallite.

Mo atoms of the CoMoS slab, Mo_{slab} and Mo atoms at the edge of the CoMoS slab Mo'_{edge} which respectively corresponds to number of Mo by MoS_2 slab and the Mo atoms at the edges of MoS_2 slab can be expressed as function of the number of Mo-Mo bonds (*n*):

$$Mo_{slab} = 3n^2 + 3n + 1 \qquad \textit{Eq. 1}$$

$$Mo'_{edge} = 6 \times n \qquad \textit{Eq. 2}$$

And by considering the average length of the slab obtained from TEM analysis, L_{TEM}, and the Mo atoms diameter d_{Mo-Mo}, n is expressed as below:

$$n = \frac{L_{TEM}}{2 \times d_{Mo-Mo}} \qquad \textit{Eq. 3}$$

Thus,

$$Mo_{slab} = 3\times\left(\frac{L_{TEM}}{2\times d_{Mo-Mo}}\right)^2 + 3\times\left(\frac{L_{TEM}}{2\times d_{Mo-Mo}}\right) + 1 \qquad \textit{Eq. 4}$$

$$Mo'_{edge} = 3\times\frac{L_{TEM}}{d_{Mo-Mo}} \qquad \textit{Eq. 5}$$

However, in the case of CoMoS catalysts, the cobalt decoration degree at the edges of the MoS_2 slab, X_{Co} , needs also to be taken into account.

$$X_{Co} = \frac{Co_{(CoMoS)}}{Mo'_{edge}} \qquad \textit{Eq. 6}$$

where $Co_{(CoMoS)}$ stands for the number of Co atoms engaged in the CoMoS phase (cobalt atoms decorated the edges) per gram of catalyst and Mo_{edge}, for the number of molybdenum atoms at the edges of MoS_2 slab.

Moreover, by XPS analysis the average (Co/Mo) ratio in the MoS_2 slab can be expressed as:

$$\left(\frac{Co}{Mo}\right)_{Slab} = \frac{Co_{(CoMoS)}}{Mo_{(slab)} - Co_{(CoMoS)}} = \frac{Co_{(CoMoS)}}{Mo_{(MoS_2)}} \qquad \textit{Eq. 7}$$

with $Mo_{(MoS2)}$, number of Mo atoms in the MoS_2 phase.

Finally, we can express the X_{Co} as function of the (Co/Mo)slab, the Mo_{slab}, and the Mo_{edge} as it follows:

$$X_{Co} = \frac{\left(\frac{Co}{Mo}\right)_{Slab}}{1+\left(\frac{Co}{Mo}\right)_{Slab}} \times \frac{Mo_{slab}}{Mo'_{edge}} \qquad \textit{Eq. 8}$$

However, the number of Mo atoms real, $Mo_{edge-real}$ at the edge can be written according to the expression below:

$$Mo_{edge-real} = Mo'_{edge} \times (1 - X_{Co}) \qquad \textit{Eq. 9}$$

And the real number of Mo atoms engaged in the MoS_2 slab can be recalculated as follow:

$$Mo_{slab/real} = Mo_{slab} - Mo'_{edge} \times X_{Co} \qquad \textit{Eq. 10}$$

Finally, we will consider that the decoration of the S-edge by Co atoms is more stable than the decoration of the M-edge, according the DFT calculations performed by Krebs *et al.*[13] This theoretical result needs to be considered in order to determine the number of Co atoms

which decorate the M- or S-edge. Finally, considering 50% of S-edge and 50% of M-edge at the edge slab, the Co atoms at the M- or S-edge respectively $Co_{S\text{-}edge}$ and $Co_{M\text{-}edge}$ and the Mo atoms at the M- or S-edge respectively $Mo_{S\text{-}edge}$ and $Mo_{M\text{-}edge}$ can be determined.

The number of slabs will be calculated by taking into account the number of sulfided Mo atoms per gram of catalyst, $Mo_{sulf/g}$, as a function of the number of the Mo total atoms, Mo_{tot}, and of the molybdenum sulfidation degree, R_S, obtained respectively by XRF and XPS analysis:

$$Mo_{sulph/g} = Mo_{tot} \times R_S \qquad \textit{Eq. 11}$$

The number of slab by g of catalyst, $N_{slab,}$ is the ratio between the sulfided Mo atoms by gram of catalyst and the real number of Mo atoms engaged in the slab :

$$N_{slab} = \frac{Mo_{sulph/g}}{Mo_{slab/real}} \qquad \textit{Eq. 12}$$

Finally, the number of slabs can be expressed per gram of catalyst or per gram of Mo respectively N_{slab} and N'_{slab}, taking into account the Mo content measured from XRF (Mo_{XRF}), the Avogadro's number (Na) and the Mo molecular weight (M_{Mo}).

$$N_{slab} = \frac{\%Mo_{XRF} \times N_a}{M_{Mo} \times (1 - PAF - \%Mo_{XRF} - \%Co_{XRF} \%P_{XRF})} \times \frac{R_S}{Mo_{slab/real}} \quad \text{by gram of catalyst,}$$

$$N'_{slab} = \frac{N_a}{M_{Mo} \times (1 - PAF - \%Mo_{XRF} - \%Co_{XRF} \%P_{XRF})} \times \frac{R_S}{Mo_{slab/real}} \quad \text{by gram of Mo,}$$

Thus, to obtain the quantification in number of $Co_{S\text{-}edge}$, $Co_{M\text{-}edge}$, $Mo_{S\text{-}edge}$ and $Mo_{M\text{-}edge}$ by gram of catalyst or Mo, previous values should be multiplied by the number of slabs by gram of catalyst or gram of Mo respectively.

3 Results and discussion

3.1 Morphology and size analysis the CoMoS nano-crystallites

3.1.1 Analysis of mean sizes and stacking number by HRTEM

After sulfidation, the mean lengths and stacking numbers of the MoS_2 nano-crystallites on each support for various dMo and Co/Mo ratio have been characterized by TEM analysis and are reported in Figure 4 and Figure 5.

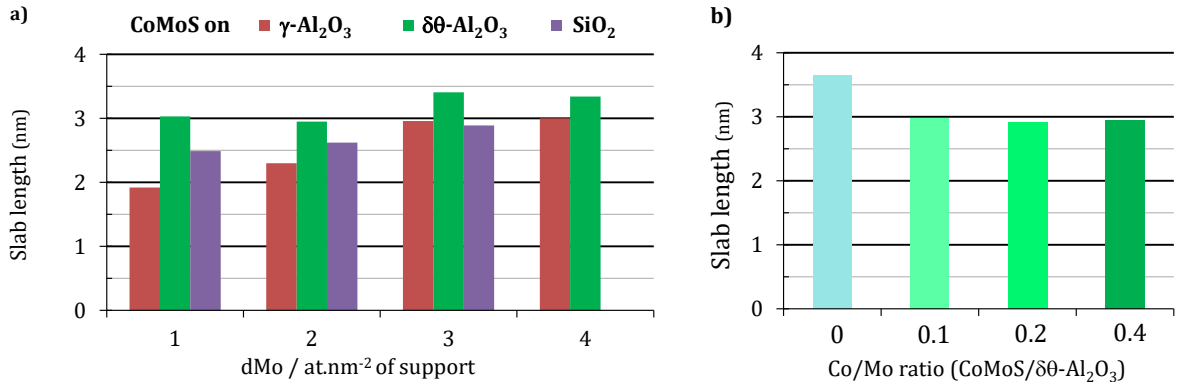

Figure 4. Average slab length as function of (a) the dMo for CoMoS γ-, δθ-Al_2O_3 and SiO_2 for a Co/Mo ratio close to 0.4 and of (b) Co/Mo molar ratio for CoMoS/δθ-Al_2O_3 with a Co/Mo equal to 0 for the unpromoted MoS_2. The relative uncertainty on the slab length is ±10%.

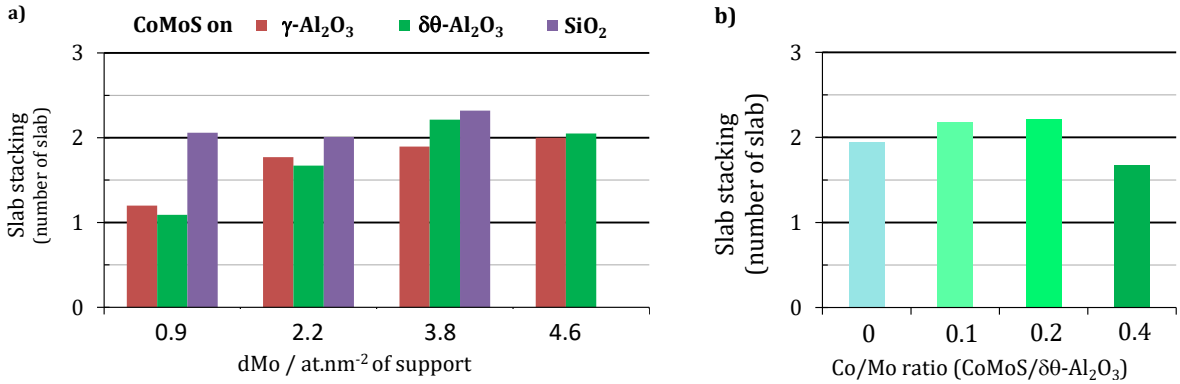

Figure 5. Average slab stacking as function of (a) dMo for CoMoS γ-, δθ-Al_2O_3 and SiO_2 for a Co/Mo ratio close to 0.4 and of (b) Co/Mo molar ratio for CoMoS/δθ-Al_2O_3 with a Co/Mo equal to 0 for the unpromoted MoS_2. The relative uncertainty on the stacking number is ±15%.

First, by comparing the slab size of the unpromoted MoS_2 catalyst with the Co-promoted catalysts at higher Co/Mo ratio, it can be noted that the slab length decreases significantly as soon as a low amount of cobalt is added (Co/Mo equal to 0.1). For Co/Mo ratio higher than 0.1, it appears that the length of the CoMoS slabs supported on the δθ-Al_2O_3 support does not strongly depend on the Co/Mo ratio. By contrast, the stacking number is weakly

modified by the Co/Mo ratio. These results are qualitatively consistent with the Co/Mo ratio effect on the slab length reported in the literature.[18,27] For silica-based catalyst, length and stacking of the slab decline significantly from the unpromoted to Co-promoted silica catalysts (Appendix 3) which is in line with previous study.[18] These results suggest that the presence of Co atoms decorating the edges of the MoS_2 slab could stabilize smaller sizes by reducing the edge energies as shown from DFT calculations.[28]

Regarding the effect of the molybdenum surface coverage (dMo), the overall trend reveals first an increase of the length as a function of dMo regardless the support. Considering the alumina supported CoMoS phases at iso-dMo, γ-Al_2O_3 exhibits mean slab lengths which are always smaller by about 0.3 to 1.1 nm than those observed on $\delta\theta$-Al_2O_3. Moreover, it appears that the size difference observed on the two alumina supports diminishes systematically when the dMo increases (from 1.1 to 0.3nm). In addition, it appears that the slab size is the most sensitive to dMo parameter on the γ-Al_2O_3 where they fluctuate from 1.9 nm to 3 nm. By contrast, on $\delta\theta$-Al_2O_3 and on silica they vary by less than 0.5 nm. This comparison of the lengths measured on each support indicates that the Mo oxide precursor may interact more strongly on γ-Al_2O_3 than on $\delta\theta$-Al_2O_3 or SiO_2 which may limit sintering of the oxide phase during sulfidation at 350°C on γ-Al_2O_3 and induce the genesis of smaller MoS_2 crystallites at lower loading.

Thus, regarding the $\delta\theta$-Al_2O_3 support, the nature of the surface hydroxyl groups is expected to be different from γ-Al_2O_3 with respect to both reactivity and concentration. Indeed, the higher thermal treatment applied on alumina supports, such as $\delta\theta$-Al_2O_3 may have thus reduce the surface concentrations of the hydroxyl groups involved in the interaction with precursors as shown by NMR analysis,[30] DFT calculations[25] and thermogravimetric measurements.[31] Moreover, as also shown by IR analysis[32] and further rationalized by DFT calculations,[25] the formation of δ-Al_2O_3 is suspected to result from the sintering of γ-Al_2O_3 particles along the (100) surface, while exposing predominantly the (110) surface. This implies that the nature of molybdenum precursors and alumina interactions will depend on the alumina type. This analysis will be further detailed in section 3.1.2.

On silica, the more covalent character of the silanol groups (vs. aluminol groups) is at the origin of a weaker interaction during the impregnation step: electrostatic interactions are thus decreased, leading to a lower dispersion: higher slab sizes compared with γ-Al_2O_3 but

also slightly higher stacking compared with both γ- and δθ-aluminas. Moreover, on silica the slab stacking depends weakly on dMo and remains comprised between 2 and 2.3, whereas on aluminas it varies more significantly between 1.1 and 2.2: the lower the coverage, the lower the stacking. This is another manifestation of the precursor-support interaction effects which are more sensitive on aluminas at low loading than on silica.

A closer analysis of the slab length distribution reveals significant and interesting differences between γ– and δθ-aluminas and silica supported catalysts. Slab length distribution of CoMoS on γ-Al_2O_3, δθ-Al_2O_3 and SiO_2 at iso-dMo of 2.2 at.nm^{-2} is presented in Figure 6.

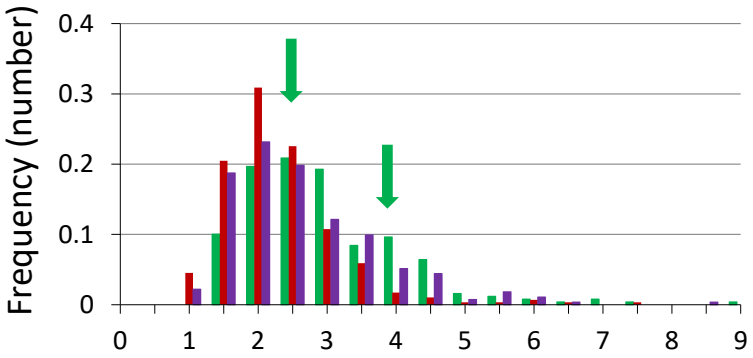

Figure 6. Slab length distribution as function of the support of CoMoS on γ-Al_2O_3 (red) , δθ-Al_2O_3 (green) and SiO_2 (purple) at iso-dMo of 2.2 at.nm^{-2} of support for a Co/Mo ratio close to 0.4. Relative uncertainty on lengths is ±10%

Indeed, whereas for CoMoS on γ-Al_2O_3 and SiO_2, the slab length distribution is mono-dispersed, it seems that for CoMoS/δθ-Al_2O_3 two populations of slabs exist centred respectively on length of 2.5 nm and 4 nm. Moreover, the frequency number of the first population (2.5 nm) is twice as high than the second population (4 nm). The same trend is observed for CoMoS/δθ-Al_2O_3 with 3.8 at.nm^{-2} (Appendix 4). However, for the lower dMo (0.9 at.nm^{-2}), the proportion of the second population of slab exhibiting the higher slab length (frequency around 0.05) is twice as low than for the highest dMo (2.2 and 3.8 at.nm^{-2}). This result may suggest that first, the two populations of slabs are growing in a consecutive way at the various surfaces exposed by δθ-Al_2O_3. This could be due either to the presence of the two δ- and θ-polymorphs or to the specific morphology of δθ-Al_2O_3 platelets. By contrast the slabs growth and/or the thermodynamic equilibrium sizes of MoS_2 particles seem to occur in a more homogeneous way on the two other supports. We will come back to this intriguing feature in the forthcoming section thanks to the HR HAADF STEM analysis.

3.1.2 HR HAADF STEM analysis

3.1.2.1 2D and 3D morphology analysis

HR HAADF-STEM have been undertaken to explore more precisely the nano-structure and two-dimensional (2D) morphology of CoMoS nano-crystallites on the three supports: γ-, δθ-alumina and silica. In this case; materials with dMo of 2.2 at.nm^{-2} have been considered (Figure 7). The determination of the morphology of the MoS_2 crystallites is feasible but remains not straightforward especially on alumina or silica supports.[14] Moreover, as already mentioned by Baubet et al. [14], the morphology features may depend on the sulfidation conditions: temperature and $p(H_2S)/p(H_2)$ ratio. In the present study, the sulfidation temperature was kept at 350°C and the H_2S/H_2 mixture at 15/85closer to our sulfidation conditions which obviously lead to less well defined crystallites' morphology with less symmetrical and faceted nano-object than at higher sulfidation temperatures[14]

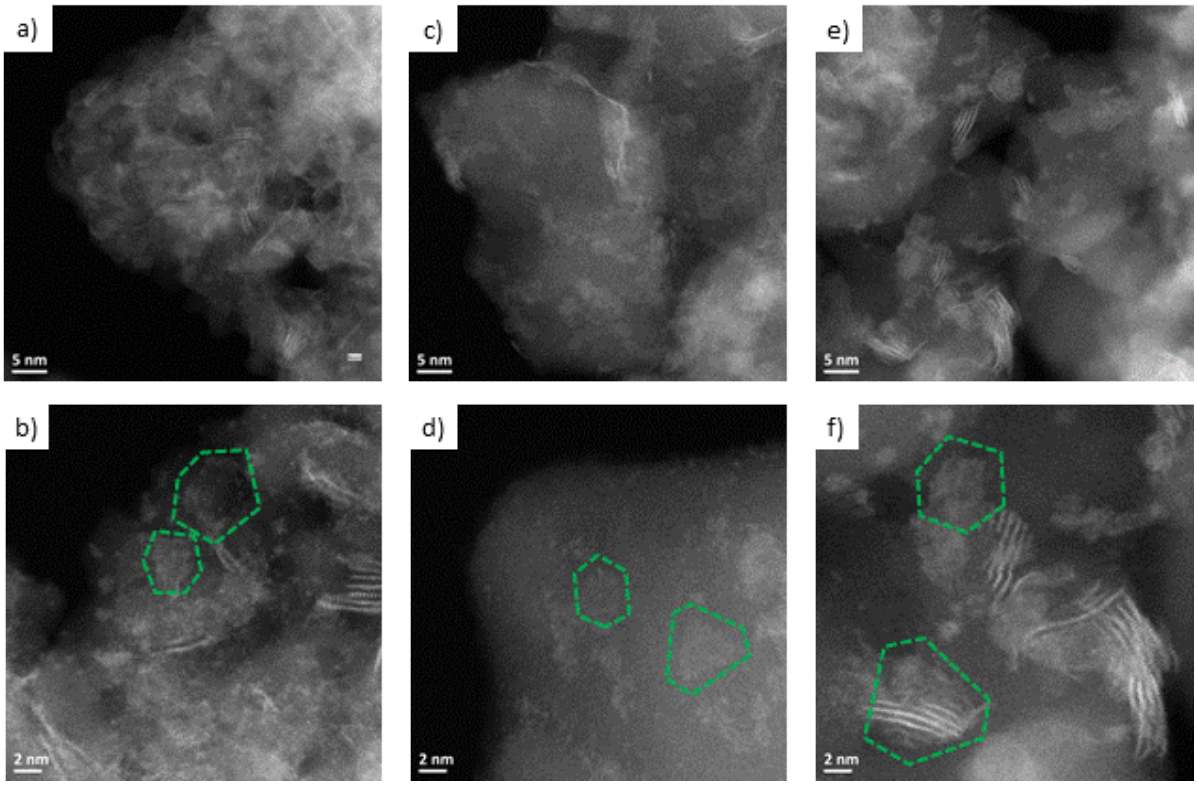

Figure 7. HR HAADF-STEM of CoMoS phase supported at iso-dMo of 2.2 at.nm^{-2} on a) and b) γ-Al_2O_3 , c) and d) δθ-Al_2O_3 and e) and f) SiO_2 sulfided at 350°C under H_2S/H_2 mixture (15/85).

Figure 7 illustrates an overview of the most relevant CoMoS nanolayers with different orientations with respect to the electron beam: either perpendicular or parallel to the basal plane of MoS_2 crystallites. In Figure 7 a), c) and e), mainly crystallites with their basal plane parallel to the beam are observed, while in Figure 7 b) d) and f) highlight some crystallites

with their basal plane perpendicular to the beam. For silica supported catalyst Figure 7 (e, f), CoMoS slabs are heterogeneously dispersed on the support with aggregation area where slabs are entangled each other forming superposed layers. This observation agrees with our previous TEM analysis that mentioned lower metal support interactions in the case of SiO_2 than on alumina which lead to the aggregation of CoMoS slabs, corroborating the slightly higher stacking reported for this dMo (Figure 2 a). The γ-alumina supported CoMoS crystallites (Figure 7a, b) present a homogenous repartition of the CoMoS slab on the support. For $\delta\theta$-alumina (Figure 7 c, d), the CoMoS crystallites are less dispersed than on the γ-Al_2O_3 surface but significantly better than on SiO_2.

Moreover, although this is more challenging and the statistics remains limited, we also attempted to analyze the morphology of the Co-promoted MoS_2 phase with HAADF-STEM experiments. According to previous scanning tunneling microscopy (STM) experiments[33] and density functional theory (DFT) calculations,[34,35] it is known first that for rather model nano-objects at equilibrium, the 2D morphology of the MoS_2 based crystallites should be closed to either hexagonal or triangular truncated shape depending also on the presence of the Co-promoter.[33,35] In particular, the truncated triangular shape of non-promoted MoS_2 is changed into a quasi-perfect hexagonal shape in the presence of Co as promoter on the edges.[33,35] This general trend was recently confirmed by HR STEM analysis of CoMoS/δ-Al_2O_3 catalysts by Baubet et al.[14] For all the supported samples studied here, both hexagonal and truncated triangular shapes have been observed (Figure 7 b, d, f). Even if a very few numbers of crystallites with their basal planes perpendicular to the electron beam have been detected, Table 4 attempts to draw a 2D shape distribution as a function of the support.

Table 4. Distribution of the 2D shape of the nano-crystallites for the supported CoMoS materials at dMo=2.2 at.nm^{-2}.

Support	Total number of crystallites observed on the basal facets	Shape distribution	
		Hexagonal	Truncated triangular
γ-Al_2O_3	4	3	1
$\delta\theta$-Al_2O_3	8	3	5
SiO_2	5	3	2

In order to explain the observed 2D shapes, it is assumed that the trends reported by STM and DFT calculations can be applied here as a starting point although we are well aware that support effect could change this trend. Thus, if two main morphology families of MoS_2 based crystallites are revealed: the truncated triangular shapes could be assigned to MoS_2 with a lower degree of promotion where one kind of edge represents 70% of the total edge (M-edge) and the other one, 30% (S-edge).[35] In the 3 catalytic samples (Table 4), 8 truncated triangular crystallites have been more specifically analyzed and the proportion of the long and short edges was estimated at 70%-30% respectively which may correspond to unpromoted MoS_2 crystallites. Simultaneously, on the same samples, about 9 quasi perfect hexagonal shapes have been observed: they could be related to the MoS_2 slabs decorated by cobalt atoms as predicted by DFT calculations[28] and observed by STM experiments[33] or by previous HR STEM.[14] Since the proportion of each morphology differs from one support to the other, one may suspect that it could be due to different promotion degrees induced by each support. However, since the statistics sampling remains low, it is difficult to give a unambiguous conclusion. This point will be further discussed through the XPS analysis detailed in the next section.

A second possible interpretation is to consider that the presence of truncated triangular shapes could result from a direct interaction of the support with the nano-crystallites. Such an effect could be either thermodynamic by modifying the final S- or M-edge energies interacting with the support or kinetic by changing the mechanisms of the genesis of the crystallites. According to previous DFT thermodynamic simulation of alumina supported MoS_2 and CoMoS models, it was reported that this covalent interaction between the final MoS_2 edges and the alumina surface should remain restricted to clusters of sizes significantly smaller than those observable by HR STEM.[36,37] In the case of silica, it is also intuited that this interaction should be even weaker than on alumina.

As a consequence, either kinetic effects occurring during the genesis of MoS_2 nano-crystallites or the promotion degree at edges can be the driving forces for the different observed morphologies.

3.1.2.2 Effect of δθ-Al_2O_3 facets on the CoMoS crystallites' sizes

At this stage, a complementary interesting observation must be underlined. Thanks to the larger sizes of δθ-Al_2O_3 platelets estimated at about 30 nm (Figure 7 c), we attempted to analyze the length distribution of the CoMoS crystallites as function of two main facets exposed by the δθ-Al_2O_3 platelets: the basal facets and the lateral facets (without distinction among the types of lateral facets). Thanks to the bright field image of Figure 8 a), the contour shape of one alumina platelet can be highlighted and identified in the Figure 8 b). According to this image, it can be observed first that a non-negligible number of CoMoS crystallites are almost perfectly aligned in a flat position on the lateral facets. On the basal planes, crystallites are also revealed: they are belonging to the family of those previously discussed in the morphology analysis. Indeed, the 2D shape of the crystallites in STEM can be only observed if the thickness of the support is thin enough to obtain a sufficient contrast. Thus, according to the geometry considered of δθ-Al_2O_3 platelets, the 2D shape of the crystallites (hexagonal or triangular truncated) is essentially observed on the basal plan (Figure 8 b). As a consequence, the mean length of CoMoS crystallites observed on the basal facets can be evaluated independently from the ones located on the lateral facets: two families of crystallites can be thus distinguished on the two facets (Figure 8b).

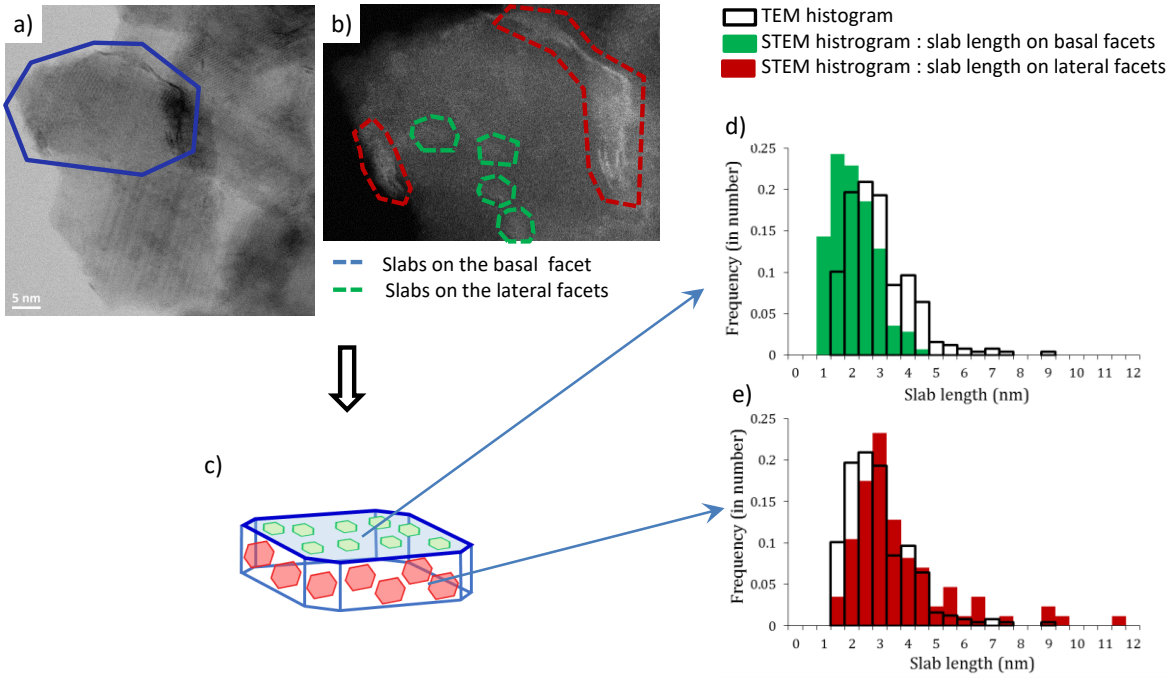

Figure 8. a) HR HAADF-STEM of $\delta\theta$-Al_2O_3 supported CoMoS catalyst at iso-dMo of 2.2 at.nm^{-2} sulfided at 350°C under H_2S/H_2 mixture (15/85). b) Zoom on the $\delta\theta$-Al_2O_3 platelet c) Contour shape of one alumina platelet (blue) where slabs are represented on the basal facets (green) and on the lateral facets (red). Length distribution of the CoMoS slabs as function of the alumina facets exposed: d) basal facets (green histogram) and e) lateral facets (red histogram). The overall length distribution of the CoMoS slab obtained by TEM analysis (black histogram) have been superposed to the length distribution of the CoMoS slabs obtained by HR-STEM. Length and stacking of MoS_2 nano-layers were calculated by analyzing at least 80 nano-layers on basal facets and 80 nano-layers on lateral facets.

Two length distributions of the CoMoS slabs as function of the exposed facets of alumina, either basal Figure 8 d) or lateral Figure 8 e) have been determined and compared to TEM analysis which gives access to the average length slab as mentioned previously. Moreover, this analysis clearly shows that a higher average of slab length is observed on the lateral facets ($\bar{L}_{lf} = 3.7$ nm) whereas a lower average length slab is preferentially observed on the basal alumina facet ($\bar{L}_{bf} = 2.08$ nm). Average length of CoMoS slabs calculated from lateral and basal facets (2.9 nm) is close to the average length obtained by TEM measurement (2.95 nm). Thus, it is highlighted that the MoS_2 crystallites are either growing in a different way, or are stabilized differently according to the type of alumina facet (either basal or lateral). It may be a strong indication of the support effect on the genesis of CoMoS crystallites which could be directly dependent of the hydroxyl speciation present on the lateral and basal $\delta\theta$-alumina facets. On the lateral facets, the average slab stacking around 1.6 is close to the average stacking obtained by TEM measurement (Figure 5). Thus it can be

suggested that the stacking is not strongly dependent of the slab location on the lateral or basal facet.

3.1.2.3 Role of hydroxyls groups as function of the exposed facets

Figure 9 reports the FTIR spectra of the γ-Al_2O_3 and $\delta\theta$-Al_2O_3 supports after activation at 450°C under vacuum. Different hydroxyl spectral bands can be distinguished on the two supports. Let us start recalling the knowledge on γ–alumina.

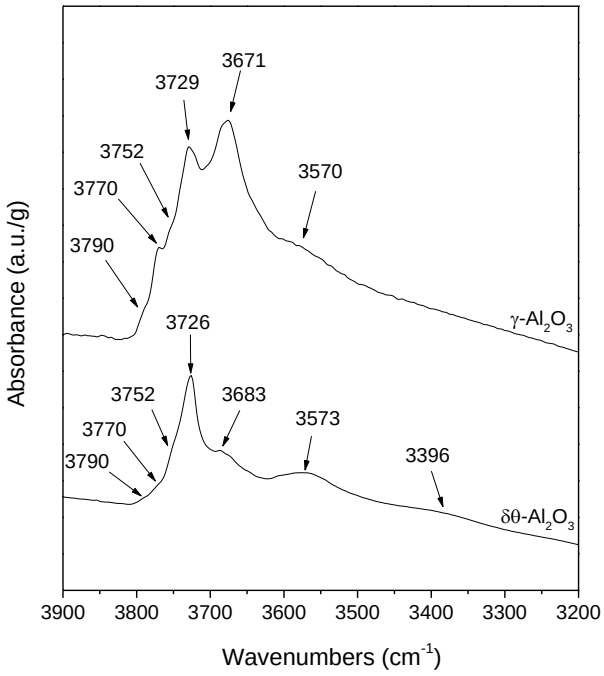

Figure 9: FTIR spectra of γ-Al_2O_3 and $\delta\theta$-Al_2O_3 supports after activation at 450°C under vacuum during 2 h.

As identified by DFT calculations[25,38] in agreement with infrared experiments on γ–alumina (Figure 9) [39] the two most basic OH groups according to their highest stretching frequencies are :

- the μ_1-Al_{IV}-OH (ν_{OH} ~ 3790 cm^{-1}) located on the (110) facet (Figure 10.a) with an intrinsic concentration of about 1.48 site per nm^2 of (110) surface, corresponding to 1.33 site.nm^{-2} for the whole $\delta\theta$-Al_2O_3 platelet (assuming 90% of (110) facet)
- the μ_1-Al_{VI}-OH (ν_{OH} ~ 3770 cm^{-1}) located on the (100) facet (Figure 10.b) with an intrinsic concentration of about 2.14 site per nm^2 of (100) surface, corresponding to 0.21 site.nm^{-2} for the whole $\delta\theta$-Al_2O_3 platelet (assuming 10% of (100) facet)

In addition, the (110) facet exhibits a neutral μ_1-Al_V-OH sites with ν_{OH} ~3729 cm^{-1}.

It should be also recalled that the (111) surface should also be considered as a lateral facet but it exhibits mainly acidic sites μ_3-Al_{VI}-OH (ν_{OH} ~ 3752 cm^{-1}) or μ_2-Al_V-OH sites with ν_{OH} very close to the μ_1-Al_V-OH sites of the (110) surface. (Figure 10.c) Finally, the intense band at 3671 cm^{-1} may correspond to two types of hydroxyls: μ_2-Al_{VI}-OH located either on the (110) surface or on the (111) surface.

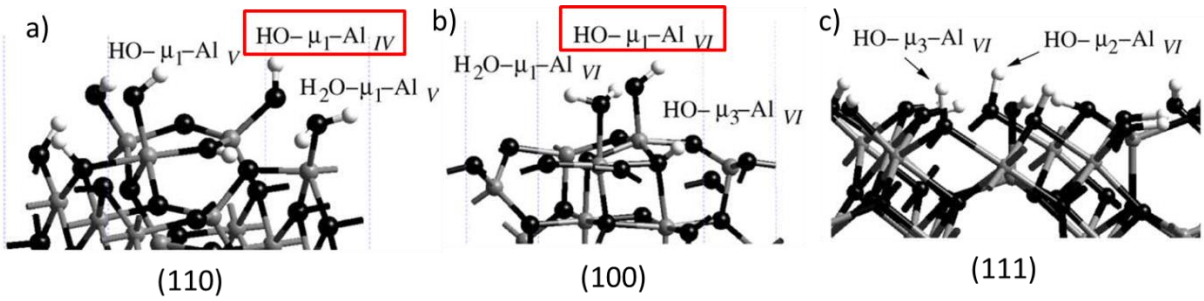

Figure 10. Nature of the hydroxyl groups on the three facets of a γ– or δ–alumina: a) basal (110), b) lateral (100) and c) lateral (111). adapted from Digne et al.[25]

As we previously discussed, the formation of δ-Al_2O_3 is considered as a result of the sintering of γ-Al_2O_3 platelet along the (100) surface.[32,38] This means that on the δθ-Al_2O_3 support, the (110) surface is predominant (probably more than 90% of the entire platelet surface) and it can be considered as the basal facet, while the lateral facets is composed of the (100) and (111) surfaces.[38] Considering the presence of θ-Al_2O_3 polymorph in the δθ-Al_2O_3 support, it is worth recalling that the content of tetrahedral Al in bulk θ-Al_2O_3 is half the total amount of aluminum. Moreover, it is often invoked that the $(010)_\theta$ and $(100)_\theta$ surfaces with a predominance of the $(010)_\theta$ (note : the $(010)_\theta$ and $(100)_\theta$ crystallographic planes correspond respectively to the (110) and (100) planes of γ– or δ–alumina).[40,41]

Figure 9 reveals a strong growth of the hydroxyl band at 3730 cm^{-1} which may confirm that the (100) facet disappears at the profit of the (110) facet δθ-Al_2O_3. This qualitative trend is linked to the structural evolution of γ-Al_2O_3 platelets into the two polymorphs δ-Al_2O_3 and θ-Al_2O_3 during the thermal treatment. The absorbance of each peak is reported in Table 5 below. It thus appears that the ratio of the absorbance of the more basic μ_1-Al_{IV}-OH groups with respect to the neutral ones μ_1-Al_V-OH (both located on the (110)) surface are diminishing by a factor of about 2.6 on the γ-Al_2O_3 (7.2) support with respect to δθ-Al_2O_3 (18.7). The absorbance corresponding to the basic μ_1-Al_{VI}-OH groups located on the (100) surface also strongly decreases by a factor of around 2.9. Last but not least, the most acidic

μ_2-Al_{VI}-OH (ν_{OH}=3752 cm^{-1}) and μ_3-Al_{VI}-OH (ν_{OH}=3671 and 3683 cm^{-1}) groups are also strongly affected by a factor of 1.4 to 3, respectively, after transformation from γ-Al_2O_3 to the $\delta\theta$-Al_2O_3 polymorph. This change of the nature of hydroxyls between the two supports may have significant impact on two levels: the genesis of the active phase, on the one hand, and the reactivity of the support during catalytic tests.

Table 5: Absorbance ratio of the hydroxyl contributions for γ-Al_2O_3 and $\delta\theta$-Al_2O_3. Absorbance of each hydroxyl contribution is measured from the IR spectra in Figure 9.

Absorbance ratio	γ-Al_2O_3	$\delta\theta$-Al_2O_3
$A_{\mu1\text{-Al(V)-OH-(110)}}/A_{\mu1\text{-Al(IV)-OH-(110)}}$ ($\sim A_{3730}/A_{3790}$)	7.2	18.7
$A_{\mu1\text{-A(V)-OH-(110)}}/A_{\mu1\text{-Al(VI)-OH-(100)}}$ ($\sim A_{3730}/A_{3770}$)	2.2	6.4
$A_{\mu1\text{-A(V)-OH-(110)}}/A_{\mu3\text{-Al(VI)-OH-(111)}}$ ($\sim A_{3730}/A_{3752}$)	1.7	2.4
$A_{\mu1\text{-A(V)-OH-(110)}}/A_{\mu2\text{-Al(VI)-OH-(111) or (110)}}$ ($\sim A_{3730}/A_{3671\text{-}3683}$)	0.9	2.7

3.1.3 Impact on the catalytic activity and genesis of the active phase

Regarding first the catalytic activity, it has been observed that the selectivity into olefinic compounds is enhanced on the CoMoS/$\delta\theta$-Al_2O_3 catalysts than on the CoMoS/γ-Al_2O_3 ones (Chapter III). According to the previous analysis, it appears that the acid-basic properties of the OH groups are significantly modified on the two supports and particularly, we observed the decrease of the most acid μ_2-Al_{VI}-OH and μ_3-Al_{VI}-OH sites with respect to the neutral ones. As a consequence, the π-complex involving olefinic compounds and the acid OH groups, will be less strongly stabilized on the $\delta\theta$-Al_2O_3 support than on γ-Al_2O_3. As a consequence, the residence time of the olefinic molecules on the catalysts will be lower on $\delta\theta$-Al_2O_3 which diminishes its probability of being hydrogenated by the CoMoS phase.

Regarding secondly the genesis of the active phase, for very similar systems, the most basic and neutral hydroxyl groups have been proposed to be the most easily exchanged by the molybdate precursors[42], like other anionic species present in the impregnation solution such as silicate[43] or chlorine.[38] Since the dMo value is 2.2 $at.nm^{-2}$, we cannot exclude that the molybdate precursors interact with the two kinds of sites of the two facets and also with the neutral ones, which will thus generate MoS_2 crystallites located on basal and lateral facets as observed in the HR STEM images. Due to the different nature of these hydroxyls

and of the two surfaces, we may suspect that the physico-chemical properties of the CoMoS crystallites differ from one facet to another as it is also highlighted by the HR STEM results where the observed CoMoS crystallites sizes are smaller on the (110) basal facet than on the (100)/(111) lateral facets. As discussed previously, this result may have several origins either thermodynamic (intrinsic stability) or kinetic (growing rates of the crystallites during their genesis). On the (110) surface, the presence of the μ_1-Al_{IV}-OH sites could lead to stronger Mo-Al-O interaction due to the low coordination number of the Al anchoring site, than on the (100) surface where the μ_1-Al_{VI}-OH sites are involved. This result is fully consistent with the recent work done by Bara et al.[19] Smaller MoS_2 particle sizes were observed on the R ($1\bar{1}02$) plane of α–alumina monocrystal where μ_1-Al_{IV}-OH sites are dominating,[44] whereas larger sizes were found on the A ($11\bar{2}0$) and M ($10\bar{1}0$) planes bearing μ_1-Al_{VI}-OH sites. In addition, the highest concentration of the μ_1-Al_{VI}-OH groups located on the (100) surface (2.14 site. nm^{-2} of (100) facet) induces a closer vicinity of the nucleation centers which may be more favorable to the growing rates.

The case of the (111) surface is interesting to consider also as a possible lateral facet of $\delta\theta$-Al_2O_3. It is a polar surface (Figure 10 c) exhibiting very strong similarities with the C (0001) plane of α–alumina. Bara et al. found that this plane is rather inert with respect to molybdate precursors which can be understood by considering the predominance of μ_3 or μ_2-OH sites on it. Hence, it leads to the formation of MoS_2 crystallites with even larger sizes and higher stacking on the C (0001) plane of α–alumina.[19]

If we transpose this result to the (111) surface contributing to the lateral facets of $\delta\theta$-Al_2O_3, this result is fully consistent with our HR STEM observations of larger CoMoS crystallites located on these lateral facets with a certain degree of stacking.

Considering now the θ-Al_2O_3 polymorph, if we assume that the nature of OH sites assigned for γ–alumina can be extrapolated to θ-Al_2O_3,[25,38] the strong increase of the band at 3730 cm^{-1} (Figure 9) should indicate that the μ_1-Al_V-OH sites on the $(010)_\theta$ facet (homologous to (110) basal facet of γ–alumina) are predominant on the θ-Al_2O_3 polymorph. Tetrahedral Al sites can be exposed on both $(010)_\theta$//(110) and $(100)_\theta$//(100) surfaces,[45] however considering the local atomic structure of the two surfaces, μ_1-Al_{IV}-OH sites should be predominantly generated on the (010) surface (i.e. (110) for γ– or δ–alumina). Moreover, if the corresponding vibrational band is expected at 3795 cm^{-1} (by analogy with the γ–alumina

μ_1-Al_{IV}-OH sites) is not strongly enhanced in Figure 9, this would mean that the $\delta\theta$-polymorph exhibits more neutral OH sites than the strongest basic ones. Finally, Figure 9 reveals that vibrational frequencies assigned to μ_2-OH and μ_3-OH sites of the lateral (111) surface are still present on the $\delta\theta$-polymorph. Hence, even if more detailed atomistic studies would be mandatory on this θ-Al_2O_3 polymorph, one would expect at this stage similar conclusions on the CoMoS particles' size distributions as the aforementioned ones proposed for δ–alumina surface.

This HR STEM analysis thus completes fruitfully the TEM results discussed previously. It is revealed that the two populations of MoS_2 particles which are related to the distinct properties of lateral and basal facets: the basal facets bear the smaller particle sizes whereas the lateral ones bear the larger ones. This also explains why for the dMo of 0.9 Mo at.nm^{-2}, only one population of small size is still observed in the TEM histogram due to the interaction of Molybdate precursors predominantly with the most basic μ_1-Al_{IV}-OH sites (1.33 sites/nm^2).

3.1.4 Possible role of the corners and edges of γ–Al_2O_3 crystallites

Coming back to the comparison between the $\delta\theta$-Al_2O_3 and γ-Al_2O_3 supports, and assuming that the two supports first differ by their respective proportions of (110) and (100) facets: a slightly larger proportion (~30%) of (100) is reported on γ-Al_2O_3 (before sintering), one would expect larger CoMoS crystallites' sizes on this support. However, the mean CoMoS crystallites' size analyzed by HRTEM is smaller on γ-Al_2O_3 than on $\delta\theta$-Al_2O_3 (Figure 4a). This apparent contradiction implies that more complex phenomena occur during the genesis of the CoMoS crystallites on γ-Al_2O_3 which involve other parameters than the effect of the proportion of the basal and lateral facets. For instance, due to the significantly smaller dimensions of the γ-Al_2O_3 platelets (see methods), we cannot exclude that corner and/or edge Al sites with lower coordination number located at the intersection of two or three facets may play a key role as nucleation sites of the MoS_2 phase. In same spirit as previously discussed, they would thus favored the genesis of smaller and more dispersed CoMoS crystallites due to stronger Mo-Al-O interactions along edge and corner sites. The existence of such sites at the (110)/(100) edges of the γ–alumina has been invoked by G. Busca in a recent review[46] and the coordination number of such aluminum site is expected to be as

low as 3 (Figure 11) and thus could form new basic μ_1-Al_{IV}-OH sites (upon hydroxylation) interacting strongly with the molybdate precursors. This effect has also been proposed to play a key role in alumina supported platinum catalyst as used in reforming.[47] It is also particularly interesting to notice that for the low dMo=0.9 the CoMoS crystallites' size is even smaller (< 2 nm) due to the possible even more pronounced effect of edges and corners sites.

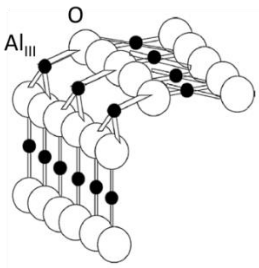

Figure 11. Schematic view of the dehydroxylated tricoordinated Al sites located along the edge at the intersection of the (110) and (100) planes of γ–alumina according to Busca et al.[46]

3.2 Molybdenum and cobalt surface speciation

The mass percentage of molybdenum obtained by XPS was first compared with the mass percentage of Molybdenum obtained by XRF (Figure 12). It can be noted that the amount of Mo measured by XPS is lowered for γ-Al_2O_3 and silica supported catalysts compared to XRF analysis and the gap is increasing with the dMo. This may be explained by non-uniformly distributed Mo atoms at the support surface. Regarding CoMoS/δθ-Al_2O_3, the Mo weight % measured by XPS values is matching with the Mo weight % measured by XRF even if the XPS values are slightly higher**.** Thus, in the following section dealing with 2D morphology model, XRF values will be considered.

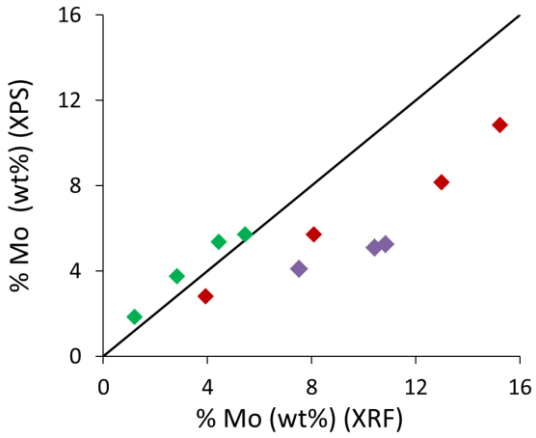

Figure 12. Comparison between the global amounts of molybdenum (wt.%) determined by XPS for sulfided CoMoS on γ-Al_2O_3 (red), δθ-Al_2O_3 (green) and on SiO_2 (purple) and determined by XRF (wt.%).

As well as the Molybdenum, the mass percentage of cobalt obtained by XPS was compared with the mass percentage of cobalt obtained by XRF (Figure 13). It can be noted that the amount of Co measured by XPS is lowered for γ-Al_2O_3 and silica supported catalysts and that the gap with the XRF values is increasing with the dMo. This may be explained by non-uniformly distributed Co atoms at the support surface $CoMoS/SiO_2$. Regarding $CoMoS/\delta\theta$-Al_2O_3, the Co weight % measured by XPS values is matching with the Mo weight % measured by XRF even is the XPS values are slightly higher**.** Thus, in the following section dealing with 2D morphology model, XRF values will be used.

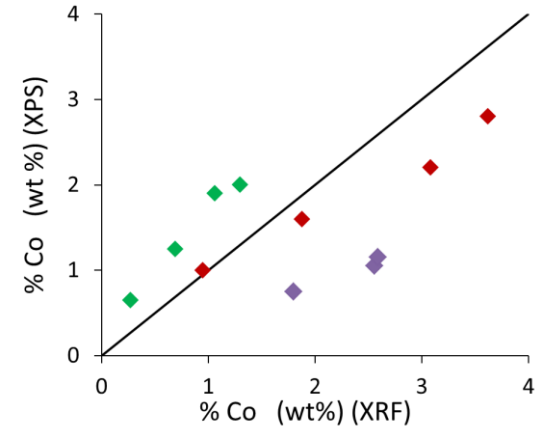

Figure 13. Comparison between the global amounts of cobalt (wt.%) determined by XPS for sulfided CoMoS on γ-Al_2O_3 (red), $\delta\theta$-Al_2O_3 (green) and on SiO_2 (purple) and determined by XRF (wt.%).

Finally, the molar percentage of Co/Mo ratio obtained by XPS was compared with molar percentage of Co/Mo ratio obtained by XRF (Figure 14). It can be noted that the amount of Co/Mo ratio measured by XPS is higher for γ-Al_2O_3 and $\delta\theta$-Al_2O_3 supported catalysts compared with silica catalysts. The gap with the XRF values is the highest for $CoMoS/\delta\theta$-Al_2O_3. This may be explained by non-uniformly distributed Co and Mo atoms at the support surface. Regarding $CoMoS/SiO_2$ the Co/Mo ratio measured by XPS values is matching with the Co/Mo ratio measured by XRF**.** Thus, in the following section dealing with 2D morphology model, XRF values will be preferentially used.

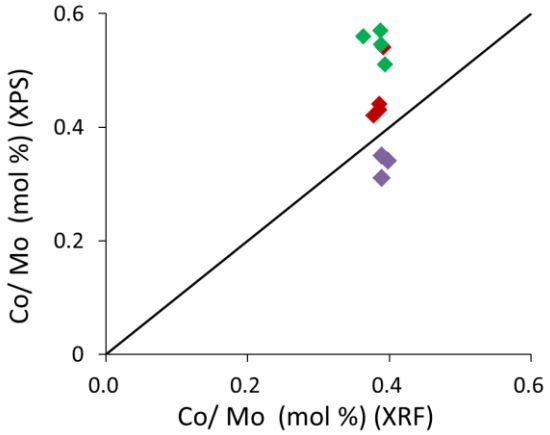

Figure 14. Comparison between the global amounts of cobalt (mol.%) determined by XPS for sulfided CoMoS on γ-Al_2O_3 (red), $\delta\theta$-Al_2O_3 (green) and on SiO_2 (purple) and determined by XRF (mol.%).

In order to characterize qualitatively and quantitatively the Mo and Co sulfided species present on the three supports, XPS analysis has been reported in more details in the next section.

3.2.1 Analysis of Mo 3d levels BE by XPS and DFT

3.2.1.1 Case of dMo=2.2 at.nm^{-2}

Figure 15 presents the Mo 3d XPS spectra of some supported phases at dMo=2.2 at.nm^{-2}. According to the previous work by Gandubert et al.[27], Mo 3d spectra can be decomposed into three components corresponding to three Mo species in different oxidation state. Generally, the main Mo species corresponds to the Mo in (+IV) oxide state which is attributed to the to MoS_2 species. Two minor Mo species are related to Mo in (+V) and (+VI) oxide states corresponding respectively to oxysulfide species (MoS_xO_y) and to Mo oxide phase. Each Mo^{+X} species will be characterized by a Mo 3d doublet ($3d_{3/2}$ and $3d_{5/2}$). An example of the decomposition of Mo 3d is shown Figure 3.a.

In order to study qualitatively a possible binding energy shift due to the support or the dMo effect, the study will focus on the value of the binding energy related to BE3 which is the main contribution of the MoS_2 species. Table 6 presents the binding energy (BE) of this contribution.

However, in order to perform a quantitative analysis (section 3.2.1.6), all Mo species and Mo spectral contributions are taken into account i.e the oxysulfide phase. Contribution at

226.2 eV related to the S2s contribution will be also considered for the decomposition but is not taken into account for the quantification step.

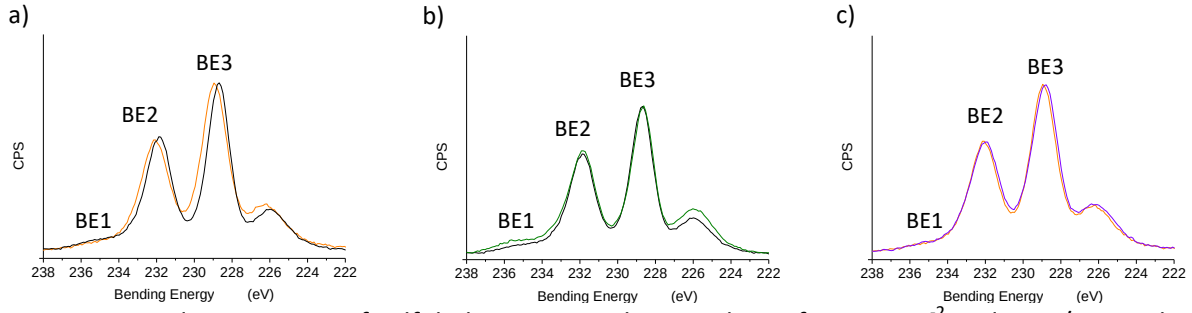

Figure 15. Mo 3d XPS spectra of sulfided CoMoS catalysts at dMo of 2.2 at.nm^{-2} and a Co/Mo molar ratio of 0.4 (a) MoS_2 on $\delta\theta$-Al_2O_3 and SiO_2 respectively in black and orange (b) $MoS_2/\delta\theta$-Al_2O_3 and CoMoS /$\delta\theta$-Al_2O_3 respectively in black and green (c) MoS_2/SiO_2 and $CoMoS/SiO_2$ respectively in orange and purple. Spectra intensities are normalized by the peaks around 228.6 eV. The spectra are calibrated with respect to the C1s main peak at 284.6 eV.

Table 6. Binding energy, FWHM and ratio intensities of the different contributions of Mo 3d XPS spectra obtained for γ- $\delta\theta$-Al_2O_3 and SiO_2 supported MoS_2 and CoMoS catalysts at dMo of 2.2 at.nm^{-2} and Co/Mo molar ratio of 0.4. Absolute uncertainties on binding energies is ± 0.05 eV).

Catalysts	Co/Mo	BE3 (eV) $3d_{5/2}Mo^{+IV}$	FWHM (BE3)
$CoMoS/\gamma$-Al_2O_3	0.4	228.65	1.30
$MoS_2/\delta\theta$-Al_2O_3	0	228.69	1.46
$CoMoS/\delta\theta$-Al_2O_3	0.4	228.67	1.44
MoS_2/SiO_2	0	228.96	1.62
$CoMoS/SiO_2$	0.4	228.84	1.66
Bulk MoS_2[a]		229.1	

[a] ref Gandubert et al.[27]

By comparing the unpromoted MoS_2 phases (Table 6), it can be observed higher Mo BE3 for MoS_2/SiO_2 than for $MoS_2/\delta\theta$-Al_2O_3 by about +0.25±0.05 eV. Note that the BE is even higher (by about +0.45 eV) for the unsupported bulk MoS_2 at 229.1 eV according to ref[27]. Moreover this trend remains true for the promoted catalysts.. However, the precise origin of this effect is not easy to determine because it may results from various intricate effects discussed in what follows.

3.2.1.2 Electronic effect of the support

If we first exclude any size or stacking effects, the electron transfer between the support and the MoS_2 phase can be first considered. According to the IR analysis of CO adsorption on Mo sites, Crépeau et al.[48] proposed that the stronger the acidity of the protons of the support, the greater electronic transfer from the sulfided phase to the support (the smaller the CO vibrational shift due to less back donation effect). So the aluminol groups which are expected to be more acidic than silanols should imply a stronger electron depletion from the sulfided phase by alumina than by silica, which is not consistent with the previous observed trends. In addition, previous IR of adsorbed CO also observed a stronger CO shift for the unsupported (bulk) reference than for the alumina or silica supported systems.[49,50] This means that the electron depletion on Mo site (probed by CO) is greater on alumina and silica supported systems. This trend should reinforce the BE value measured by XPS which is not consistent with the result reported in Table 6. By contrast, charge transfer from the support to the sulfided phase occurs if a metallic support is used such as gold in STM experiments which induces an enhancement of the electronic density close to the Fermi level of the MoS_2 crystallites and also a decrease of ~0.4 eV in BE measured by XPS even if they are oriented in a flat position without direct chemical bonds between the gold support and MoS_2.[51] Considering the case of alumina support (large band gap materials), such a phenomenon is difficult to imagine. DFT calculations on Pd_{13} and Pt_{13} clusters supported on γ–alumina[52,53] have shown that on the hydroxylated (110) surface, the metallic cluster is usually electronically depleted due to the predominant interaction of the metallic atoms with the oxygen atoms of the hydroxyl groups. However, on the dehydroxylated (100) surface of γ–alumina the metallic cluster can be electronically enriched only if direct chemical bonds are formed between the metallic atoms and Lewis Al sites of the support. As a consequence for MoS_2 phases, one should imagine that Mo atoms directly interact with Lewis Al sites located on the (100) alumina surface. This scenario remains very difficult to admit due to presence of the first sulfur neighbors (connected to Mo) which would simultaneously interact with the support oxygen atoms (connected to Al sites). As a consequence, Mo atoms generally prefer to interact directly with O while S atoms interact with Al sites as shown by previous DFT calculations.[37]

3.2.1.3 Size effect correlated with low coordination edge sites

A second hypothesis could be related either to the size effect. For metallic particles, it has been shown that the electronic properties of alumina supported Pt clusters clearly depend on the size of the cluster.[53] XPS studies have also shown that the binding energies of the metal directly depend on the cluster sizes: the smaller the size, the greater the binding energy.[54] For MoS_2 materials, Mattila et al.[55] have shown by high resolution XPS of big size MoS_2 samples cleaved in ultra-high vacuum that the Mo $3d_{5/2}$ peak can be decomposed into 4 peaks corresponding to various contributions of Mo atoms located in the bulk and at edges: the edge contributions are found at lower BE than the bulk. This would thus imply that the trend is the reverse than for metallic particles: the smaller the size, the larger the edge contribution and the lower the BE. Combining also HR-XPS and DFT calculations on gold supported MoS_2 clusters, Bruix et al.[51] have shown that the binding energies of the Mo $3d_{5/2}$ peak may also depend on the sulfidation degree of the Mo atoms at the edges. Since gold is directly involved in the charge transfer impacting the BE values in the study by Bruix et al., we report here previous DFT calculations of edge core level shift, ECLS (see methods in Appendix 5) for various Mo atoms located at the edge of MoS_2 and CoMoS by considering periodic MoS_2 slabs without any support. These calculations have been undertaken at IFPEN by Krebs et al.[56] We have thus used the M- and S-edge models determined by previous DFT studies.[13,35] Table 7 summarizes all the values obtained for the most relevant configurations involving different S-coverage (Mo coordination number, N_{Mo}). In the case of CoMoS, the M-edge with 50% Co has been considered. The ECLS shows that the results within the initial and final state approximation are coherent, even if the final state gives always lower ECLS values by about (0.1-0.4 eV) due to screening effect as this has been reported for other systems.[57] As expected and also reported by Bruix et al.[51], in the case of the most highly desulfurized M-edge of MoS_2 (0%S, NMo=4, Figure 16a), the ECLS is strongly negative (-0.77 eV) due to the high metallic character of such uncoordinated sites as shown by the high occupation at the Fermi level in the density of states analysis of the Mo 4d orbitals.[58] A similar trend is observed for the Mo atoms located on the S-edge at 50% S coverage (Figure 16d), with coordination number of 4. If we consider however that due to the presence of H_2S in the sulfur-reductive conditions, extra S-atoms may be adsorbed on the M- or S-edge, ECLS can be significantly shifted to higher values. In the case of 50%S on the

M-edge with S bridging atoms (Figure 16b), two ECLS values are found positive +0.26/+0.35 corresponding to 2 non-perfectly equivalent Mo edge sites (slight Mo-Mo relaxation leading to short-long-short-long Mo-Mo distance at edge). Finally, for the S-edge with 100% S which is rather close to the bulk configuration, we find that the ECLS value is slightly negative (-0.12 eV). If we further increase the pressure of H_2S, it is known that the M-edge with 100% S (Figure 16e) may be stabilized, so leading to N_{Mo}=6 but with a different local configuration than with 50%S and the resulting ECLS is close to -0.31 eV.

Table 7. 3d core level shift (in eV) of Mo edge atoms at the M-edge of MoS_2 and CoMoS (ref. Mo in the center of the slab).

	MoS_2 – M-edge			**MoS_2 – S-edge**		**CoMoS – M-edge (50% Co)**		
configuration	**0% S**	**50% S bridge**	**100%S**	**50% S**	**100% S**	***alternate**** **25% S top**	***paired**** **12.5% S bridge**	***paired**** **25%S top**
N_{Mo}	4	6	6	4	6	5	5	5
$ECLS_{initial}$	-0.41	+0.62 / +0.64	-0.04	-0.37	+0.01	+0.32	+0.18	+0.36
$ECLS_{final}$	-0.77	+0.26 / +0.35	-0.31	-0.77	-0.12	+0.17	+0.04	+0.28

* alternate Co-Mo-Co-Mo or paired Co-Co-Mo-Mo configuration at the M-edge

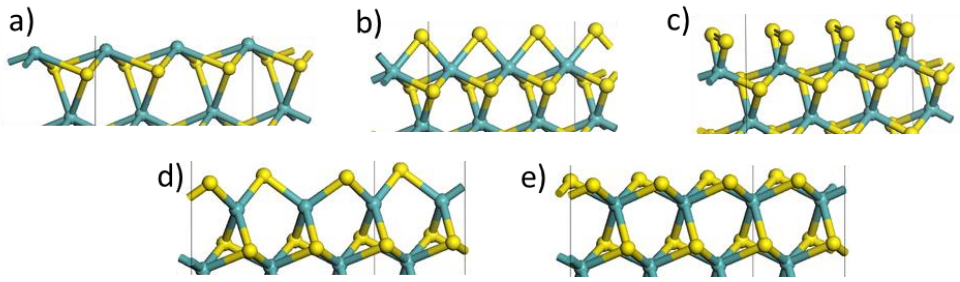

Figure 16. DFT molecular models of the non-promoted MoS_2 edges: a) M-edge with 0%S, b) M-edge with 50% S (bridge), c) M-edge with 100%S, d) S-edge with 50%S, e) S-edge with 100%S. Color legend: Mo: green balls, S: yellow balls.

Hence, we confirm that the ECLS and as a matter of fact, XPS BE of the Mo 3d levels are significantly different at the edges than in the bulk part of MoS_2 particles. We also highlight that the ECLS value may depend on the relative proportion of the S-edge or the M-edge on MoS_2 particles. In particular, this result calls for a complementary important interpretation of the NAP-XPS results reported by Bruix et al.[51] By increasing the partial pressure of hydrogen, Bruix et al. invokes the formation of M-edge with close eventually 0%S due to the intensity increase of the lowest BE peak. However, according to the present complementary calculations, we cannot exclude that S-edge exposing 50% S are formed since the BE is

expected to be as low as the M-edge with 0%S (-0.77 eV). Such an edge configuration has been shown to be more stable than the M-edge with 0%S.[35] This would also be a manifestation of the shape modification of the MoS_2 nano-crystallites under reductive conditions, from triangular to hexagonal shape, as it has been already proposed by DFT calculations[35] and further confirmed by STM experiments.[59]

In summary, since on the $\delta\theta$-Al_2O_3 supports and silica supported MoS_2, lower XPS BE values are found than in the reference bulk MoS_2, we propose that on the support, non-promoted MoS_2 nano-crystallites of smaller sizes are present. The non-negligible contribution of edges in supported systems could thus explain the lower BE, considering also that after sulfo-reduction M-edge and S-edge, crystallites with edge Mo coordination number close to 4 as on the S-edge with 50% S (ECLS=-0.77 eV), and edge Mo coordination number close to 6 as on the M-edge with 50%S in bridging position (ECLS=+0.26/+0.35 eV). Since, according to DFT calculations, the proportion of M-edge/S-edge is slightly in favor of the M-edge (~70%) under the sulfo-reduction conditions as used here,[35] both contributions compensate leading to an overall small negative shift. In addition, if a small amount of coordinatively unsaturated sites exist on the M-edge, the negative ECLS should be further enhanced. Since diminishing the MoS_2 size enhances the effect of edges, we can definitely not exclude that such a size effect directly impacts the XPS peak positions, even if no straightforward correlation can be drawn as a function of the supports investigated here: $\delta\theta$-Al_2O_3 exhibits larger MoS_2 sizes than silica and smaller BE values, whereas it is the reverse for γ-Al_2O_3.

3.2.1.4 Promoter effect on Mo binding energy

Regarding the Co-promoted phases, an earlier theoretical study proposed that when cobalt promotes the MoS_2 phase, a shift at lower energy is observed compare with the unpromoted or bulk MoS_2 catalyst as reported in Table 6.[60] This observation could be due to the fact that cobalt promoter should increase the electron density on Mo atoms by electron transfer from Co to Mo atoms.[60] According to more recent DFT calculations,[28] we can check if this effect is valid only on the M-edge with 50% Co (Figure 17) which allows the simultaneous presence of Co and Mo at the edge in two configurations either paired or alternate as detailed elsewhere. On the S-edge, only Co atoms are present (Figure 17d). If we compare two competing structures at the M-edge: the non-promoted edge with 50%S (bridge) and the

promoted M-edge with 50% Co, we observe that the ECLS values calculated at Mo site is reduced from +0.26/0.35 eV to +0.04/+0.17/+0.28 eV. We have also tested a virtual case (not stable according to energetic), where the Mo-atoms on the non-promoted M-edge are coordinated to 5 S atoms located on top of Mo. In that case, the ECLS is also slightly positive: (+0.12 eV in the final state approximation) but significantly lower than the ECLS of a M-edge with bridging S-atoms. Hence, the promoter effect is not strictly speaking an electronic transfer but it must also be attributed to the decrease of coordination number of Mo atom from 6 (non-promoted) to 5 (promoted) when cobalt is present on the same edge. On the S-edge, since the Co atoms are occupying the former position of the Mo atoms, one predicts that the contribution of the S-edge on the Mo 3d XPS spectrum should vanish if the promotion level is 100%. However, in catalysts such as the one synthetized here, this promotion level is at best 50% (see next section), thus the contribution of non-promoted MoS_2 crystallite cannot be neglected.

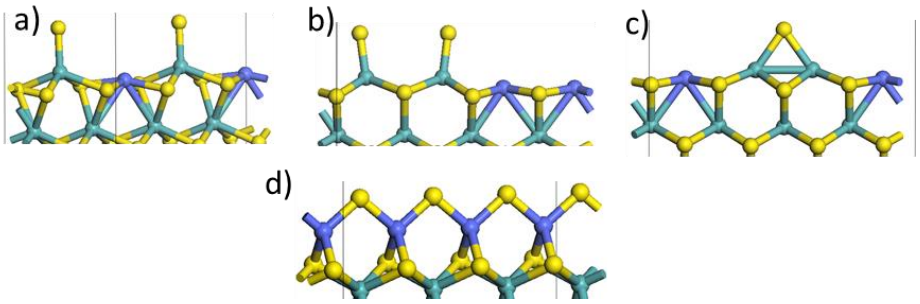

Figure 17. DFT molecular models of the Co promoted MoS_2 edges: a) M-edge with 50%Co in alternate position and 25% S (top of Mo), b) M-edge with 50%Co in paired position and 25% S (top of Mo), c) M-edge with 50%Co in paired position and 12.5% S (bridge), d) S-edge with 100%Co (no Mo at edge). Color legend: Mo: green balls, Co: blue balls, S: yellow balls. Adapted from ref.[28]

Experimentally, a small binding energy shift of the core level exists when adding cobalt but this effect is less than 0.05 eV between the unpromoted and promoted MoS_2 phases. Thus, assuming that core level shifts are correlated to valence level shift, since the cobalt promotion of the MoS_2 phase impact modestly the binding energy of BE3, this suggests that this parameter cannot explained the observed trends.

3.2.1.5 Effect of Mo surface coverages

Figure 18 presents the Mo 3d XPS spectra of CoMoS phases supported on the three supports for various dMo and a Co/Mo molar ratio. The corresponding numerical values of the binding energy of the Mo contributions, BE1 (Mo oxide phase, $Mo^{+VI}_{3/2}$), BE2 and BE3 (MoS_2

species, $Mo_{3/2}$ and $Mo_{5/2}$ of Mo^{+IV} and Mo^{+IV}) previously detailed in 3.2.1.1, are reported in Table 8. In order to study qualitatively a possible binding energy shift due to support or dMo effect, focus will be done on the value of the binding energy related to BE3 which is the main contribution of the MoS_2 species.

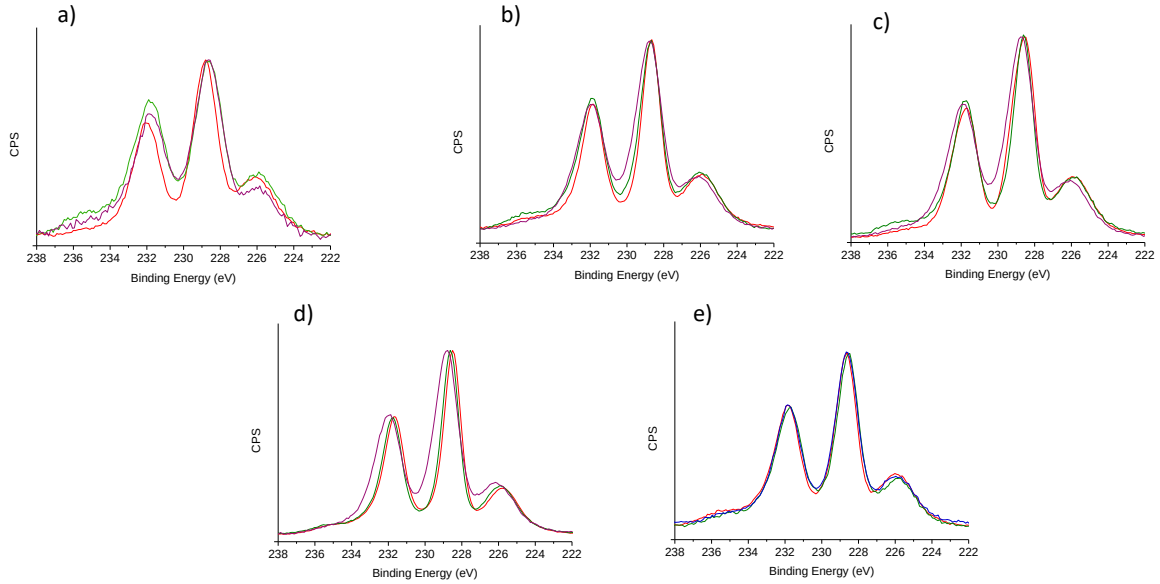

Figure 18. Mo 3d XPS spectra of sulfided CoMoS/γ-Al_2O_3 (red), CoMoS/$\delta\theta$-Al_2O_3 (green) and CoMoS/SiO_2 (purple) respectively at a dMo of (a) 0.9, (b) 2.2, (c) 3.8 and (d) 4.8 at.nm^{-2}. (e) Mo 3d XPS spectra of CoMoS/$\delta\theta$-Al_2O_3 with a Co/Mo molar ratio of 0.1 (purple), 0.2 (red) and 0.4 (green) respectively, at dMo = 2.2 at.nm^{-2}. Spectra are normalized by the main 3d5/2 peak around 228.6 eV. The spectra are calibrated with respect to the C1s main peak at 284.6 eV.

It can be observed that the binding energies BE3 do not differ significantly from γ-Al_2O_3 to $\delta\theta$-Al_2O_3 (Table 8) which means that the electronic property of the Mo atoms in the promoted as well as in the unpromoted MoS_2 as measured by XPS does not depend on the alumina support at iso-dMo. However, for silica supported catalysts, as it has already been noticed for dMo=2.2, the binding energy BE3 are closer to the unpromoted bulk MoS_2 than those on alumina supported catalysts at iso-dMo, if one except the smallest dMo value.

For the Co/Mo ratio of 0.4, the increase of Mo coverage on alumina supports seems to imply a small decrease of BE3 from dMo=0.9, 2.2 and 3.8 at.nm^{-2}. Considering that the size is increasing with the Mo coverage (Figure 1), it is difficult to correlate this with the number of edge sites without changing their quality. Moreover for the highest dMo=4.8 at.nm^{-2} the trend seems to be changed: the BE values are increasing with respect to dM=3.8 at.nm^{-2}.

Finally, since the stacking number are slightly higher on silica than on aluminas, it may imply that the nature of the MoS_2 phase becomes slightly closer to the bulk MoS_2 on silica which is known to be a more inert support than alumina. Moreover, with higher stacking, the MoS_2 layers located at the top of the stacked structure will be less influenced by the support and thus closer to the bulk MoS_2 as well. However, for aluminas support, increasing the stacking implies the reverse trend for BE3. So the stacking effect alone as well as the size effect alone cannot explain the observed trends as a function of Mo coverages.

Table 8. Binding energy and FWHM of the different contributions of Mo 3d XPS spectra obtained for supported CoMoS catalysts. BE1, BE2 and BE3 are respectively associated to Mo^{VI}, and Mo^{IV}.

Support	dMo	Co/Mo	BE3 (eV) $Mo_{5/2}$ of Mo^{+IV}	FWHV (BE3)
γ-Al_2O_3	0.9	0.4	228.78	1.58
	2.2		228.65	1.30
	3.8		228.49	1.54
	4.8		228.55	1.22
$\delta\theta$-Al_2O_3	0.9	0.4	228.65	1.64
	2.2		228.67	1.44
	3.8		228.53	1.31
	4.8		228.68	1.22
	2.2	0.2	228.62	1.51
	2.2	0.1	228.52	1.48
SiO_2	0.9	0.4	228.65	1.74
	2.2		228.83	1.66
	3.8		228.73	1.66

3.2.1.6 Mo species quantification

The decomposition of Mo 3d was performed according to the method exposed in the experimental part and as previously mentioned in the part 3.2.1.1. The BE of the Mo species (Mo^{IV}, Mo^{V} and Mo^{VI}) and relative quantities associated are presented in the Table 9. An example of the decomposition of Mo 3d is shown in the experimental part, section 2.2, Figure 3.a.

The S/Mo atomic ratios calculated (corresponding to the ratio between the S and Mo atoms engaged in the sulfided phase) are closed to 2 for the supports CoMoS/γ-Al_2O_3, CoMoS/$\delta\theta$-Al_2O_3 and CoMoS/SiO_2, reflecting a MoS_2 phase well formed after sulfidation (except for CoMoS/SiO_2 at dMo 2.2 at.nm^{-2} probably related to a low Mo sulfidation degree).

For CoMoS on γ-Al_2O_3 and $\delta\theta$-Al_2O_3, the dMo has no real effect of the distribution of Mo species with around [70-80]% of the Mo(+VI) transformed into MoS_2 during the sulfidation step. Besides, Mo(+V) and Mo(+VI) are constant around 10%. For CoMoS on $\delta\theta$-Al_2O_3 at Co/Mo variable from 0.1 to 0.4, it can be noticed that the relative distribution of the Mo species is similar. The amount of Co is not affected by the sulfidation of the Mo.

Regarding CoMoS/SiO_2, whereas relative content of Mo(+VI) species is similar to alumina supported catalyst, distribution of MoS_2 and of Mo(+V) seems to indicate a lower sulfidation level of the Mo(+VI) to MoS_2. Indeed, Mo(+VI) is transformed to MoS_2 and to Mo(+V) respectively with a relative content around 55% and 30% regardless the dMo.

Table 9. XPS relative and atomic surface concentrations of the different Mo species for supported CoMoS catalysts.

Support	dMo	Co/Mo	Mo^{VI} (MoO_x)		Mo^{V} (MoO_xS_y)		Mo^{IV} (MoS_2)		S/Mo
			%rel.	%at.	%rel.	%at.	%rel.	%at.	
γ-Al_2O_3	0.9	0.4	7	0.28	14	0.55	79	3.12	2.02
	2.2		13	1.05	16	1.30	71	5.75	2.08
	3.8		11	1.43	17	2.21	72	9.36	2.14
	4.8		12	1.83	15	2.29	73	11.1	2.16
$\delta\theta$-Al_2O_3	0.9	0.4	26	0.31	17	0.21	57	0.69	2.23
	2.2		17	0.48	16	0.46	67	1.91	2.06
	3.8		13	0.58	17	0.75	70	3.11	2.01
	4.8		13	0.71	14	0.76	73	3.99	2.27
	2.2	0.2	16		16		68		2.12
	2.2	0.1	14		16		70		2.10
SiO_2	0.9	0.4	17	0.44	34	0.88	49	1.26	1.62
	2.2		10	0.75	34	2.55	56	4.21	2.02
	3.8		10	1.08	32	3.47	58	6.29	1.9

3.2.2 Analysis of Co 2p levels BE by XPS

Figure 19 presents the Co2p XPS spectra of alumina and silica supported catalysts at each dMo (0.9, 2.2, 3.8, 4.8 at.nm^{-2}) and Co/Mo ratio equal to 0.4 as well CoMoS/$\delta\theta$-Al_2O_3 at dMo 2.2 at.nm^{-2} at Co/Mo ratio variable.

According to work conducted at IFPEN by Gandubert et al.[27], Co2p spectra can be decomposed into three components corresponding to three different Co species. Generally, the main Co specie corresponds to the Co engaged into the CoMoS phase. Two minor Co species are related to the cobalt sulfided (Co_xS_y) and to Co in (+II) oxidation states which

could correspond to Co oxide phase. Each Co species is characterized by a Co 2p doublet (Co2p $_{1/2}$ and Co2p $_{3/2}$). An example of the decomposition of Mo 3d is shown in the experimental part, section 2.2, Figure 3.b.

Binding energy (BE) corresponding to the maximum of the two main peaks around 793.4 eV (BE5, Co $2p_{1/2}$) and 778.5 eV (BE6, Co $2p_{3/2}$) are essentially related to the cobalt atoms engaged in the CoMoS phase. In order to study qualitatively a possible binding energy shift due to support or dMo effect, we will focus on the main contribution reported in Table 10.

In order to performed a quantitative analysis, all Co species and Co spectral contributions are taken into account (section 3.2.2.1) i.e the sulfided cobalt phase with BE related to $Co2p_{1/2}$ (BE around at 793.2 eV) and $Co2p_{3/2}$ (BE around at 778.1 eV) and the Co oxide phase with BE related to to Co2p $_{1/2}$ (BE around at 781.5 eV) and $Co2p_{3/2}$ (BE around at 797eV).

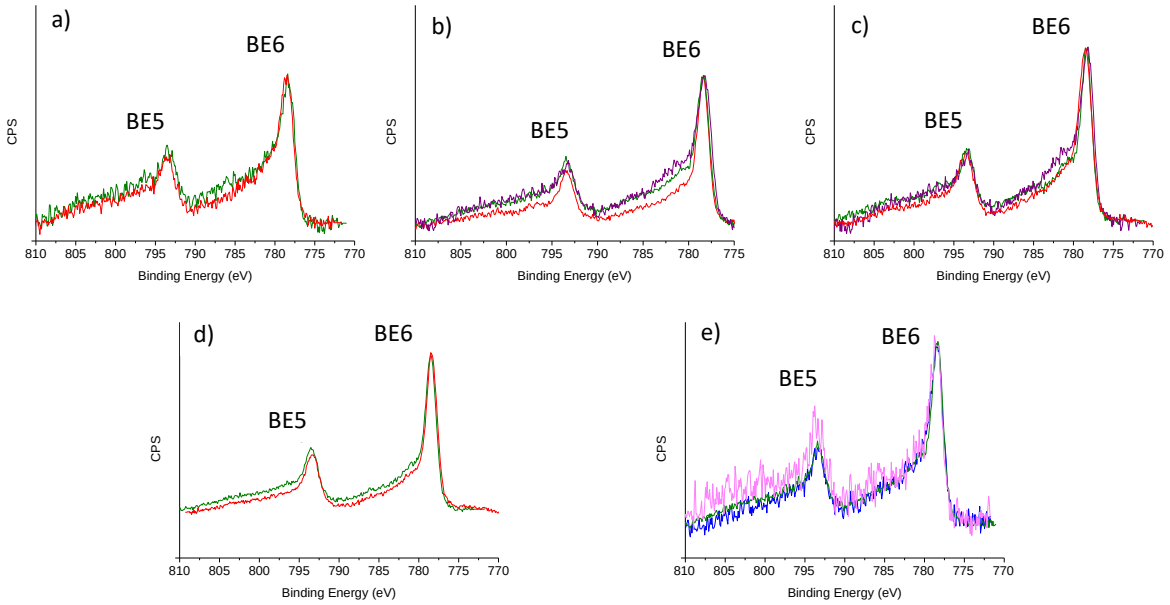

Figure 19. Co 2p XPS spectra of CoMoS/γ-Al_2O_3 (red), CoMoS/δθ-Al_2O_3 (green) and CoMoS/SiO_2 (purple) at dMo equal to (a) 0.9 (b) 2.2 and (c) 3.8 and d) 4.8 at.nm^{-2}. Co 2p XPS spectra of (e) CoMoS/δθ-Al_2O_3 with a Co/Mo molar ratio of 0.1 (pink), 0.2 (blue) and 0.4 (green) at dMo= 2.2 at.nm^{-2}. Spectra are normalized by the $2p_{3/2}$ peaks(around 778.6 eV).

Table 10. Binding energies of the different contributions of Co 2p XPS spectra obtained for the various supported CoMoS catalysts.

Support	dMo	Co/Mo	BE6 (eV) $Co2p_{3/2}$
γ-Al_2O_3	0.9	0.4	778.55
	2.2	0.4	778.30
	3.8	0.4	778.47
	4.8	0.4	778.52
$\delta\theta$-Al_2O_3	0.9	0.4	778.42
	2.2	0.4	778.42
	3.8	0.4	778.35
	4.8	0.4	778.58
	2.2	0.2	778.42
	2.2	0.1	778.42
SiO_2	0.9	0.4	n.a.*
	2.2	0.4	778.35
	3.8	0.4	778.22

n.a. * not accessible due to a low amount of Co leading to a too low S/N ratio

The binding energy of the Co $2p_{3/2}$ level (at low energies, BE6, around 778.40 eV) varies of 0.25, 0.16 and 0.13 eV at iso-support respectively for γ-Al_2O_3, $\delta\theta$-Al_2O_3 and SiO_2. As for the fluctuation of the Mo 3d binding energies previously discussed in details, this variation may result from several intricate effects. As it was shown by DFT calculations[61], this variation may reflect different cobalt environment at the edges of the CoMoS. Gandubert et al.[27] have shown that the ECLS value of the Co 2p is lower on the M-edge than on the S-edge. Moreover it cannot be excluded also the role of size and stacking effects as well as the electronic transfer between the support and the promoter atoms.

3.2.2.1 Co species quantification

In order to obtain the relative quantities between the Co species (Co(II), Co_9S_8 and CoMoS phase), decomposition of Co 2p spectra was performed according to the method exposed in the experimental part, section 2.2. An example of the decomposition of Mo 3d is shown in the experimental part, section 2.2, Figure 3.b. The BE of the Co species (CoO, CoMoS and Co_9S_8) and relative quantities associated are presented in the Table 11.

Table 11. XPS relative and atomic surface concentrations of the different Co species for supported CoMoS catalysts.

Support	dMo	Co/Mo	Co(II) phase		CoS_x		CoMoS	
			%rel.	%at.	%rel.	%at.	%rel.	%at.
γ-Al_2O_3	0.9	0.4	n.a.*	n.a.*	n.a.*	n.a.*	n.a.*	n.a.*
	2.2	0.4	24	0.45	48	0.90	28	0.53
	3.8	0.4	28	0.86	30	0.92	42	1.29
	4.8	0.4	29	1.50	22	0.80	49	1.77
$\delta\theta$-Al_2O_3	0.9	0.4	36	0.10	26	0.07	38	0.10
	2.2	0.4	32	0.22	33	0.23	35	0.24
	3.8	0.4	28	0.31	32	0.34	40	0.42
	4.8	0.4	35	0.46	15	0.2	50	0.65
	2.2	0.2	33		27		40	
	2.2	0.1	n.a.* *	n.a.* *	n.a.* *	n.a.* *	n.a.* *	n.a.* *
SiO_2	0.9	0.4	n.a.* *	n.a.* *	n.a.* *	n.a.* *	n.a.* *	n.a.* *
	2.2	0.4	39	0.71	39	0.71	22	0.39
	3.8	0.4	38	0.98	50	1.30	12	0.31

*not accessible due to large shift of Mo 3d photoemission peak (used as reference) leading to a too large error in the Co species quantification

* * not accessible due to a low amount of Co leading to a too low Signal/Noise ratio

In contrast with the results obtained for the Mo species, modification of the dMo leads to different Co species distribution. In this study, for alumina supported catalysts (γ and $\delta\theta$) when the dMo increases, an increase of the relative content of cobalt engaged in the CoMoS phase is observed while the relative content of sulfided cobalt, Co_9S_8, reaches a plateau and decreases for a dMo higher than 2.2 at.nm^{-2}. Relative concentration of CoO species is almost unchanged. This phenomenon may result from the nature of interaction of the Co(II) precursor with the alumina support. The strong interaction of Co(II) precursor via a surface molecular recognition process with the (110) or (100) surfaces as recently studied by DFT calculation,[62] may thus explain why cobalt atoms instead of being easily incorporated in the CoMoS phase, remain in the Co(II) state or are sulfided in the Co_9S_8 phase. The low migration capacity of these strongly interacting Co(II) may also explain this trend. When increasing the dMo, the molybdate precursor species competing with the same aluminols sites and prevent a certain proportion of cobalt(II) precursor from their strong interaction with the alumina sites. Hence, this will favor the migration of the cobalt species into the CoMoS phase. This may thus explain why the relative content of cobalt in the CoMoS may increase with dMo.

When considering CoMoS/SiO_2, high amount of CoO species is reported compared to alumina catalyst. In addition, the relative content of CoMoS is dramatically reduced over

silica supported catalysts at the expanse of Co_9S_8 phase, compared with alumina ones. Moreover, the relative content of CoMoS phase decrease with dMo.

Contrary to alumina, on silica, the interactions of Co and Mo species are expected to be the weaker, so the afore mentioned analysis on alumina does not hold. Thus, we may suspect that if the Co(II)-support interaction becomes too weak on silica, the $Co(OH)_2$ and molybdate precursor agglomerate more easily due to their higher diffusion capability and are more heterogeneously dispersed on the silica surface which leads to the formation of the CoO (not observed) and MoO_3 phases (observed by XRD, chapter II, Section 2.3) with bigger sizes. Although, further analyses on the oxides phases would be required to better understand this phenomenon, one may suggest that an optimal interaction strength between the oxide precursor and the support is mandatory to enable the formation of the wished CoMoS phase. .

3.2.2.2 $(Co/Mo)_{slab}$ atomic ratio

$(Co/Mo)_{slab}$ atomic ratio is defined as the ratio between the cobalt decorating the edge of the MoS_2 slab and the Mo atoms engaged in the MoS_2 slab (section 2.2.3 ,Eq.7) .

In order to evaluate the Co-promotion level in the MoS_2 slab, the $(Co/Mo)_{slab}$ atomic ratio defined as the ratio between the cobalt decorating the edge of the MoS_2 slab and the Mo atoms engaged in the MoS_2 slab (Table 12).

Table 12. $(Co/Mo)_{slab}$ atomic ratio as function of the dMo for CoMoS/ γ-, $\delta\theta$-Al_2O_3 and SiO_2.

Support	dMo	Co/Mo	$(Co/Mo)_{slab}$
γ-Al_2O_3	0.9	0.4	n.a.*
	2.2		0.16
	3.8		0.25
	4.8		0.29
$\delta\theta$-Al_2O_3	0.9	0.4	0.38
	2.2		0.27
	3.8		0.31
	4.8		0.39
	2.2	0.2	0.20
	2.2	0.1	0.12
SiO_2	0.9	0.4	n.a.**
	2.2		0.12
	3.8		0.07

*not accessible due to large shift of Mo 3d photoemission peak (used as reference)

leading to a too large bias in the Co species quantification
* * not accessible due to a low amount of Co leading to a too low S/N ratio

For the δθ alumina supported CoMoS phases, the $(Co/Mo)_{slab}$ atomic ratio decreases slightly from a dMo of 0.9 to 2.2 at.nm^{-2}. Then, the $(Co/Mo)_{slab}$ atomic ratio increases slightly from a dMo of 2.2 to 4.8 at.nm^{-2}. For CoMoS/γ-Al_2O_3, the $(Co/Mo)_{slab}$ atomic ratio increases continuously from 2.2 to 4.8 at.nm^{-2}. By contrast, for CoMoS/SiO_2, the $(Co/Mo)_{slab}$ atomic ratio decreases from a dMo of 2.2 to 3.8 at.nm^{-2}. If we consider the two highest dMo loading (dMo of 2.2, 3.8 at/nm²), the $(Co/Mo)_{slab}$ at iso-dMo increases in the following order as a function of the support:

$$CoMoS/SiO_2 < CoMoS/\gamma\text{-}Al_2O_3 < CoMoS/\delta\theta\text{-}Al_2O_3$$

$(Co/Mo)_{slab}$ of CoMoS/SiO_2 is significantly lower (1.5 to 3 times) compared to alumina supports for both dMo of 2.2 and 3.8 at.nm^{-2} of support. One should recall that this $(Co/Mo)_{slab}$ ratio results from several factors: not only the percentage of the Co atoms engaged in the mixed phase, but also indirectly the degree of sulfidation of the Mo atoms.

For CoMoS on δθ-Al_2O_3, the $(Co/Mo)_{slab}$ is increasing concomitantly with the Co/Mo molar ratio, as it was also observed on γ-alumina by Gandubert et al.[27]
Moreover, XPS and TEM have given insights into the Mo and Co species present at the catalyst surface and the size and stacking characteristics of the nano-crystallites. By combining both and considering DFT geometrical model developed by Krebs et al.[63], a nano-scale description of Co distribution at the edges of the crystallites will be proposed in the forthcoming section.

3.3 2D morphology model of the CoMoS slab

3.3.1 Distribution of Co and Mo atoms at M-edge and S-edge

Results of characterization (TEM analysis, FX analysis and XPS experiments) and previously published DFT calculations can be combined in order to obtain a 2D morphology model of the CoMoS slab. In practice, an hexagonal morphology for the CoMoS nano-crystallites has been assumed in line with the same DFT calculations and earlier geometrical models.[29] In addition, by considering the slab length obtained by TEM analysis, the quantification of the Mo atoms contained in each slab, at the edges and at the basal plane can be determined for each individual crystallite from the methodology described in experimental part 2.2.3. The results obtained are reported on Table 13. It can be noticed that the number of atoms at the

edge increases with the dMo because of the slab length is increasing, as mentioned in Figure 6.

Table 13. Distribution of the Mo atoms by considering an hexagonal shape MoS_2 slabs according the DFT geometrical model. Relative uncertainties to consider for the value obtained are ±10%.

dMo	Support	Co/Mo	Metallic atoms in the slab, M_{slab}	Metallic atoms at edges, M_{edge}	Mo atoms in the bulk Mo_{basal}	Dipersion M_{edge} / M_{slab}
0.9	γ-Al_2O_3	0.4	38	18	20	0.47
	$\delta\theta$-Al_2O_3		84	29	56	0.35
	SiO_2		59	24	36	0.41
2.2	γ-Al_2O_3	0.4	52	22	30	0.42
	$\delta\theta$-Al_2O_3	0.1	82	28	54	0.34
	$\delta\theta$-Al_2O_3	0.2	78	28	51	0.36
	$\delta\theta$-Al_2O_3	0.4	80	28	52	0.35
	SiO_2	0.4	65	25	40	0.38
3.8	γ-Al_2O_3	0.4	81	28	53	0.35
	$\delta\theta$-Al_2O_3		105	32	72	0.30
	SiO_2		77	27	50	0.35
4.8	γ-Al_2O_3	0.4	83	28	54	0.34
	$\delta\theta$-Al_2O_3		101	32	69	0.32

To evaluate the dispersion of the active phase for each catalyst, the ratio between the number of atoms at the edge of slabs and the number of total atoms of slabs (M_{edge}/M_{slab} ratio) is calculated (Table 13). It can be observed that dispersion of the MoS_2 active phase generally decreases as a function of dMo regardless the support considered. This is consistent with the increase of TEM size with dMo (Figure 4a). For CoMoS/$\delta\theta$-Al_2O_3 at iso-dMo of 2.2 at.nm^{-2}, it can be noted that the dispersion is constant regardless the Co/Mo ratio considered, which is constant with the previous observation that the TEM size remains almost unchanged whatever the Co/Mo ratio (Figure 4b)

In order to describe the morphology of the Co-promoted slab, the cobalt decoration degree at the edge, called X_{Co}, is calculated (Experimental part 2.2.3), following the rule that the S-edge of the MoS_2 slab is firstly decorated before the M-edge according to the thermodynamic stability at edges given by DFT calculations.[28] One may underline that we thus assume that all MoS_2 crystallites are promoted and exhibit an hexagonal shape for the

CoMoS crystallites. This assumption is a simplified one since we know that two predominant morphologies have been observed by STEM hexagonal and truncated triangular shapes.

Thus, by taking into account the decoration degree of cobalt promoter at the edge, X_{Co}, the proportion of non-promoted and promoted edges: $Mo_{M\text{-}edge}$ and $Co_{M\text{-}edge}$, $Mo_{S\text{-}edge}$ and $Co_{S\text{-}edge}$ have been determined. Figure 20 presents respectively the relative (a) and effective (b) contents for CoMoS/$\delta\theta$-Al_2O_3 at dMo of 2.2 at.nm^{-2} at various Co/Mo ratio. Numerical values associated are reported in the Appendix 6.

It can be noted that the relative and effective Co contents on the S-edge increase when the Co/Mo ratio is increasing, whereas the Mo on the S-edge decreases. Moreover, the Co-promotion of the M-edge is non nul only at Co/Mo ratio of 0.4.

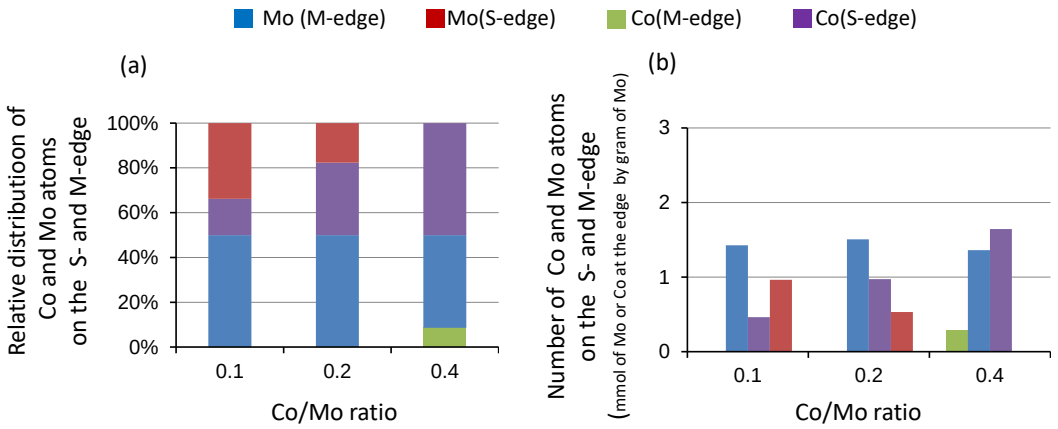

Figure 20. (a) Relative distribution of the number of Co and Mo atoms on the S and M edge, (b) Number of Co and Mo atoms on the S and M edge (mmol of Mo at the edge by gram of Mo) for CoMoS/$\delta\theta$-Al_2O_3 at dMo of 2.2 at.nm^{-2} at Co/Mo ratio variable. Relative uncertainties to consider for the obtained values are around ±25%.

In order to evaluate the support and dMo effect, Figure 21 presents respectively the relative (a) and effective (b) content for each catalyst at various dMo. Numerical values associated are reported in the Appendix 6.

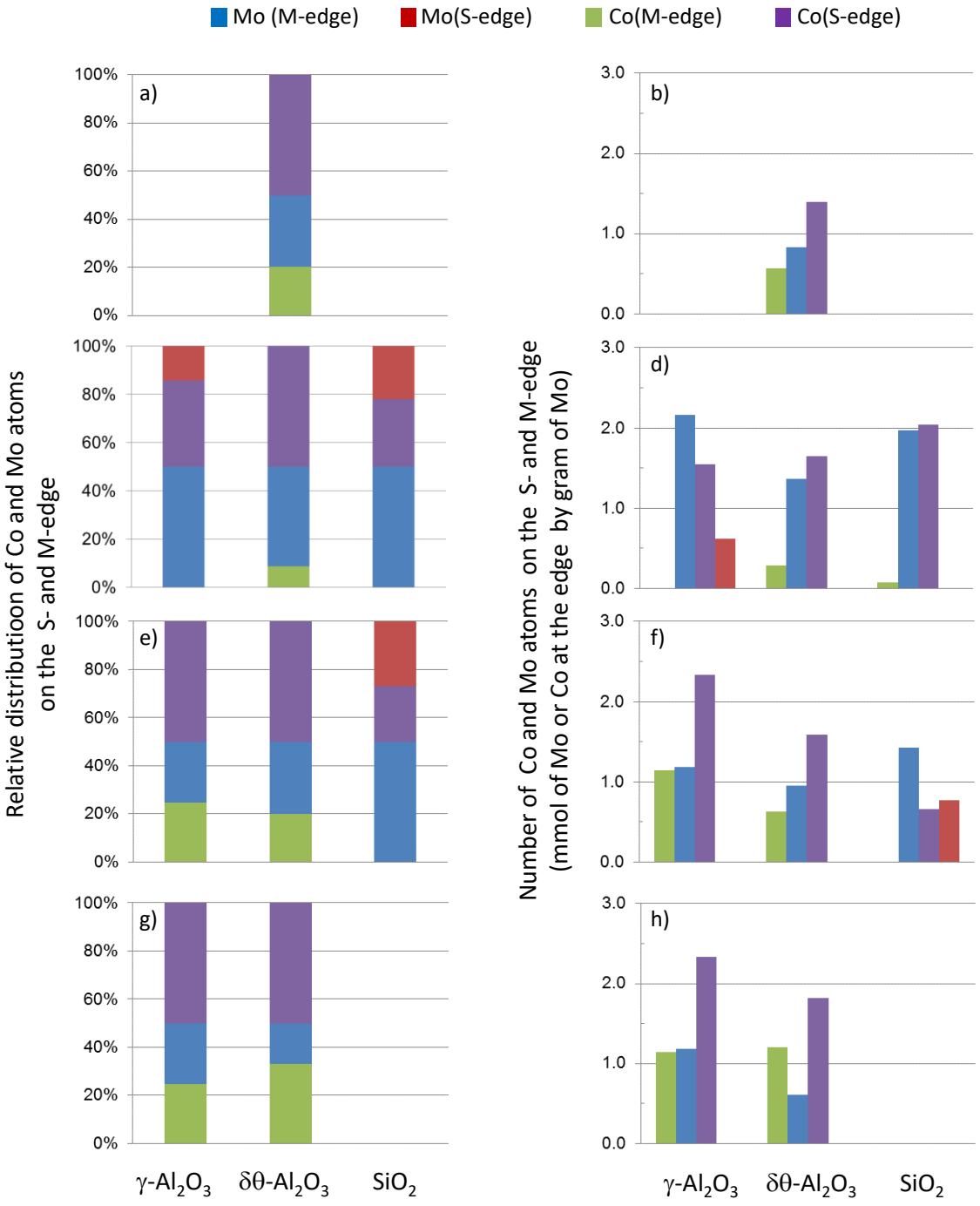

Figure 21. Graphs on the left column report the elative distribution of the number of Co and Mo atoms on the S and M edge, and graphs on the right column report the number of Co and Mo atoms on the S and M edge (mmol of Mo at the edge by gram of Mo) for CoMoS on γ-Al_2O_3, $\delta\theta$-Al_2O_3 and SiO_2 at each dMo (a,b) 0.9, (c,d) 2.2, (e,f) 3.8, and (g,h) 4.8 at.nm^{-2} of support. Relative uncertainties to consider for the obtained values are around ±25%.

Regarding the relative content at iso-dMo, it can be noted that for CoMoS/SiO_2 only the S-edge is promoted but with a significantly lower amount than on γ- $\delta\theta$-Al_2O_3 at iso-dMo. This distribution could explain at first sight the low activities of silica supported CoMoS.

For CoMoS on γ-, δθ-Al_2O_3, the distributions of the $Mo_{M\text{-}edge}$ and $Co_{M\text{-}edge}$, $Mo_{S\text{-}edge}$ and $Co_{S\text{-}edge}$ are closed at iso-dMo (excepted at iso-dMo 2.2 at.nm^{-2} with the S-edge not fully covered by Co).

Regarding the effective content for alumina supported catalysts, it can be noticed that the Co content on the S-edge decreases slightly in the following order for the 2 higher dMo: γ-Al_2O_3 > δθ-Al_2O_3. However, an opposite trend is observed at iso-dMo 2.2 at.nm^{-2}.

Regarding the relative content at iso-support, for CoMoS/γ-Al_2O_3, it can be noted that Co content on the M- and S-edge slightly increases when the dMo is increasing whereas the Mo content on the M- and S-edge decreases. For CoMoS/δθ-Al_2O_3 the S-edge is fully decorated by Co and the amount of Co on the M-edge increases progressively with the dMo (except for the lower dMo).

CoMoS supported on SiO_2 exhibits a different behaviour: the relative and effective content of Co at the S-edge decreases whereas at the expanse of the relative content of Mo at the S-edge whereas the Mo on the M-edge is kept constant when the dMo is increasing from 2.2 to 3.8 at.nm^{-2}.

At this stage, considering the hexagonal shape of CoMoS crystallites, no obvious trend can be found at iso-support or iso-dMo. Thus, we attempt in what follows to investigation if correlations can be found with spectroscopy and catalytic measurements.

3.3.2 2D morphology model of the CoMoS slab vs catalytic activity of the HDS catalysts

Initial activities related to the initial rates of 3MT and 23DMB2N conversion, respectively a_{3MT} and $a_{23DMB2N}$, as well as activities related to initial rate of the HDS and HYDO yield, respectively a_{HDS} and a_{HYDO}, have been determined in the chapter III.

By assuming the 2D morphology model previously exposed, we have attempted to identify correlation between catalytic activities and the Co and Mo edge atoms distribution of CoMoS/γ-,δθ-Al_2O_3 and SiO_2.

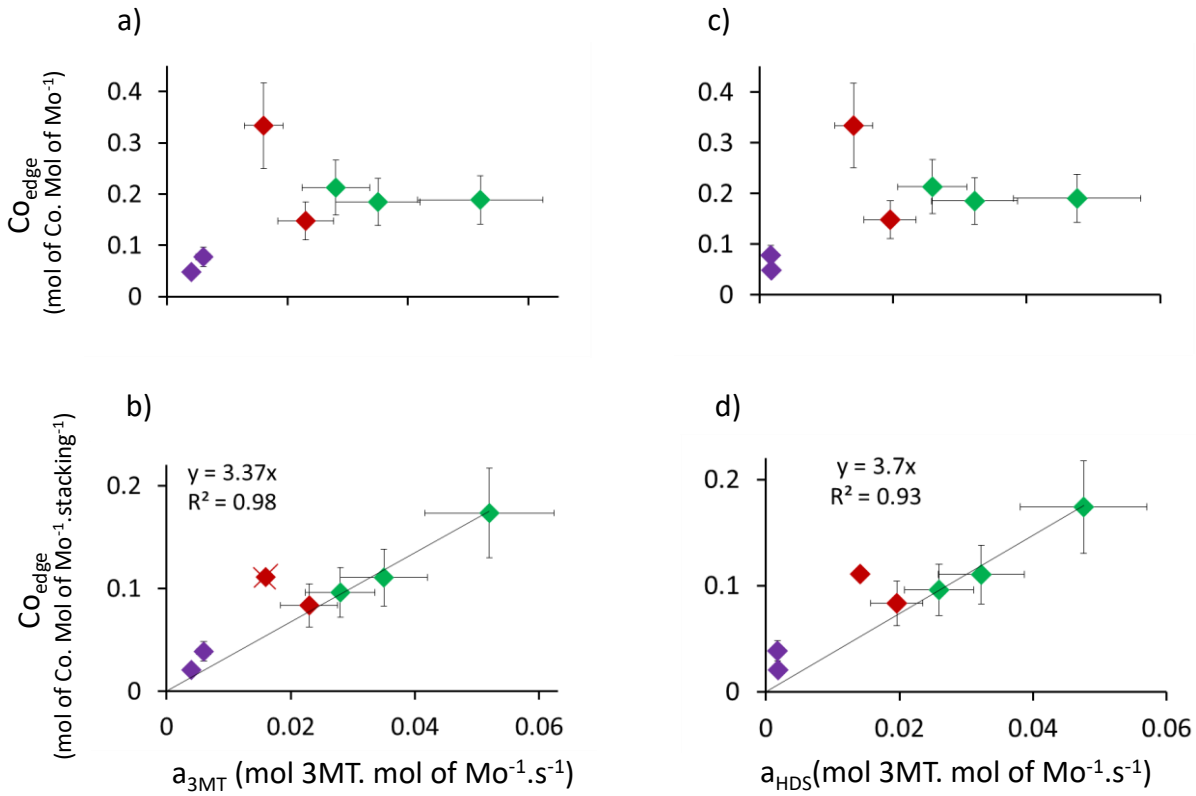

Figure 22. Correlation of the activities at 220°C related to the initial rate of 3MT reaction, a_{3MT} , and the initial rate of the HDS yield, with respectively (a), (c) the Co edge atoms (mol 3MT.mol of $Mo^{-1}.s^{-1}$) and (b), (d) the Co edge normalized by the stacking (mol 3MT.mol of $Mo^{-1}.s^{-1}$.stacking^{-1}) at the slab of the CoMoS on γ-Al_2O_3 (red), $\delta\theta$-Al_2O_3 (green) and SiO_2 (purple) previously presented in the section 3.2.2.1. Experimental points with a red cross are not taking into account to obtain the linear regression analysis. Relative uncertainties on the activity and the atoms distribution are evaluated respectively to 20% and 25%.

It can be noticed that the amount of Co_{edge} reach a plateau with the increase of both activities. Thus, the Co_{edge} alone is not a relevant parameter to explain the activities of the HDS catalysts even if several studies suggest that the cobalt at the edge should be responsible of the activities.[13,14]

However, as it will be shown for the NO correlation (chapter V, section 4.1) a linear correlation passing through the origin is improved when the number of Co_{edge} of the CoMoS phase is normalized by the stacking (Figure 22). The same linear correlations of the $a_{23DMB2N}$ and a_{HYDO} with the Co_{edge} normalized by the stacking are reported in Appendix 7, Figure 32 b) and d)). As for the NO IR experiments, this result may suggest that only the cobalt atoms decorated the edges of the slab at the top are active for the 3MT and 23DMB2N conversion. It should be underlined that all other attempts to correlate different types of edge sites have been less successful: in particular, when the total atoms at the edge, the Mo at the edge, the Mo and Co atoms at the M- and S-edge have been considered (Appendix 8-13).

4 Conclusion

First, a detailed description of the size and morphology of the CoMoS nano-crystallites have been conducted. Results on HRTEM demonstrated an effect of the Co-promoter with an increase on both length and stacking of the slab for the CoMoS slab supported over SiO_2 whereas only the length appear to be slightly impacted over $\delta\theta$-Al_2O_3. Moreover, an effect of the molybdenum surface coverage (dMo) on the length and stacking of the CoMoS slab was observed regardless the support: The higher the dMo, the larger the slab length. Support effect was also investigated. $\delta\theta$-Al_2O_3 exhibits the higher slab length regardless the dMo. In the other way, γ-Al_2O_3 shows the most sensitive to dMo parameter compare with $\delta\theta$-Al_2O_3 and SiO_2 support. To rationalize the nature of molybdenum precursors and alumina interactions, hydroxyl properties of the alumina supports ($\delta\theta$-Al_2O_3 resulting from the sintering of γ-Al_2O_3) was analyzed by IR spectroscopy, and in coherence with the alumina facet proportions: (110), (111) and (100) surfaces. In particular, on the $\delta\theta$-Al_2O_3 support, the neutral μ_1-OH-Al_V sites (v_{OH}=3730 cm^{-1}) are predominant with respect to a more diverse distributions of OH sites on the γ-Al_2O_3 support. This may impact the catalyst at two levels: the genesis of the active phase and the catalytic activity.

Regarding the catalytic activity, it appears that the higher proportion of μ_2-OH and μ_3-OH acid sites on γ-Al_2O_3 may be at the origin of the stabilization of olefinic compounds on the γ-Al_2O_3 which would promote the hydrogenation of olefins versus $\delta\theta$-Al_2O_3. On the silica support, the lower acidic character of the silanol groups (vs. aluminol groups) may also be consistent with the higher HDS/HYDO selectivity observed on this support. However our results may be somehow tone down previous interpretation proposed in the literature.[15,16] Indeed, Fan et al. demonstrated that a compromise between the dispersion and the stacking of supported CoMoS slabs is crucial in order reach the highest HDS/HYDO selectivity. Thus, according this result, stacking and length differences observed for CoMoS on γ-, $\delta\theta$-Al_2O_3 and SiO_2 at iso-dMo of 0.9 at.nm^{-2} of support should lead to significant differences on the HDS/HYDO selectivity with probably the following order: CoMoS/γ-Al_2O_3 > CoMoS/$\delta\theta$-Al_2O_3 > CoMoS/$\delta\theta$-SiO_2. However, this result is not in line with the HDS/HYDO selectivity for the CoMoS supported catalysts at iso-dMo of 0.9 at.nm^{-2} exposed in the chapter III section 3.2.3, support effect. Indeed, low difference of selectivity was demonstrated. Li et al[16] proposed that the length slab impacted by the nature of this support could drive the HDS/HYDO

selectivity. Therefore, a significant difference in selectivity should be observed for CoMoS on γ-, δθ-Al_2O_3 and SiO_2 at iso-dMo of 0.9 at.nm^{-2}. As previously mentioned, HDS/HYDO selectivity observed is constant for these catalysts. Thus, dispersion and stacking or length slab considered alone are not be sufficient to rationalize and explain the HDS/HYDO selectivity observed, whereas the distinct nature of the acid sites present on it seem to be at the origin of catalytic differences.

Following this slab size study, HR HAADF-STEM analysis have been undertaken to explore more precisely the two-dimensional (2D) morphology of CoMoS nano-crystallites. Regardless the support at iso-dMo of 2.2 at.nm^{-2}, hexagonal and truncated triangular shapes of CoMoS slab were revealed. At this stage of this present study the following two hypotheses may be formulated regarding the morphology observed:

- Based on the HR STEM observation and DFT calculations[13,34,35], two populations of slabs coexist on the support surface: the truncated triangular and the quasi-hexagonal shapes assign to unpromoted MoS_2 and Co-promoted MoS_2 respectively.

- Based on the DFT assumption the hexagonal shape is directly related to the Co-promoted MoS_2, One second interpretation is to consider that the presence of truncated triangular shapes could result from a direct effect of the support on the nano-crystallites morphology.

Thanks to the HR HAADF-STEM analysis and the well defined δθ-Al_2O_3 platelets, it was suggested that MoS_2 crystallites are either growing in different way or are stabilized differently according to the alumina facets. Indeed, particular length distributions of the CoMoS crystallites were revealed as function of three main facets exposed by the δθ-Al_2O_3 platelets: (110), (100) and (111). Higher average length of slabs is evaluated on the lateral facets (100), whereas the lower average length is on the basal alumina (110) facet. This result is consistent with the mean slab length and the slab length distribution obtained by HRTEM analysis. The higher proportion of basic hydroxyl μ_1-Al_{IV}-OH groups (more easily exchangeable with Mo precursor) known to be present on the (110) facets may be thus at the origin of the smaller CoMoS sizes observed on these facets of the δθ-Al_2O_3 platelets. In the same way, the higher proportion of basic hydroxyl μ_1-Al_{IV}-OH groups on γ-Al_2O_3 platelets than on δθ-Al_2O_3 may also explain the smaller CoMoS sizes observed on γ-Al_2O_3. However, the (110)/((100)+(111)) facet proportion, differing in the nature of its surface hydroxyls, is

not sufficient to explain the smaller sizes of CoMoS particles on γ-Al_2O_3 which exposed a higher proportion of (100) surface than $\delta\theta$-Al_2O_3. Thus, it was suggested that μ_1-Al_{IV}-OH located at the corner and/or edge at the intersection of (110)-(100) facets may also play a key role in the genesis of smaller and more dispersed CoMoS crystallites.

In order to characterize qualitatively and quantitatively the Mo and Co sulfided species present on the three supports, XPS analysis was performed. The analysis of Mo 3d levels BE by XPS reveals a binding energy shift according the nature of the support itself regardless the unpromoted or Co-promoted MoS_2 crystallites: γ-Al_2O_3 ~ $\delta\theta$-Al_2O_3 < SiO_2 < bulk. At this stage, XPS combined with DFT calculation have shown that the lower binding energy shift observed on the unpromoted MoS_2 compared with the MoS_2 bulk could be related to the nature and the proportion of M-edge/S-edge slightly in favor of the M-edge. Indeed, MoS_2 exposes M-edge and S-edge with low and high Mo coordination number on the S-edge and the M-edge with 50% S respectively could lead by compensation of both contributions to an overall small negative shift. Moreover, it was not excluded that a size effect could directly impact the XPS peak positions of Mo contribution, since diminishing the MoS_2 size enhances the edge interactions. In the same way, stacking cannot be excluded since increasing the stacking modifies the proportion of the edges in interactions with the support. Additionally, the assumption that supports govern the electronic effect observed on the binding energy of the Mo engaged in the mixed CoMoS phase was strengthening by excluding a possible Co promoter effect. Indeed, by combining the Mo binding energy shift related to the Mo engaged in the CoMoS phase and DFT calculations describing electron density on Mo atoms by the perturbation of Co atoms, it was shown that the Co-promoter effect cannot be considered.

Then, the quantification of the Mo and Co species was performed by decomposition of Mo3d and Co2p XPS spectra. It was noticed that for γ- and $\delta\theta$-alumina supported catalyst the relative content of the Co atoms engaged in the CoMoS phase was increasing with the increase of the dMo whereas the relative content of sulfided cobalt is decreasing. For silica supported catalysts, the reverse trend was observed. This Mo and Co species quantification allows us to build a 2D morphology model of the CoMoS slab providing a quantitative description of the Mo and Co atoms located at the M- or S-edge of the slab. However, no clears trends regarding the Mo or Co atoms at the M- or S-edge appear. An interesting result

is the decoration of Co atoms at the M-edges especially for alumina supported catalysts based on the combination of the XPS and TEM techniques with DFT calculation predicting it. Indeed, even if some studies[64] suggest that the promotion by Co of the M-edges is not possible on the base of STM observations of CoMoS sulfided phase on a gold support, it is still far from an industrial catalyst. Moreover, this previous result will be in line with a more refined assignment of the NO spectrum as a function of the CoMoS edge sites proposed in Chapter V.

Finally, it was attempted to make the link between the catalytic properties and the Mo and Co atoms distribution obtained by the 2D morphology model. At this stage, it was demonstrated that only the cobalt atoms at the edge (Co at the M- and S-egde) could explained initial activities of 3MT and 23DMB2N reaction as well as initial activities of HDS and HYDO yield. This correlation is in line with general understanding that the Co present at the edge is essentially responsible of the HDS activity[13]. However, to make possible this correlation, the staking was taken into account for the site normalization, leading to finally considered that only the Co edge atoms at the top of stacks might be responsible of the catalytic properties. This result strengthened the importance to consider the stacking as well as the cobalt decoration degree of the edge of the CoMoS slab. Thus, a relevant 2D morphology model was built which combined the features of the CoMoS active phase, length, cobalt decoration degree and stacking, should allow to progress in the understanding of the catalytic properties.

5 Appendices

Appendix 1. SEM image of the support

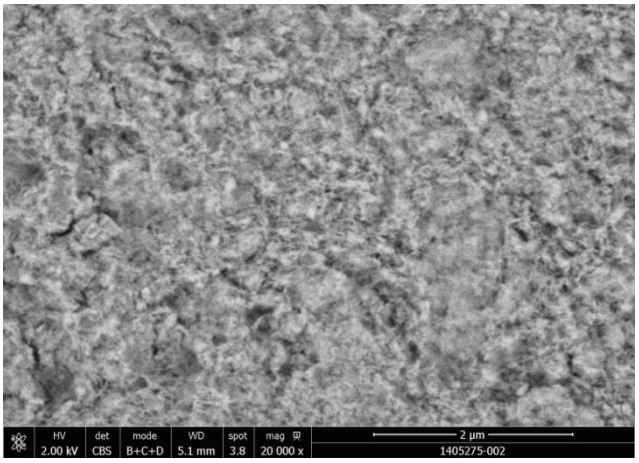

Figure 23. SEM images of γ-Al_2O_3 support.

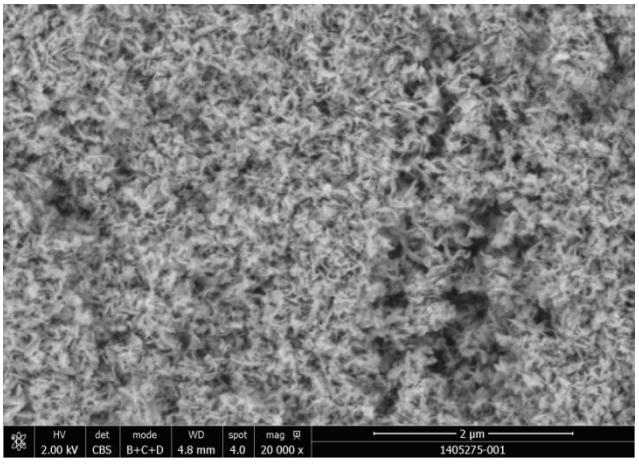

Figure 24. SEM image of $\delta\theta$-Al_2O_3 support.

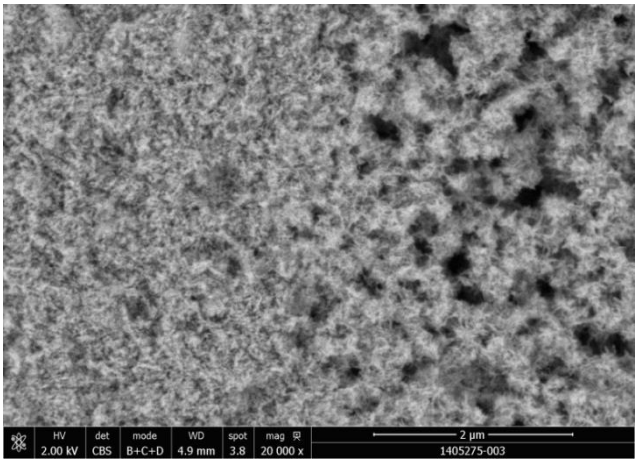

Figure 25. SEM image of SiO_2 support.

Appendix 2. X-ray Photoelectron Spectroscopy (XPS)

X-ray Photoelectron Spectroscopy (XPS) is used to describe various material surfaces up to 10 nm depth, a few atoms thick. Indeed, only electrons close to the surface of the sample have a good probability of exiting without an inelastic shock. Qualitative and quantitative analysis can be performed.

This technique consists in bombarding the surface of sample with a X-ray incident beam, in order to measure kinetic energy of the emitted photoelectrons, E_K.

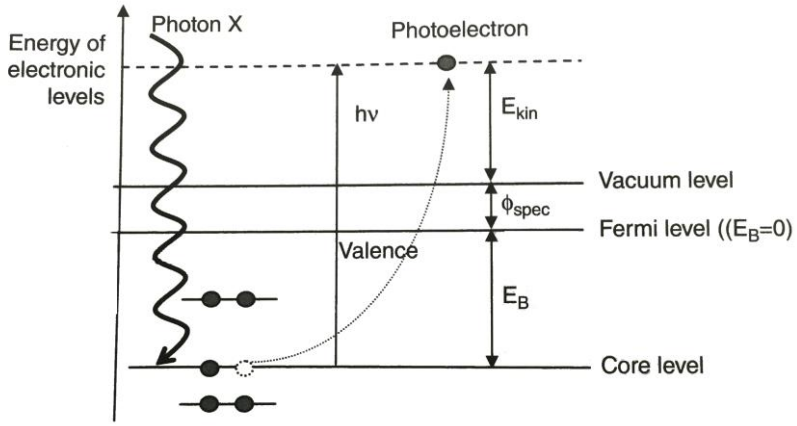

Figure 26. Diagram of the principle of the excitation.

Thus, binding energies of the electrons E_B in the excited atomic level can be determined knowing the incident photon energy hν and the emitted photoelectron kinetic energy associated using the Einstein equation:

$E_B = hn - E_K (+ \Phi a)$

Where,

h – Planck constant

ν – Frequency (Hz) of the X-ray incident radiation

E_K – the measured kinetic energy of the photoelectron leaving the solid

E_B – Binding energy of the electron in the atomic orbital in the excited state (Binding energies correspond to the difference between the energy level considered (of the excited atomic level) and the Fermi level.

Φa – intrinsic parameter of the analyzer takes into account to correct the kinetic energy by the vacuum effect.

Each binding energy corresponds to one type of atom and one specific orbital. Kinetic energy of the ejected electron is then specific to one element because of it is directly linked to the nature of the atom and the energy of the photoelectron in the excited orbital level. Moreover, the chemical environment on the atoms, oxidation state, directly impacts the binding energy.
Thus, the elements present on the surface and his chemical nature can be identified.

XPS spectra were obtained with a Kratos Axis Ultra spectrometer equipped with an Al Kα source (1486.6 eV) and a hemispherical analyzer. Measurements were carried out at room temperature under high vacuum 10^{-9} Torr in the analysis chamber with 40 eV pass energy. Calcined and sulfided samples were prepared in glovebox (under controlled atmosphere), ground and pressed in indium foil.
Subsequently, the samples were transferred to a vessel for transport under N_2 to the XPS apparatus. XP spectra were fitted with Casa XPS (version 2.0.71). A Shirley background subtraction was applied and Gauss–Lorentz (30%-70%) curves were used.
The measurement was done at 0.05 eV intervals for the Cobalt and 0.1 eV intervals for the molybdenum, phosphor, sulfur, aluminum and the contamination carbon. Carbon contamination is chosen has charge reference. The binding energies of each of elements are referenced to the binding energy of the C1s level of the contamination carbon at 284.6 eV.

Quantification of Mo and Co species, are performed based on the work of Gandubert. [65]
Identified Mo species correspond to Mo(+IV) correspond to MoS_2 species , Mo (+V) oxide state is attributed to oxysulfide species (MoS_xO_y) and Mo in (+VI) oxide state is attributed to an Mo oxide phase.
Identified Co species correspond to a Co(+II) specie attributed to a Co oxide phase which is not sulfided (as CoO), a Co specie attributed to the Co sulfided to form Co_9S_8 sulfided specie and a Co specie attributed to the mixed phase composed of Co and Mo which is sulfided to form a CoMoS phase.

Appendix 3. Average length and stacking for the unpromoted MoS_2/SiO_2 and for the promoted $CoMoS/SiO_2$.

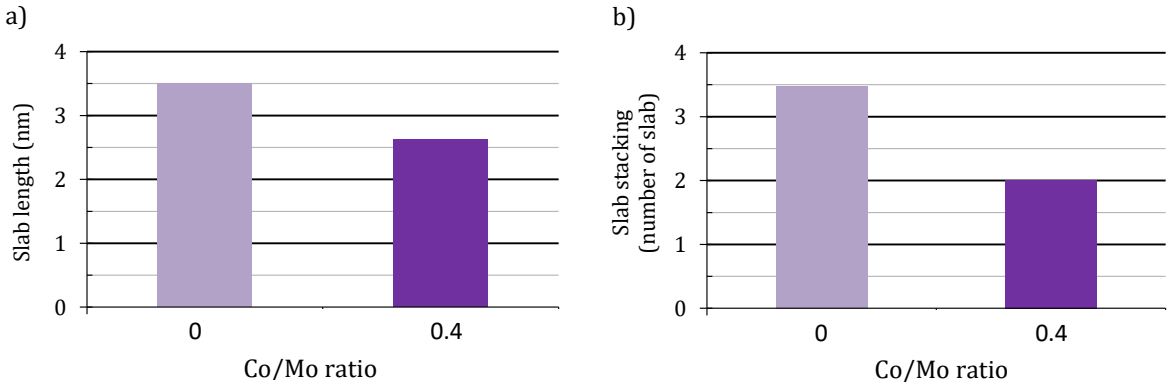

Figure 27. Average (a) length and (b) stacking for the unpromoted MoS_2/SiO_2 and for the promoted $CoMoS/SiO_2$ with a Co/Mo ratio equal to 0.4 at iso-dMo of 2.2 at.nm^{-2} for both. Relative uncertainties on the length and stacking of the slab are respectively ±10% and ±15%.

Appendix 4. Slab length distribution as function of the support of CoMoS on γ-Al_2O_3, $\delta\theta$-Al_2O_3 and SiO_2 at iso-dMo of 0.9 and 3.8 at.nm^{-2} of support for a Co/Mo ratio close to 0.4.

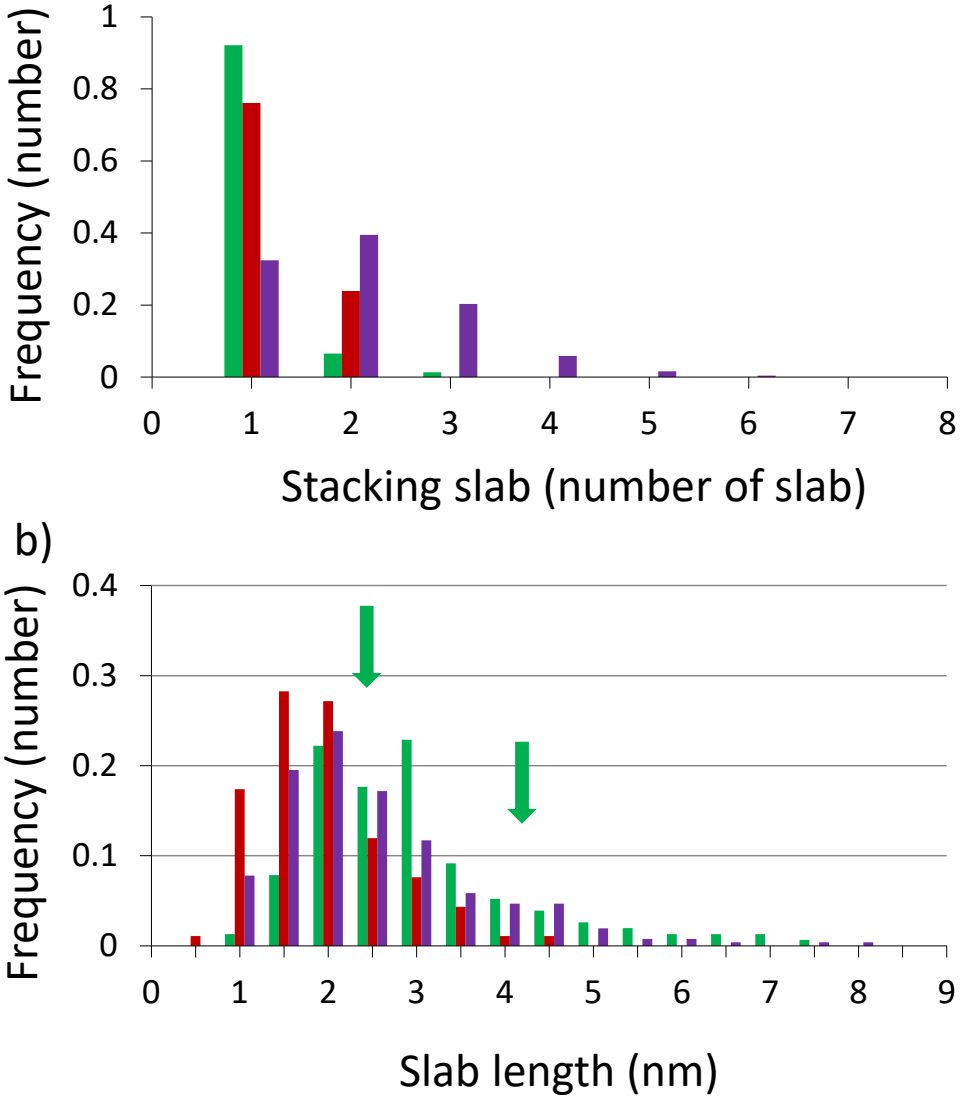

Figure 28. (a) Stacking and (b) length distributions of the slab as function of the support of CoMoS on γ-Al_2O_3 (red) , $\delta\theta$-Al_2O_3 (green) and SiO_2 (purple) at iso-dMo of 0.9 at.nm^{-2} of support for a Co/Mo ratio ratio close to 0.4. Relative uncertainties on stacking and the length is respectively ±15% and ±10%.

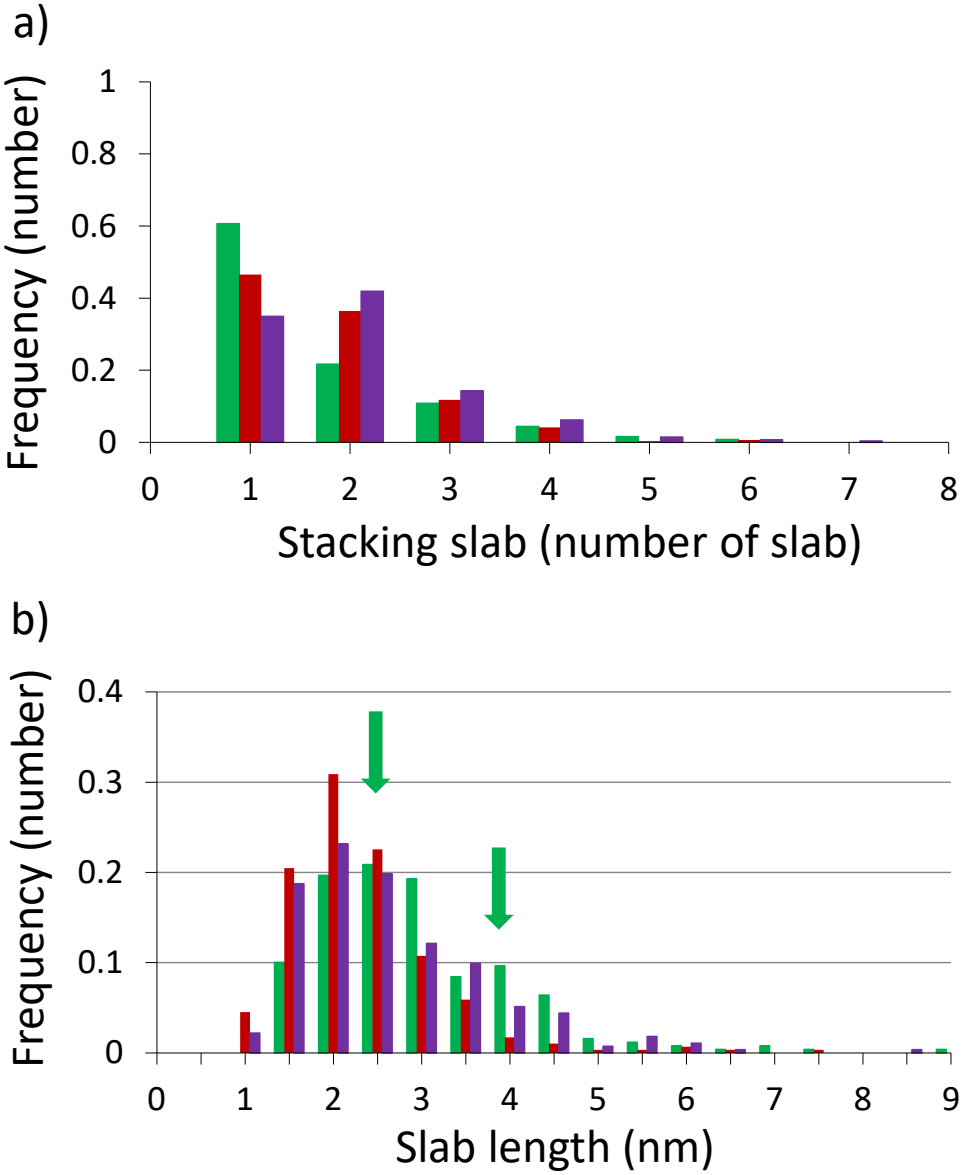

Figure 29. (a) Stacking and (b) length distributions of the slab as function of the support of CoMoS on γ-Al_2O_3 (red) , $\delta\theta$-Al_2O_3 (green) and SiO_2 (purple) at iso-dMo of 2.2 at.nm^{-2} of support for a Co/Mo ratio ratio close to 0.4. Relative uncertainties on stacking and the length is respectively ±15% and ±10%.

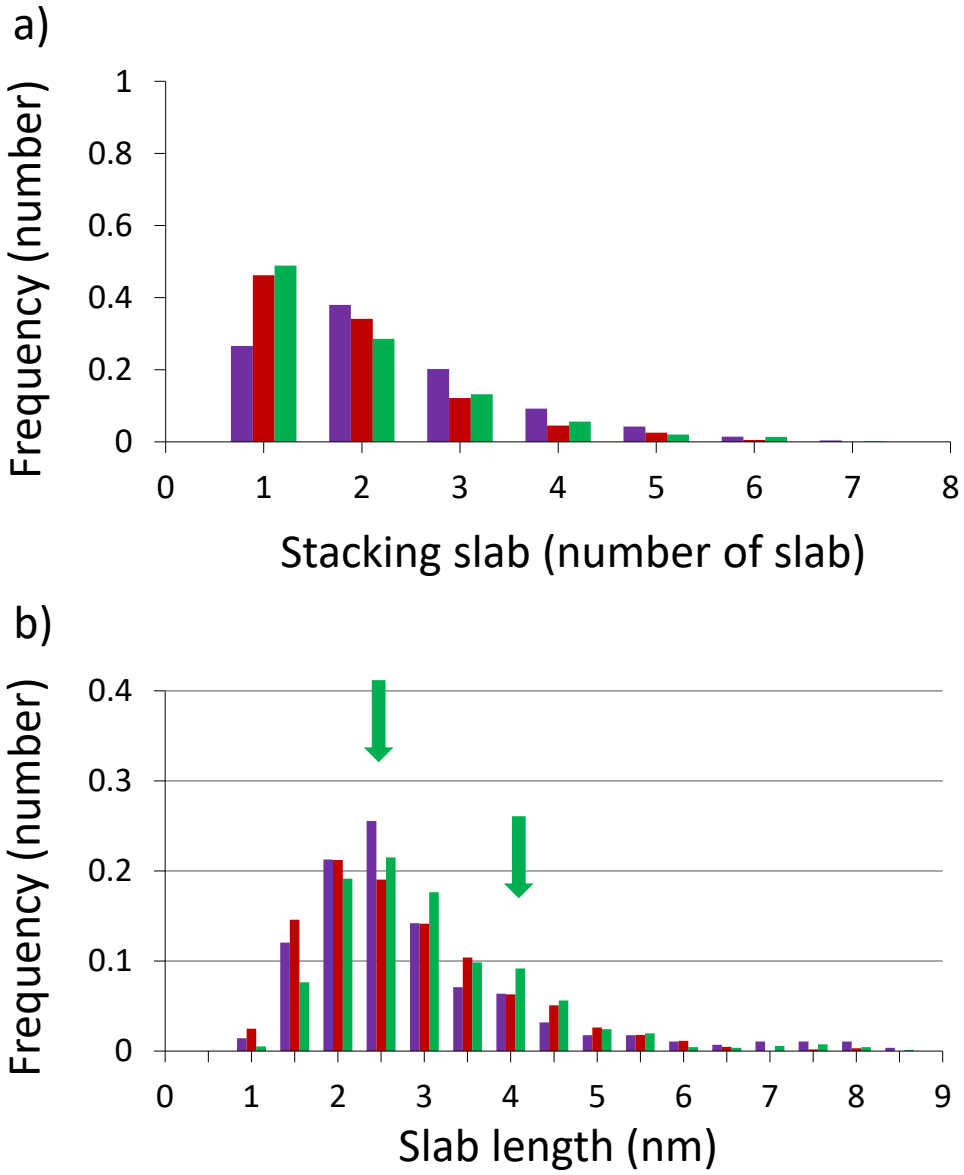

Figure 30. (a) Stacking and (b) length distributions of the slab as function of the support of CoMoS on γ-Al_2O_3 (red) , $\delta\theta$-Al_2O_3 (green) and SiO_2 (purple) at iso-dMo of 3.8 at.nm^{-2} of support for a Co/Mo ratio close to 0.4. Relative uncertainties on stacking and the length is respectively ±15% and ±10%.

Appendix 5. Methods for Core level Shift calculations

To measure the binding energy (*BE*) of core electrons using DFT calculations, two approximations can be made. In the "initial state approximation", it is assumed that the binding energy of the core electron is directly related to the energy level of its core orbital, $\varepsilon_c(n_c)$, following the Koopmans' theorem[66]. In the "final state approximation", one must calculate the energy difference between two distinct states:

$$BE = E(n_c - 1) - E(n_c)$$

$E(n_c)$ is energy of the unexcited groundstate, and $E(n_c\text{-}1)$ is the energy of the excited state where one electron is transferred from the core level of one particular atom (n_c) to the valence band. For such DFT calculation, we take advantage of the PAW formalism implemented in VASP because such an all electron method with frozen core approximation also allows the generation of the corresponding core excited ionic potential during the calculations. Following the so-called "(Z+1) approximation", the core hole (n_c-1) is modeled by adding one nuclear charge to the core atom and simultaneously one valence electron.[67,68] Hence, the screening by other valence electrons is included, whereas the screening by the core electrons is not taken into account. Actually, the difference given by equation (7) can be obtained using the Slater-Janak theorem[69]:

$$BE = E(n_c - 1) - E(n_c) \approx -\varepsilon_c(n_c - 1/2)$$

$\varepsilon(n_e - 1/2)$ is the Kohn-Sham eigenvalues of the given core level with an occupation decreased by half an electron. This approach corresponds to the final state approximation used in the current study. However, the absolute value of $\varepsilon(n_e - 1/2)$ cannot be directly compared to experimental values (according to different reference energies in experiment and theory). As a consequence, only binding energy differences, ΔBE, for core states of the given atom in two different environments (Mo in the center of the slabs and Mo at the edge), are relevant for a comparison with data obtained from XPS analysis. Hence, the Mo 3d "edge core level shift" (*ECLS*) is calculated as:

$$ECLS_{Mo} = BE(Mo_{edge}) - BE(Mo_{bulk}) = -\varepsilon_{Mo/edge}(n_c - 1/2) + \varepsilon_{Mo/bulk}(n_c - 1/2)$$

The slab used for such calculation contain 7 MoS_2 layer in direction perpendicular to the edges and 4 non-equivalent sites on the edges.

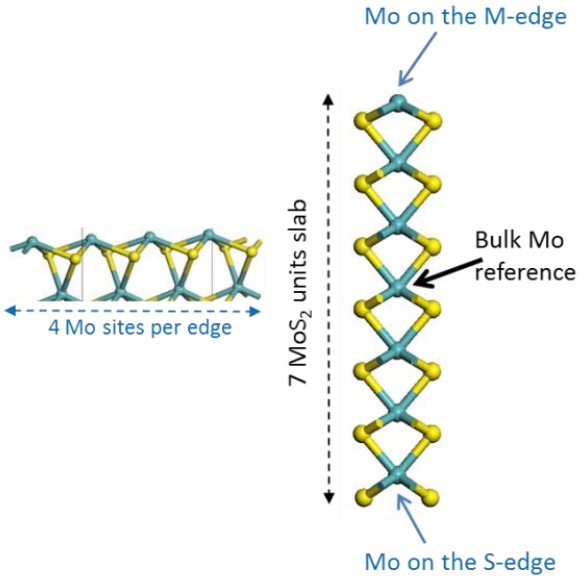

Figure 31. Slab molecular model used for the DFT calculations of core level shift. Color legend: Mo: green balls, S: yellow balls.

Appendix 6. Relative and effective distribution of the number of Co and Mo atoms on the slab for CoMoS on γ-Al_2O_3, $\delta\theta$-Al_2O_3 and SiO_2 at each dMo for a Co/Mo variable.

Table 14. Relative distribution of the number of Co and Mo atoms on the slab, on the basal plan and on the M and S-edge for CoMoS on γ-Al_2O_3, $\delta\theta$-Al_2O_3 and SiO_2 at variable dMo and Co/Mo molar ratio. Relative uncertainties to consider for the obtained values are at least ±20%.

				Slab atoms distribtuion								
dMo	**Support**	**Co/Mo**	**X_{Co}**	Slab atoms	Atoms at the edge	Mo_{basal}	Mo_{edge}	Co_{edge}	Mo_{Medge}	Mo_{Sedge}	Co_{Medge}	Co_{Sedge}
	γ-Al_2O_3		**-**	38	18	20	-	-	-	-	-	-
0.9	**$\delta\theta$-Al_2O_3**	**0.4**	**70**	84	29	56	9	20	9	0	6	14
	SiO_2		**-**	59	24	36	-	-	-	-	-	-
	γ-Al_2O_3	**0.4**	**36**	52	22	30	14	8	11	3	0	8
	$\delta\theta$-Al_2O_3	**0.1**	**16**	82	28	54	24	4	14	10	0	4
2.2	**$\delta\theta$-Al_2O_3**	**0.2**	**32**	78	28	51	19	9	14	5	9	9
	$\delta\theta$-Al_2O_3	**0.4**	**59**	80	28	52	12	16	12	0	2	14
	SiO_2	**0.4**	**28**	65	25	40	18	7	12	6	0	7
	γ-Al_2O_3		**64**	81	28	53	10	18	10	0	4	14
3.8	**$\delta\theta$-Al_2O_3**	**0.4**	**70**	105	32	72	10	22	10	0	6	16
	SiO_2		**18**	77	27	50	22	5	13	9	0	5
4.8	**γ-Al_2O_3**	**0.4**	**75**	83	28	54	7	21	7	0	7	14
	$\delta\theta$-Al_2O_3		**70**	101	32	69	5	27	5	0	11	16

Table 15. Effective distribution of the number of Co and Mo atoms on the slab, on the basal plan and on the M- and S-edge for CoMoS on γ-Al_2O_3, δθ-Al_2O_3 and SiO_2 at variable dMo and Co/Mo molar ratio. Relative uncertainties to consider for the obtained values are at least ±20%.

					Site contributions (mmol.g^{-1} of Mo)						
dMo	**Support**	**Co/Mo**	Slab atoms	Atoms $_{edge}$	Mo_{basal}	Mo_{edge}	**Co_{edge}**	Mo_{Medge}	Mo_{Sedge}	Co_{Medge}	Co_{Sedge}
	γ-Al_2O_3		10.5	5.1	5.4	3.6	**1.4**	2.5	1.1	0	1.4
0.9	**δθ-Al_2O_3**	**0.4**	8.2	2.8	5.4	0.8	**2.0**	0.8	0	0.6	1.4
	SiO_2		6.4	2.5	3.9	1.6	**0.9**	1.3	0.4	0	0.9
	γ-Al_2O_3	**0.4**	10.2	4.3	5.9	2.8	**1.5**	2.2	0.6	0	1.5
	δθ-Al_2O_3	**0.1**	8.3	2.9	5.4	2.4	**0.5**	1.4	1.0	0	0.5
2.2	**δθ-Al_2O_3**	**0.2**	8.5	3.0	5.5	2.0	**1.0**	1.5	0.5	0	1.0
	δθ-Al_2O_3	**0.4**	9.4	3.3	6.1	1.4	**1.9**	1.4	0	0.3	1.6
	SiO_2	**0.4**	8.8	4.1	4.7	2.1	**0.8**	1.4	0.6	0	0.8
	γ-Al_2O_3		13.6	4.7	8.9	1.2	**3.5**	1.2	0	1.1	2.3
3.8	**δθ-Al_2O_3**	**0.4**	10.2	3.2	7.1	1.0	**2.2**	1.0	0	0.6	1.6
	SiO_2		7.9	2.8	5.1	2.3	**0.5**	1.4	0.9	0	0.5
4.8	**γ-Al_2O_3**	**0.4**	13.6	4.7	8.9	1.2	**3.5**	1.2	0	1.1	2.3
	δθ-Al_2O_3		11.5	3.6	7.9	0.6	**3.0**	0.6	0	1.2	1.8

Appendix 7. Correlation of the activities at 220°C related to the initial rate of 23DMB2N reaction, $a_{23DMB2N}$ with the Co atoms located at the edge of the CoMoS slab.

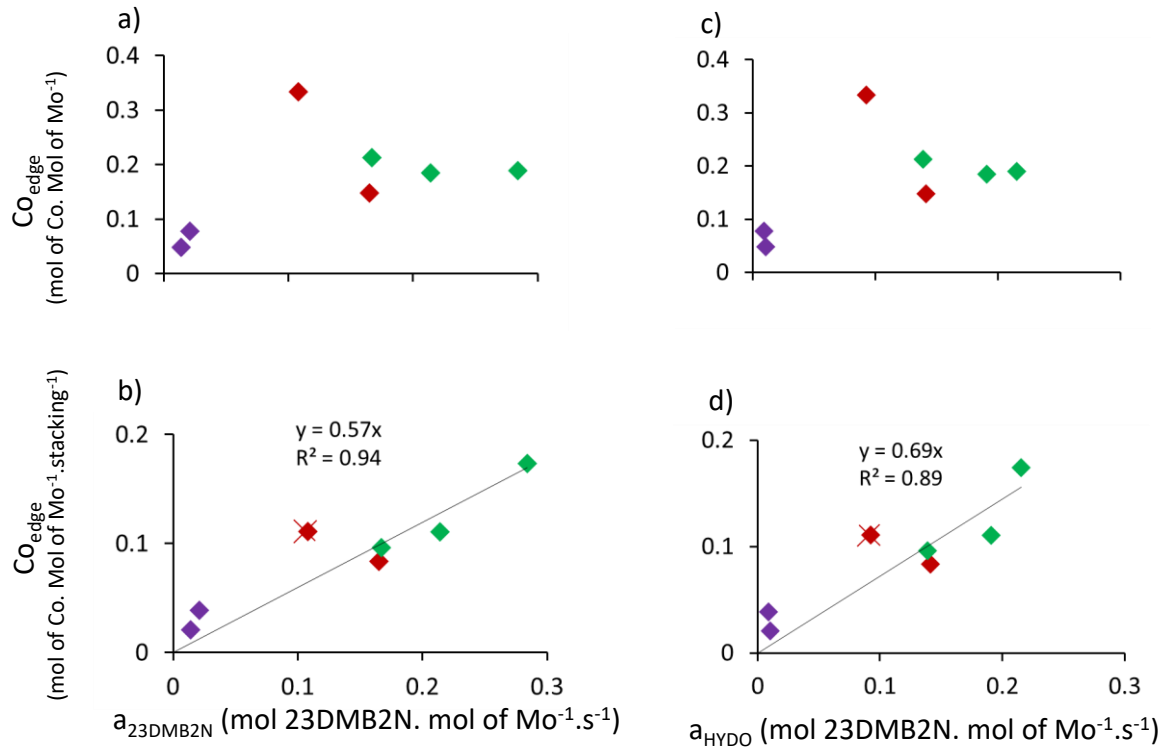

Figure 32. Correlation of the activities at 220°C related to the initial rate of 23DMB2N reaction, $a_{23DMB2N}$, and the initial rate of the HYDO yield, with respectively (a), (c) the Co edge (mol 23DMB2N.mol of $Mo^{-1}.s^{-1}$) and (b), (d) the Co edge normalized by the stacking (mol 23DMB2N.mol of $Mo^{-1}.s^{-1}$.stacking^{-1}) at the slab of the CoMoS on γ-Al_2O_3 (red), $\delta\theta$-Al_2O_3 (green) and SiO_2 (purple) previously present in the section 3.2.2.1. Experimental points with a red cross are not taking into account to obtain the linear regression analysis. Relative uncertainties on the activity and the atoms distribution are evaluated respectively to 20% and 25%.

Appendix 8. Correlation of the activities at 220°C related to the initial rate of 23DMB2N and 3MT reaction, $a_{23DMB2N}$ with the atoms located at the edge of the CoMoS slab.

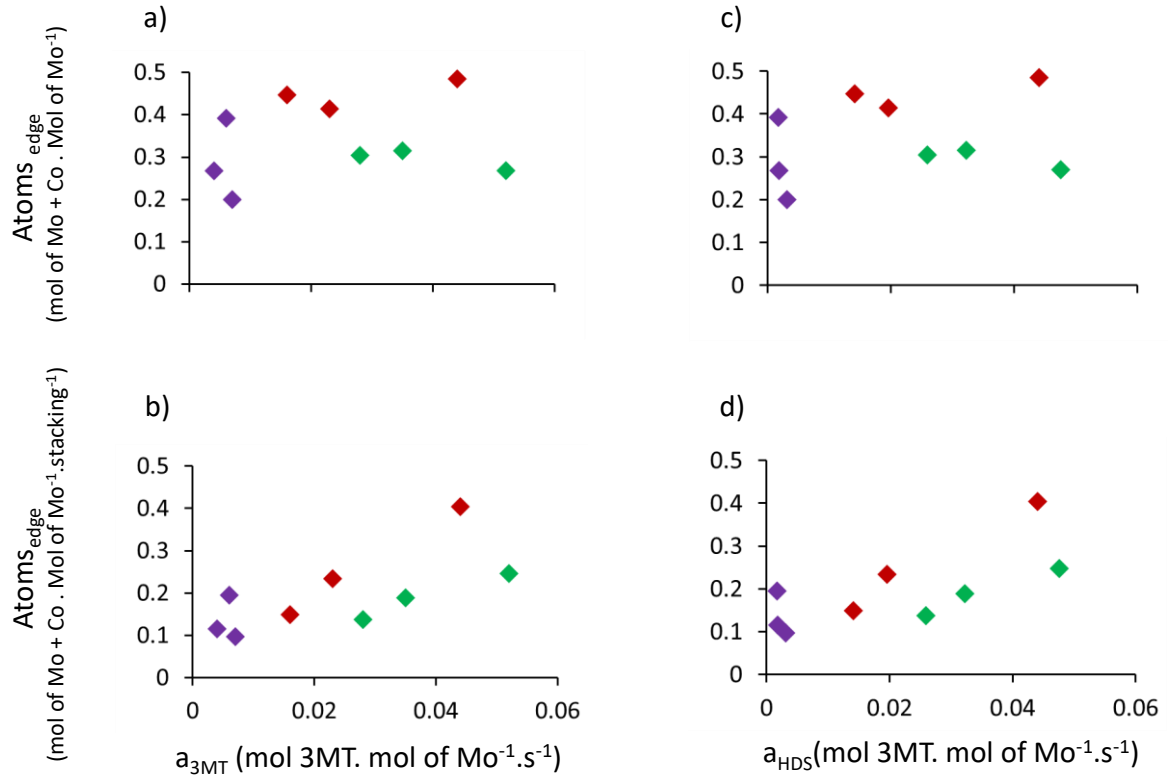

Figure 33. Correlation of the activities at 220°C related to the initial rate of 3MT reaction, a_{3MT} , and the initial rate of the HDS yield, with respectively (a), (c) the atoms at the edge (mol 3MT.mol of $Mo^{-1}.s^{-1}$) and (b), (d) the atoms at the edge normalized by the stacking (mol 3MT.mol of $Mo^{-1}.s^{-1}.stacking^{-1}$) at the slab of the CoMoS on γ-Al_2O_3 (red), $\delta\theta$-Al_2O_3 (green) and SiO_2 (purple) previously present in the section 3.2.2.1. Experimental points with a red cross are not taking into account to obtain the linear regression analysis. Relative uncertainties on the activity and the atoms distribution are evaluated respectively to 20% and 15%.

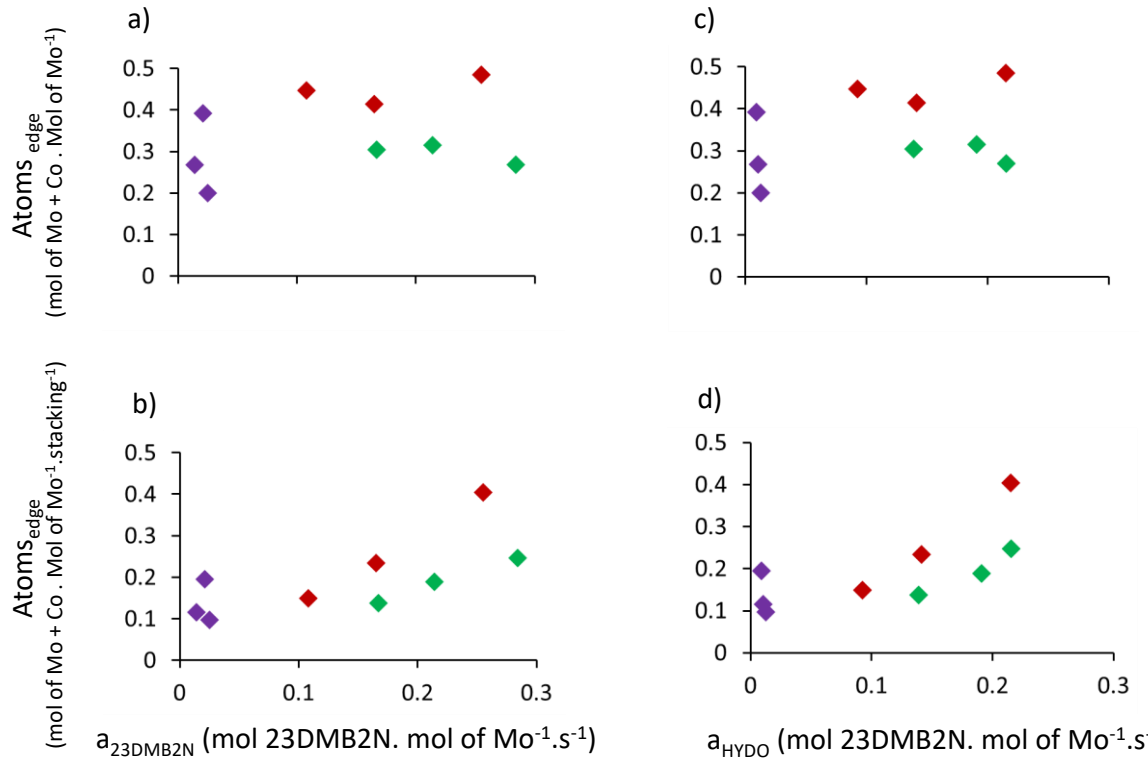

Figure 34.Correlation of the activities at 220°C related to the initial rate of 23DMB2N reaction, $a_{23DMB2N}$, and the initial rate of the HYDO yield, with respectively (a), (c) the atoms at the edge (mol 23DMB2N.mol of $Mo^{-1}.s^{-1}$) and (b), (d) the atoms at the edge normalized by the stacking (mol 23DMB2N.mol of $Mo^{-1}.s^{-1}$. $stacking^{-1}$) at the slab of the CoMoS on γ-Al_2O_3 (red), $\delta\theta$-Al_2O_3 (green) and SiO_2 (purple) previously present in the section 3.2.2.1. Experimental points with a red cross are not taking into account to obtain the linear regression analysis. Relative uncertainties on the activity and the atoms distribution are evaluated respectively to 20% and 15%.

Appendix 9. Correlation of the activities at 220°C related to the initial rate of 23DMB2N and 3MT reaction with the Mo atoms located at the edge of the CoMoS slab.

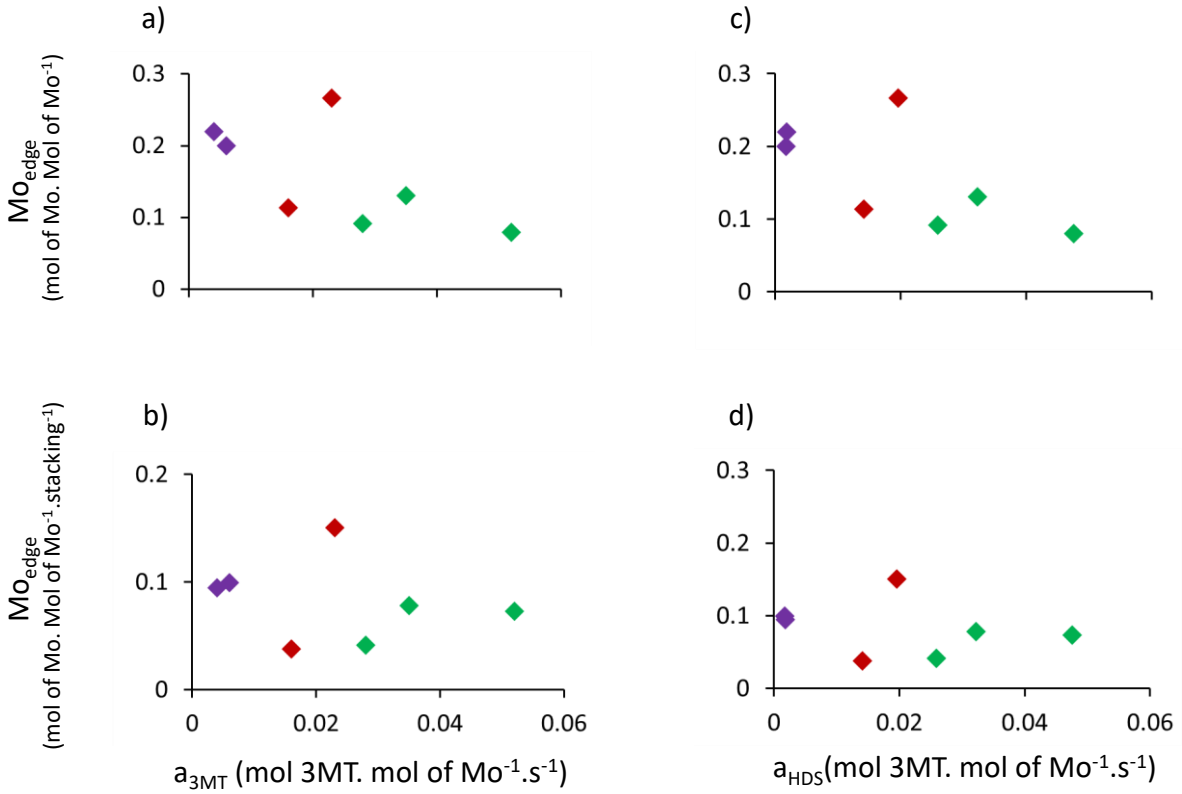

Figure 35. Correlation of the activities at 220°C related to the initial rate of 3MT reaction, a_{3MT} , and the initial rate of the HDS yield, with respectively (a), (c) the Mo atoms at the edge (mol 3MT.mol of $Mo^{-1}.s^{-1}$) and (b), (d) the Mo atoms at the M-edge normalized by the stacking (mol 3MT.mol of $Mo^{-1}.s^{-1}$.stacking^{-1}) at the slab of the CoMoS on γ-Al_2O_3 (red), $\delta\theta$-Al_2O_3 (green) and SiO_2 (purple) previously present in the section 3.2.2.1. Experimental points with a red cross are not taking into account to obtain the linear regression analysis. Relative uncertainties on the activity and the atoms distribution are evaluated respectively to 20% and 25%.

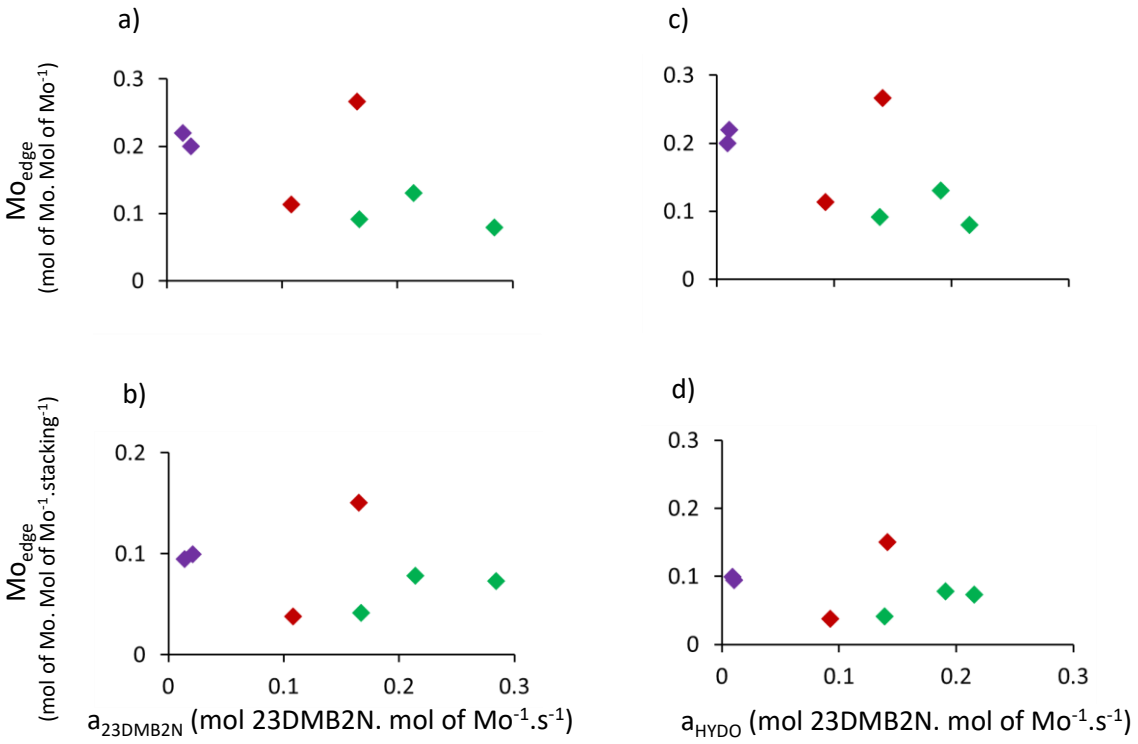

Figure 36. Correlation of the activities at 220°C related to the initial rate of 23DMB2N reaction, $a_{23DMB2N}$, and the initial rate of the HYDO yield, with respectively (a), (c) the Mo atoms at the edge (mol 23DMB2N.mol of $Mo^{-1}.s^{-1}$) and (b), (d) the Mo atoms at the M-edge normalized by the stacking (mol 23DMB2N.mol of $Mo^{-1}.s^{-1}$stacking^{-1}) at the slab of the CoMoS on γ-Al_2O_3 (red), $\delta\theta$-Al_2O_3 (green) and SiO_2 (purple) previously present in the section 3.2.2.1. Experimental points with a red cross are not taking into account to obtain the linear regression analysis. Relative uncertainties on the activity and the atoms distribution are evaluated respectively to 20% and 25%.

Appendix 10. Correlation of the activities at 220°C related to the initial rate of of 23DMB2N and 3MT reaction with the Mo atoms located at the M-edge of the CoMoS slab.

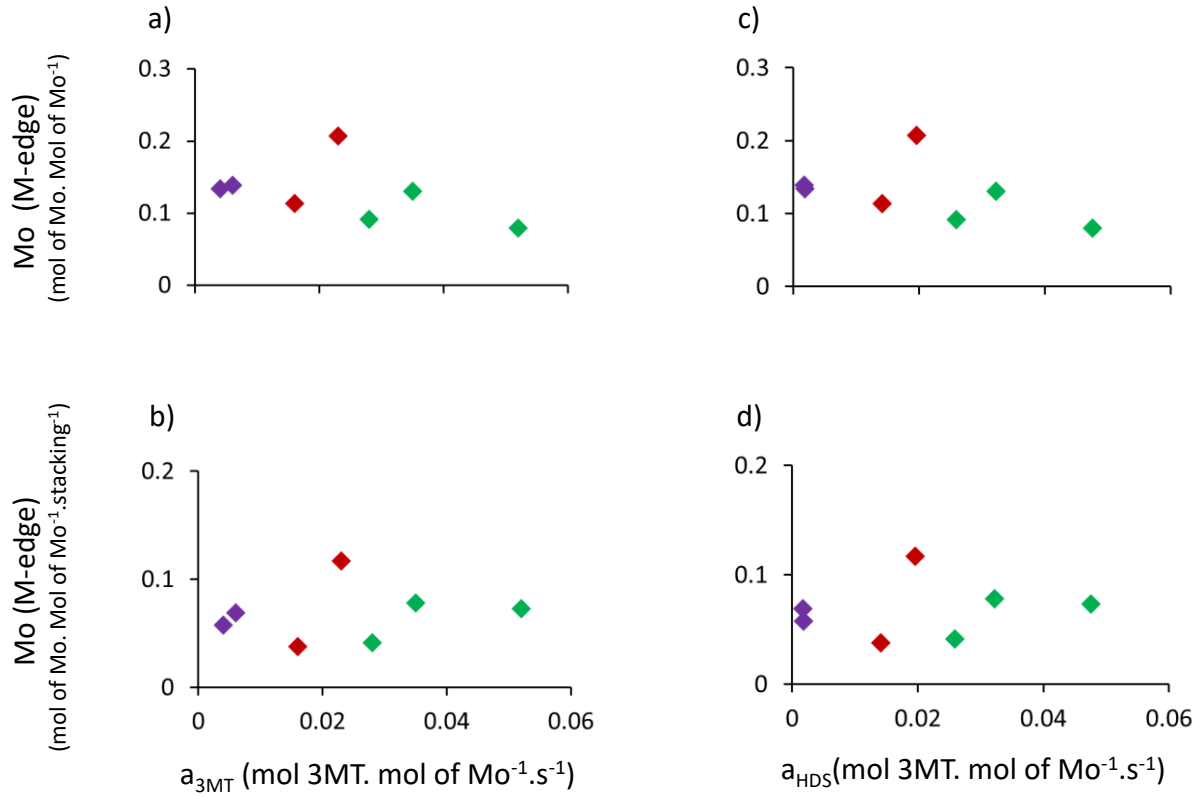

Figure 37. Correlation of the activities at 220°C related to the initial rate of 3MT reaction, a_{3MT} , and the initial rate of the HDS yield, with respectively (a), (c) the Mo atoms at the M-edge (mol 3MT.mol of $Mo^{-1}.s^{-1}$) and (b), (d)) the Mo atoms at the M-edge normalized by the stacking (mol 3MT.mol of $Mo^{-1}.s^{-1}.stacking^{-1}$) at the slab of the CoMoS on γ-Al_2O_3 (red), $\delta\theta$-Al_2O_3 (green) and SiO_2 (purple) previously present in the section 3.2.2.1. Experimental points with a red cross are not taking into account to obtain the linear regression analysis. Relative uncertainties on the activity and the atoms distribution are evaluated respectively to 20% and 25%.

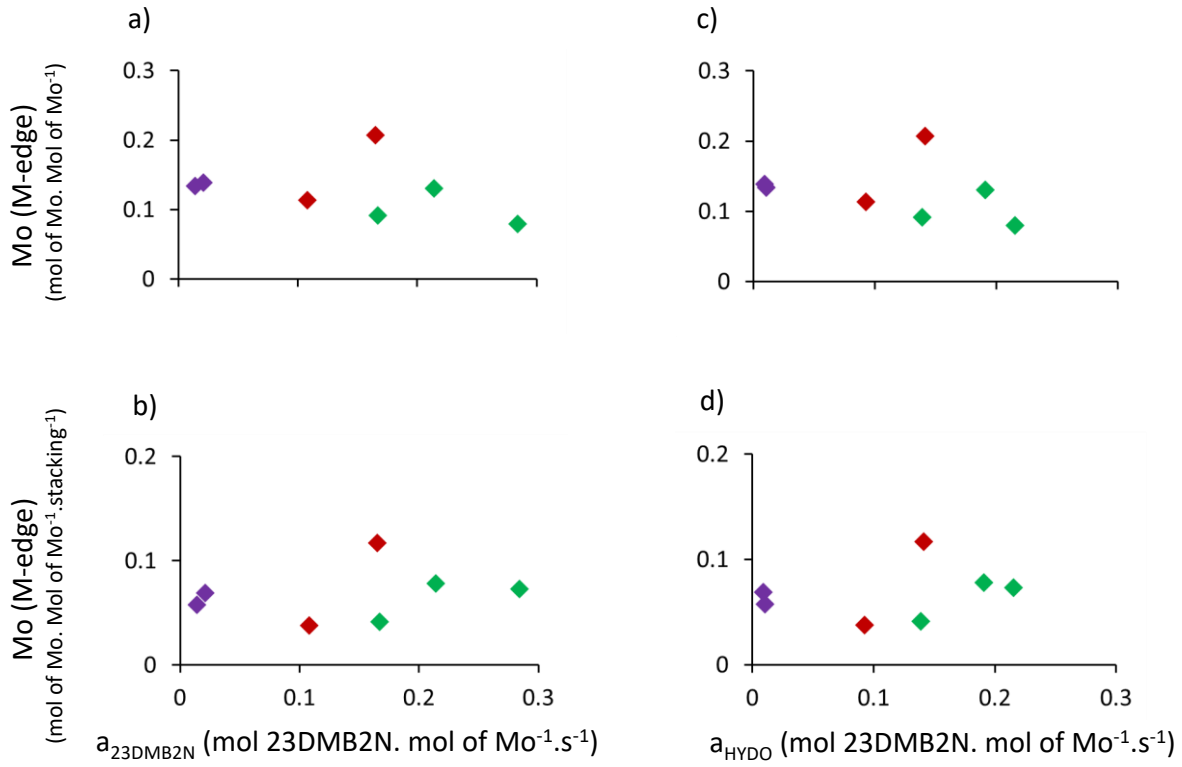

Figure 38. Correlation of the activities at 220°C related to the initial rate of 23DMB2N reaction, $a_{23DMB2N}$, and the initial rate of the HYDO yield, with respectively (a), (c) the Mo atoms at the M-edge (mol 23DMB2N.mol of $Mo^{-1}.s^{-1}$) and (b), (d) the Mo atoms at the M-edge normalized by the stacking (mol 23DMB2N.mol of $Mo^{-1}.s^{-1}.stacking^{-1}$) at the slab of the CoMoS on γ-Al_2O_3 (red), $\delta\theta$-Al_2O_3 (green) and SiO_2 (purple) previously present in the section 3.2.2.1. Experimental points with a red cross are not taking into account to obtain the linear regression analysis. Relative uncertainties on the activity and the atoms distribution are evaluated respectively to 20% and 25%.

Appendix 11. Correlation of the activities at 220°C related to the initial rate of 23DMB2N and 3MT reaction with the Mo atoms located at the S-edge of the CoMoS slab.

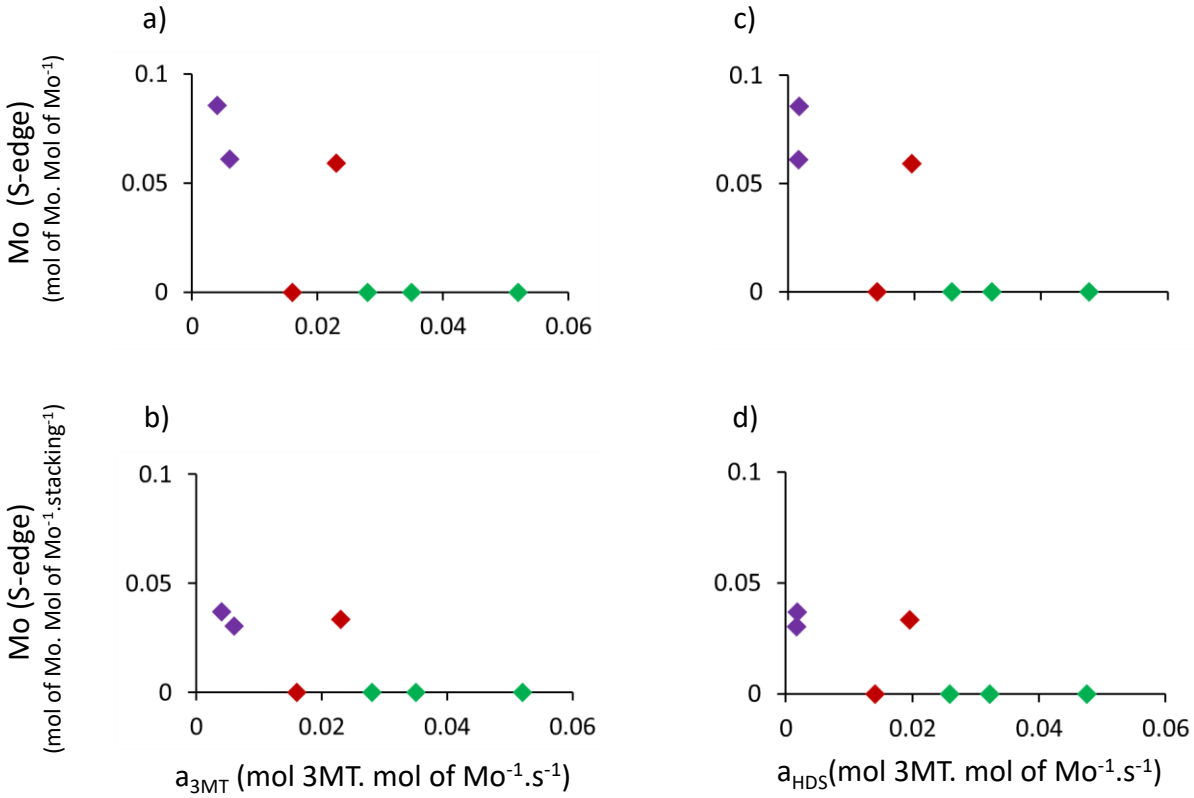

Figure 39. Correlation of the activities at 220°C related to the initial rate of 3MT reaction, a_{3MT} , and the initial rate of the HDS yield, with respectively (a), (c) the Mo atoms at the S-edge (mol 3MT.mol of $Mo^{-1}.s^{-1}$) and (b), (d)) the Mo atoms at the S-edge normalized by the stacking (mol 3MT.mol of $Mo^{-1}.s^{-1}.stacking^{-1}$) at the slab of the CoMoS on γ-Al_2O_3 (red), $\delta\theta$-Al_2O_3 (green) and SiO_2 (purple) previously present in the section 3.2.2.1. Experimental points with a red cross are not taking into account to obtain the linear regression analysis. Relative uncertainties on the activity and the atoms distribution are evaluated respectively to 20% and 25%.

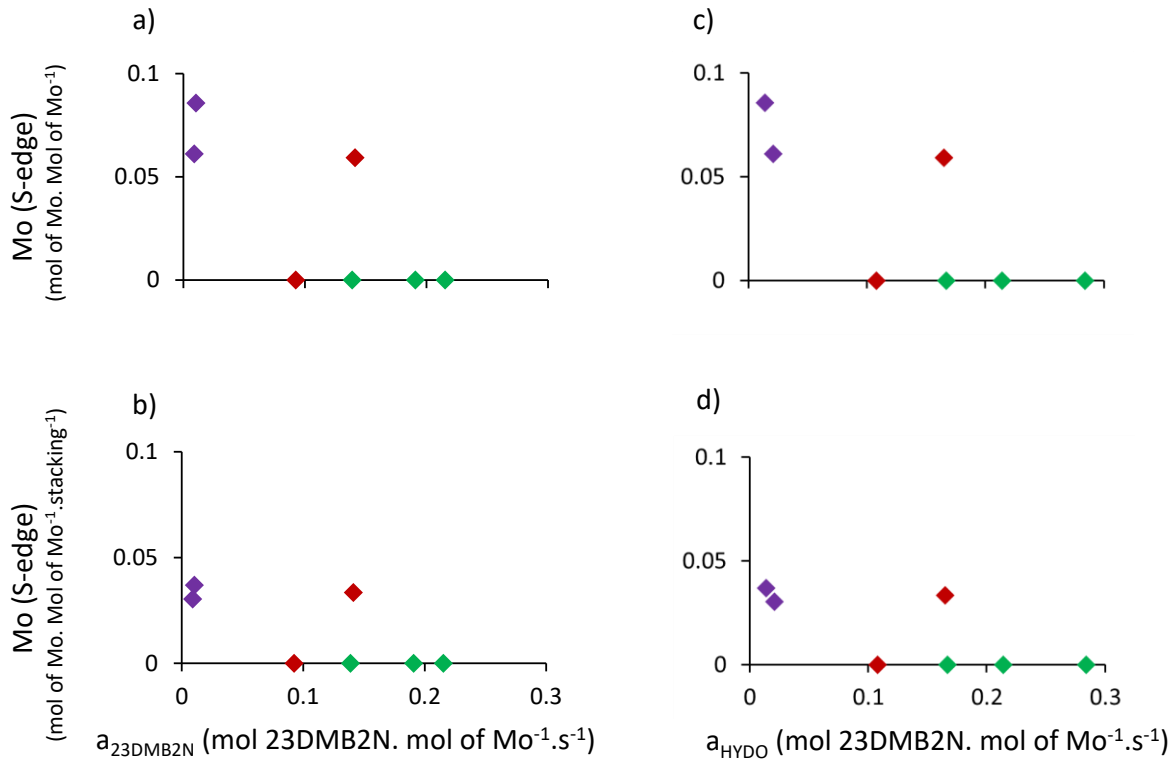

Figure 40. Correlation of the activities at 220°C related to the initial rate of 23DMB2N reaction, $a_{23DMB2N}$, and the initial rate of the HYDO yield, with respectively (a), (c) the Mo atoms at the S-edge (mol 23DMB2N.mol of $Mo^{-1}.s^{-1}$) and (b), (d) the Mo atoms at the S-edge normalized by the stacking (mol 23DMB2N.mol of $Mo^{-1}.s^{-1}.stacking^{-1}$) at the slab of the CoMoS on γ-Al_2O_3 (red), $\delta\theta$-Al_2O_3 (green) and SiO_2 (purple) previously present in the section 3.2.2.1. Experimental points with a red cross are not taking into account to obtain the linear regression analysis. Relative uncertainties on the activity and the atoms distribution are evaluated respectively to 20% and 25%.

Appendix 12. Correlation of the activities at 220°C related to the initial rate of 23DMB2N and 3MT reaction with the Co atoms located at the M-edge of the CoMoS slab.

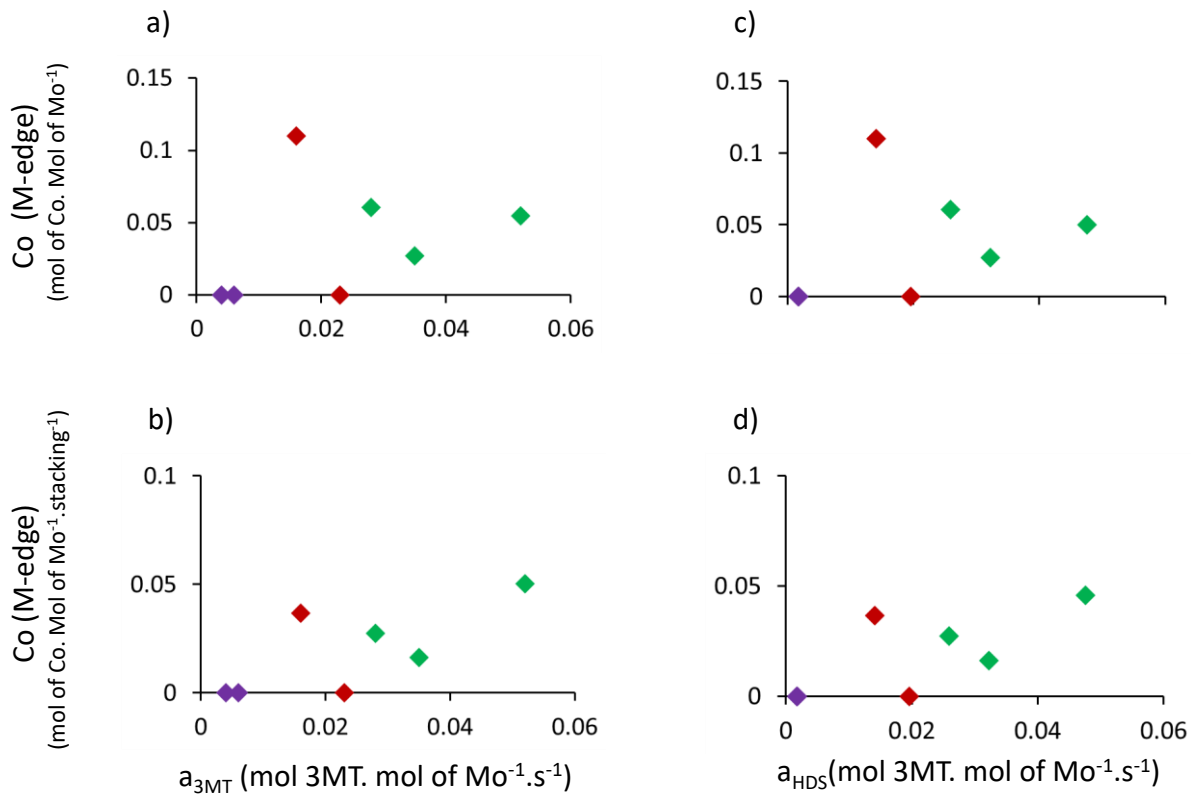

Figure 41.Correlation of the activities at 220°C related to the initial rate of 3MT reaction, a_{3MT} , and the initial rate of the HDS yield, with respectively (a), (c) the Co atoms at the M-edge (mol 3MT.mol of $Mo^{-1}.s^{-1}$) and (b), (d)) the Co atoms at the M-edge normalized by the stacking (mol 3MT.mol of $Mo^{-1}.s^{-1}$.stacking^{-1}) at the slab of the CoMoS on γ-Al_2O_3 (red), $\delta\theta$-Al_2O_3 (green) and SiO_2 (purple) previously present in the section 3.2.2.1. Experimental points with a red cross are not taking into account to obtain the linear regression analysis. Relative uncertainties on the activity and the atoms distribution are evaluated respectively to 20% and 25%.

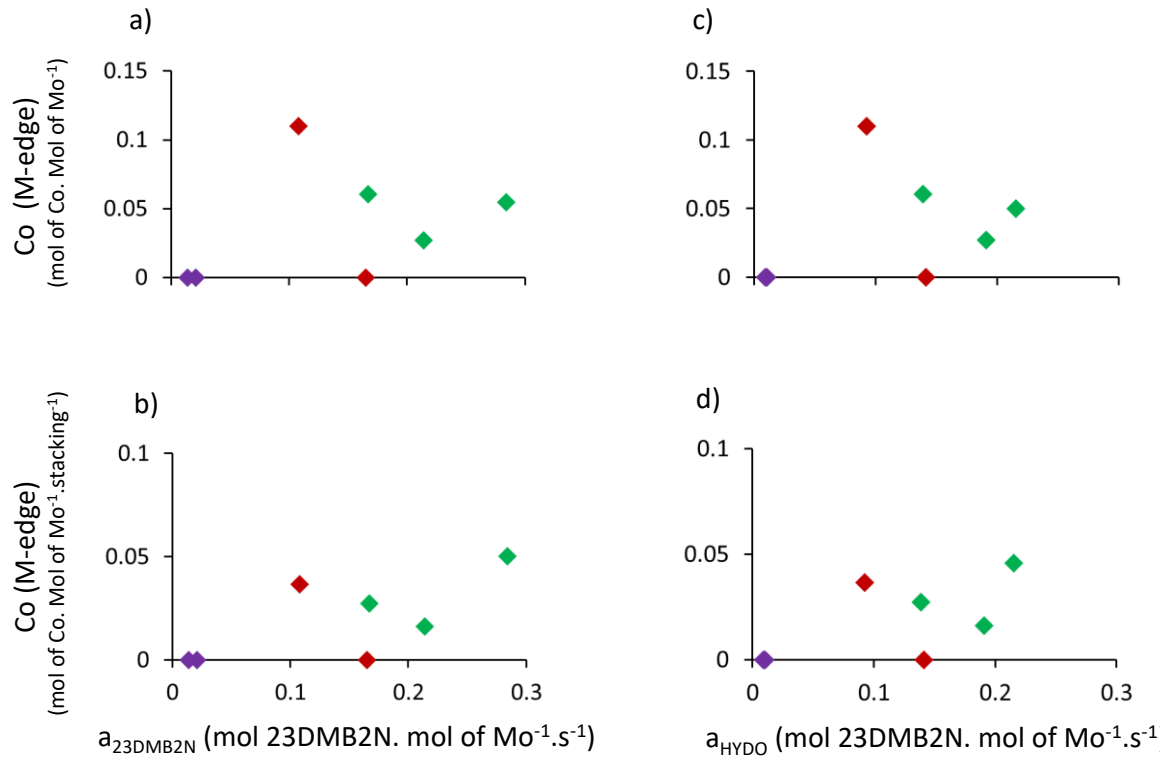

Figure 42. Correlation of the activities at 220°C related to the initial rate of 23DMB2N reaction, $a_{23DMB2N}$, and the initial rate of the HYDO yield, with respectively (a), (c) the Co atoms at the M-edge (mol 23DMB2N.mol of $Mo^{-1}.s^{-1}$) and (b), (d) the Co atoms at the M-edge normalized by the stacking (mol 23DMB2N.mol of $Mo^{-1}.s^{-1}.stacking^{-1}$) at the slab of the CoMoS on γ-Al_2O_3 (red), $\delta\theta$-Al_2O_3 (green) and SiO_2 (purple) previously present in the section 3.2.2.1. Experimental points with a red cross are not taking into account to obtain the linear regression analysis. Relative uncertainties on the activity and the atoms distribution are evaluated respectively to 20% and 25%.

Appendix 13. Correlation of the activities at 220°C related to the initial rate of 23DMB2N reaction, $a_{23DMB2N}$ with the Co atoms located at the S-edge of the CoMoS slab.

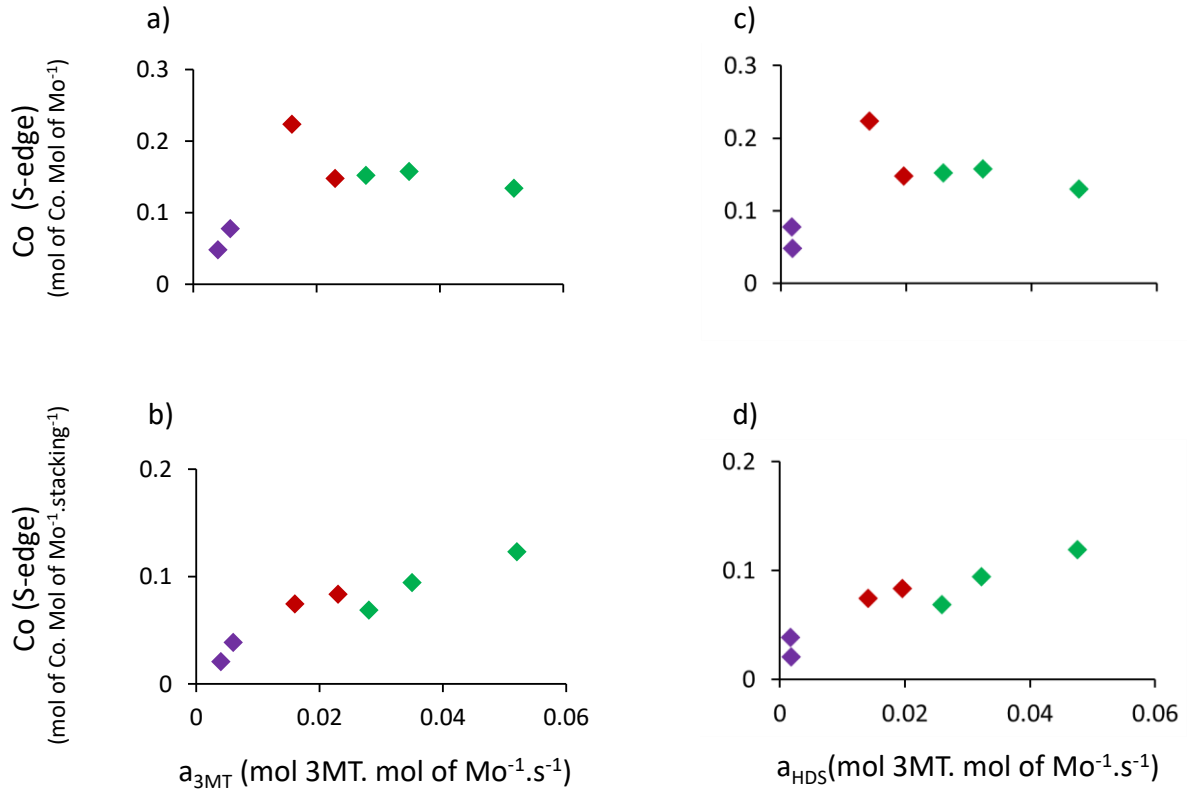

Figure 43. Correlation of the activities at 220°C related to the initial rate of 3MT reaction, a_{3MT} , and the initial rate of the HDS yield, with respectively (a), (c) the Co atoms at the S-edge (mol 3MT.mol of $Mo^{-1}.s^{-1}$) and (b), (d)) the Co atoms at the S-edge normalized by the stacking (mol 3MT.mol of $Mo^{-1}.s^{-1}.stacking^{-1}$) at the slab of the CoMoS on γ-Al_2O_3 (red), $\delta\theta$-Al_2O_3 (green) and SiO_2 (purple) previously present in the section 3.2.2.1. Experimental points with a red cross are not taking into account to obtain the linear regression analysis. Relative uncertainties on the activity and the atoms distribution are evaluated respectively to 20% and 25%.

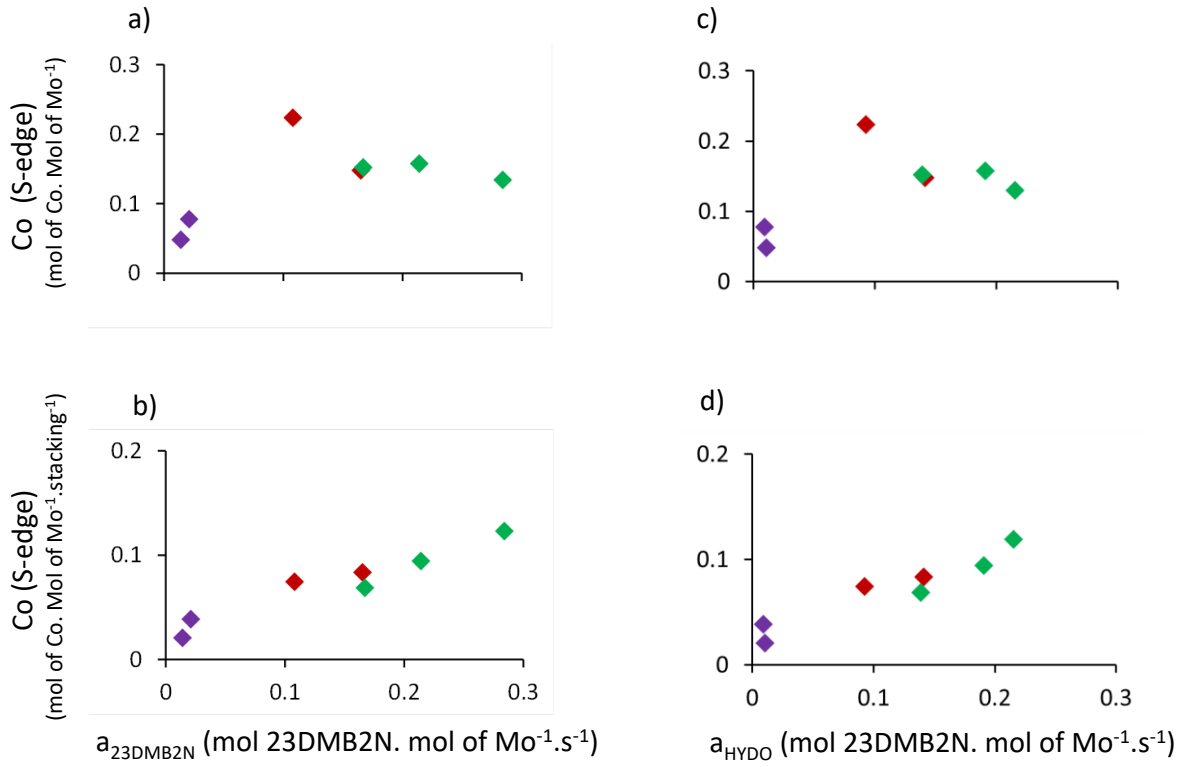

Figure 44. Correlation of the activities at 220°C related to the initial rate of 23DMB2N reaction, $a_{23DMB2N}$, and the initial rate of the HYDO yield, with respectively (a), (c) the Co atoms at the S-edge (mol 23DMB2N.mol of $Mo^{-1}.s^{-1}$) and (b), (d) the Co atoms at the S-edge normalized by the stacking (mol 23DMB2N.mol of $Mo^{-1}.s^{-1}.stacking^{-1}$) at the slab of the CoMoS on γ-Al_2O_3 (red), $\delta\theta$-Al_2O_3 (green) and SiO_2 (purple) previously present in the section 3.2.2.1. Experimental points with a red cross are not taking into account to obtain the linear regression analysis. Relative uncertainties on the activity and the atoms distribution are evaluated respectively to 20% and 25%.

6 References

[1] *US Environ. Prot. Agency "EPA Propos. Tier 3 Mot. Veh. Emiss. Fuel Stand. ,***2013***.*

[2] Official Journal of the European Union, **2009**, *L 140/88*, 88–113.

[3] *Int. Counc. Clean Transp. "China Announc. Breakthr. timeline Implement. ultra-low sulfur fuel Stand.,***2013***.*

[4] Bjerne S. Clausen, B. Lengelerb, R. Candia, J. Ah-Nielsen, H. Topsøe, *Bull. des Sociétés Chim. Belges* **1981**, *90*, 1249–1259.

[5] H. Toulhoat, P. Raybaud, *Catalysis by Transition Metal Sulphides*, Editions TECHNIP, Paris, **2013**.

[6] F. E. Massoth, *Jounral Catal.* **1974**, *36*, 164–184.

[7] F. E. Massoth, *Adv. Catal.* **1979**, *27*, 265–310.

[8] R. Prins, V. H. J. De Beer, G. A. Somorjai, *Catal. Rev.* **1989**, *31*, 1–41.

[9] H. Topsøe, B. S. Clausen, *Appl. Catal.* **1986**, *25*, 273–293.

[10] N.-Y. Topsøe, H. Topsøe, *Jounral Catal.* **1983**, *84*, 386–401.

[11] M. Daage, R. R. Chianelli, *J. Catal.* **1994**, *149*, 414–427.

[12] A. Daudin, S. Brunet, G. Perot, P. Raybaud, C. Bouchy, *J. Catal.* **2007**, *248*, 111–119.

[13] E. Krebs, B. Silvi, a. Daudin, P. Raybaud, *J. Catal.* **2008**, *260*, 276–287.

[14] B. Baubet, M. Girleanu, A. S. Gay, A. L. Taleb, M. Moreaud, F. Wahl, V. Delattre, E. Devers, A. Hugon, O. Ersen, et al., *ACS Catal.* **2016**, *6*, 1081–1092.

[15] Y. Fan, G. Shi, H. Liu, X. Bao, *Appl. Catal. B Environ.* **2009**, *91*, 73–82.

[16] M. Li, H. Li, F. Jiang, Y. Chu, H. Nie, *Catal. Today* **2010**, *149*, 35–39.

[17] Qiherima, L. Huifeng, Y. Hui, Z. Yunhong, X. Guangtong, *Chinese J. Catal.* **2011**, *32*, 240–249.

[18] T. K. T. Ninh, D. Laurenti, E. Leclerc, M. Vrinat, *Appl. Catal. A, Gen.* **2014**, *487*, 210–218.

[19] C. Bara, L. Plais, K. Larmier, E. Devers, M. Digne, A. Lamic-humblot, G. D. Pirngruber, X. Carrier, *J. Am. Chem. Soc.* **2015**, *137*, 15915–15928.

[20] E. Krebs, B. Silvi, P. Raybaud, *Catal. Today* **2008**, *130*, 160–169.

[21] S. J. Wilson, *J. Solid State Chem.* **1979**, *30*, 247–255.

[22] X. Krokidis, P. Raybaud, A. Gobichon, B. Rebours, P. Euzen, *J. Phys. Chem. B* **2001**, *105*, 5121–5130.

[23] X. Krokidis, P. Euzen, P. Raybaud, H. Toulhoat, J. L. L. Loarer, J. P. Jolivet, C. Froidefond, *Handbook of Porous Materials*, Wiley-VCH Verlag GmbH, Weinheim, Germany, **2002**.

[24] G. Busca, *Structural , Surface , and Catalytic Properties of Aluminas*, **2014**.

[25] M. Digne, P. Sautet, P. Raybaud, P. Euzen, H. Toulhoat, *J. Catal.* **2004**, *226*, 54–68.

[26] D. Laurenti, B. Phung-Ngoc, C. Roukoss, E. Devers, K. Marchand, L. Massin, L. Lemaitre, C. Legens, A. A. Quoineaud, M. Vrinat, *J. Catal.* **2013**, *297*, 165–175.

[27] A. D. Gandubert, C. Legens, D. Guillaume, S. Rebours, E. Payen, **2007**, *62*, 79–89.

[28] E. Krebs, B. Silvi, P. Raybaud, *Catal. Today* **2008**, *130*, 160–169.

[29] S. Kasztelan, H. Toulhoat, J. Grimblot, J. P. Bonnelle, D. Lille, *Appl. Catal.* **1984**, *13*, 127–159.

[30] J. Hietala, A. Root, P. Knuuttila, *J. Catal.* **1994**, *150*, 46–55.

[31] M. Lagauche, K. Larmier, E. Jolimaitre, K. Barthelet, C. Chizallet, L. Favergeon, M. Pijolat, *J. Phys. Chem. C* **2017**, *121*, 16770–16782.

[32] L. Marchese, S. Bordiga, G. M. Salvatore Coluccia, A. Zecchina, *J. Chem. Soc., Faraday Trans.* **1993**, *89*, 3483–3489.

[33] J. V. Lauritsen, S. Helveg, E. Lægsgaard, I. Stensgaard, B. S. Clausen, H. Topsøe, F. Besenbacher, *J. Catal.* **2001**, *197*, 1–5.

[34] H. Schweiger, P. Raybaud, G. Kresse, H. Toulhoat, *J. Catal.* **2002**, *207*, 76–87.

[35] H. Schweiger, P. Raybaud, *Jounral Catal.* **2002**, *38*, 33–38.

[36] D. Costa, C. Arrouvel, M. Breysse, H. Toulhoat, P. Raybaud, **2007**, *246*, 325–343.

[37] C. Arrouvel, M. Breysse, H. Toulhoat, P. Raybaud, *J. Catal.* **2005**, *232*, 161–178.

[38] M. Digne, P. Sautet, P. Raybaud, P. Euzen, H. Toulhoat, *J. Catal.* **2002**, *211*, 1–5.

[39] C. Morterra, G. Magnacca, *Catal. Today* **1996**, *27*, 497–532.

[40] P. Nortier, P. Fourre, A. B. M. Saad, O. Saur, J. C. Lavalley, *Appl. Catal.* **1990**, *61*, 141–160.

[41] J.-P. Beaufils, Y. Barbaux, *J. Chim. Phys.* **1981**, *78*, 347–352.

[42] P. Sarrazin, S. Kasztelan, E. Payen, J. P. Bonnelle, J. Grimblot, *J. Phys. Chem.* **1993**, *97*, 5954–5961.

[43] P. Sarrazin, S. Kasztelan, N. Zanier-Szydlowski, J. P. Bonnelle, J. Grimblot, *J. Phys. Chem.* **1993**, *97*, 5947–5953.

[44] A. Tougerti, C. Méthivier, S. Cristol, F. Tielens, M. Che, X. Carrier, *Phys. Chem. Chem. Phys.* **2011**, *13*, 6531−6543.

[45] Z. Łodziana, N.-Y. Topsøe, J. K. Nørskov, *Nat. Mater.* **2004**, *3*, 289–93.

[46] G. Busca, *Catal. Today* **2014**, *226*, 2–13.

[47] R. Koerin, Influence du mode de synthèse de la boehmite sur l'état de surface de l'alumine-γ mise En forme ; application au reformage catalytique., PhD thesis IFPEN - Université de Caen Basse-Normandie, **2011-2014**

[48] G. Crépeau, V. Montouillout, A. Vimont, L. Mariey, T. Cseri, F. Maugé, *J. Phys. Chem. B* **2006**, *110*, 15172–15185.

[49] F. Maugé, J. Lamotte, N. S. Nesterenko, O. Manoilova, A. A. Tsyganenko, *Catal. Today* **2001**, *70*, 271.

[50] A. Travert, C. Dujardin, F. Maugé, S. Cristol, J. F. Paul, E. Payen, D. Bougeard, *Catal. today* **2001**, *70*, 255–269.

[51] A. Bruix, H. G. Füchtbauer, A. K. Tuxen, A. S. Walton, M. Andersen, S. Porsgaard, F. Besenbacher, B. Hammer, J. V Lauritsen, *ACS Nano* **2015**, *9*, 9322–9330.

[52] C. H. Hu, C. Chizallet, C. Mager-Maury, M. Corral-Valero, P. Sautet, H. Toulhoat, P. Raybaud, *J. Catal.* **2010**, *274*, 99–110.

[53] C. Mager-Maury, C. Chizallet, P. Sautet, P. Raybaud, *ACS Catal.* **2012**, *2*, 1346–1357.

[54] W. Eberhardt, P. Fayet, D. Cox, Z. Fu, A. Kaldor, R. Sherwood, D. Sondericker, *Phys Rev Lett.* **1990**, *64*, 780–783.

[55] S. Mattila, J. A. Leiro, M. Heinonen, T. Laiho, *Surf. Sci.* **2006**, *600*, 5168–5175.

[56] E. Krebs, Modélisation Moléculaire Ab Initio Des Effets de Morphologie En Catalyse Par Les Sulfures, **2007**.

[57] S. Lizzit, A. Baraldi, A. Groso, K. Reuter, M. V Ganduglia-Pirovano, C. Stampfl, M. Scheffler, M. Stichler, C. Keller, W. Wurth, et al., *Phys. Rev. B* **2001**, *63*, 205419.

[58] P. Raybaud, J. Hafner, G. Kresse, S. Kasztelan, H. Toulhoat, *J. Catal.* **2000**, *189*, 129–146.

[59] J. V. Lauritsen, M. V. Bollinger, E. Lægsgaard, K. W. Jacobsen, J. K. Nørskov, B. S. Clausen, H. Topsøe, F. Besenbacher, *J. Catal.* **2004**, *221*, 510–522.

[60] S. Harris, R. R. Chianelli, **1984**, *412*, 400–412.

[61] A. D. Ganduberta, E. Krebs, C. Legens, D. Costa, D. Guillaume, P. Raybaud, *Catal. Today* **2008**, *130*, 149–159.

[62] K. Larmier, C. Chizallet, P. Raybaud, *Angew. Chem. Int. Ed. Engl.* **2015**, *127*, 6928–6931.

[63] E. Krebs, a. Daudin, P. Raybaud, *Oil Gas Sci. Technol. - Rev. l'IFP* **2009**, *64*, 707–718.

[64] J. Lauritsen, J. Kibsgaard, G. Olesen, P. Moses, B. Hinnemann, S. Helveg, J. Norskov, B. Clausen, H. Topsøe, E. Lagsgaard, *J. Catal.* **2007**, *249*, 220–233.

[65] A. Gandubert, Caractérisaion et quantification de la phase sulfure des catalyseurs d'hydrotraitement: influence devla nature des précruseurs oxydes et des conditions de sulfuration, **2006**.

[66] T. Koopman, *Phys. 1* **1933**, *104*, 24.

[67] L. Köhler, G. Kresse, *Phys. Rev. B* **2004**, *70*, 165405.

[68] B. Johansson, N. Mårtensson, *Phys. Rev. B* **1980**, *21*, 4427–4457.

[69] J. F. Janak, *Phys. Rev. B* **1978**, *18*, 7165–7168.

- Chapter V -
Surface sites speciation of supported CoMoS phases probed by NO molecule: a combined IR and DFT study

Table of contents

1 Introduction 256

2 Experimental and theoretical methods 258

2.1 Catalysts preparation 258

2.2 FTIR experiment 259

2.3 Chemometric method 260

2.4 DFT calculations 260

2.4.1 Total energy 260

2.4.2 Frequency calculations 262

3 Results and discussion 263

3.1 δθ-Al_2O_3 supported CoMoS catalysts 263

3.2 DFT calculation of NO adsorption on CoMoS edges 267

3.3 Comparison of Al_2O_3 and SiO_2 supported catalysts 276

3.4 Chemometric analysis 279

4 NO FTIR – structure – catalytic activity relationships 283

4.1 Total area of NO sorbed on HDS catalyst vs 2D morphology model of the CoMoS slab 283

4.2 Total area of NO sorbed on HDS catalyst vs catalytic activity of the HDS catalysts 284

5 Conclusions 286

6 References 288

- Chapter V -
Surface sites speciation of supported CoMoS phases probed by NO molecule: a combined IR and DFT study

1 Introduction

Many worldwide environmental regulations aimed at decreasing toxic compound contents, especially sulfur-based ones, in the gasoline formulation.[1–3] Hydrodesulfurization (HDS) is a key industrial process to reach these targeted specifications of clean fuels. Focusing on the gasoline produced from the fluid catalytic cracking (FCC) unit, HDS is specifically used to remove undesirable sulfur compounds while maintaining the combustion quality (octane number) owed to olefins. Industrial catalysts involved in the HDS process are based on an active transition metal sulfides (TMS) phase, usually MoS_2 phase supported on alumina, where the MoS_2 nano-slabs are decorated at the edges by cobalt atoms to form the mixed CoMoS phase.[4–10] Research has to address a threefold challenge which is to selectively desulfurize sulfur compounds while the olefins hydrogenation (HYDO) must be avoided in order to keep a high octane number of the gasoline product. Thus, the design of more efficient selective HDS catalysts has become a major concern for research in order to understand the catalytic behavior of the CoMoS active phase and also the important direct or indirect roles played by the support.

Regarding the active phase, several studies based on spectroscopic techniques (UV-Vis, Raman, XPS, EXAFS) were conducted to understand the surface features of the CoMoS phase with the aim of designing new selective HDS catalysts. In order to evidence surface sites of hydrotreatment catalysts, probe molecules could be used. In that case, probe molecule interactions are generally followed by Fourier transform infrared spectroscopy (FTIR) because of its high surface sensitivity. For instance, CO is widely used to describe the site nature of the sulfided phase. Indeed, for the unpromoted MoS_2, CO adsorption leads to different vibrational signals, which along with DFT calculations, allow to differentiate Mo atoms at the edge of the slab according to their coordination state.[11] However,

interpretation of the vibrational bands related to the CO adsorbed on the M- and S-edges of the CoMoS phase are not yet clearly attributed and are still under debate.[12] Moreover, it is well admitted that CO molecule is only probing the coordinatively unsaturated sites (CUS) over the sulfided phase and therefore sites covered by sulfur atoms are not considered by this CO-FTIR method.[13–15] Thus, the change of sulfur coverage of the Mo and Co atoms, related to the partial pressure of H_2S and H_2 and post treatment done prior to analysis, is directly impacting the relative distribution of the CO vibrational bands observed.[11]

NO probe has also been used to shed light into the surface state of the CoMoS active phase catalyst and surface modifications (before/after) HDS reaction. Similarly to CO, NO-FTIR technique could provide information on the nature and quantity of active sites by sorbing on MoS_2 edges and not on the basal planes. [16–20] But in addition, it has been shown that NO is able to probe all the active sites of the CoMoS without being affected by the sulfur coverage. It has been even claimed that NO molecules sorption on the sulfided phase could lead to a total removal of the S atoms at 298K.[21,22]

Interpretations of the NO-contributions have been first done based on experimental results obtained for sulfided Co or Mo metals supported on η-Al_2O_3.[18] Three contributions have been observed around 1850, 1790 and 1690 cm^{-1} attributed to NO adsorbed respectively on i) the Co-promoted edge, ii) the Co-promoted and un-promoted edges and iii) the un-promoted edge of the MoS_2 slabs.

More recently, Tøpsøe et al. [20] performed experimental studies and DFT calculations in the goal to link more precisely the edge nature of the promoted and un-promoted edges of the MoS_2 slab with the vibration bond frequencies experimentally observed of the NO adsorbed on the MoS_2 and CoMoS phase. The three vibrational contributions of NO bond are related to the NO adsorbed on the promoted MoS_2. They assumed that the contribution at 1850 cm^{-1} is attributed to NO sorbed as di- or mononitrosyl complexes on the promoted S-edge, the contribution at 1790 cm^{-1} is attributed to NO sorbed as dinonitrosyl complex on the S-edge (promoted and un-promoted) and the contribution at 1700 cm^{-1} is attributed to NO sorbed as mononitrosyl complex on un-promoted M-edge.[20,23] In these studies, promotion by Co of the M-edges is generally not considered on the base of STM observations of CoMoS sulfided phase on a gold support, which is far from an industrial catalyst.

This contribution constitutes an additional building block to previous studies related to the FTIR/NO, in order to investigate the edge nature of the CoMoS slabs (M- or S-edge decorated by the Co atoms or not). CoMoS/$\delta\theta$-Al_2O_3 catalyst as well as MoS_2/$\delta\theta$-Al_2O_3 and Co_9S_8/$\delta\theta$-Al_2O_3 reference materials were prepared by conventional wetness impregnation and sulfidation. Second derivative and chemiometric treatments on IR spectra series (MCR-ALS method) combined with DFT calculations were used to provide a new insight on the edges of the CoMoS slabs as a function of NO coverage. Moreover, a comparison between CoMoS phase supported on /γ-Al_2O_3 or /SiO_2 or /$\delta\theta$-Al_2O_3 has been done in order to evaluate the support effect on the edge features of the CoMoS phase (at equivalent Mo loading and Co/Mo ratio).

2 Experimental and theoretical methods

2.1 Catalysts preparation

The various transition metal sulfides catalysts were prepared on three different supports: γ-Al_2O_3, $\delta\theta$-Al_2O_3 and SiO_2. The alumina supports were used as extrudates (around 2 – 4 mm with diameter of 1.6 mm) and the silica support as porous pellets (diameter around 0.315 – 1 mm). $\delta\theta$-Al_2O_3 is obtained by high temperature hydrothermal treatment from γ-Al_2O_3 sample. Support characteristics are reported in Table 1.

Table 1. Physical properties of the γ-Al_2O_3, $\delta\theta$-Al_2O_3 and SiO_2.

Supports	γ-Al_2O_3	$\delta\theta$-Al_2O_3	SiO_2
S_{BET} ($m^2.g^{-1}$)	285	81	232
$V_{mesopores}$ ($ml.g^{-1}$)	0.65	0.76	0.78
$V_{macropores}$ ($ml.g^{-1}$)	0.01	-	0.21
Pore diameter (nm)	7.0 – 11.0	36	15
Al_2O_3 platelet (nm)*	50 – 100	200 – 250	-

*determined by scanning electron microscopy

HDS catalysts were prepared by incipient wetness impregnation. Impregnation solutions were prepared from MoO_3 and $Co(OH)_2$ precursors dissolved in aqueous solution in presence of H_3PO_4. Impregnation was performed on various supports followed by an ageing step for 12 h to allow metal diffusion throughout the extrudate or pellets. Then, solids were dried in an oven at 393K for 24h and calcined in air at 723K for 2h15. Finally, oxide catalysts are presulfided ex situ by heating at $5K.min^{-1}$ from 298 to 623K at atmospheric pressure in a flow

of 15vol.%H_2S in H_2 (1.5 $L.h^{-1}g^{-1}$ of catalyst). Sulfidation was achieved at 623K for 2h15. The ex situ sulfided catalysts were then isolated under vacuum at 473K in a sealed glass flask.

On each support, molybdenum loadings were selected to obtain fixed molybdenum surface densities (labeled dMo in what follows) of 2.2 atoms by nm² of support. In order to compare catalysts at iso-dMo and iso-support, Co/Mo and P/Mo molar ratios are also kept constant respectively 0.4 and 0.27 (Table 2). $MoS_2/\delta\theta$-Al_2O_3 and $Co_9S_8/\delta\theta$-Al_2O_3 reference materials are also prepared on $\delta\theta$-Al_2O_3 (according to the same preparation procedure mentioned above for CoMoS supported catalysts). The XRF elemental analysis of Co, Mo and P on different supports (Table 2), ensures the consistency with the targeted elemental contents.

Table 2. XRF elemental analysis on the calcined oxide CoMo, Co and Mo precursor of respectively the CoMoS, Co_9S_8 and MoS_2 phase over the three supports.

Catalysts	dMo (at.nm^{-2} of support)	(Co/Mo) molar	(P/Mo) molar	% Co	% Mo	% P
CoMoS/γ-Al_2O_3	2.1	0.38	0.29	1.95	8.40	0.79
CoMoS/$\delta\theta$-Al_2O_3	2.2	0.39	0.27	0.71	2.94	0.26
$MoS_2/\delta\theta$-Al_2O_3	2.3	-	0.27	-	3.06	0.26
$Co_9S_8/\delta\theta$-Al_2O_3	-	-	-	0.74	-	0.97
CoMoS/SiO_2	2.4	0.39	0.23	1.86	7.78	0.58

2.2 FTIR experiment

Characterization NO-FTIR experiments were performed with a static experimental set-up under vacuum. An IR cell made in quartz equipped with KBr windows was used. The *ex situ* sulfided catalyst powder is pressed and used as wafer of 20 mg which represent 10 $mg.cm^{-2}$ under controlled atmosphere (argon). Catalyst wafer is introduced in the IR cell under argon. Prior to NO contact, the cell is evacuated under primary vacuum and closed. The vacuum line is then filled with NO at pressure equilibrium of 150 mbar. NO is afterwards expanded in the FTIR cell to reach 70 mbar equilibrium pressure. Interactions of NO on the surface of the sulfided catalyst wafer are followed by FTIR as function of time. After 5 min NO contact, gas phase spectra is recorded and the in situ FTIR cell and schlenck line are evacuated under primary vacuum. A spectra of the catalyst after NO evacuation is recorded. Subtractions of IR spectra of the catalyst wafer under vacuum before adding NO (reference spectrum) and of the NO gas phase spectra to catalyst wafer under NO atmosphere are performed in order to

evidence the IR contributions of the stable nitrosyl species sorbed on the surface of sulfided phases: CoMoS, MoS_2 and Co_9S_8. Second derivatives of the IR spectra absorbance of the NO sorbed on $\delta\theta$-Al_2O_3 supported catalysts were calculated with a Savitzky-Golay function (9 points, 3 order polynomial).

2.3 Chemometric method

Chemometric calculations were performed by using the multivariate curve resolution-alternating least squares (MCR-ALS) method directly on the subtracted FTIR spectra. MCR-ALS is based on a linear model assuming the generalized law of Lambert–Beer where the individual response of each component is addable. The aim of this method is the decomposition of the original data matrix, which contains all the spectra recorded during NO adsorption, into the product of two matrices, which contain the calculated concentration profiles and corresponding reference IR spectra respectively. Calculations were performed under Matlab.

2.4 DFT calculations

2.4.1 Total energy

Periodic density functional calculations have been performed using the VASP code[24–28]. Spin polarized general gradient approximation (GGA) with PW91 [27,28] exchange correlation functional and projected augmented-wave (PAW) formalism have been used for total energy calculations. The cut-off energy for the plane-wave basis was fixed to 500 eV and the Brillouin zone integration is performed on a (3×3×1) k-point mesh with a Methfessel and Paxton smearing method (σ=0.1).

The geometry optimization has been completed when the convergence criteria on forces becomes smaller than 0.02 eV/Å. The cell parameters (12.29 Å, 12.8 Å and 27 Å) have been used for the supercell, which ensures a sufficient vacuum interlayer when adsorbing NO molecules to avoid spurious interactions between the adsorbed molecule and the neighboring edge. In the z(z')direction, the slab contains four Mo layers for the MoS_2 model and five Mo layers for the CoMoS model. In the x(x') direction, four edge-sites have been considered. The most relevant structural models used for the MoS_2 edges and CoMoS edges are reported in Table 3 and 4 respectively.

Table 3. M-edge and S-edge of MoS_2 slabs with different sulfur coverage (yellow balls: S, green balls: Mo, blue balls: Co).

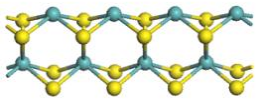 M-edge 0%S	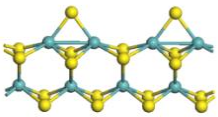 M-edge 25%S	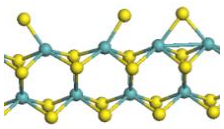 M-edge 37.5%S
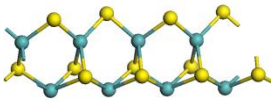 S-edge 50%S	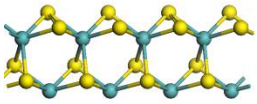 S-edge 100%S	

Table 4. M-edge and S-edge of CoMoS slabs with different sulfur coverages (yellow balls: S, green balls: Mo, blue balls: Co).

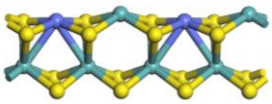 M-edge 50%Co 0%S	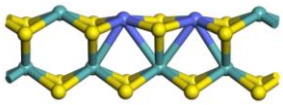 M-edge 50%Co pair 0%S	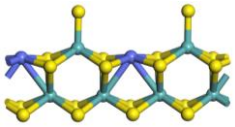 M-edge 50%Co 25%S
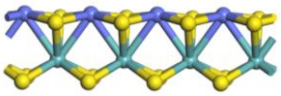 M-edge 100%Co 0%S	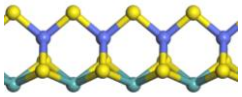 S-edge 100%Co 50%S	

The configurations reported in this paper result from geometry optimization performed in two steps: (i) First the free surface composed of four (or five in the case of CoMoS) atomic layers have been fully optimized, (ii) Then the geometry of the adsorption of the n NO molecules adsorbed on the adsorption site has been optimized, relaxing the atoms of the molecules and the ones of the two atomic layers of the surface, and fixing the position of the atoms of the two (or three) deepliest atomic layers. Determining the stable adsorption on each edge requires the calculation of the adsorption energies of the molecules in various initial configurations, on different sites.

The electronic adsorption energy (ΔE_{ads}) is calculated at 0 K for each configuration using the following expression:

$$\Delta E_{ads} = E(n.NO/Mo_xS_y) - E(Mo_xS_y) - n.E(NO(g)) \quad (1)$$

$E(Mo_xS_y)$ is the energy of MoS_2 or CoMoS clean surface of the given edge, E(NO(g)) is the energy of the NO gas phase molecule, and $E(n.NO/Mo_xS_y)$ is the energy of the n molecules adsorbed on the surface.

2.4.2 Frequency calculations

Harmonic frequency calculations for the NO molecules were performed with VASP through numerical differentiation of the force matrix, including all degrees of freedom of the molecules and of the metallic atoms of the adsorption sites. Including the relaxation of the neighboring sulfur atoms of the adsorption sites was found not to influence the frequency values. The calculations were performed on the configuration that was previously subjected to a geometry optimization. The displacement step was fixed to 0.02 Å. In order to compare the theoretical frequencies to the experimental frequencies, a scaling factor of 0.985 has been used, which corresponds to the ratio between the experimental frequency of the NO gas phase (1876 cm^{-1}) and the calculated frequency (1905 cm^{-1}).

3 Results and discussion

3.1 δθ-Al_2O_3 supported CoMoS catalysts

Infrared spectra of NO adsorbed on the calcined Mo, Co and CoMo oxide and the sulfided CoMoS (means CoMo sulfided material) supported on δθ-Al_2O_3 are shown in Figure 1.

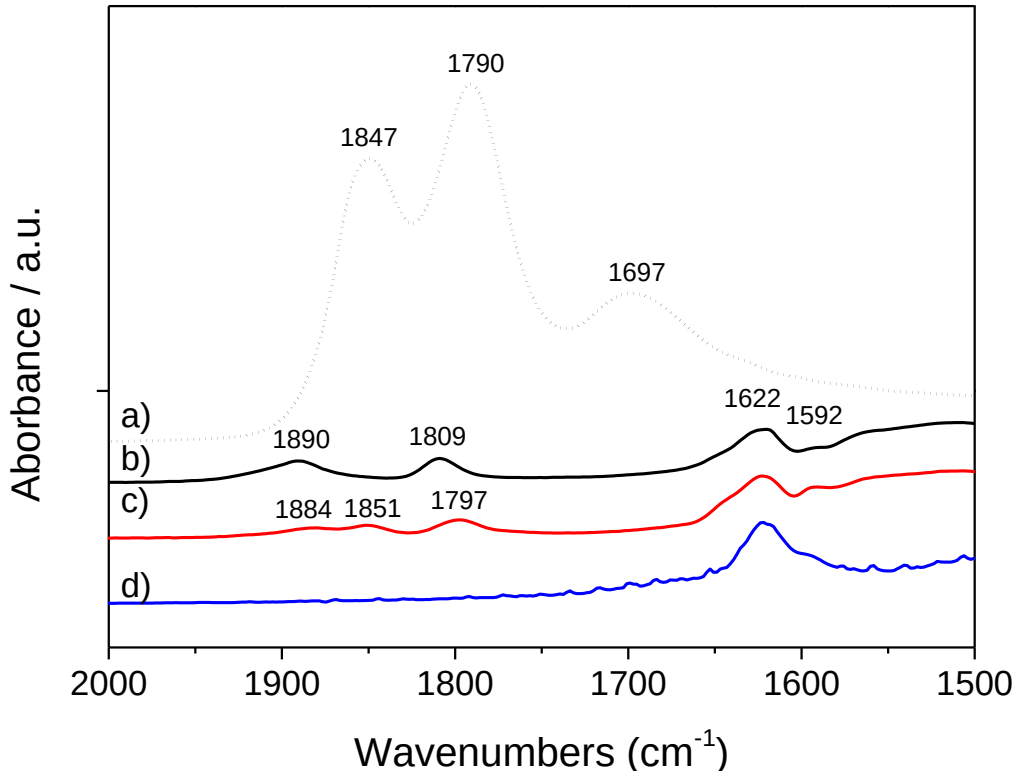

Figure 1. IR spectra (background subtracted and normalized by the mass of the wafer) of δθ-Al_2O_3 supported Mo (blue), Co (red), CoMo (black) oxides. For comparison, sulfided CoMoS (dotted line) after 5 min contact in NO (P = 70 mbar) and subsequent evacuation at 298K is reported.

In the spectra obtained for metal oxide supported on δθ-Al_2O_3, two regions can be distinguished: at 1650 – 1500 and at 2000 – 1650 cm^{-1} which are attributed to nitrate species formed upon NO contact and to nitrosyl adsorbed on the surface of the oxide or sulfided phases respectively. The contributions of the NO adsorbed on the oxide Mo, Co and CoMo on δθ-Al_2O_3 are weak. Indeed, for calcined Mo/ and Co/δθ-Al_2O_3 samples, Mo and Co are present as Mo^{6+} and Co^{2+} (d^0 and d^5 states respectively) which are not expected to adsorb strongly NO molecule.[18] For the oxide Co/δθ-Al_2O_3, three distinct NO contributions appear at 1884, 1851 and 1797 cm^{-1} in the nitrosyl region. The two bands at 1884 and 1797 cm^{-1} are due to the formation of $Co^{2+}(NO)_2$ complexes (ν_s(NO) and ν_{as}(NO) modes respectively), while

the band at 1851 cm^{-1} is assigned to mono-nitrosyl Co^{2+} species. [29] Oxide Mo/$\delta\theta$-Al_2O sample does not display any contribution due to nitrosyl species in the spectrum. In that case, only nitrates species formation is observed (1620 and 1570 cm^{-1}).[30] Considering the CoMo oxide material, two contributions are found at 1890 cm^{-1} and 1809 cm^{-1}. These components are close to those observed for the oxide Co/$\delta\theta$-Al_2O_3 sample and could be assigned to $Co^{2+}(NO)_2$ species.[29] It is interesting to note first that the di-nitrosyl contributions are more intense than on Co/$\delta\theta$-Al_2O_3 and secondly that mono-nitrosyl species is not observed on CoMo sample. It may indicate that cobalt oxide is better dispersed when introduced in presence of molybdenum. The nature of the species in the aqueous solution of impregnation should be different and may lead to different state of metal dispersion.

For comparison, NO titration has been done on CoMoS materials after sulfidation. In that case, the corresponding IR spectrum after NO saturation reports three distinct contributions in the 1850 – 1700 cm^{-1} range. The contributions are much more intense compared to the oxide materials due to i) the great affinity of NO towards edge sites of the promoted / non-promoted sulfided phases and the surface sites of Co_9S_8, ii) the possible higher molar absorption coefficient of nitrosyl adsorbed sulfided species and iii) the better dispersion/concentration of surface sites prompt to adsorb NO. Thus, NO is a relevant probe molecule of the sulfided phase in agreement to published results.[29] NO molecule has often been claimed to be a reactive probe towards the sulfided phase. Indeed, oxidation and sulfur removal mechanisms have been a lot discussed in the scientific community, but in the present case, one can remark that unlike metal oxide supported, formation of nitrates species is very limited on CoMoS catalyst in interaction with NO at 298 K.

More in details, IR spectra of NO adsorbed on sulfided CoMoS and references MoS_2, Co_9S_8 supported on $\delta\theta$-Al_2O_3 with constant Mo and Co loading are shown in Figure 2A. Table 5 presents the vibrational frequencies of the NO bond when NO is in contact with the oxide materials or the sulfided catalysts.

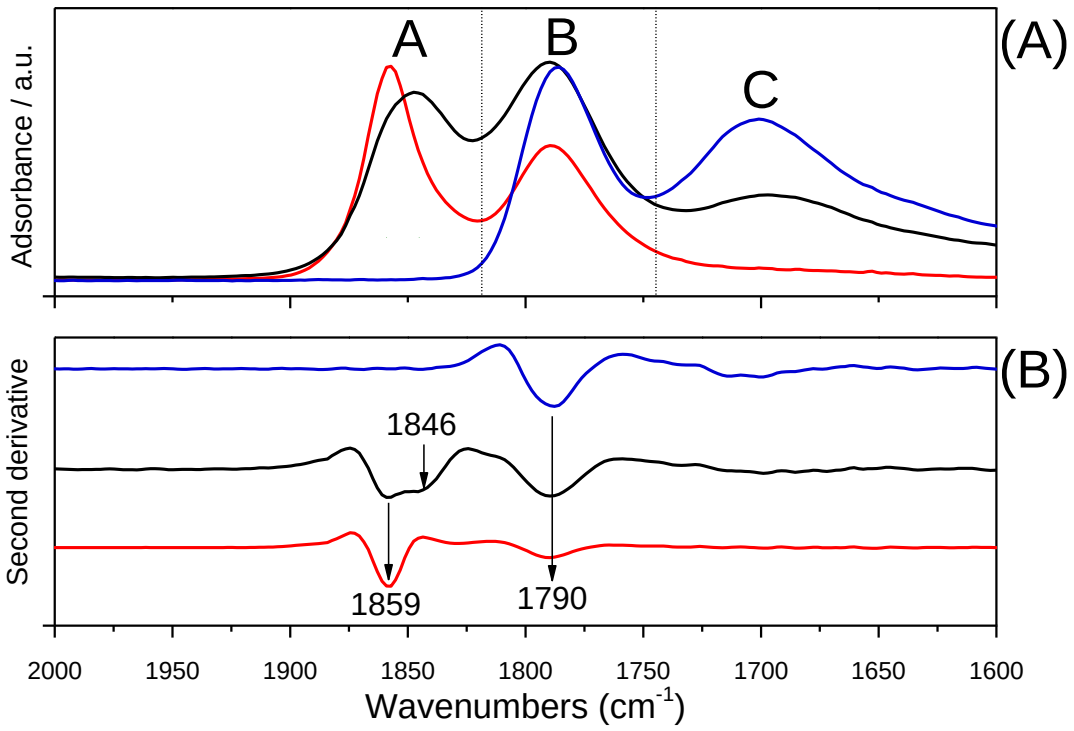

Figure 2. (A) Top panel IR spectra of sulfided catalysts MoS_2 (blue), Co_9S_8 (red) and CoMoS (black) on $\delta\theta$-Al_2O_3 (normalized by gram of catalyst) after 5 min contact in NO (P = 70 mbar) and subsequent evacuation at 298K; and (B) Bottom panel corresponding Second derivative spectra (similar code color).

Table 5. Vibrational frequencies of the NO adsorbed on the sulfided catalysts MoS_2 (blue), Co_9S_8 (red) and CoMoS (black) supported samples.

Region	ν (cm^{-1})	CoMoS	MoS_2	Co_9S_8
A	1859			✓
	1846	✓		
B	1790	✓		
	1789			✓
	1785			
C	1701		✓	
	1697	✓		

As previously discussed, three components are observed in the IR spectra recorded at NO saturation for the series of samples supported on $\delta\theta$-Al_2O_3 : 1880 6 - 1840 cm^{-1} ; 1810 - 1790 cm^{-1} and 1710 - 1700 cm^{-1} (broad) which will be hereafter referenced as (A), (B) and (C) components respectively. IR spectrum of NO on Co sulfided sample gives rise to (A) and (B) components respectively due to the symmetric and antisymmetric stretching vibrations of

dinitrosyl species adsorbed on coordinatively unsaturated sites (CUS) of Co. Similarly, IR spectrum of Mo sulfided sample in interaction with NO exhibits contributions (B) and (C) assigned to the symmetric and antisymmetric stretching vibrations of di-nitrosyl species adsorbed on CUS of Mo. These two contributions (B) and (C) are close to those generally observed for reduced Mo supported catalyst in interaction with NO. [30–32]

Promoted CoMoS/$\delta\theta$-Al_2O_3 reports (A), (B) and (C) components located 1849, 1790 and 1697 cm^{-1}. IR NO spectra obtained on CoMoS /$\delta\theta$-Al_2O_3 is almost the superposition of the two doublet bands observed for sulfided Mo/$\delta\theta$-Al_2O_3 and Co/$\delta\theta$-Al_2O_3.[17,33–35] Hence, vibrational contributions of NO adsorbed on MoS_2 and Co_9S_8/$\delta\theta$-Al_2O_3 overlap or are very close with the contributions of NO adsorbed on CoMoS on $\delta\theta$-Al_2O_3. It is thus difficult to identify the contributions due to the nitrosyl species adsorbed on the edges of the promoted CoMoS slabs.

To obtain a more detailed description of the vibrational contributions observed after NO contact on CoMoS, MoS_2 Co_9S_8, the second derivative spectra was obtained from the difference spectra (Figure 2B). Second derivative spectroscopy allows more specific identification of small and overlapping contributions which are not resolved in the initial spectrum.

The second derivative spectra obtained for NO sorbed on sulfided Co/ and Mo/$\delta\theta$-Al_2O_3 confirm the presence of doublet components already evidenced in the initial spectra (1859 A / 1790 B and 1790 B / 1700 C respectively), while sulfided CoMoS/$\delta\theta$-Al_2O_3 catalyst reports four intense contributions located at 1859 (A), 1846 (A'), 1789 (B) and 1700 cm^{-1} (C). Hence, two contributions were overlapped in the IR band (A) for CoMoS/$\delta\theta$-Al_2O_3. They reveal that either CoMoS edges exhibit edge sites with similar electronic properties as on the un-promoted Mo edge and Co_9S_8 sites or that non promoted MoS_2 crystallites and/or Co_9S_8 phases are present. However, the band located at 1846 cm^{-1} (A') seems to be specific to the promoted CoMoS phase. This feature may be critical to identify the CoMoS phase and will be discussed later by considering DFT calculations.

Minor components are also observed at lower wavenumbers for the different samples. Some of these vibrational contributions can be assigned exclusively to NO adsorbed on the CoMoS sites: 1657, 1672, 1814 cm^{-1}. In addition, the minor contribution at 1830 cm^{-1} seems also to be specific of the Co_9S_8 phase.

3.2 DFT calculation of NO adsorption on CoMoS edges

Schweiger *et al.*[36] studied the impact of the chemical potential of sulfur on the 2D morphology of the un-promoted MoS_2 slab by combining the calculation of the most stable surface edge energy (S or M) as a function of $\Delta\mu_S$ with the Gibbs–Curie–Wulff.[37] This morphology diagram of MoS_2 shows that in sulfo-reductive conditions (623 K and pH_2S/pH_2 = 0.18) the predicted shape is a deformed hexagon where 75-70 % of the edge are the M-edge and both M- and S-edges are covered by 50% of sulfur.

In a similar way as for non-promoted catalyst, the equilibrium morphologies of CoMoS phase can be expressed to describe specifically the nature, shape and edge composition of the MoS_2 slab considered.[8] From this equilibrium phase diagram, the morphology of the CoMoS can be determined according to the ($P(H_2S/H_2)$, T(K)) operating conditions. For instance, if the CoMoS phase is obtained from sulfidation conditions corresponding to a $\Delta\mu_S$ around – 0.8 eV, the proportion of M-edge is close to 50% indicating an hexagonal shape. The composition of the edge is recalled in Table 6.

Table 6. Composition of M- and S-edges as function of the operating conditions.

Nature of the edge	Sulfidation conditions $\Delta\mu_S$ around – 0.8 eV corresponding
M-edge	Mo non-promoted covered by 50% S or Mo promoted by 50% Co covered by 25% S
S-edge	Mo promoted by 100% Co covered by 50% S

According to these sulfidation conditions, DFT calculations were performed in order to determine the most stable adsorption mode of NO on the M- and S-edges of the MoS2 and CoMoS phases as a function of S and NO coverages (Table 6 and 7).

Before making a detailed comparison with experimental results, it is worth presenting a preliminary theoretical analysis of NO adsorption on the different type of sites at low NO coverage in order to provide general chemical trends.

- The M-edge case, at low NO coverage

If we first compare the non-promoted M-edge sites at 0% S-coverage with Co-promoted M-edge sites, (Table 7) we may remark that the NO adsorption energy is significantly stronger on the Mo site than on the Co site. Simultaneously the NO bond is weakened and the vibrational frequency is shifted to higher wavenumbers (close to free NO molecules in gas phase, ν_{NO} 1876 cm^{-1}) : the frequency increases as the back donation effect in the NO acceptor π orbital with the sorbing site is weaker. As expected the adsorption energies are significantly higher than those calculated for CO on the same systems.[11,12] Due to the presence of the odd extra electron in the $\pi*$ orbital of NO, this molecule is highly reactive and interacts more strongly with any Lewis Mo or Co sites than CO. In particular, Table 7 shows that the adsorption energy of NO molecule is more favorable on any Mo Lewis acid sites (when no sulfur atom is present), while the downward frequency shift is significantly larger on Mo than on Co sites: the difference between the two sites is close to 200 cm^{-1} for the ideal case of isolated mononitrosyl species. These results from two intricate effects: on the one hand, the acceptor character (involved in the donation) of the Co site is weaker than the Mo site, on the other hand, the d-π overlap (resulting from back donation) is also weaker for the Co-3d electrons than for the Mo-4d electrons. Although these ideal edge configurations simulated here are not obligatory relevant of the experiments, they readily help to understand the intrinsic site-driven parameters of the vibrational frequencies of NO adsorbed on the CoMoS systems. The experimental main bands are covering a wide range of about 170 cm^{-1} where Mo sites should generate vibrational frequencies located at the lower region of the IR spectrum, whereas some Co sites should impact the upper region.

Table 7. Calculated adsorption energies and corresponding vibrational frequencies of NO adsorbed on the various possible M-edge sites at low NO coverage.

Sites	Adsorption configurations	ΔE_{ads} (kJ/mol)	Vibrational frequency (cm^{-1})*
Mo on non promoted M-edge with 0%S	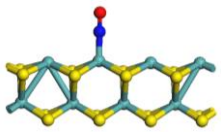	-361.5	1671
Mo on non promoted M-edge with 25 %S	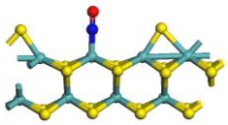	-355.3	1690
Mo on non promoted M-edge with 37.5 %S	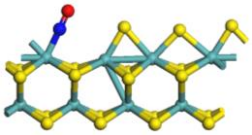	-214.4	1714
Mo on the promoted M-edge with 50% Co (alternated) and 0%S	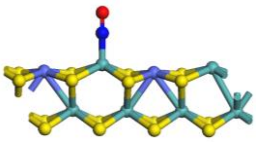	-335.4	1682
Mo on the promoted M-edge with 50% Co (paired) and 0%S	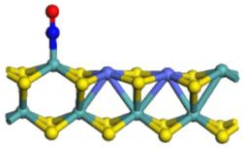	-344.3	1687
Co on the promoted M-edge with 100% Co and 0%S	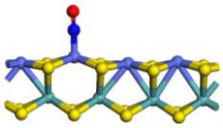	-242.1	1868
Co on the promoted M-edge with 50% Co (alternated) and 0%S	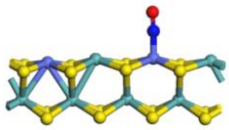	-176.7	1834
Co on the promoted M-edge with 50% Co (alternated) and 25%S	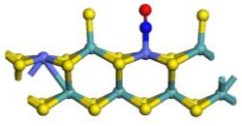	-191.2	1882
Co on the promoted M-edge with 50% Co (paired) and 0%S	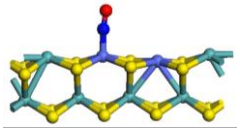	-199.1	1831

*vibrational frequency is corrected by a factor of 0.985 (see methods for explanation)

Moreover, it is important to notice that the vibrational frequency depends on the nature of the neighboring sites and local environment on the edge. In particular, on the partially promoted M-edge, the presence of Co atoms in the close vicinity of the Mo site where NO is adsorbed, induces a slight increase (+20 – 25 cm^{-1}) of the vibrational frequency. Conversely, the presence of Mo atoms in the close vicinity of the Co site where NO is adsorbed induces a slight decrease (-34 – 37 cm^{-1}) of the vibrational frequency.

Another environment effect may be studied here by considering the presence of sulfur atoms on the neighboring sites. For the non-promoted and promoted M-edge, adding 2 and 3 sulfur atoms on the neighboring sites where NO is adsorbed leads to an increase of the vibrational frequency by up to + 40 – 50 cm^{-1}. This may be considered as a surface coverage effect with dipole-dipole interaction between the neighboring Mo^{4+}---S^{2-} and Mo^{4+}---NO species due to the overlap between the Mo 4d electrons and $\pi*$ orbital of NO.

- S-edge case, at low NO coverage

Table 8. Calculated adsorption energies and corresponding vibrational frequencies of NO adsorbed on the various possible S-edge sites at low NO coverage.

Sites	Adsorption configurations	ΔE_{ads} (kJ/mol)	Vibrational frequency (cm^{-1})*
Mo on non-promoted S-edge with 50%S	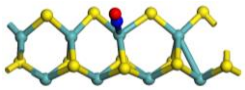	-169.7	1726
Mo on non-promoted S-edge with 50 %S (S-exchange)	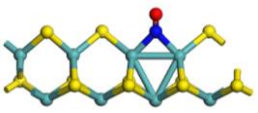	-320.8	1456
Mo on non-promoted S-edge with 100 %S	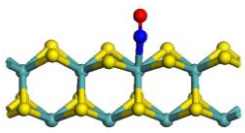	-107.1	1760
Co on the promoted S-edge with 100% Co and 75%S	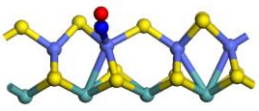	-60.3	1863
Co on the promoted S-edge with 100% Co and 50%S (S-exchange)	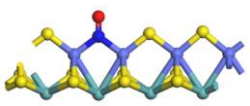	-286.5	1574

*vibrational frequency is corrected by a factor of 0.985 (see methods for explanation)

If we now consider the adsorption of NO on the S-edge, Table 8 shows first that on the non-promoted S-edge with a S-coverage of 50% as encountered in usual sulfidation conditions, the NO adsorption energy is significantly lower than on the M-edge with 0% S. At the same time, the corresponding vibrational frequency is also higher at 1726 cm^{-1} for the isolated mononitrosyl. If we consider the higher S-coverage (100%), the calculated NO vibrational frequency is even higher 1760 cm^{-1}. As a consequence, in these two S-edge cases as well as for the M-edge, it appears difficult to find Mo sites where the NO vibrational frequency is greater than 1800 cm^{-1}, which seems to be consistent with the experimental observations where the two main observed frequencies are below 1800 cm^{-1}. It should also be noticed that when one S atom is exchanged by one NO molecule in a bridging position, the NO vibrational frequency decreases tremendously at 1456 cm^{-1}. A similar trend is observed for the Co-promoted (1574 cm^{-1}, Table 8) and for S-edge the non-promoted M-edge (for specific NO bridging position not reported here). These low frequency values do not match the main observed bands. Considering the analysis of the second derivatives of the absorbance, one may not exclude that some minor contributions at low frequencies could be eventually assigned to isolated defect sites, if not beyond the experimental accuracy. Considering the Co-promoted S-edge with S-coverage of 75%, when NO is adsorbed on top of a Co site, it is observed that the calculated adsorption energy is significantly lower than on the M-edge while the vibrational frequency is equal to 1864 cm^{-1} as high as for the Co site on the M-edge with neighboring S-sites. Due to the very low adsorption energy on this Co S-edge site, it cannot be considered as relevant.

- Effect of the NO coverage

Due to the rather strong adsorption energy of NO adsorbed on the Mo or Co sites (often more than -200 kJ/mol NO), it is expected that even small doses of NO as used experimentally may induce a high coverage of NO at the edges, even if the initial S-coverage is high. Hence, the S-exchange process will be thermodynamically favored, and may lead to the complete removal of S-atoms on the edges and allowing NO molecules to be adsorbed. As previously explained in the literature, adsorption of NO could occur according a “push-pull” mechanism where NO replaces the edge S species.[20] Thus, the sulfur coverage should drastically diminish with respect to the sulfiding conditions, while the NO coverage increases as a function of the experimental pressure of NO applied.

Considering first the non-promoted M-edge, increasing the NO coverage may lead either to dinitrosyl species or neighboring mononitrosyls which exhibit coupled vibrational modes: generally one symmetric and one asymmetric mode. If these species are assumed to be isolated, Table 9 shows that the adsorption energies remain highly exothermic in both cases, while the symmetric modes exhibit higher frequencies (1705 and 1718 cm^{-1} respectively) than the isolated mononitrosyl (1671 cm^{-1}). This well-known coverage effect results from the through space interaction of the Mo^{4+}---NO dipole leading to dynamic shifts of about +34-47 cm^{-1} which are in line with those reported for NO on NiO surface.[38] At the same time, the asymmetric modes appear at significantly lower frequencies (1604 and 1670 cm^{-1} respectively). If the NO coverage is increased up to one dinitrosyl species per Mo site (saturation level in the experiments), an even broader distribution of frequencies is found from 1625 cm^{-1} to 1809 cm^{-1}. It can be thus noticed that the dinitrosyl coverage increase induces the appearance of higher frequencies closer to the main region (B) located around 1787 cm^{-1} on the experimental spectrum of the non-promoted MoS_2. The lower frequencies of coupled dinitrosyl species at 1712 cm^{-1} and 1688 cm^{-1}, may correspond to the main region (C) which is slightly more broaden according to the second derivative analysis. Finally, the other minor contributions at lower wavenumbers are also recovered by the DFT vibrational frequencies. If one considered the case of multiple mononitrosyl species, it appears that the highest band is at 1769 cm^{-1}, which is slightly lower to the experimental (B) band but cannot be totally ruled out, considering also that vibrational frequency calculated at 1708 cm^{-1} may also correspond to contributions of the observed (C) band.

Table 9. Calculated adsorption energies and corresponding vibrational frequencies of NO adsorbed on the various possible M- and S-edge sites of non-promoted MoS_2 at various NO coverages (yellow balls: S, green balls: Mo, blue balls: NO, red balls: O).

Site	Type	Adsorption configuration	E_{ads} (kJ/mol NO)	Calculated vibrational frequency (cm^{-1})*	Experimental vibrational frequency (cm^{-1})**
Mo on the non promoted M-edge with 0%S	Dinitrosyl	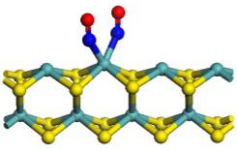	-223.58	1705 (s) 1604 (as)	
	Coupled mononitrosyl	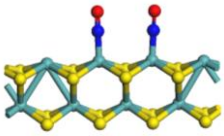	-349.20	1718 (s) 1670 (as)	
	Multiple mononitrosyl	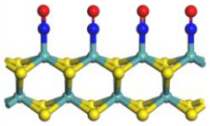	-343.18	**1769 (B)** **1708 (C)** **1708 (C)** 1660	
	Multiple dinitrosyl	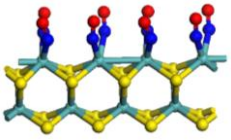	-189.01	**1809 (B)** 1762, 1740 **1712 (C)** **1688 (C)** 1659, 1650 1625	**1787 (B)** 1747, 1733 **1714 (C)** **1699 (C),** **1685 (C)** 1650 1637
Mo on the non promoted S-edge	Multiple mononitrosyl	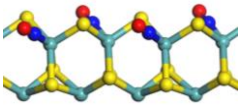	-167.29	1763 1745 1738 1736	
	Multiple dinitrosyl	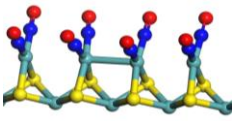	Exchange energy = -272.75***	1831, 1772 1770, 1739 1768, 1731 1727, 1693	

*vibrational frequency is corrected by a factor of 0.985 (see methods for explanation).

* and ** bold values correspond to the experimentally observed main regions (A), (B) or (C). Non bold values correspond the minor peaks also identified in the second derivative analysis.

***The exhange energy corresponds to the removal of one or several sulfur atoms when adsorbing nNO molecules, which creates n vacancies:

$\Delta E_{ads+vac} = E(n.NO/Mo_xS_{y-n}) - E(Mo_xS_y) - n.E(NO(g)) + n.E(H_2S(g)) - n.E(H_2(g))$, where $E(n.NO/Mo_xS_{y-n})$ is the energy of the n molecules adsorbed on the surface where nS atom have been removed, $E(H_2S)(g)$ and $E(H_2)(g)$ are the energies of the H_2S and H2 gas phase molecule.

According to DFT calculations, the predicted shape of the MoS_2 is a deformed hexagon where 70-75 % of the edges are constituted of the M-edge in sulfo-reductive conditions as used for the synthesis of the sulfided catalyst. Hence, we have also checked the vibrational frequencies in the cases of the multiple mononitrosyls and dinotrosyls adsorbed on the S-edge with 50% S and 0% S respectively. Apparently the dinitrosyl configuration leads to vibrational frequency calculated at 1831 cm^{-1} which is rather too high to be compatible with the experimental (C) band. The mononitrosyl configuration seems to be compatible with the (B) band but does not recover the (C) band. So the predominance of the M-edge could explain the fact that NO adsorption structures obtained on this edge should be satisfactory to interpret the experimental observations, while the contribution of NO adsorbed on the S-edge would be less predominant.

Table 9. Calculated adsorption energies and corresponding vibrational frequencies of NO adsorbed on the various possible Co promoted M- and S-edge sites at various NO coverages (yellow balls: S, green balls: Mo, purple balls: Co, blue balls: NO, red balls: O).

Site	Type	Adsorption configuration	E_{ads} (kJ/mol NO)	Calculated vibrational frequency (cm^{-1})*	Experimental vibrational frequency (cm^{-1})
Co on the promoted M-edge with 50% Co	Dinitrosyl	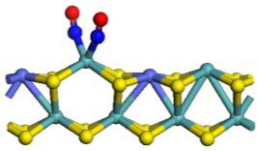	-206.08	1772 (s) 1708 (as)	
	Coupled mononitrosyl	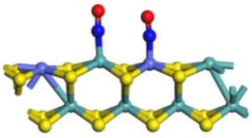	-250.69	1858 (s) 1655 (as)	
	Multiple mononitrosyl	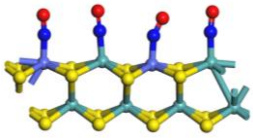	-251.25	1887 1808 1662 1649	
	Multiple dinitrosyl	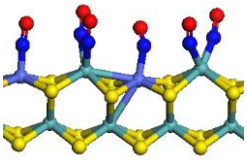	-184.24	**1867 (A')** **1774 (B)** 1740, 1670 1656, 1639	**1846 (A')** **1790 (B)** 1747, 1672 1657, 1633
Co on the promoted S-edge with 100% Co	Multiple dinitrosyl	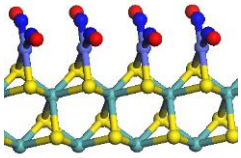	Not. Calc. Exchange = -108.38	**1787 (B)** 1729, 1720 **1719 (C)** **1689, 1686 (C)** 1678, 1650	**1790 (B)** 1734, 1716 **1704 (C)** **1699, 1685 (C)** 1672, 1647

*vibrational frequency is corrected by a factor of 0.985 (see methods for explanation).
* and ** bold values correspond to the experimentally observed main regions (A), (B) or (C). Non bold values correspond the minor peaks also identified in the second derivative analysis.

On the cobalt promoted M-edge with 50% cobalt and 50% Mo sites, the dinitrosyl species cannot be stabilized on Co sites: only mononitrosyl species are stable. On the Mo site, it appears that the two vibrational frequencies corresponding to the symmetric and asymmetric modes are shifted to higher values (1772 and 1708 cm^{-1} respectively) than the ones of the non-promoted edge. This confirms the non-negligible effect of the chemical nature of neighboring sites on the NO vibrational frequencies. At the highest NO coverage which may correspond to the saturation level, Mo sites are covered by dinitrosyl species and Co sites by mononitrosyl ones which generate a range of vibrational frequencies from 1639

up to 1867 cm^{-1}. This trend is in line with our previous analysis on the low NO coverage regime, and highlights that the M-edge partially decorated by cobalt may contribute to the band (A') around 1846 cm^{-1} as observed in the IR experiments to be specific of the CoMoS/$\delta\theta$-Al_2O_3 catalyst (Figure 4). In addition, a frequency calculated at 1774 cm^{-1} may correspond to band (B) observed on promoted, non-promoted MoS_2 and also Co_9S_8. By contrast, NO adsorbed on this edge (either as multiple mononitrosyls or dinitrosyls) does not contribute to band (C). Considering NO saturating the cobalt sites located on the S-edge, the dinitrosyl species present on each cobalt site lead to vibrational frequencies in the range of 1650 to 1787 cm^{-1} with possible contribution in the range of regions (B) and (C) but not in region (A). This interesting result thus reveals that the partially promoted M-edge and fully promoted S-edge do not contribute exactly to the same main IR bands, which may give an appealing way of distinguishing the two types of sites at high level of NO saturation. This result gives thus a complementary view as the one provided by the combined experimental STM, IR and DFT studies by N-Y. Tøpsøe et al.[20] where the partial promotion of the M-edge was excluded.

Since region (A') is not experimentally observed on the non-promoted MoS_2 (even at high NO coverage) and not on the Co_9S_8 phase but is present on the promoted MoS_2/$\delta\theta$-Al_2O_3 samples, it is clearly a signature of the presence of the promoter at the M-edge in CoMoS/$\delta\theta$-Al_2O_3. Coming back to the second derivative analysis (Figure 4), the overlap between NO-CoMoS and NO-Co_9S_8 in region (A) was proposed to be limited to the highest frequencies. For CoMoS/$\delta\theta$-Al_2O_3, the shoulder at 1847 cm^{-1} may thus correspond to the NO adsorption on the specific Co sites present in the CoMoS phase (and not in Co_9S_8) as identified by the DFT calculations. The impact of this important feature will be further considered in the next section where support effects are analyzed.

3.3 Comparison of Al_2O_3 and SiO_2 supported catalysts

To evaluate potential support effect on sulfided phase promotion and morphology, the second derivatives method was applied to spectra of NO adsorbed on CoMoS supported on γ-Al_2O_3, $\delta\theta$-Al_2O_3 and SiO_2 (Figure 3).

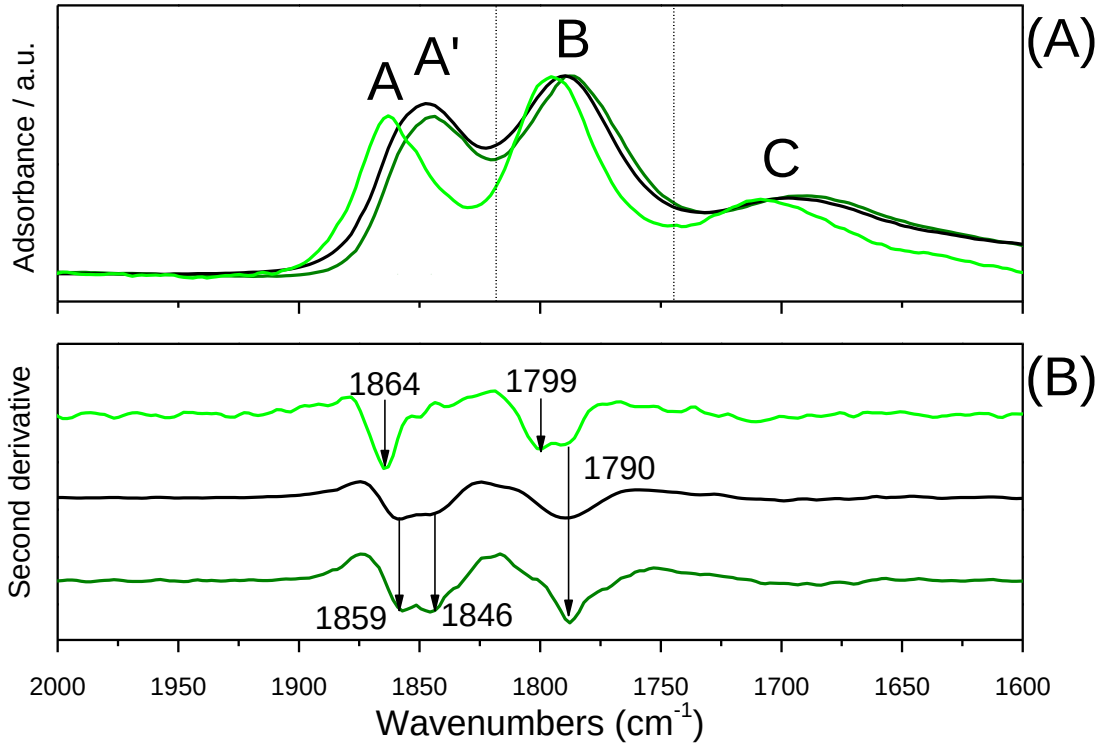

Figure 3. (A) IR spectra of NO adsorbed on sulfided catalysts CoMoS supported on γ-Al_2O_3 (dark green), δθ-Al_2O_3 (black) and SiO_2 (green) (normalized by gram of catalyst) after 5 min contact in NO (P = 70 mbar) and subsequent evacuation at 298K; and (B) corresponding Second derivative spectra (similar code color). Signal to noise ratio of spectrum of silica supported sample is low, the S/N of its second derivative spectra is consequently even poorer.

The A, A', B and C components are observed for the three different CoMoS supported catalysts. In the case of alumina supported catalysts, the component located at high wavenumbers reports clearly two maxima A and A' (1859 and 1846 cm^{-1}), while for silica supported catalyst a very short shoulder is present at 1849 cm^{-1} (spectrum reports low S/N ratio). Since IR spectrum of NO-Co_9S_8/δθ-Al_2O_3 reports a highest band (A) very close to 1859 cm^{-1}, the second peak at 1846 cm^{-1} (A') is unambiguously assigned to NO-CoMoS/γ-Al_2O_3. At this high NO coverage, A' contribution should even correspond to multi-nitrosyl complexes stabilized on cobalt promoted M-edge according to DFT calculations (Table 9). This spectral feature (A') evidenced from second derivative data treatment is clearly due to specific promoted sites and may consequently reveal the promotion degree reached on the different samples. In that case, the promotion degree seems to be significantly enhanced on alumina supported catalysts compared to silica sample.

For NO-CoMoS/SiO_2, the main band (B) is composed of two distinct contributions at 1799 and 1790 cm^{-1} respectively B and B' which is not the case for Al_2O_3 supported samples. Coming back to our previous DFT calculations at maximal NO coverage (Table 9), the calculated frequencies which would at best correspond to bands B and B' are either originating from the cobalt promoted M-edge and S-edge (1774 and 1787 cm^{-1} respectively), but may also be originated from the non-promoted M-edge (1809 cm^{-1}). Several interpretations can be thus proposed. Since on silica supported sample the level of cobalt promotion is expected to be low compared to alumina supported catalysts due to very low A' component (low concentration of promoted M-edge sites), the two peaks B and B' should correspond respectively to the non-promoted M-edge and to the promoted S-edge. In any case, the DFT calculations show that the CoMoS phase is also contributing to this band (B) and most probably to the lower frequency peak part of this band (B'). Regarding the third main contribution (C), different maxima can be identified which may also be assigned to the combination of non-promoted MoS_2 and promoted sites (mainly S-edge) as calculated by DFT.

More in details about silica supported CoMoS catalyst, it can be first noticed that the frequency shift of the three main contributions at 1869, 1799 and 1711 cm^{-1} are slightly shifted at higher frequencies and have narrower full width at half maximum (FHWM) than the alumina supported catalysts. It might be due to several effects. First, we cannot exclude an indirect effect of the silica support on the NO frequency shift. Due to the stronger Brønsted acidity of the hydroxyl groups present on aluminas than on silica, the electronic density withdrawing from the active phase to alumina supports is enhanced which reinforces the Lewis acidic character of the metallic adsorption site (either Co or Mo) and thus result in a higher frequency shift on aluminas than on silica.

Moreover, since the FWHM of the bands (A) and (B) are significantly narrower, this could also indicate that the types of sites involved in NO adsorption are less numerous. If we consider the reference sample NO-Co_9S_8/$\delta\theta$-Al_2O_3, it appears that the positions of bands (A) and (B) are rather close to the ones of NO-CoMoS/SiO_2. As a consequence, this suggests that part of this sample may contain a larger proportion of the Co_9S_8 phase and less contribution from the promoted MoS_2 phases, with a lower concentration of promoted M-edge in particular. This observation is also in agreement with the well-known lower

hydrodesulfurization activities usually reported for silica supported catalysts compared to the alumina supported ones (at iso Co/Mo ratio and dMo).[39]

3.4 Chemometric analysis

In order to complete the second derivative spectra analysis, a chemometric approach was applied to spectra series of NO sorbed (in excess) on CoMoS phase supported on alumina and silica. This mathematical method has already been successfully applied for size discrimination of supported Pt particles populations.[40] In the present work, the objective is to determine the number and the spectral features of the different population of surface sites probed by NO. For CoMoS phase supported on $\delta\theta$-Al_2O_3 and SiO_2 catalysts (Figure 4 and Figure 5 respectively), more than one single principal component have been used to decompose the spectral evolution, which indicate the presence of different surface site populations.

More in details, in the case of CoMoS/$\delta\theta$-Al_2O_3, three main Reference Spectra RS (1-3) has been used to explain more than 99.98% of the IR spectra evolution recorded as function of NO contact time (Table 10). The reference spectra are normalized as function of the total IR absorbance area in the 2000 – 1400 cm^{-1}. The concentration profiles of the different RS increase as soon as NO is introduced in the IR cell (t = 0), which may indicate that the RS are not dealing with the same populations of surface sites interacting with NO.

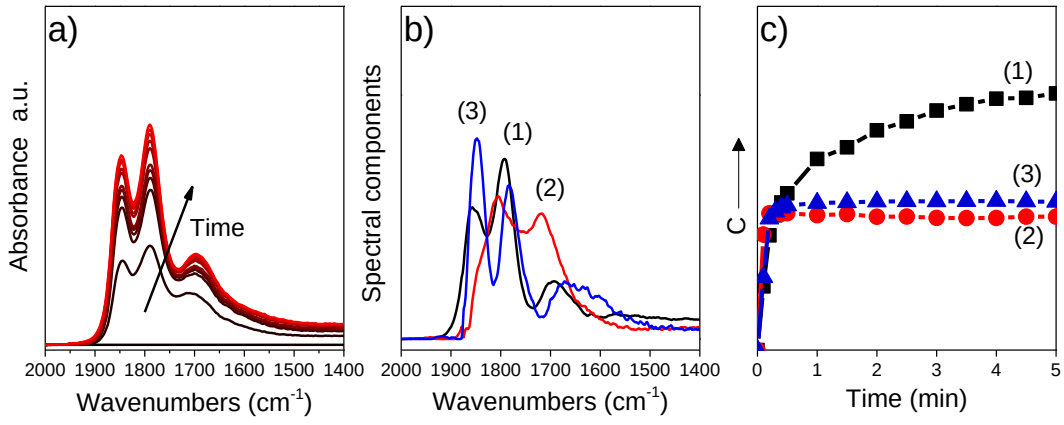

Figure 4. (a) Evolution in the IR spectra (background subtracted) of CoMoS/$\delta\theta$-Al_2O_3 as a function of NO contact time at RT (from black to red); (b) It is not clear how the curves 1-3 have been obtained. Corresponding MCR decomposition into 3 reference spectra and (1 – 3); (c) concentration profiles of each reference spectrum. C is dimensionless and expressed as the relative contribution of the three reference spectra in (b) to the spectra displayed in (a).

Table 10. Proportions of variations explained and NO vibrational frequency of each reference spectrum obtained on CoMoS/$\delta\theta$-Al_2O_3.

Reference Spectrum (RS)	Variations explained (%)	A or A' (cm^{-1})	B (cm^{-1})	C (cm^{-1})
(1)	51.85	1857	1792	1695
(2)	22.57	-	1805	1718
(3)	25.56	1847	1785	1670

The reference spectra (1) and (3) explain about 77% (51.85 and 25.56% respectively) of the variation observed in the spectra as a function of NO contact time. They both report 3 main contributions located at 1857-47 and 1792-85 and 1695-70 cm^{-1} (referred as A (A'), B, C in Table 10). The profiles shape observed indicate that different surface sites are contributing in these two reference spectra. Considering DFT calculations, it has been evidenced that the presence of partially promoted M-edge and fully promoted S-edge sites may lead after interaction with NO (high NO coverage) to A', B and C contributions. Consequently, RS(3) would be the spectral feature of NO on promoted CoMoS phase. Considering RS(1), the contribution centered at high wavenumbers 1857 cm^{-1} (A) is close to what is observed for supported Co_9S_8 reference (Figure 2). It seems that RS(1) corresponds to a mix between Co_9S_8 and sulfided phases since contributions B and C are also present in the spectrum. Even if the molar absorption coefficient of NO vibration due to nitrosyl sorbed on the surface of Co_9S_8 is not determined, the concentration of Co_9S_8 is clearly not negligible on support $\delta\theta$-Al_2O_3 catalyst. The last reference spectrum RS(2) reports two maxima at 1805 and 1718 cm^{-1} (B and C). In that case, the nature of the corresponding sulfided phase population is expected to be non-promoted. Hence, from the chemometric analysis, it becomes possible to distinguish different populations of phases present on $\delta\theta$-Al_2O_3 support which report different behavior in presence of nitric oxide: RS(1) assigned to a combination of Co_8S_9 and MoS_2 (promoted/non-promoted); RS(2) due to MoS_2 phase and RS(3) due to a mixture of promoted and non-promoted MoS_2 phases.

Similar chemometric decomposition done for silica supported catalyst is reported in Figure 5. Two main reference spectra (RS) were sufficient to decompose (at 99.59%) the IR spectra evolution recorded as function of NO contact time (Table 11).

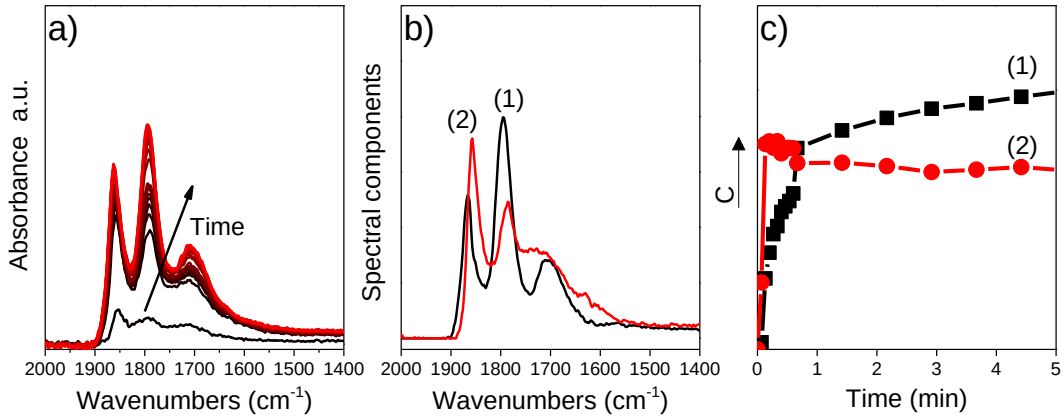

Figure 5. (a) Evolution in the IR spectra (background subtracted) of $CoMoS/SiO_2$ as a function of NO contact time at RT (from black to red); (b) Corresponding MCR decomposition into 3 reference spectra and (1 – 3); (c) concentration profiles of each reference spectrum. C is dimensionless and expressed as the relative contribution of the three reference spectra in (b) to the spectra displayed in (a).

Table 11. Proportions of variations explained and NO vibrational frequency of each reference spectrum obtained on $CoMoS/SiO_2$.

Reference Spectrum (RS)	Variations explained (%)	A or A' (cm^{-1})	B (cm^{-1})	C (cm^{-1})
1	49.39	1867	1795	1705
2	50.20	1857	1786	1726

Each reference spectra (1) and (2) explain half of the variation observed in the spectra as a function of NO contact time. RS(1) reports three maxima and amongst them, one centered at high wavenumber 1867 cm^{-1} (A) which may indicate the presence of Co_9S_8 phase. In addition B and C components are also present, as a consequence, RS(1) seems to be related to a mix between Co_9S_8 and MoS_2 phases (promoted/non-promoted) which express a similar behavior in contact with NO. The concentration profile of RS(1) progressively increases as function of NO contact time. This observation is very similar to what is observed for RS(1) of $CoMoS/\delta\theta\text{-}Al_2O_3$ sample which also contains a significant proportion of Co_9S_8 phase. It could be due to the significant evolution of nitrosyl speciation at the surface of Co_9S_8 phase as function of NO contact time (see chemometric analysis of $NO\text{-}Co_9S_8/\delta\theta\text{-}Al_2O_3$ in supplementary). The second reference spectrum RS(2) of $CoMoS/SiO_2$ reports A', B and C components and could be due to a mixture between promoted and non-promoted MoS_2 phases.

A chemometric treatment has also been performed for CoMoS/γ-Al_2O_3 sample (Figure 6). In that case, one single reference spectrum was appropriate to explain 99.91% of the whole set of IR data recorded while the catalyst was sorbing NO (Table 12).

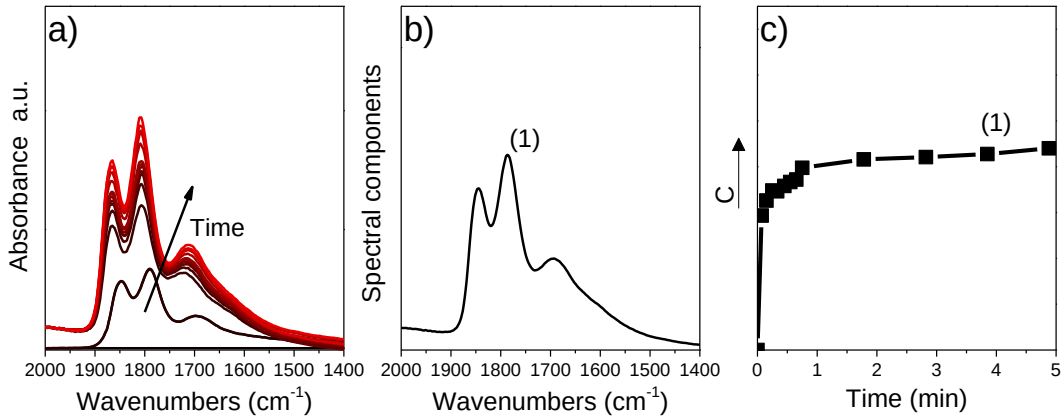

Figure 6. (a) Evolution in the IR spectra (background subtracted) of CoMoS/γ-Al_2O_3 as a function of NO contact time at RT (from black to red); (b) Corresponding MCR decomposition into 3 reference spectra and (1 – 3); (c) concentration profiles of each reference spectrum. C is dimensionless and expressed as the relative contribution of the three reference spectra in (b) to the spectra displayed in (a).

Table 12. Proportions of variations explained and NO vibrational frequency of each reference spectrum obtained on CoMoS/γ-Al_2O_3.

Reference Spectrum (RS)	Variations explained (%)	A' (cm^{-1})	B (cm^{-1})	C (cm^{-1})
1	99.91	1845	1786	1695

Three components A', B and C constitute the calculated reference spectrum (1), which indicate that CoMoS/γ-Al_2O_3 sample is mainly composed of a mix between promoted and non-promoted MoS_2 phases. The presence of Co_9S_8 phase is not discarded on γ-Al_2O_3 supported sample but its concentration is surely not as high as observed on $\delta\theta$-Al_2O_3 and SiO_2 supports.

4 NO FTIR – structure – catalytic activity relationships

Finally, an additional part will be presented with the objective to correlate the total are of NO adsorbed on the CoMoS phase with the 2D morphology model of a CoMoS slab developed previously in the chapter IV as well as with the catalytic performances of the HDS catalyst (chapter III).

4.1 Total area of NO sorbed on HDS catalyst vs 2D morphology model of the CoMoS slab

In order to validate this quantification of edge sites, correlation between the area of the contributions of the NO adsorbs on the CoMoS supported catalysts have been performed. As previously demonstrated in the literature, NO is adsorbed exclusively on the active sites which are located at the edge of the CoMoS slab. [16–20] Figure 7 presents the total area of the NO adsorbed (normalized by gram of Mo) on the CoMoS phase for CoMoS on γ-, δθ-Al_2O_3 and SiO_2 as function of (a) the total number of edge atoms of the CoMoS slab and (b) the total number of edge atoms of the slab normalized by the stacking expressed respectively in mmol of edge atoms by gram of Mo.

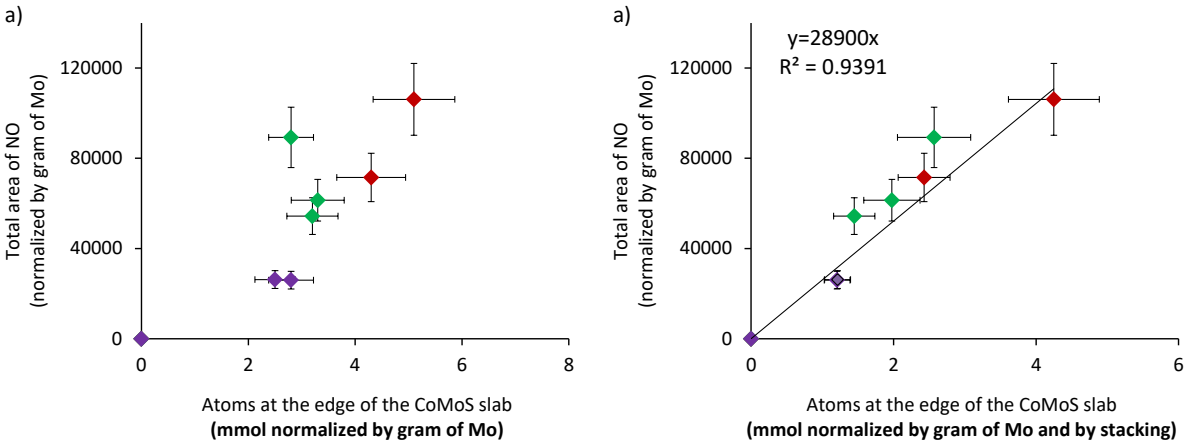

Figure 7. Total area of the NO adsorbed on the CoMoS phase for CoMoS on γ-Al_2O_3 (red diamond), δθ-Al_2O_3 (green diamond) and SiO_2 (purple diamond) as function of (a) the total number of edge atoms of the CoMoS slab and (b) the total number of edge atoms of the slab normalized by the stacking. Parameters are normalized by gram of Mo obtained from XRF. Relative uncertainties on the atoms at the edges and the total area of NO measured is evaluated, for both, to 15%.

It can be observed that the direct correlation of the number of edge atoms of the CoMoS phase with the total area of NO adsorbed on the CoMoS phase is not well matching (Figure 7 a). However, the straight line correlation passing through the origin is improved when the number of edge atoms of the CoMoS phase is normalized by the stacking (Figure 7 b). Deviation of the experimental point with the straight line could be explained by the uncertainties of the atoms at the edge which is around +/- 10% according TEM analysis. It can also be assumed that the molar extinction coefficient of NO could change according to the kind of the support considered and the electronic density effects. Moreover, the unwished phase Co_xS_y is also probe by the NO molecule. It implies that the total quantified area of adsorbed NO might overestimate the contribution of the CoMoS phase. However, at this stage, we assumed that the NO area related to the NO adsorbed on the Co_xS_y phase is almost constant regardless the dMo or the support according the XPS quantification previously presented (Chapter IV, section 3.2.2.1). Thus, if the CoMoS phase is described as a stack of several slabs, it could suggest that only the edges of the slab at the top are probed by the NO molecule which could be related to the "rim-edge'' concept. Moreover, by the stacking normalization, it is noticed that the slabs stack between each other to form the CoMoS could be not equivalent with regard to the reactant adsorption. Indeed, it could easily understand that the top slab of the CoMoS crystallite is more reactive and available (low hindrance compare with the other slab) according is particular localization. Finally, this result also shows that the assumption of an hexagonal shape for all CoMoS slabs is sufficient to build 2D morphology model even if some triangular truncated shapes are revealed by HR STEM-HAADF. This 2D morphology model of the CoMoS slab is thus relevant to correlate with NO IR experiments and obtain a nanoscale description of the CoMoS phase especially a quantification of the edge sites.

4.2 Total area of NO sorbed on HDS catalyst vs catalytic activity of the HDS catalysts

Initial activities related to the initial rate of 3MT and 23DMB2N reaction, respectively a_{3MT} and $a_{23DMB2N}$, as well as activities related to initial rate of the HDS and HYDO yield, respectively a_{HDS} and a_{HYDO}, have been determined in the chapter III.

Here, correlation between catalytic activities and total are of NO sorbed of CoMoS on γ- and δθ-Al_2O_3 and SiO_2 have been undertaken (Figure 8). At this stage, the total area of NO is not easily related to the HDS or 3MT activities. Indeed, it is assumed that NO is probing all the edges of the CoMoS slab. Previously, it was demonstrated that the total area of NO was correlated with the amount of atoms at the edges. On the other hand, the HDS and 3MT activities were correlated with the total amount of Co decorating the edges of the CoMoS slab. Thus, the no correlation obtained in the Figure 8 is in line with the previous results. Moreover, as it was shown on the part 3.1, total area of NO recorded is due to the CoMoS phase but also to the undesirable cobalt sulfided phase, Co_9S_8.

In perspectives, it will be interesting to decompose the infrared spectra of NO sorbed in the HDS catalysts thanks to the derivative treatment in order to quantify the NO area fractions of the CoMoS and Co_9S_8 phases, respectively.

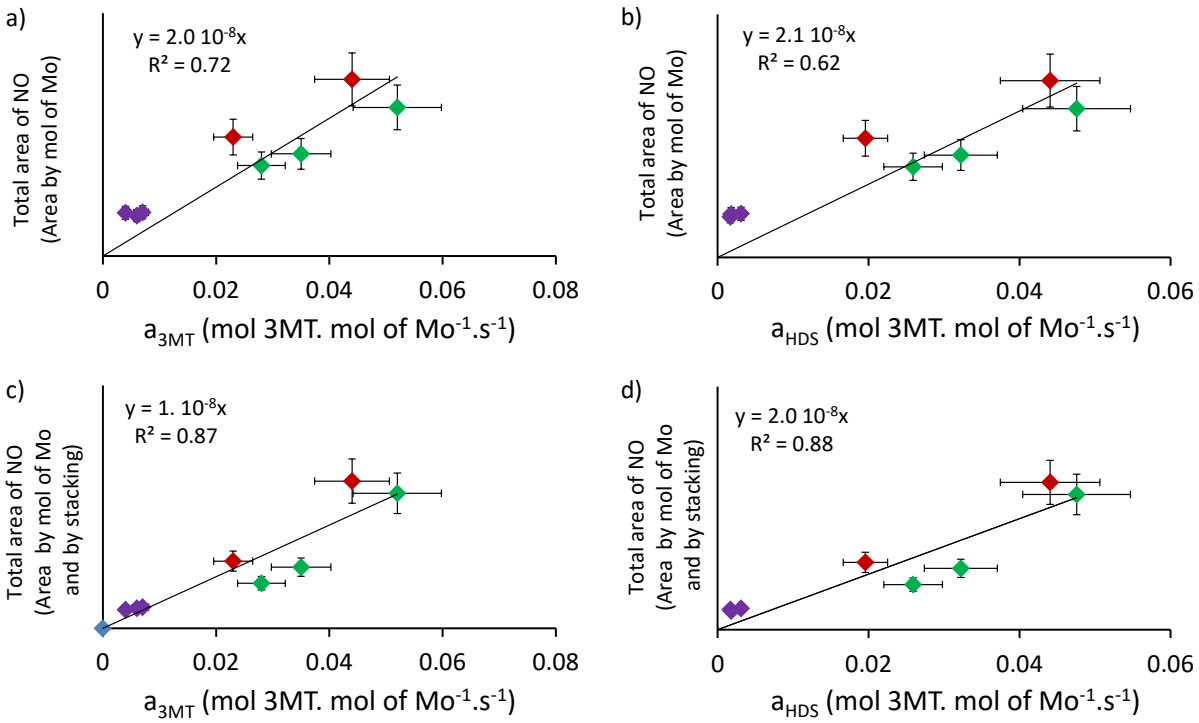

Figure 8. Correlation of the activities at 220°C related to the initial rate of 3MT reaction, a_{3MT} , and the initial rate of the HDS yield, a_{HDS}, with respectively (a), (c) total area of NO (Absorbance.mol of Mo^{-1}) and (b), (d) the total area of NO normalized by the stacking (Absorbance.mol of Mo^{-1}.$stacking^{-1}$) at the slab of the CoMoS on γ-Al_2O_3 (red), δθ-Al_2O_3 (green) and SiO_2 (purple) previously present in the section 3.2.1.8. Relative uncertainties on the activity and the total area of NO measured is evaluated respectively to 20% and 15%.

5 Conclusions

By combining FTIR spectroscopy and DFT calculations, we have investigated the nature of sites of sulfided phases probed by the NO molecule. We have shown that NO molecule is relevant to probe and discriminate the surface of promoted sulfided phases (MoS_2, CoMoS and Co_9S_8) supported on three relevant supports: $\delta\theta$-Al_2O_3, γ-Al_2O_3 and SiO_2. The interactions have been followed by FTIR spectroscopy at high NO coverage (70 mbar) and at 298 K. Different mathematical approaches have been used to output the maximum information from the IR spectra recorded. To help for the interpretation of the FTIR spectra, we have simultaneously undertaken periodic boundary DFT calculations of NO adsorbed at various coverages and on the various possible MoS_2 and CoMoS sites.

Second derivative spectroscopy has been used to output the overlapped contributions which are not resolved in the initial IR spectrum of alumina supported systems. In that case, specific contributions at 1846 and 1790 cm^{-1} (A' and B' respectively) have been identified for alumina supported samples which are related to the promoted sites. From DFT calculations, it is shown that A' component would be the specific spectral signature of multiple nitrosyl complexes formed on cobalt promoted M-edge sites at high NO coverage. The B' component is assigned either to promoted M-edge or S-edge, according to DFT calculations.

The silica supported catalyst revealed a different spectroscopic feature which helped to refine further the spectroscopic assignment. Indeed, silica supported sample does not display such A' component but exhibits an intense contribution at 1799 cm^{-1} (B distinct from B') which could be related to the presence of non-promoted sites. According to DFT calculations, dinitrosyls on the non-promoted M-edge exhibit slightly higher frequency than the promoted M- or S-edge. This latter observation is consistent with XPS analysis and may also explain the lower HDS activities generally measured for silica supported catalysts compared to the alumina ones (at iso Co/Mo ratio and dMo).

It has been observed that the different catalysts supported on $\delta\theta$-Al_2O_3, γ-Al_2O_3 and SiO_2 behave differently towards NO molecule interaction due to various surface sites present at different concentration levels. A chemometric decomposition of the IR spectra series has been performed as function of NO contact time, in order to discriminate the presence and nature of the different populations of NO-sorbing phases : MoS_2 promoted/non promoted

and Co_9S_8. The distribution of each population varies as function of the support nature. In the present case, the concentration of Co_9S_8 phase seems to be lower on γ-Al_2O_3, which may imply a higher promotion degree of the sulfided phase (compared to $\delta\theta$-Al_2O_3, and SiO_2 supports).

Finally, we have identified linear spectroscopic – structure – activity relationships correlating the total area of sorbed NO on the edges, amount of edge sites and intrinsic HDS or HYDO activities. To the best of our knowledge, this is the first time that such a quantitative correlation was found especially when considering three different types of support. In the future, such correlations should be refined further, particularly by considering the distinct contribution of M-edge and S-edge sites.

We hope this detailed combined spectroscopic and DFT analysis offers a more rational interpretation of the nature of edge sites of the MoS_2 and CoMoS phase. This more quantitative analysis will provide a more robust methodology allowing a better control and design of these catalytic active phases.

6 References

[1] US Environ. Prot. Agency (2013).
[2] Official Journal of the European Union (2009) 88–113.
[3] Int. Counc. Clean Transp. (2013).
[4] Blaise Didillon, Nathalie Marchal, Denis Uzio EP 1077247 A1.
[5] J.T. Miller, W.J. Reagan, J.A. Kaduk, C.L. Marshall, A.J. Kropf, Journal of Catalysis 193 (2000) 123–131.
[6] J. Wu, C. Bai, T. Halbert, S. Soled, S. Miseo WO 2007/084439 A1.
[7] H. TOPSOE, Journal of Catalysis 68 (1981) 433–452.
[8] E. Krebs, B. Silvi, A. Daudin, P. Raybaud, Journal of Catalysis 260 (2008) 276–287.
[9] P. Raybaud, H. Toulhoat, Catalysis by transition metal sulfides: From molecular theory to industrial application, Editions Technip, Paris, 2013.
[10] S. Brunet, D. Mey, G. Pérot, C. Bouchy, F. Diehl, Applied Catalysis A: General 278 (2005) 143–172.
[11] A. Travert, C. Dujardin, F. Mauge, S. Cristol, J.F. Paul, E. Payen, D. Bougeard, Catalysis Today 70 (2001) 255–269.
[12] A. Travert, C. Dujardin, F. Maugé, E. Veilly, S. Cristol, J.-F. Paul, E. Payen, The journal of physical chemistry. B 110 (2006) 1261–1270.
[13] J.B. Peri, J. Phys. Chem. 86 (1982) 1615–1622.
[14] M.I. Zaki, B. Vielhaber, H. Knoezinger, J. Phys. Chem. 90 (1986) 3176–3183.
[15] T. Zeng, X.-D. Wen, Y.-W. Li, H. Jiao, Journal of Molecular Catalysis A: Chemical 241 (2005) 219–226.
[16] L. van Haandel, E. Hensen, T. Weber, Catalysis Today 292 (2017) 67–73.
[17] N.-Y. Topsøe, H. Topsøe, Journal of Catalysis 84 (1983) 386–401.
[18] N. Topsoe, Journal of Catalysis 75 (1982) 354–374.
[19] Y. Okamoto, M. Kawano, T. Kawabata, T. Kubota, I. Hiromitsu, The journal of physical chemistry. B 109 (2005) 288–296.
[20] N.-Y. Topsøe, A. Tuxen, B. Hinnemann, J.V. Lauritsen, K.G. Knudsen, F. Besenbacher, H. Topsøe, Journal of Catalysis 279 (2011) 337–351.
[21] X.-D. Wen, T. Zeng, Y.-W. Li, J. Wang, H. Jiao, The journal of physical chemistry. B 109 (2005) 18491–18499.
[22] X.-D. Wen, J. Ren, Y.-W. Li, J. Wang, H. Jiao, Chemical Physics Letters 436 (2007) 209–212.
[23] J. LAURITSEN, J. KIBSGAARD, G. OLESEN, P. MOSES, B. HINNEMANN, S. HELVEG, J. NORSKOV, B. CLAUSEN, H. TOPSOE, E. LAGSGAARD, Journal of Catalysis 249 (2007) 220–233.
[24] G. Kresse, D. Joubert, Phys. Rev. B 59 (1999) 1758–1775.
[25] G. Kresse, J. Furthmüller, Phys. Rev. B 54 (1996) 11169–11186.
[26] G. Kresse, J. Hafner, Phys. Rev. B 47 (1993) 558–561.
[27] J.P. Perdew, J.A. Chevary, S.H. Vosko, K.A. Jackson, M.R. Pederson, D.J. Singh, C. Fiolhais, Phys. Rev. B 46 (1992) 6671–6687.
[28] J.P. Perdew, Y. Wang, Phys. Rev. B 45 (1992) 13244–13249.
[29] K.I. Hadjiivanov, Catalysis Reviews 42 (2000) 71–144.
[30] J.P. Thielemann, J. Kröhnert, C. Hess, J. Phys. Chem. C 114 (2010) 17092–17098.
[31] A. KAZUSAKA, Journal of Catalysis 63 (1980) 447–455.

[32] J.E. Herrera, L. Balzano, A. Borgna, W.E. Alvarez, D.E. Resasco, Journal of Catalysis 204 (2001) 129–145.
[33] S. Kasahara, N. Koizumi, M. Yamada, Y. Udagawa, Sekiyu Gakkaishi (1995) 439.
[34] N. Koizumi, K. Takahashi, M. Yamazaki, M. Yamada, Catalysis Today 45 (1998) 313–318.
[35] L. Portela, P. GRANGE, B. DELMON, Catalysis Reviews 37 (1995) 699–731.
[36] H. Schweiger, P. Raybaud, G. Kresse, H. Toulhoat, Journal of Catalysis 207 (2002) 76–87.
[37] G. Wulff, Zeitschrift Fur Kryst. Und Mineral (1901) 449.
[38] C. Lamberti, A. Zecchina, E. Groppo, S. Bordiga, Chemical Society reviews 39 (2010) 4951–5001.
[39] T. Wang, Y. Fan, X. Wang, L. Chou, H. Lin, Fuel 157 (2015) 171–176.
[40] M. Rivallan, E. Seguin, S. Thomas, M. Lepage, N. Takagi, H. Hirata, F. Thibault-Starzyk, Angewandte Chemie (International ed. in English) 49 (2010) 785–789.

- Chapter VI -
In situ and operando DRIFT and ATR-IR characterization of 3-methylthiophene interactions on CoMoS/γ-alumina and CoMoS/silica catalysts

Tables of contents

1 Introduction 292

2 Experimental 296

2.1 Catalysts preparation 296

2.2 Characterization 297

2.2.1 Injection system set-up 297

2.2.2 DRIFT spectroscopy 298

2.2.3 ATR-IR spectroscopy 299

3 Results and discussion 299

3.1 In situ DRIFT 299

3.1.1 Alumina supported catalyst 299

3.1.2 Silica supported catalyst 303

3.2 Operando DRIFT Reaction of 3MT on CoMoS/γ-Al_2O_3 306

3.3 Insights into surface species by ATR-IR 308

4 Conclusion and perspectives 311

5 Appendices 313

6 References 317

- Chapter VI - In situ and operando DRIFT and ATR-IR characterization of 3-methylthiophene interactions on CoMoS/ γ-alumina and CoMoS/silica catalysts

1 Introduction

Industrial catalysts involved in the HDS process are based on an active transition metal (TMS) phase, usually MoS_2 phase supported on alumina[1–3] where MoS_2 forms slabs decorated at the edge by cobalt atoms within the Co- promoted MoS_2 phase.

Characterization of surface atoms species of HDS catalysts is conventionally done via the use of probe molecules like CO or NO. Upon adsorption of the probes, characteristic IR features can be observed in the IR spectra of the activated catalyst (oxided, reduced), which shed light on surface speciation (nature, structure, degree of unsaturation), dispersion (when extinction coefficients of each surface species are defined), oxidation state. As shown in the previous chapter, NO can be used as a probe molecule due to its strong interaction on the surface of the phase in order to identify the nature of edge sites[4–7]. We proposed also an interesting IR NO – activity relationship for several support.

CO probe has been also often used in the last decade for HDT catalysts characterization since limited surface reactions between HDT catalyst and CO are expected at low temperature. CO contact on MoS_2 catalysts leads to two main spectral contributions at 2110 cm^{-1} (strong) and 2070 cm^{-1} (weak) assigned to CO adsorption on the edge sites of the MoS_2 slabs.[8] The situation seems rather simple for such non promoted catalyst and after confront of CO titration by IR with HDS reactivity of the catalysts, these two contributions have been described as the signature of active sites.[9] CO titration on promoted CoMoS catalysts leads to additional IR components, implying the presence of new surface sites due to the cobalt decoration of MoS_2 at the edges. The carbonyl spectral profile of promoted catalyst is dominated by the component at 2070 cm^{-1} (str). The intensity of the new band at 2070 cm^{-1} has been shown as proportional to the HDS catalytic activity of the material.[10] In the previous reference[10], model catalysts have been studied with Co content ranging from 1.3 to 3.6 wt% at constant 8 wt% Mo content (Co/Mo ratio from 0.15 to 0.45), which enhance

the spectral discrepancies and facilitate the confront between IR characterization and reactivity. However, for CO probe methodology it is important to note that:

- industrial catalysts have generally a restricted Co/Mo ratio held between to 0.3 - 0.4, consequently the difference in surface carbonyl speciation of the real catalysts are generally very short,
- the quantification of the active sites is indirect i.e. via probe molecule interaction, and so the analysis is dependent of the extinction coefficients of each ad-species. Part of the coefficients have already been calculated and reported in the literature elsewhere for a given alumina support.
- CO adsorbed on promoted and non promoted species contributes in the same spectral range ca. 2070 cm^{-1} and the deconvolution of the spectra is not easy before quantification,
- the exact nature, structure and coordination sphere surrounding the probed sites are not fully determined,
- the reductive post treatment prior CO titration could redistribute the speciation present on the active state (the probed reduced sample is different from the active sample).

As a consequence, it is difficult to determine a correlation between catalytic HDS activity and IR CO observations and for promoted CoMoS catalysts. Although we have shown interesting IR NO – edge structure – activity relationships, this limitation remains also for the NO probe molecule. CO and NO probes are probably too sensitive for revealing the surface atoms speciation and not enough selective to the active species present on HDT catalyst (Co_9S_8 and surface acid sites are also probed). Efforts have to be done in the search of more specific probe for in situ FTIR characterization of HDT catalysts. HDS reactions occurs specifically on sulphur vacancies or CUS sites which bind the sulphur atoms present in the feed, so that we could wonder if the best probes for IR characterization could be the sulfur reactants itselves like alkylthiophene derivate compounds.

A lot of theoretical studies have been done in order to identify the different modes of adsorption of thiol and thiophenic compounds on promoted or non promoted phases. The density functional theory (DFT) is one of the most successfull approach to compute the electronic structure of the surface catalyst. In fact, DFT calculations could provide a

quantitative determination of the morphology of CoMoS nanoparticles.[11] Interaction of different sulfur compounds like thiols[12], methylthiophene[13], dibenzothiophene and dimethyldibenzothiophene[14] have been reported in the literature[15]. Experimental spectroscopic proof of concept about adsorptions modes of the HDS reactants are less numerous. Some articles deal with the use of sulfur compounds as probes from the most simple thiophene to more complex like benzothiophene.[16–18] In general the interactions between thiophene and CoMoS catalysts are found extremely weak and require sorption measurement at low temperature in order to prevent from surface reaction and to enhance surface coverage. But in that case, the discrimination between molecules sorbed on the CoMoS phase or on the support becomes extremely difficult.

In order to get rid of such limitations and to go further in the CoMoS surface description, an interesting alternative methodology consists in performing *in situ* characterizations of the surface catalyst reactivity using reactants in pseudo realistic working conditions. Such characterization techniques started already in the late 80's. They require specific reactors with direct access to the catalytic bed for conventional spectroscopies (by means of well suited windows). In parallel to the analysis of the surface catalyst, products of the reactions could be also followed in order to determine catalyst activity and selectivity at a given reactants composition, temperature, pressure, time on stream and catalyst surface state, in that case we are dealing with the so-called "*operando*" approach. *In situ* and *operando* characterization methods may profit to the development of new generation of catalysts. For instance,

Few operando studies[20,21] have been devoted to HDS catalysis, but on the model of "in situ era" it represents a promising challenge, since a direct insight into the adsorption and reaction mechanisms occurring on the surface of HDS catalyst (support and sulfide phase) in 'real' HDS conditions should lead to the description and understanding of the main catalyst properties which govern the HDS activity and selectivity.

The HDS reaction is not straightforward for *operando* measurement compared to Fischer Tropsch (syngas) or DeNOx reactions (atmospheric pressure). Indeed, in the case of industrial HDS process, the reactants (i.e. a complex mixture of unsaturated and sulfur compounds) interact on high metal containing catalyst (> 20 %wt), where competitive Hydrogenation/HDS reactions occur at relatively high pressure in presence of H_2 and

formation of corrosive and toxic H_2S gas (high concentration of H_2S especially use in the sulphidation step). The literature is consequently not abundant on HDS, and we may also understand why the first building block of *operando* HDS measurement should be shifted from real to pseudo real conditions: atmospheric pressure with the use of model reactant molecules and catalysts (low metal content).

In the present work, interactions of 3-methylthiophene (3MT), model molecule representative of sulphur compounds from feedstock of FCC gasoline, have been followed by *in situ*/*operando* IR spectroscopy. Adsorption and desorption measurements have been performed in dynamic conditions by using Diffuse and Attenuated Total Reflectance approaches (DRIFT and ATR-IR). The complementarity of the two IR acquisition modes is shown and new insights into the supported CoMoS catalyst surface reactivity are brought from the spectroscopic observations.

2 Experimental

2.1 Catalysts preparation

HDS catalyst prepared is a transition metal d phase based on Co and Mo dispersed on two supports. γ-Al_2O_3 and SiO_2 supports are chosen. Alumina support are used as extrudates and silica support as pellets having respectively dimensions around 2-4 mm with diameter of 1.6mm and diameter around 0.315-1mm. Main textural characteristics of both support are resumed in Table 1. Specific surface area (S_{BET}), meso and macroporous volumes and pore diameter are presented.

Table 1. Physical properties of the γ-Al_2O_3, and SiO_2.

Supports	γ-Al_2O_3	SiO_2
S_{BET} ($m^2.g^{-1}$)	285	232
V mesopores ($ml.g^{-1}$)	0.65	0.78
Vmacropores ($ml.g^{-1}$)	0.01	0.21
Pore diameter (nm)	7-11	15

HDS catalysts are prepared by incipient wetness impregnation. Impregnation solution is prepared from MoO_3 and $Co(OH)_2$ precursors dissolved in aqueous solution in presence of H_3PO_4. Impregnation is performed on shaped support (extrudates or pellets) followed by an ageing step for 12 h to allow metal diffusion throughout the extrudate. Then, solids are dried in an oven at 393 K for 24h and calcined in air at 450 °C for 2h15. Finally, oxide catalysts are d ex situ by heating at 5 °C.min^{-1} from room temperature to 350 °C at atmospheric pressure in a flow of 15 vol.%H_2S in H_2 (1.5 $L.h^{-1}g^{-1}$ of catalyst). Sulfidation temperature is maintained at 350 °C for 2h15. The catalysts are then isolated under vacuum at 200°C before sealing in glass flask.

On each support, molybdenum loadings are selected to obtain molybdenum surface densities (called dMo) of 2.2 Mo atoms by nm^2 of support. In order to compare catalysts at the same dMo, Co/Mo and P/Mo molar ratio are also kept constant respectively 0.4 and 0.27 (Table 2).

The element contents of Co, Mo and P deposited on different supports have been analyzed by XRF to ensure that it consistent with the element content target. Table 2 summarizes the element content obtained by XRF for CoMoS catalysts before sulfidation.

Table 2. XRF analysis of the element content deposited on each oxide CoMoS/support catalyst.

Supports	dMo (at.nm-² of support)	(Co/Mo) molar	(P/Mo) molar	% Co	% Mo	% P
γ-Al_2O_3	3.8	0.39	0.26	3.19	13.48	1.12
SiO_2	3.7	0.39	0.23	2.68	11.22	0.83

2.2 Characterization

In the following, it is described the spectroscopic methodology developed for the understanding of the HDS catalyst.

A DRIFT and ATR reactor has been combined to a gas chromatographer allowing reaction products analysis (from GC) at a given surface catalyst state (from IR).

2.2.1 Injection system set-up

The liquid feedstock (3-methylthiophene referred as 3MT hereafter) is introduced by a syringe pump and vaporized into a known gas mixture by a thermostatic chamber (fixed at T = 150 – 175 °C). The gas mixture is afterwards diluted in a liquid/gas cross mixing with H_2 or Ar (used as carrier gas) and bring to the inlet of IR reactor (ATR or DR mode) via 1/8" lines heated at 150 – 175°C. The gas composition at the outlet of the reactor is analyzed by online gas chromatography. Figure 1 presents a simplified scheme of the DRIFT-GC and ATR-GC set-up unit.

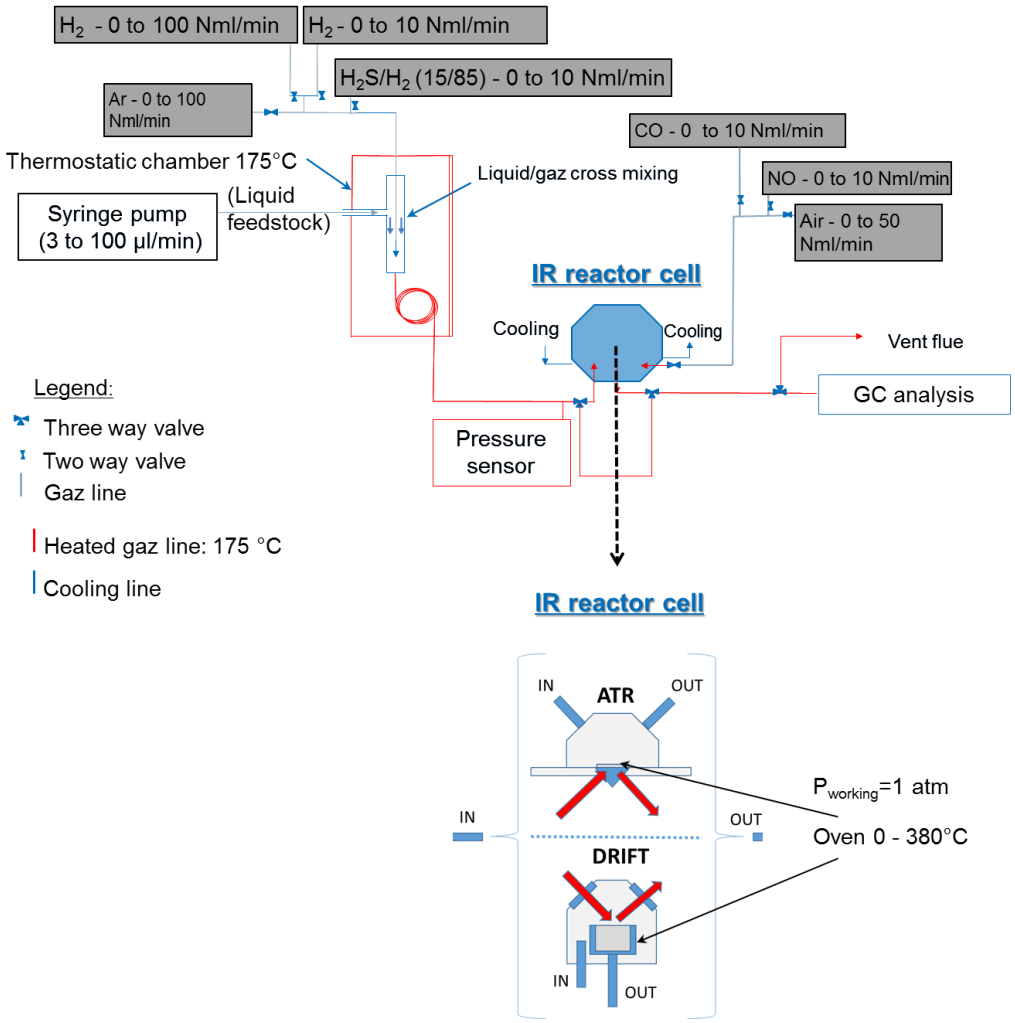

Figure 1. DRIFT-GC and ATR-GC set-up unit.

2.2.2 DRIFT spectroscopy

DRIFT experiments were performed in a commercial Praying Mantis cell from Harrick's with ZnSe windows, where meshed catalyst (250 – 350 µm) is loaded in a reactor oven. Spectra were recorded on a Vertex70 spectrometer from Bruker with a resolution of 4 cm^{-1}. Owing to the use of external mirrors, IR beam is focalized on the surface catalytic bed through windows (ZnSe, transmits in the 4000 – 600 cm^{-1}) to collect information modulating experimental conditions (gas composition, temperature) at constant atmospheric pressure.

Prior to DRIFT analysis, γ-Al_2O_3 and SiO_2 supports were activated in situ at 350°C under Ar (9 $cm^3.min^{-1}$) for 2 hours while both CoMo catalysts were sulfided in situ under H_2S/H_2 mixture (15/85 v/v, 9 $cm^3.min^{-1}$) at 350°C for 2 hours. Afterwards, the temperature of the DRIFT reactor is cooled down either i) to 120°C under Ar where 3MT is introduced (2-20.10^{-3} $cm^3.min^{-1}$) in order to follow 3MT adsorption / desorption; or ii) to 280°C under H_2

(9 $cm^3.min^{-1}$) where 3MT is introduced (1-5.10^{-3} $cm^3.min^{-1}$) to follow the catalysts surface reactivity.

2.2.3 ATR-IR spectroscopy

ATR-IR experiments were performed using a mono-reflexion Golden Gate Heated with ZnSe Lenses (from Specac). The high temperature top plate option allows sample heating from ambient to 200**°**C. In that case, finely grounded sample powder was suspended in ethanol solvent. Drops of the suspension were then evaporated on the ATR crystal in order to create a thin film. Thickness of the film has been checked in real time from the analysis of low wavenumber region due to Al-O or Si-O modes. Addition of the drops was done up to obtain a constant signal indicating that the deposited film was thick enough to solely limit the IR analysis to the solid in contact. Spectra were recorded on a Vertex70 spectrometer from Bruker with a resolution of 4 cm^{-1}.

An anvil was placed on the top of the ATR plate in order to isolate sample film. Prior to ATR-IR analysis, γ-Al_2O_3 and SiO_2 supports were treated in situ at 200°C under Ar (9 $cm^3.min^{-1}$) for 1 hour, while CoMoS/γ-Al_2O_3 catalyst were reduced in situ under H_2 (9 $cm^3.min^{-1}$) at 200°C for 1 hour. Sulphidation was done ex situ due to low working temperature range of the ATR plate RT – 200°C. After thermal treatment, the temperature of the ATR plate is cooled down under Ar to 150°C before introduction of 3MT (2-20.10^{-3} $cm^3.min^{-1}$) diluted either i) in Ar to follow 3MT adsorption / desorption from the solids; or ii) in H_2 (9 $cm^3.min^{-1}$) to follow the catalyst surface reactivity.

3 Results and discussion

3.1 In situ DRIFT

3.1.1 Alumina supported catalyst

In situ DRIFT experiments were carried out to follow the interaction of 3MT on the surface of CoMoS catalysts and corresponding γ-Al_2O_3 support (Figure 2 and Figure 3). Introduction of 3MT in the DRIFT reactor leads to the progressive appearance of additional contributions compared to 3MT gas phase due to the interaction of 3MT on the surface of the solids at 120°C (Figure 2 and Figure 3). After activation at 350°C, alumina support exhibits two distinct contributions centered at 3723 and a shoulder 3775 cm^{-1} in the hydroxyl region (Figure 3. A). The diminution of these OH vibration bands is not accompanied with a corresponding

increase in the 3600 - 3400 cm^{-1} region, which indicates that the consumption of OH groups is not simply due to 3MT hydrogen bonding perturbation, but more likely due to the chemical interaction or even a reaction of 3MT on OH groups at 120°C. Indeed corresponding spectra in the low wavenumbers region show IR contributions centered at 1692 and 1592 cm^{-1} which were not present on the free 3MT gas phase spectrum (Figure 4C). Note that for more information, the reader may refer to vibrational frequencies of pure 3MT in liquid phase reported in supporting information. The contribution at 3100 – 3070 cm^{-1} is still present which may indicate that the thiophene ring is preserved after interaction with γ-Al_2O_3, however the modification in the profile shapes in the 3000 – 2800 and 1000 – 600 cm^{-1} regions point out the formation of new surface species. Indeed, the progressive increase of these regions as function of time may suggest that polymerization occurs at the surface[22–25]. Hence, the weak acidity of the hydroxyl groups (already discussed in the previous chapters) confers to γ-Al_2O_3 a specific surface reactivity towards 3MT.

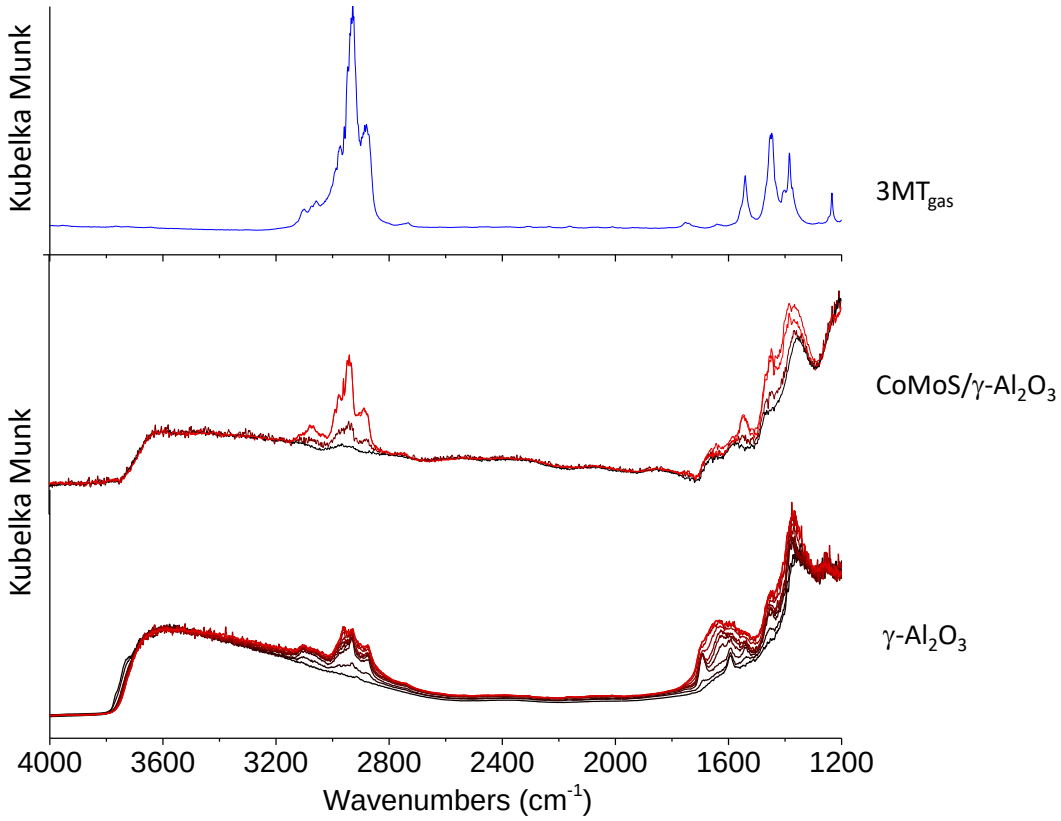

Figure 2. Evolution of the DRIFT spectra as a function of 3MT contact time on γ-Al_2O_3 and CoMoS/γ-Al_2O_3. 3MT adsorption is done at 120°C and atmospheric pressure during 4h (from black to red spectrum). For comparison, DRIFT spectrum of 3MT gas phase is reported in blue on the top.

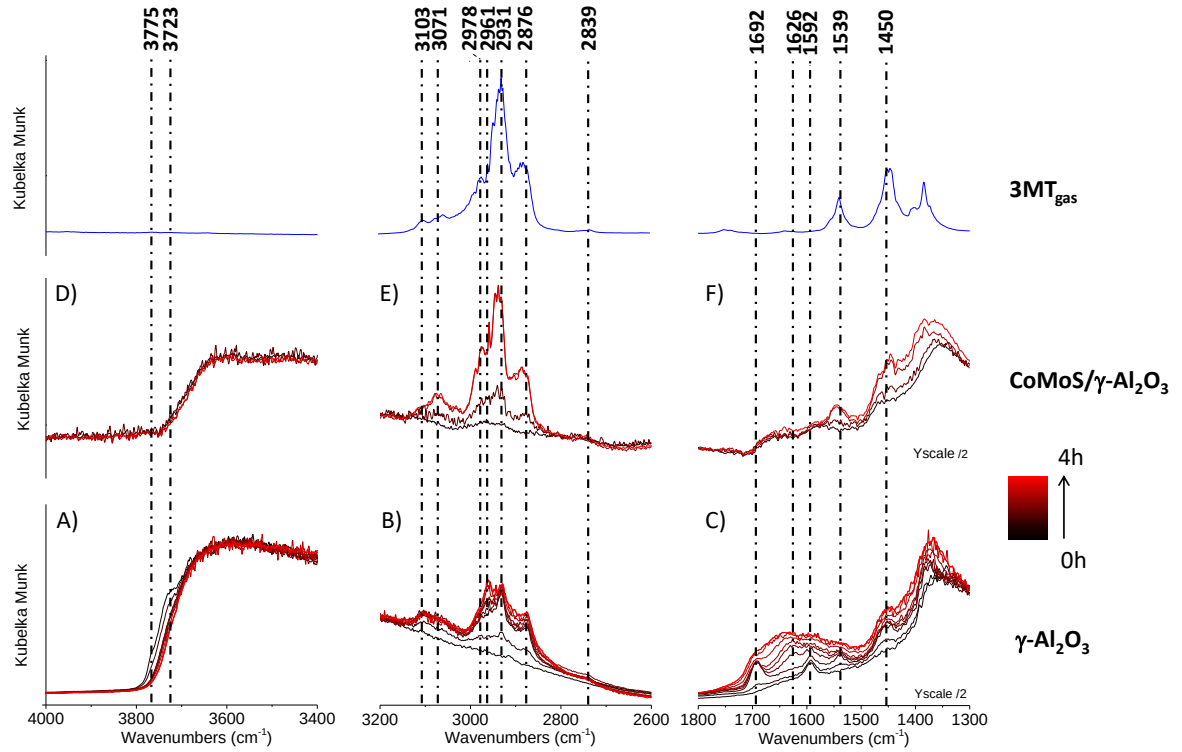

Figure 3. Comparison of the evolutions of the DRIFT spectra of 3MT adsorption as a function of contact time on (A-C) γ-Al_2O_3 and on (D-F) CoMoS/γ-Al_2O_3. 3MT adsorption is done at 120°C and atmospheric pressure during 4h (from black to red spectrum) at a rate of 0.005 $cm^3.min^{-1}$ of 3MT diluted in 9 $cm^3.min^{-1}$ of Ar. For comparison, DRIFT spectrum of 3MT gas phase is reported in blue on the top.

Synchronous 2D-correlation map of γ-Al_2O_3 support during the 3MT adsorption (Figure 4) shows the correlation between the vibrational band of the hydroxyl groups and the vibrational band of 3MT in the CH and CC vibrational band regions. It can be noted that hydroxyls are consumed or perturbed (decline of the vibrational around 3750 cm^{-1}) at the profit of species formed at the surface (increase of vibrational contributions between 1400 and 1800cm^{-1}).

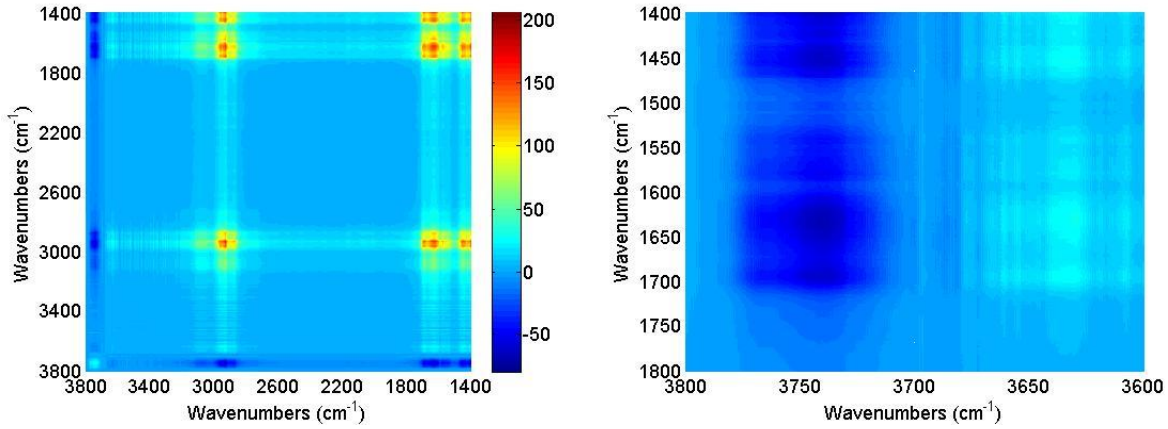

Figure 4. 2D-correlation map of γ-Al_2O_3 support during 4 h of 3MT adsorption at 393 K (A) the correlation between the evolution of the OH and CH and CC vibrational regions bands and (B) only the correlation between the evolution of the OH and CC vibrational regions bands. Negative (positive) correlation peaks, in blue (in red), mean that the two correlated frequencies evolve in opposite directions (in the same direction).

IR spectra obtained for CoMoS/γ-Al_2O_3 supported catalyst report a low signal to noise ratio due to the dark color of the catalyst after sulphidation (Figure 2). Profile shape of the contributions observed after 3MT introduction is pretty close to that of 3MT gas phase. In that case, most of surface aluminols are at the interface between bulk γ-Al_2O_3 support and CoMoS slabs which limits their further interaction with 3MT. A small contribution is nevertheless observed at 1800 – 1600 cm^{-1} possibly due to residual alumina surface not covered by the CoMoS phase in interaction with 3MT. The main spectral contributions observed are due to 3MT molecules. The full width at half maximum (FWHM) of the components are larger than that of the gas phase, which indicate that the signal is due to 3MT weakly adsorbed species. In addition, it is interesting to note that the $C_\alpha H$ and $C_\beta H$ stretching modes between 3110 and 3050 cm^{-1} are different between the gas phase and the CoMoS/γ-Al_2O_3. It is observed a diminution of the $C_\alpha H$ band in favor of an increase of the $C_\beta H$ band. It could be due to the close spatial proximity of the $C_\alpha H$ with CoMoS phase, resulting in lower molar extinction coefficient of $C_\alpha H$ stretching mode, and /or a lower strength of the C-H bond which overlapped with the $C_\beta H$ band after the adsorption of 3MT by its S atom.

The reversibility of 3MT adsorption has also been checked by *in situ* DRIFT spectroscopy. Figure 5 reports the evolution in the DRIFT spectra after flushing to pure Ar flow at 120°C.

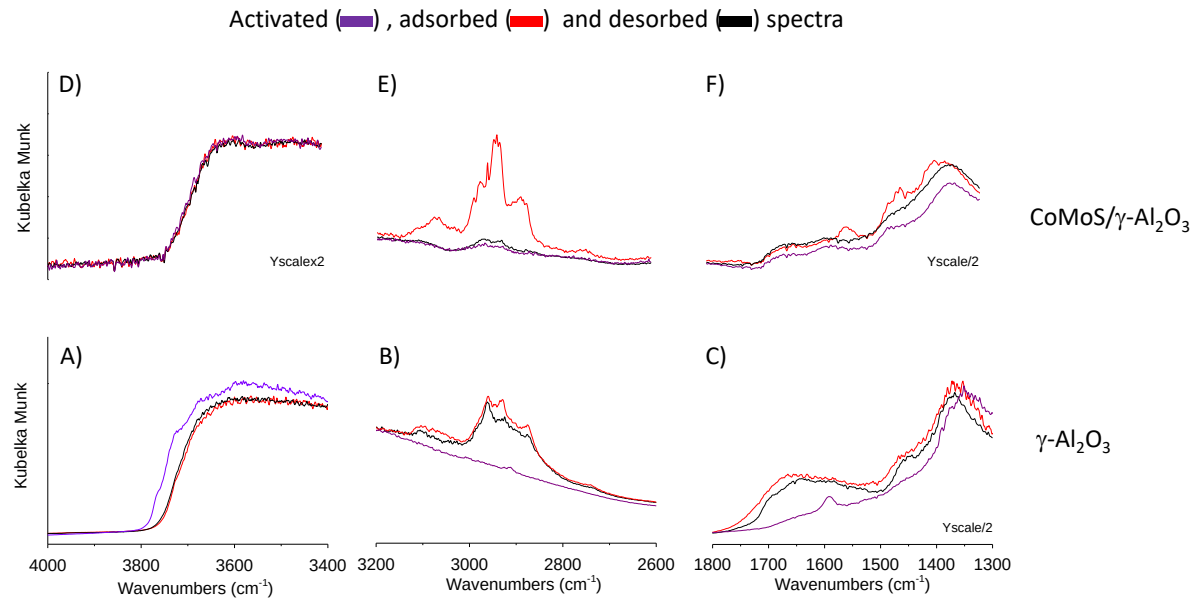

Figure 5. Comparison of the evolutions in the DRIFT spectra as a function of desorption time on (A-C) γ-Al_2O_3 and on (D-F) CoMoS/γ-Al_2O_3. 3MT adsorption (red spectra) and desorption (black spectra) are done at 120°C and atmospheric pressure during 4h at a rate of 0.005 $cm^3.min^{-1}$ of 3MT diluted in 9 $cm^3.min^{-1}$ of Argon. Activated spectra (before the adsorption step) under argon at 120°C is in purple.

The adsorption of 3MT under CoMoS/γ-Al_2O_3 catalyst is shown to be almost totally reversible, since the CH modes of thiophenic compound almost disappear after purging under Ar at 120°C. It confirms the relatively low interaction of 3MT over the CoMoS phase (residual broad contributions at lower wavenumbers are nevertheless observed). On the other hand, 3MT desorption from γ-Al_2O_3 is not reversible. In that case, hydroxyls are not recovered after 5h desorption. This is consistent with the formation of new strongly chemisorbed surface species on the γ-alumina support.

3.1.2 Silica supported catalyst

Similar DRIFT adsorption/desorption experiments have been performed on CoMoS/SiO_2 and corresponding silica support (Figure 6 to Figure 8). Low frequency region (< 1200 cm^{-1}) related to the fingerprint and overtone structure vibration of silica support is not reported due to the strong absorbance.

After 3MT contact on silica support, part of the SiOH are perturbed (Figure 7 A). A broad component at 3620 cm^{-1} appears due to the hydrogen bonding interaction of 3MT on accessible silanols. The interaction of 3MT is weak and the contributions observed in the stretching ν_{CH} region almost match with 3MT IR gas phase spectrum (2600-3200 cm^{-1}).

Considering the adsorption on $CoMoS/SiO_2$ catalyst (Figure 7C-D), it is interesting to notice that sulfided catalyst exhibits still intense and distinct free silanols contribution at 3750 cm^{-1}. It may indicate that the CoMoS slabs are not well dispersed on the surface of SiO_2 support or do not cover totally it. Even if the Mo surface density is close to that of alumina supported catalyst (Table 2), the length of the slab and stacking are expected to be larger on SiO_2 than on alumina oxide (Chapter IV). A more detailed analysis in the 3200 – 2600 cm^{-1} region, reveals that aromatic CH contributions are present after activation due to possible contamination from impurities present in the gas lines. The interpretation after 3MT introduction is thus made more difficult, since this latter contribution overlaps with those due to 3MT. Nevertheless, it seems that 3MT interaction on $CoMoS/SiO_2$ surface leads to a less intense $\nu_{CH,aro}$ (at 3050 cm^{-1}) compared to the reference silica support.

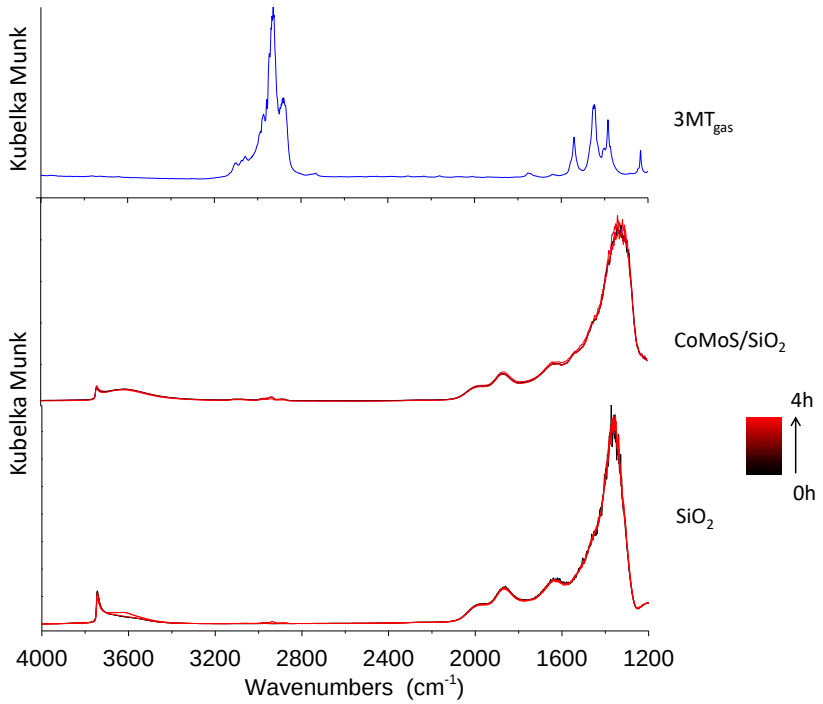

Figure 6. Evolution in the DRIFT spectra as a function of 3MT contact time on SiO_2 and $CoMoS/SiO_2$. 3MT adsorption is done at 120°C and atmospheric pressure during 4h. For comparison, DRIFT spectrum of 3MT gas phase is reported in blue on the top.

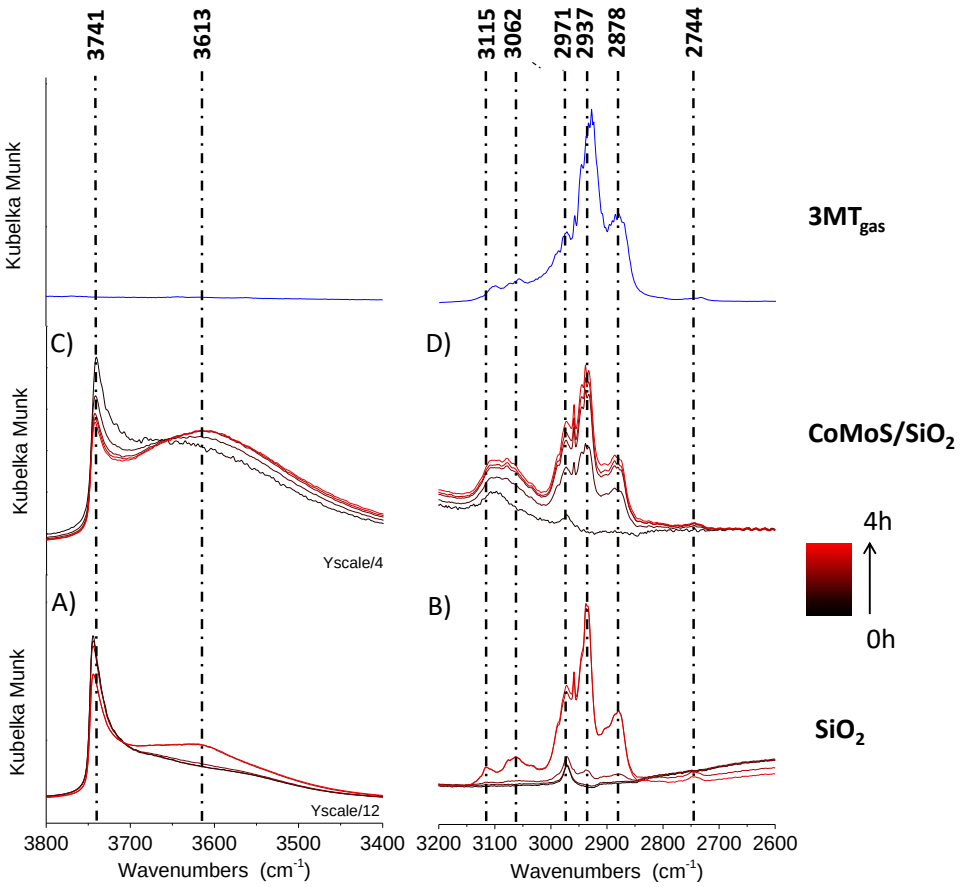

Figure 7. Comparison of the evolutions in the DRIFT spectra as a function of 3MT contact time on (A-B) SiO_2 and on (C-D) $CoMoS/SiO_2$. 3MT adsorption is done at 120°C and atmospheric pressure during 4h. For comparison, DRIFT spectrum of 3MT gas phase is reported in blue on the top.

In contrast with γ-Al_2O_3 support (Figure 5 A-B), the adsorption of 3MT on SiO_2 is almost reversible upon DRIFT reactor evacuation under Ar (Figure 8 A-B). While 3MT adsorption on SiO_2 occurs mainly through hydrogen bonding interactions, on alumina the 3MT molecule could interact on coordinately unsaturated Al^{3+} sites produced after thermal activation at 350°C.

Similarly to alumina supported CoMoS, the 3MT desorption from CoMoS supported on silica is found reversible with total recovering of initial silanols and little changes in the CH region. One could at first conclude that the surface reactions at 120°C are very limited between 3MT molecules and the sulfided phase. At this stage, one should admit that it is clearly difficult to demonstrate the 3MT adsorption on the CoMoS active phase by DRIFT methodology, since the interactions between the sulfur compound and surface sites remain weak and if present, the expected contributions would be probably hidden by those due to the gaseous species,

and the molar extinction coefficient of the adsorbed species on the CoMoS phase could be very low.

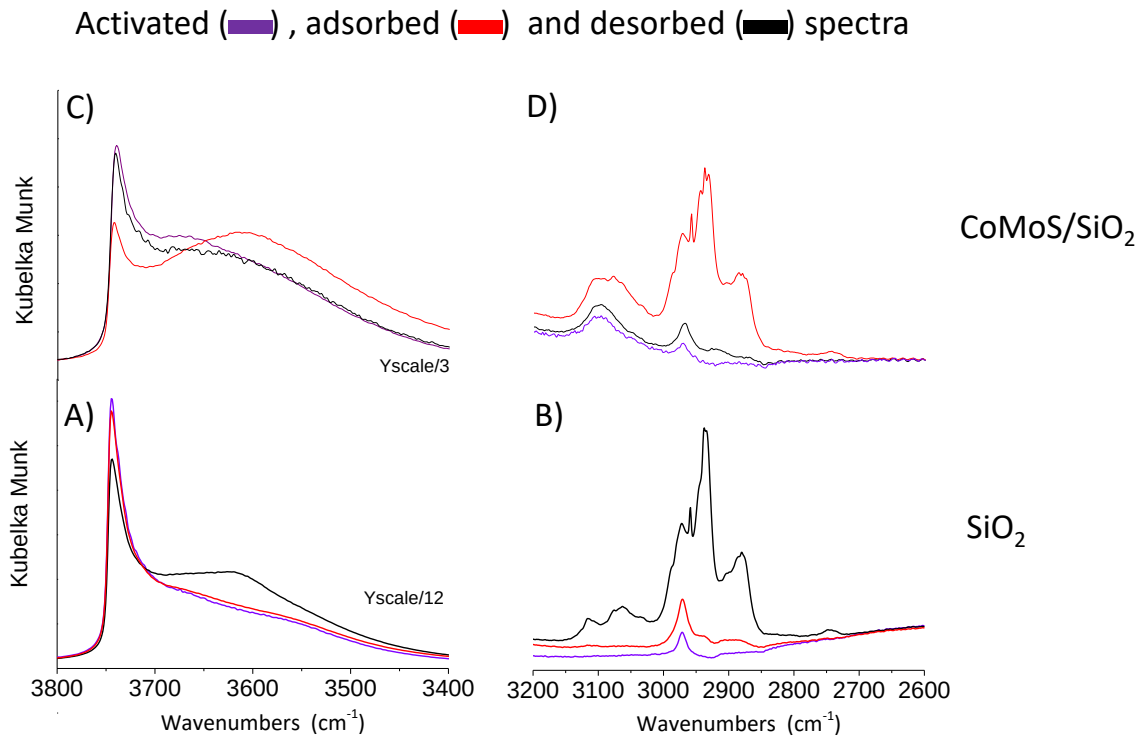

Figure 8. Comparison of the evolutions in the DRIFT spectra as a function of 3MT desorption time on (A-B) SiO_2 and on (C-D) $CoMoS/SiO_2$. 3MT adsorption (red spectra) and desorption (black spectra) are done at 120°C and atmospheric pressure during 4h at a rate of 0.005 $cm^3.min^{-1}$ of 3MT diluted in 9 $cm^3.min^{-1}$ of Argon. Activated spectra (before the adsorption step) under argon at 120°C are in purple.

3.2 Operando DRIFT Reaction of 3MT on CoMoS/γ-Al_2O_3

In order to probe the CoMoS surface reactivity, H_2 has been introduced in the reactor in presence of 3MT. CoMoS catalyst supported on alumina has been selected since this catalyst displays a better dispersion and a higher HDS activity is expected. DRIFT-GC operando measurements have been conducted at 280 °C (typical temperature range used in HDS process) at two different molar ratios of n_{H2}/n_{3MT} = 8 and 38 (5 and 1 µL/min of 3MT in 9 mL/min of H_2). This ratio is low compared to conventional ratio uses in HDS catalytic test n_{H2}/n_{3MT} > 500, because of the working pressure and flow meters limitations of the DRIFT cell.

Introduction of 3MT at n_{H2}/n_{3MT} = 38 on the surface of CoMoS catalyst leads to IR contributions close to those observed for 3MT gas phase (Figure 9). Even after decreasing the molar ratio up to n_{H2}/n_{3MT} = 8, it is difficult to shed light on the products of reaction from those due to the thiophenic reactant by comparing the vibrational contributions with that for the 3MT gas phase(Figure 9). Hence, 3MT gas phase present in the reactor may still overshadow the contribution due to adsorbed species. At 280 °C, the level of 3MT conversion measured from GC analysis in outlet of the DRIFT reactor is close to 50%, but no spectral contribution due to any products or intermediates formed is observed (even gaseous). It may be due to the pathway followed by the gases: from the top to the bottom of the catalytic bed reactor, where GC analysis is afterwards done. In that configuration, gas composition at the top of the cell analyzed by the IR beamlight is mainly 3MT (and H_2, non IR active). Gas flow has been used in that direction in order to limit the catalyst powder to fly away from the basket oven when switching the valves.

DRIFT analysis has also been carried out in static conditions, i.e. batch experiment, at 280 °C after feeding the reactor with 3MT/H_2 gas phase at a molar ratio of n_{H2}/n_{3MT} = 38 (Figure 9).

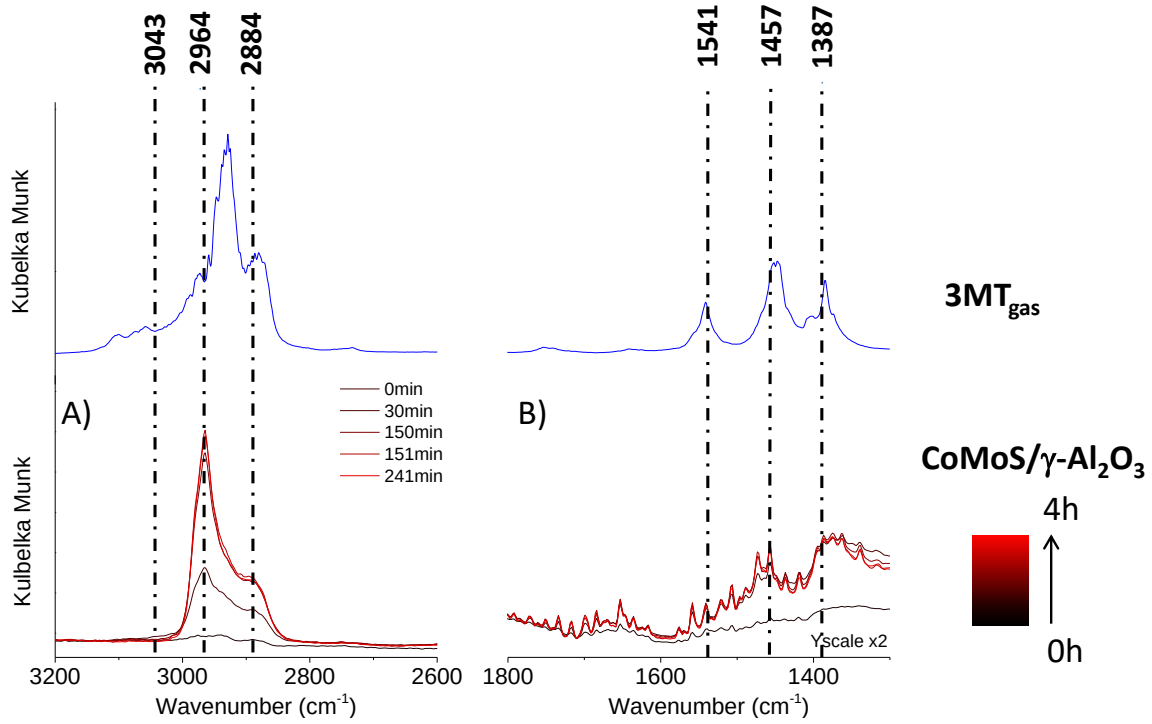

Figure 9. Evolution of the DRIFT spectra in static conditions as a function of reaction time of 3MT/H_2 mixture (n_{H2}/n_{3MT} = 38) on CoMoS/γ-Al_2O_3 at 280 °C and atmospheric pressure (from black to red yellow spectrum). For comparison, spectrum of 3MT gas phase is reported in blue on the top.

After 2 h at 280 °C, the IR profile shape spectrum is drastically modified with the disappearance of the IR bands corresponding to aromatic CH (ν_{CH} 3100 – 3000 cm^{-1}) and C=C (ν_{CC} at 1540 cm^{-1}). It indicates that the hydrogenation of 3MT proceeds. Simultaneously, an intense contribution centered at 2964 cm^{-1} and additional components at lower wavenumbers 1470-50 and 1386 cm^{-1} are observed possibly assigned to the formation of 3-methyl di- or tetra-hydrothiophenic compounds resulting from the partial hydrogenation of 3MT. [26]

At 280 °C, these products of reactions are in weak interaction on the surface catalyst. Formation of byproducts species remaining adsorbed at the surface of the catalyst cannot be discarded, but their concentrations are maybe too low (compared to gaseous products) to be detected in the fingerprints region.

3.3 Insights into surface species by ATR-IR

According to the previous analysis, *in situ* and *operando* characterizations of the surface of CoMoS catalyst by the means of DRIFT spectroscopy remains challenging, since diffuse reflectance mode does not selectively focus on the analysis of the catalyst surface. Indeed gas phase is also contained in the resulting spectrum (vide supra). Moreover, it is difficult to get information at low wavenumbers due to intense vibration mode of Al-O bond of alumina oxide (Figure 2). Attenuated total reflectance mode could override such limitations. In that case, the solid to be analyzed is deposited in intimate contact on the surface of an internal reflectance element (IRE, diamond). The depth of the IR evanescent wave propagating in the solid is dependent of the wavelength and reflective index of the solid, but it does not cross the sample thickness. Hence, ATR mode minimizes the contribution of the gas phase and maximizes those due to the solid and interfaces between solid/gas.[27] *In situ* ATR-IR technique remarkably sensitive to surface species has been used in order to solely evidence the surface mechanisms occurring on Al_2O_3 and CoMoS/Al_2O_3 catalyst in interaction with 3MT (Figure 10).

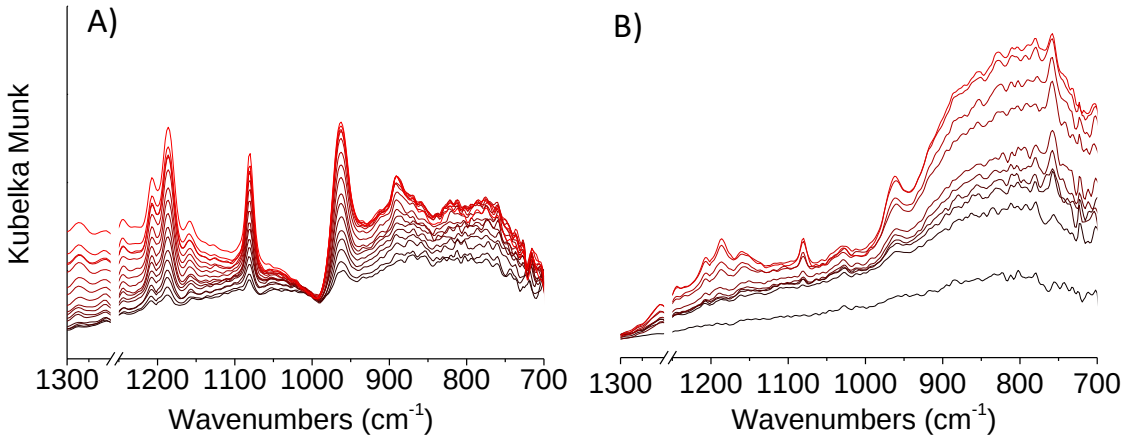

Figure 10. Evolution in the ATR-IR spectra (background subtracted) as a function of 3MT contact time (up to 4 h) at 150 °C and atmospheric pressure (from 5 up to 15 µl/min of 3MT diluted in 9 mL/min Ar) on A) γ-Al_2O_3 and B) CoMoS/γ-Al_2O_3 previously activated at 200 °C; (from black to red spectrum) in the CS and CC region between 1300 and 700 cm^{-1}.

3MT interaction on alumina surface progressively modifies ATR-IR spectrum with contributions centered at 1207, 1186, 1080, 962 and 870(sh) cm^{-1} (Figure 10 A). These components are very close to those observed on 3MT (gas and liquid phases) and indicate that reactions are rather limited on alumina after activation at 200 °C (temperature max reached by the ATR plate), in contrast to alumina annealed at 350°C (DRIFT mode, Figure 3 B-C). In this latter case, the strongly bounded species originates from the surface reactivity of dehydroxylated alumina, where Lewis acidity of surface alumina may lead to the progressive polymerization of 3MT.

ATR-IR spectra after 3MT contact on CoMoS/γ-Al_2O_3 (pre-reduced at 200 °C under H_2) show similar features than the corresponding reference support but in a less extent (Figure 10 B). Introduction of the metal sulfide phase diminishes available sites for 3MT interaction. The variation in the baseline is due to the modification of the refractive index of the solid upon 3MT interaction. The depth of penetration of the evanescent wave into the material increases and Al-O vibration modes (below 1000 cm^{-1}) become gradually more and more intense. In both cases, 3MT sorption is not reversible upon purging under Ar gas at 150 °C (not shown) and may discard hydrogen bonding interactions type.

In situ ATR-IR analysis of 3MT reaction on surface catalyst has been performed in presence of H_2 (Figure 11). Evolution of the gaseous products formed cannot be determined by GC

due to the too low conversion level (ca. 1 mg of catalyst is placed on the heated ATR crystal, corresponding to extremely low reactant contact time).

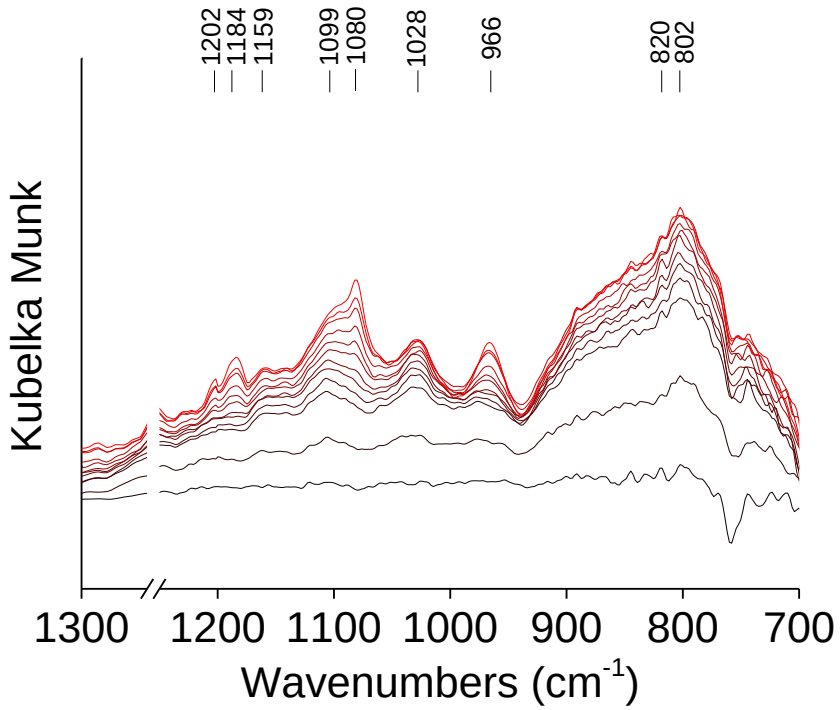

Figure 11. Evolution in the ATR-IR spectra (background subtracted) as a function of reaction time of 3MT/H_2 mixture (n_{H2}/n_{3MT} = 4) on CoMoS/γ-Al_2O_3 at 150 °C and atmospheric pressure (from black to red spectra during 5h30) in the CS and CC region between 1300 and 700 cm^{-1}.

Spectra of CoMoS/γ-Al_2O_3 surface (pre-reduced at 200 °C under H_2) in interaction with 3MT/H_2 gas mixture show several components centered at 1200, 1180, 1080, 960 cm^{-1} and a large massif at lower wavenumber due to the alumina support (Figure 11). In addition two bands centered at 1100 and 1020 cm^{-1} appear in the spectra (not observed for alumina support and CoMoS without H_2). These two bands grow at first in the IR spectra and may originate either i) from the formation of new surface products resulting from the transformation of 3MT on the surface of the CoMoS phase in presence of H_2, either ii) from the interaction of 3MT on coordinatively unsaturated sites of CoMoS phase generated by the presence of H_2, or iii) both phenomena. The small changes observed in IR spectra compared to the experiment without H_2 (Figure 10A), may favor hypothesis ii), where the presence of H_2 would enhance 3MT surface coverage of the CoMoS phase. Thiophenic compounds interaction on CoMoS slabs is generally favored on sulphur edges sites (S-edge)[13] by their

S-atoms. Even if the concentration of sites located at the S-edges of the slabs is not high, ATR mode is sufficiently sensitive to evidence 3MT sorption on the CoMoS phase.

4 Conclusion and perspectives

FTIR spectroscopy has been used to follow the interactions of 3-methylthiophene (3MT), model molecule representative of sulphur compounds from feedstock of FCC gasoline on the surface of promoted CoMoS catalysts supported on alumina or silica. Different acquisition modes (diffuse and attenuated total reflectance; DRIFT and ATR) have been used in order to evidence by IR the surface mechanisms occurring while the catalysts are interacting with 3MT.

At first, *in situ* DRIFT experiments have been performed to follow adsorption and subsequent desorption of 3MT from SiO_2 and γ-Al_2O_3 supports and sulfided catalysts. While 3MT adsorption on SiO_2 support and both catalysts (CoMoS/SiO_2 and CoMoS/ γ-Al_2O_3) is found reversible upon evacuation, γ-Al_2O_3 support reports additional spectral features due to the formation of new species which are thermally stable. The weak acidity of the hydroxyl groups confers to γ-Al_2O_3 surface a specific reactivity towards 3MT, where polymerization mechanisms could occur. Description of surface species on CoMoS phase in diffuse reflectance is clearly difficult, since the interactions between the 3MT sulfur compound and surface sites remain weak and if present, the expected contributions are hidden by those due to the gaseous species.

In situ ATR-IR technique has been used in order to minimize the contributions of the 3MT gas phase and to maximize those due to the adsorbed surface species. ATR-IR spectra obtained for γAl_2O_3 in contact with 3MT (diluted in inert gas) shows contributions due to polymerized species in agreement with DRIFT experiments. No additional IR component is observed when CoMoS/γ-Al_2O_3 catalyst is interacting with 3MT, which at first indicates that the surface species are similar than those observed on γ-Al_2O_3 but also that they are located on alumina surface sites. As a consequence, the ad-species concentration is lower on the catalyst, since CoMoS phase covers part of the γ-Al_2O_3 surface. ATR-IR spectra recorded after introduction of 3MT in presence of H_2 on the surface of the catalyst exhibit new contributions, which may originate from the adsorption of 3MT on coordinatively unsaturated sites present on the surface of the CoMoS phase.

Moreover, ATR-IR spectroscopy seems to be sensitive for *in situ* characterization of adsorbed surface species on CoMoS phase. In perspectives to this work, it would be very interesting to get closer to the real conditions of HDS process. Unlike DRIFT set-up, increasing the working pressure will not limit ATR-IR characterization of the catalyst surface since the gas phase is not measured in ATR mode. In order to fulfill *operando* methodology, modification of the set-up would be necessary to be able to measure the catalytic performances (increase the volume of the catalytic bed, and/or contact time).

5 Appendices

Appendix 1: Model molecule

3 methyl-thiophene (3MT) was chosen as representative model molecule of the sulphur compounds in the Fluid Catalytic Cracking feedstock. Spectra of 3MT in liquid and gas phase were recorded respectively by ATR and DRIFT measurements (Figure 12). Each vibrational contribution of 3MT and relative intensity is reported in Table 3. It can be noted that the 3MT vibrational contributions recorded in ATR and DRIFT are consistent with previous work conducted by Hernandez et al.[28] in which each experimental vibrational band of 3MT bonds in liquid was assigned by performing molecular modeling. Three frequency ranges can be distinguished: one between [3150-2700] cm^{-1} related to the vibrational frequency of the CH bonds, a second [1700-1200] cm^{-1} related essentially to the vibrational frequency of the single and double CC bonds and single CS bond and the third [900-500] cm^{-1} related essentially to the vibrational frequency of the single CS bond and the CC bond engaged on the aromatic ring. The Intensity of 3MT vibrational contributions is lower in ATR spectra (mono-reflexion) than in DRIFT spectra but well defined. Moreover, the relative intensity of the frequency range between [3900-1800] and [1800-400] cm^{-1} are different in ATR and DRIFT. Indeed, in ATR, the depth of penetration is inversely proportional to increasing wavelength. Therefore, contributions at low wavenumbers [1800-400] cm^{-1} will be more evidenced in ATR than in diffuse reflectance mode.

Table 3. Free vibrational contributions of 3MT in liquid obtained using FT-IR by Hernandez et al.[29] and 3MT in liquid and gas obtained respectively using DRIFT and ATR at atmospheric pressure and respectively at 120°C and room temperature. Relative intensity of each contribution is described as strong (s), medium (m), and weak (w).

FT-IR (liquid) [28]		DRIFT (gas)		ATR (liquid)	
$\nu_{experimental}$ liquid phase (cm^{-1})	Vibrational attribution[a]	$\nu_{experimental}$ (cm^{-1})	Intensity[b]	$\nu_{experimental}$ (cm^{-1})	Intensity[b]
3101	$\nu_{C□H}$	3101	w-m	3101	m
		3078	w-m		
3056	$\nu_{C□H}$	3057	w-m	3056	w
2971	$\nu_{a,CH3}$	2973	m	2969	m
-	-	2958	m		
2945	$\nu_{a,CH3}$	2947	s	2945	m
		2938	s		
2923	$\nu_{s,CH3}$	2927	s	2922	s
2890	$\delta_{a,CH3}$	2889	m	2889	w
2867	$\delta_{a,CH3}$	2875	w	2866	m
2732	$\delta_{s,CH3}$	2734	w	2732	w
1753	$\delta_{CH} + \gamma_{CH}$	1752	w	1752	vw
1642	$2\nu_{s,CS}$	1641	w	1643	vw
1563	$R_{CH3} + \delta_{ring}$	-	-	-	-
1542	$\nu_{a,C=C}$	1541	w	1541	m
1452	$\delta_{a,CH3}$	1453	m	1452	m
1447	$\delta_{a,CH3}$	1445 (shoulder)	m	1447	w-m , shoulder
1408	$\nu_{s,C=C}$	1404	m , shoulder	1407	m
1385	$\delta_{s,CH3}$	1384 (with shoulder at	s	1385	m

		higher and lower wavenumbers)			
1373	ν_{CC}	1373	w , shoulder	1373	m , shoulder
1276	$\nu_{C\text{-}S} + \gamma_{ring}$	1279	vw	1276	vw
1234	δ_{CH}	1234	m	1235	m
1201	$2\gamma_{ring}$	1201	vw	1200	vw
1155	δ_{CH}	1154 (m) (with shoulder at higher wavenumbers)	m	1155	m
1080	δ_{CH}	1080	m	1081	m
-	-	1051	w		
1036	r_{CH3}	1037	w	1036	w
993	r_{CH3}	992	m	992	w
931	ν_{CX}	930	m	930	w
914	$2\delta_{ring}$	910	w	914	vw
877	γ_{CH}	898	w		
857	$\nu_{a,C\text{-}S}$	859	s	857	m
830	$\nu_{s,C\text{-}S}$	829	s	829	m
762	γ_{CH}	-	-	760	s
685	γ_{CH}	-	-	684	m
659	δ_{ring}	-	-	660	w
594	δ_{ring}	-	-	591	s
542	δ_{ring}	-	-	542	w
464	γ_{ring}	-	-	-	-

[a] Vibrational modes: ν, stretching ; δ,bending ; *r,* rocking ; σ, torsion. [b] s: strong, m: medium, w: weak, vw: very weak.

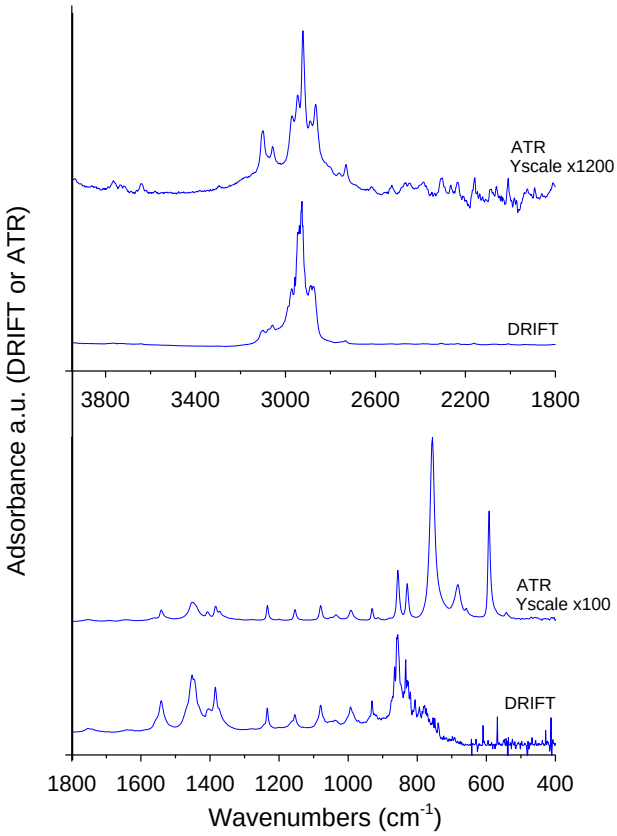

Figure 12. DRIFT and ATR infrared spectra of 3MT respectively in liquid and gas. Y scale of ATR spectra is multiplied by 1200 and 100 respectively in the range region between 3900 and 1800 cm^{-1} and between 1800 and 400 cm^{-1}. ATR spectra of 3MT is recorded at room temperature and 1 atm. DRIFT spectra of 3MT is recorded at 120°C and 1 atm.

6 References

[1] B. Didillon, D. Uzio, N. Marchal, *Procédé de Production D'essences à Faible Teneur En Soufre*, **2001**.

[2] J. T. Miller, W. J. Reagan, J. a. Kaduk, C. L. Marshall, a. J. Kropf, *J. Catal.* **2000**, *193*, 123–131.

[3] J. Wu, C. Bai, T. Halbert, S. Soled, S. Miseo, *Selective Catalysts Having Silica Supports for Naphtha Hyddrodesulfurization*, **2007**, WO 2007/084439 A1.

[4] L. van Haandel, M. Bremmer, P. J. Kooyman, J. a. R. van Veen, T. Weber, E. J. M. Hensen, *ACS Catal.* **2015**, 7276–7287.

[5] N.-Y. Topsoe, H. Topsoe, *J. Catal.* **1983**, *84*, 386.

[6] N.-Y. Topsøe, H. Topsoe, *J. Catal.* **1982**, *75*, 354–374.

[7] N. Y. Topsoe, E. Al., *J. Catal.* **2011**, *279*, 337–351.

[8] B. Mueller, A. D. van Langeveld, J. A. Moulijn, H. Knoezinger, *J. Phys. Chem.* **1993**, *97*, 9028–9033.

[9] A. Travert, C. Dujardin, F. Mauge, E. Veilly, S. Cristol, J. Paul, E. Payen, **2006**, 1261–1270.

[10] F. Maugé, A. Vallet, J. Bachelier, J. C. Duchet, J. C. Lavalley, *J. Catal.* **1996**, *162*, 88–95.

[11] E. Krebs, a. Daudin, P. Raybaud, *Oil Gas Sci. Technol. - Rev. l'IFP* **2009**, *64*, 707–718.

[12] T. TODOROVA, R. PRINS, T. WEBER, *J. Catal.* **2007**, *246*, 109–117.

[13] E. Krebs, B. Silvi, a. Daudin, P. Raybaud, *J. Catal.* **2008**, *260*, 276–287.

[14] S. Cristol, J.-F. Paul, E. Payen, D. Bougeard, F. Hutschka, S. Clémendot, *J. Catal.* **2004**, *224*, 138–147.

[15] J.-F. Paul, S. Cristol, E. Payen, *Catal. Today* **2008**, *130*, 139–148.

[16] J. Zhang, W. Yin, H. Shang, C. Liu, *J. Nat. Gas Chem.* **2008**, *17*, 165.

[17] T. L. Tarbuck, K. R. Mccrea, J. W. Logan, J. L. Heiser, M. E. Bussell, W. Washington, V. Uni, **1998**, *5647*, 7845–7857.

[18] C. H. Mitchell, A. Green, E. Payen, J. Tomkinson, F. Parker, *Phys. Chem. Chem. Phys.* **1999**, *1*, 3357.

[19] G. Delahay, A. Guzmán-Vargas, B. Coq, *Appl. Catal. B Environ.* **2007**, *70*, 45–52.

[20] M. De Pontes, R. L. Espinoza, C. P. Nicolaides, J. H. Scholz, **1997**, *107*, 187–192.

[21] J. Scalbert, I. Clémençon, P. Lecour, L. Braconnier, C. Legens, *Catal. Sci. Technol.* **2015**,

5, 4193–4201.

[22] F. Bauer, H. G. Karge, *Mol. Sieves - Sci. Technol.* **2006**, *5*, 249–364.

[23] J. A. Juárez, J. Ancheyta, *Deactivation of Heavy Oil Hydroprocessing Catalysts: Fundamentals and Modeling*, New Jersey, **2016**.

[24] E. G. Derouane, V. Parmon, F. Lemos, F. R. Ribeiro, *Sustainable Strategies for the Upgrading of Natural Gas: Fundamentals, Challenges, and Opportuities*, Dordrecht, **2006**.

[25] Z. Sarbak, *React. Kinet. Catal. Lett.* **2000**, *69*, 117.

[26] I. Bezverkhyy, K. Bouguessa, C. Geantet, M. Vrinat, *Appl. Catal. B Environ.* **2006**, *62*, 299–305.

[27] B. L. Mojet, S. D. Ebbesen, L. Lefferts, *Chem. Soc. Rev.* **2010**, *39*, 4643–4655.

[28] V. Hernandez, F. J. Ramırez, J. Casado, J. T. L. Navarrete, *J. Phys. Chem.* **1996**, *100*, 2907–2914.

[29] P. Schacht, G. Hernandez, L. Cedeno, J. H. Mendoza, S. Ramirez, L. Garcia, J. Ancheyta, *Energy and Fuels* **2003**, *17*, 81–86.

- General Conclusions and Perspectives -

- General Conclusions and perspectives -

Preliminary notes: for sake of clarity, and to avoid redundancies, perspectives are directly written in italic after each main set of conclusions.

Within this research work, catalysts based on the CoMoS active phase supported on three different supports, γ-Al_2O_3, $\delta\theta$-Al_2O_3 and SiO_2 were the subject of a comprehensive study of hydrodesulfurization and hydrogenation. The main objective was to evaluate the respective role of the CoMoS active phase and of the support:

- sizes, 2D and 3D (stacking) morphology, active sites speciation of the CoMoS particles
- acido-basicity of the supports, morphology of the supports platelets

We pay particular attention on the possible interplay between each of them in order to attempt to streamline the catalytic performances: HDS activity as well as HDS/HYDO selectivity.

As a first step, a large set of experimental data was collect by performing high pressure catalytic test in order to evaluate the HDS activity and selectivity of well-defined CoMoS supported catalysts.

CoMoS phase supported on γ-Al_2O_3, $\delta\theta$-Al_2O_3 and SiO_2 were prepared at different Mo coverage (dMo, molybdenum surface density by nm² of support) from 0.9 to 3.8 at.nm^{-2} with a Co/Mo atomic ratio constant equal to 0.4 in order to investigate the support effect and the impact of the dMo on the activity and the selectivity. CoMoS on $\delta\theta$-Al_2O_3 and SiO_2 was prepared at atomic Co/Mo ratio from 0 (unpromoted catalyst) to 0.4 at iso-dMo of 2.2 at.nm^{-2} in order to explore the atomic Co/Mo ratio and Co-promoter effects on the activities and the selectivity.

It has been demonstrated that the Co-promoted MoS_2 on $\delta\theta$-Al_2O_3 and SiO_2 provide a higher HDS/HYDO selectivity than the unpromoted equivalent catalyst. The reason of the decline of the selectivity over the unpromoted catalyst is due to the presence of the hydrogenated 3MT product, 3MTHT, responsible of a significant lower HDS yields. Regarding

the support effect, **alumina supported catalysts** have demonstrated **a higher activity than on silica supported catalysts** which is **attributed to the lower Co/Mo ratio in the CoMoS crystallites as characterized by XPS and also NO FTIR.**

However, whereas the HDS/HYDO selectivity reported is shown to be quasi-equivalent at low HDS regardless the support, selectivity differences are revealed for higher HDS reaction progress (except for the lowest dMo). The **following order of selectivity is demonstrated at high HDS reaction progress: CoMoS/SiO_2 >CoMoS/$\delta\theta$-Al_2O_3 >CoMoS/γ-Al_2O_3.**

Finally, a quantitative analysis of initial activities (related to the HDS and HYDO reactions and the corresponding selectivity) have been undertaken on the purpose of making the link with the CoMoS phase and support features.

In the future, it will be interesting to refine the kinetic analysis of the selectivity by performing a complete kinetic model. In line with the HDS catalysts activity in presence of thiophenic or olefinic feedstocks bringing forward the adsorption competition phenomena between thiophenic or olefin compounds (Chapter III. Appendix 19), a Langmuir-Hinshelwood kinetic model has been initiated within the framework of this work and should be continued. Indeed pursuing this approach could further to take into account both adsorption and reaction steps related to the reactant and products formed (especially alkene, H_2S, alkylthiophene and hydrogenated 3MT) and determine which predominant(s) step(s) and intermediates could impact the HDS/HYDO selectivity.

Subsequently, a detailed description of the CoMoS phase has been undertaken by direct spectroscopic approach. HRTEM analysis has enabled to evaluate the promotor, support and Mo coverage effect on the size of the CoMoS phase. It was demonstrated that the **Co-promoter affect directly the size slab by a decrease of the slab length only for $\delta\theta$-Al_2O_3 supported catalyst and both length and stacking of the slab for SiO_2 supported catalyst**. Thus, combined with DFT calculation study, the presence of Co atoms decorating the edges of the MoS_2 slab could explain the stabilization of smaller sizes by reducing the edge energies at the support surface. Since, on silica this effect is not observed, this could be also due to a less promotional degree reached on this support as quantified by XPS and FTIR NO.

Moreover, an effect of the dMo on the length and stacking of the CoMoS slab was observed regardless the support: **the higher the dMo, the larger the slab length observed**. Moreover,

nature of the hydroxyls located at the alumina surfaces was characterized by IR analysis in combination with available DFT calculations in order to explain the higher sensitivity of the slab size to the dMo parameter as well as the lower slab sizes observed on γ-Al_2O_3 than on $\delta\theta$-Al_2O_3.

Regarding the microscopy technique, a significant support effect on the size and stacking of the slab was observed between alumina and silica supported catalysts. **Larger slab sizes of the CoMoS phase was observed on silica support compared with γ-Al_2O_3 but also slightly higher stacking compared with both γ- and $\delta\theta$-aluminas.**

To explore more precisely the nano-structure and two-dimensional (2D) morphology of CoMoS nano-crystallites interacting with the three different supports, HR HAADF STEM analysis was performed. More precise investigation has been undertaken on the speciation of the CoMoS phase supported on the well defined $\delta\theta$-Al_2O_3 platelets. It is suggested that **MoS_2 crystallites are either growing in different way or are stabilized differently according to the alumina facet.** Indeed, particular length distributions of the CoMoS crystallites were revealed as function of the main facets exposed by the $\delta\theta$-Al_2O_3 platelets: basal (110) facet, and lateral (100) and (111) facets. **Larger average length of slab is found on the lateral facets (100) and a smaller one is found on the basal alumina facet.** This smaller size may be assigned to the presence of the μ_1-OH-Al_{IV} sites on these specific facets. Thus, **the (110)/(100) facet ratio, differing in the nature of its hydroxyls, could be a relevant parameter driving the slab length on $\delta\theta$–Al_2O_3 and more extensively to the alumina support.** In parallel, FT-IR spectroscopy of the alumina supports demonstrated that on the $\delta\theta$-Al_2O_3 support, the neutral μ_1-OH-Al_V sites (ν_{OH}=3730 cm^{-1}) are predominant with respect to a more diverse distributions of OH sites on the γ-Al_2O_3 support. This may impact the catalyst at two levels: the genesis of the active phase and the catalytic activity. Regarding the catalytic activity, it appears that the **higher proportion of μ_2-OH and μ_3-OH acid sites on γ-Al_2O_3 may be at the origin of the stabilization of olefinic compounds on the γ-Al_2O_3 surface which would promote the hydrogenation of olefins versus $\delta\theta$-Al_2O_3.** In the case of silica, due to the even lower acidity character of silanols, the olefinic molecules are even less stable than on aluminas. This parameter could explain in part the order of HDS/HYDO selectivity observed: CoMoS/γ-Al_2O_3 < CoMoS/$\delta\theta$-Al_2O_3 < CoMoS/SiO_2.

In perspectives, it will be interesting to conduct a specific study on the genesis of the CoMoS slab regarding the nature of the alumina support used. To realize this research work, model aluminas, γ, δ, θ and α should be used with the aims to strengthen the results obtained so far in this work i.e. nature of the alumina facets and its associated hydroxyls engaged in the speciation and stabilization of the oxide precursors as well as on of the resulting CoMoS phase. Moreover, Deuterium-DRIFT experiments could be used to characterize and discriminate the hydroxyl impacted or consumed by the oxide precursors and CoMoS phase presence.

Additionally, thanks to this high resolution technique, the **two-dimensional (2D) morphology of CoMoS nano-crystallites** was observed. Regardless the support, hexagonal and truncated triangular shapes of CoMoS slab were revealed. Based on the HR STEM observation and DFT calculations, two populations of slab could coexist at the support surface: the **truncated triangular and the quasi-hexagonal shapes assign to unpromoted MoS_2 and Co-promoted MoS_2 respectively.** Other possible interpretations are to consider either two major different promotions or a possible direct support effect leading to observe the truncated triangular and the quasi-hexagonal shapes of the CoMoS slab.

The next step would be to obtain a statistic of both populations MoS_2 slab, hexagonal and triangular truncated shape. This could allow to refine the 2D morphology model of the CoMoS slab by considering two morphology of slab which may intrinsically depends on the promoter/molybdenum ratio in the slab. Moreover, by correlating it with the catalytic performances, it could provide confirmation on the origin of slab population. This could help to better quantify the heterogeneity of unpromoted and promoted slabs, instead of assuming an mean promoter/molybdenum ration inside the slabs as assumed today. Such a refined quantification should certainly improve the prediction of catalytic activity and selectivity.

Then, interactions between the CoMoS phase and the support was investigated thanks to the **XPS analysis combined with DFT calculation.** Qualitative analysis on peak positions of the Mo3d contribution related to the MoS_2 could suggest that the S coverage of the M-edge and S-edge could be different. Moreover, size effect could directly impact the XPS peak positions of Mo contribution, since diminishing the MoS_2 size enhances the edge

contributions. The assumption that supports could govern through electronic transfer the lower binding energy of the Mo engaged in the supported CoMoS phase was also addressed but this seems to be incompatible. Then, relative quantification of the Mo atoms engaged in the MoS_2 as well as the Co decorating the edge of the CoMoS slab was determined. This XPS quantification combined with XRF, TEM analysis (slab length) and previous DFT calculations has made it possible to build a 2D morphology model of the CoMoS slab providing so, a nanoscale description of the CoMoS slab. Furthermore, this model takes various parameters (length slab, promotion, morphology as function of the support, dMo or Co/Mo ratio) in consideration together leading to explore the interplay between each of them. The quantitative description of the Mo and Co atoms located at the M- or S-edge of the CoMoS slab have made it possible to streamline partly the catalytic activity of the HDS catalysts. **Thus, the lower HDS activity observed for the silica-based catalysts was suggest related to the significant low relative and effective amount of Co atoms on the S-edge.** Moreover, more specifically on $\delta\theta-Al_2O_3$ supported catalysts, the HDS activity increasing with the Co/Mo ratio could be related to the increase of the cobalt atoms located at the edges, as well. As a consequence, a **correlation can be found between activities and the edge sites population quantified so far.** Indeed, **the higher correlation was found by correlate the 3MT or HDS activities with the Co atoms located at the edge (M- and S-edge)** which is consistent with the literature assuming that 3MT is adsorbed strongly on both M- and S-edge promoted by Co atoms. However, **to make possible this correlation, the intrinsic activity has to be normalized by the stacking number** into account leading to finally considered that only the Co edge atoms located at the top of the stacking might be responsible of the catalytic properties. This result could suggest that **only the edge of the top slab is (more) active or (more) available to reactant adsorption and/or transformation.** Moreover, this structure-activity relationship could suggest that the statistic slab morphology is in favor of the hexagonal shape.

At this stage no correlation was found between the HDS selectivity and a specific distribution of cobalt at the M- and/or S-edge. However, HDS selectivity values obtained for each catalysts are closed, so the 2D morphology model built could be not pertinent to discriminate such narrow spreads. More broadly, one may wonder if the unique hexagonal shape of the CoMoS crystallites is relevant as the predominant shape as previously observed

in STEM with the presence of truncated triangular shape which may correspond to unpromoted slabs. Moreover, uncertainties of the Co and Mo atoms distribution related to the XPS quantification and TEM analysis cannot be neglected.

As previously, it would be interesting to refine this model by considering the 2D morphology of the CoMoS slab observed in HRSTEM with the aim of rationalized the HDS selectivity by the 2D morphologic model, it would be interesting to study catalysts with selectivity variation reasonable faced with uncertainty of the 2D morphology model and that correlation obtained may be relevant.

A further description of the CoMoS phase and other sulphided phases such as MoS_2 and Co_9S_8) as function of the support, $\delta\theta$-Al_2O_3, γ-Al_2O_3 and SiO_2, was conducted by **indirect NO FTIR spectroscopy**. By combining FTIR spectroscopy and DFT calculations, we have investigated the nature of sites of sulfided phases probed by the NO molecule. Different mathematic approaches were used. First, the second derivative treatment was applied to output the overlapped contributions which are not resolved in the initial IR spectrum of HDS catalyst systems. According DFT calculations, two major specific contributions at 1846 and 1790 cm^{-1} have been identified on alumina-based catalysts which are respectively assigned to the cobalt promoted M-edge sites and promoted M-edge or S-edge at high NO coverage. NO adsorption on silica supported catalyst revealed a different spectroscopic feature with an intense contribution at 1799 cm^{-1} which could be related to the presence of non-promoted sites. This latter observation explains the lower HDS activities generally measured for silica supported catalysts compared to the alumina ones (at iso Co/Mo ratio and dMo). **This technique seems to be rather powerful in order to provide accurate insights into the nature of active sites present on the CoMoS phase as a function of the support.**
In addition, chemometric decomposition treatments of the IR spectra has been performed as function of NO contact time in order to discriminate the presence and nature of the different populations of NO-sorbing phases, MoS_2 promoted/non promoted and Co_9S_8, according the support used, $\delta\theta$-Al_2O_3, γ-Al_2O_3 and SiO_2. This technique could suggest that the concentration of Co_9S_8 phase seems to be lower on γ-Al_2O_3, which may correspond to a higher promotion degree of the sulphided phase (compared to $\delta\theta$-Al_2O_3, and SiO_2 supports).

The NO FTIR could be extended to other HDS catalysts at variable dMo and Co/Mo ratio in order to confirm these observations. Besides, this could contribute to reach a site quantification of the CoMoS phase (Co or Mo at the M- or Sedge) as function of the catalyst considered. Chemometric could be performed in parallel to understand more precisely the relevance of the main contributions obtained. Preparation of model catalytic system could be helpful to develop even more quantitative aspects of this technique. The first attempt proposed to correlate IR NO with catalytic activity could also be improved by refining the decomposition of each area as a function of the nature of edge sites identified in the spectrum.

At this stage, in the upper part, the discussion was focused on the use of conventional *ex situ* characterizations of HDS catalysts performed after sulfo-reductive treatment for the interpretation of the catalytic performances measured in HDS reaction. But it is important to notice that the surface active sites present in HDS conditions (temperature, pressure, H_2 excess and reactant/products presence) could differ significantly from what is observed in terms of sulphided phase morphology, sulfur coverage, CUS concentrations during the HDS reaction. In order to get rid of such limitations, alternative methodology which consists in performing in situ characterizations of the catalyst directly after activation and/or in working conditions was undertaken. To achieve this indirect and unconventional approach, a **Gas Chromatography coupled with Diffuse Reflectance InfraRed Fourier Transformed Spectroscopy (GC-DRIFTS) and with Attenuated total reflectance (GC-ATR)** were built and the dedicated methodology was developed during this PhD work.

In situ DRIFT experiments have been performed to follow adsorption and subsequent desorption of 3-methylthiophene (3MT), model molecule representative of sulphur compounds from feedstock of FCC gasoline on the surface of promoted CoMoS catalysts supported on alumina or silica. **3MT adsorption on SiO_2 support and both catalysts (CoMoS/SiO_2 and CoMoS/γ-Al_2O_3) was found reversible upon evacuation.** However, **γ-Al_2O_3 exhibits additional spectral features related to the stronger interaction of 3MT on the surface, probably inducing 3MT polymerization reaction at the alumina surface.** The weak acidity the hydroxyl groups at the γ-Al_2O_3 surface could contribute to this specific reactivity whereas on silica no such observation has been made.

Moreover, *in situ* ATR-IR technique has been used to study in more details contribution due to the adsorbed surface species related to the 3MT adsorption. ATR-IR spectra obtained for γ-Al_2O_3 in contact with 3MT (diluted in inert gas) confirmed contributions due to polymerized species in agreement with DRIFT experiments. However, because of no additional IR contributions appear when 3MT is in contact with CoMoS/γ-Al_2O_3, it indicates that the surface species observed are located on alumina surface sites. Again on silica, such an irreversible interaction was not found.

New contributions on the catalyst surface were observed when **ATR-IR spectra** were recorded after **introduction of 3MT in presence of H_2.** For the first time, **contributions of the adsorption of 3MT on coordinatively unsaturated sites present on the surface of the CoMoS phase could be observed.**

Further to this work, it would be useful to evaluate the reactant/active phase/support reactivity in presence of 23DMB2N, model olefin molecule. Thus, complementary adsorption/desorption experiments should be performed, followed by GC-DRIFT and GC-ATR. Additionally, in the same context, reactants competitive adsorption experiments between 3MT and 23DMB2N should be undertaken. According to the advantage of GC-ATR system (absence of gas phase contributions observed in the IR analytical system), it would be interesting to start investigating the reaction steps on HDS catalyst in presence of thiophenic, olefinic and more relevant FCC gasoline feedstocks.